Polarimetry of Laser Plasma Accelerated Electron Beams

Dissertation
zur Erlangung des Doktorgrades
an der Fakultät für Mathematik, Informatik und Naturwissenschaften
Fachbereich Physik
der Universität Hamburg

vorgelegt von
Jennifer Popp

Hamburg
2025

Gutachter/innen der Dissertation:	Dr. Jenny List
	Prof. Dr. Gudrid Moortgat-Pick
Zusammensetzung der Prüfungskommission:	Dr. Jenny List
	Prof. Dr. Gudrid Moortgat-Pick
	Prof. Dr. Erika Garutti
	Prof. Dr. Ingrid-Maria Gregor
	Prof. Dr. Dorota Koziej
Vorsitzende/r der Prüfungskommission:	Prof. Dr. Dorota Koziej
Datum der Disputation:	13.06.2025
Vorsitzender des Fach-Promotionsausschusses PHYSIK:	Prof. Dr. Wolfgang J. Parak
Leiter des Fachbereichs PHYSIK:	Prof. Dr. Markus Drescher
Dekan der Fakultät MIN:	Prof. Dr.-Ing. Norbert Ritter

Abstract

Laser Plasma Acceleration (LPA) with its extremely high gradients promises compact accelerators and great progress has been made in that direction. However, many applications in nuclear and high energy physics require polarised electron beams. The motivation of the LEAP project at DESY is the first time demonstration of LPA with polarisation. This thesis focuses on the design and commissioning of a Compton transmission polarimeter to verify electron polarisation in future LEAP experiments. The polarimeter makes use of the production of circularly polarised bremsstrahlung during the passage of the electrons through a suitable target. The photon polarisation is then measured with the aid of the transmission asymmetry related to the magnetisation direction of an iron absorber. A Monte Carlo design study revealed that a dedicated bremsstrahlung converter target had little impact on the asymmetry and was therefore omitted from the final design. Furthermore, resolving the small anticipated asymmetries (~ 1.5 ‰) within a feasible number of shots requires an energy resolution better than 2 % for the calorimeter detecting the transmitted photons. Consequently, a homogeneous lead-glass calorimeter was constructed.The LEAP polarimeter was commissioned using an unpolarised electron beam. It was found to perform as designed; however, the measurements were dominated by systematic uncertainties due to false asymmetries arising from fluctuations in beam charge and energy. The analysing power of the polarimeter was determined to be 11.74 ± 0.18 %.

Kurzfassung

Laser-Plasma-Beschleunigung (LPB) bietet mit ihren extrem hohen Gradienten das Potenzial für sehr kompakte Beschleuniger, und in diesem Bereich wurden bereits erhebliche Fortschritte erzielt. Allerdings erfordern viele Anwendungen in der Kern-Hochenergiephysik polarisierte Elektronenstrahlen. Das LEAP-Projekt am DESY zielt darauf ab, erstmals die Erzeugung polarisierter Elektronenstrahlen mittels LPB zu demonstrieren. Diese Arbeit konzentriert sich auf die Entwicklung und Inbetriebnahme eines Compton-Transmissionspolarimeters zur Verifizierung der Elektronenpolarisation in zukünftigen LEAP-Experimenten. Das Polarimeter nutzt die Erzeugung zirkular polarisierter Bremsstrahlung während der Passage von Elektronen durch ein geeignetes Target. Die resultierende Photonenpolarisation wird durch Messung der Transmissionsasymmetrie in Abhängigkeit von der Magnetisierungsrichtung eines Eisenabsorbers bestimmt. Eine Monte-Carlo-Designstudie ergab, dass ein spezielles Bremsstrahlungskonverter-Target nur einen geringen Einfluss auf die Asymmetrie hat. Es wurde daher in der finalen Konstruktion weggelassen. Darüber hinaus erfordert die Auflösung der sehr kleinen zu erwartenden Asymmetrien ($\sim 1,5$ ‰) innerhalb einer realistischen Anzahl von Messungen eine Energieauflösung von besser als 2 % für das Kalorimeter, das die transmittierten Photonen detektiert. Daher wurde ein homogenes Bleiglas-Kalorimeter konstruiert. Das LEAP-Polarimeter wurde mit einem unpolarisierten Elektronenstrahl in Betrieb genommen. Es zeigte sich, dass das Polarimeter wie vorgesehen funktioniert, jedoch werden die aktuellen Messungen durch systematische Unsicherheiten dominiert, die durch falsche Asymmetrien aufgrund von Fluktuationen in der Strahlladung und -energie verursacht werden. Die bestimmte Analysierstärke des Polarimeters hat einen Wert von $11,74 \pm 0,18$ %.

Eidesstattliche Versicherung

Hiermit versichere ich an Eides statt, die vorliegende Dissertationsschrift selbst verfasst und keine anderen als die angegebenen Hilfsmittel und Quellen benutzt zu haben. Sofern im Zuge der Erstellung der vorliegenden Dissertationsschrift generative Künstliche Intelligenz (gKI) basierte elektronische Hilfsmittel verwendet wurden, versichere ich, dass meine eigene Leistung im Vordergrund stand und dass eine vollständige Dokumentation aller verwendeten Hilfsmittel gemäßder Guten wissenschaftlichen Praxis vorliegt. Ich trage die Verantwortung für eventuell durch die gKI generierte fehlerhafte oder verzerrte Inhalte, fehlerhafte Referenzen, Verstöße gegen das Datenschutz- und Urheberrecht oder Plagiate.

Hamburg, den 21. Juli 2025

Contents

Chapter 1.

Introduction

Spin-polarised electron beams are a powerful tool in particle and nuclear physics, enabling precise studies of fundamental interactions [1]. In electron-positron colliders, for example, their use enhances sensitivity to the weak force, allowing for improved measurements of electroweak couplings, Higgs boson production, and potential physics beyond the Standard Model [2, 3]. By controlling beam polarisation, experiments can suppress background processes and isolate weak interaction effects (cf. section 2.1.4). Another important application of polarised electron beams is in nuclear physics, such as in deep inelastic scattering experiments at the upcoming Electron-Ion Collider [4], where polarised electrons collide with polarised nucleons to probe the spin structure of the nucleon.

In storage rings, electrons self-polarise through the Sokolov-Ternov effect [5], where their spins gradually align due to spin-flip transitions in the magnetic field, leading to spontaneous polarisation. In contrast, at other accelerators, external methods are necessary to polarise the electrons. Nowadays most often Gallium Arsenide photo-cathodes within DC high voltage photo-guns are used for this purpose [6]. For instance, the Stanford Linear Collider achieved beam polarisation of $76 \pm 4\%$ [7] and the International Linear Collider envisions electron beam polarisation levels exceeding 80% using this technology [8].

However, these sources rely on further acceleration, which is typically achieved using radio frequency (RF) resonators. The acceleration gradient in such structures is fundamentally limited by RF breakdown at very high acceleration gradients, restricting the achievable energy gains. Plasma-based accelerators, on the other hand, do not suffer from these limitations. By using intense laser or particle beams to drive waves in a plasma, they can sustain acceleration gradients up to three orders of magnitude higher [9], making them a promising candidate for compact sources of polarised electron

beams.
While the potential of plasma accelerators is clear, their impact on electron polarisation remains an open question. Theoretical studies predict that electron beam polarisation can be maintained during plasma acceleration [10], and several simulation-based concepts for generating polarised electron beams using Laser Plasma Acceleration (LPA) with a prepolarised plasma source have been proposed [11–14]. However, experimental verification is still lacking.
This is precisely what the LEAP (**L**aser **E**lectron **A**cceleration with **P**olarization) project at the Deutsches Elektronen-Synchrotron DESY aims to address. It serves as a proof-of-principle experiment designed to demonstrate the generation of spin-polarised electron beams from an LPA source, along with their successful transport. To verify this, the degree of polarisation of the accelerated electron beam must be measured.
The aim of this work, as part of the LEAP effort, is to design and commission a Compton Transmission Polarimeter. In this setup, γ-rays produced by bremsstrahlung pass through an iron absorber core that is magnetised by a surrounding solenoid. The transmission rate depends on the relative orientation between the photon spin and the magnetisation direction of the iron. The resulting transmission asymmetry with respect to the magnetisation direction is proportional to the initial electron polarisation.

This thesis is structured as follows: It begins with the theoretical foundations of polarised electron beams and laser plasma acceleration from a prepolarised plasma source (cf. chapter 2), polarimetry (cf. chapter 3), and the use of Monte Carlo simulations and Geant4 (cf. chapter 4). This is followed by a description of LEAP_SIMS, a software framework developed for simulation studies of the polarimeter (cf. chapter 5). Next, a design study is presented (cf. chapter 6) followed by a detailed description of the polarimeter that was constructed (cf. chapter 7). Finally, the commissioning of the polarimeter using an unpolarised LPA electron beam for a zero-polarisation measurement is described (cf. chapter 8), followed by the conclusion in chapter 9.

Chapter 2.

Laser Plasma Acceleration of Polarised Electron Beams

This chapter provides a brief overview of the fundamental concepts related to Laser-Plasma Acceleration (LPA) of polarised electron beams. The discussion begins with an introduction to polarised beams, followed by an explanation of the working principles of LPA. The mechanism of accelerating a polarised electron beam using a prepolarised plasma source is then examined.
Additionally, the LEAP project at DESY and its objectives are introduced, along with FLARE as a key experimental facility. Finally, an overview of beam diagnostics and the role of plasma lenses in controlling and focusing electron beams is provided.
This chapter sets the foundation for the subsequent discussion on polarimetry, which is crucial for verifying the successful acceleration of polarised electron beams.

2.1. Polarisation

To understand the generation of polarised electron beams, it is essential to first explore the concept of polarisation. At its core, polarisation is based on spin, a fundamental property of particles (cf. section 2.1.1). This work primarily focuses on the spin polarisation of electrons, which is examined in detail in section 2.1.2. However, photon polarisation also plays a crucial role in measurement processes (cf. chapter 3). Unlike electron polarisation, which involves spin alignment, photon polarisation generally refers to the geometric orientation of the electric and magnetic field vectors. This concept is further discussed in section 2.1.3. The following sections build on

well-established principles of spin physics, polarisation, quantum theory, and optics, drawing from foundational works such as [1, 15–23], which provide a comprehensive treatment of these concepts.

2.1.1. Spin as a Quantum Observable

Spin angular momentum is an intrinsic quantum mechanical property of particles. Unlike orbital angular momentum, it is not associated with any physical rotation or motion of the particle in space and has no direct classical analogue [19]. Because of this, spin cannot be understood in classical terms and must be described entirely within the mathematical framework of quantum mechanics. The latter allows for statistical statements to be made about the outcomes of measurements performed on an ensemble of quantum states.
Mathematically, the physical observable spin angular momentum is represented by the spin operator $\vec{\hat{S}}$, a vector of operators $(\hat{S}_x, \hat{S}_y, \hat{S}_z)$ that act on the quantum state $|\psi\rangle$ of a particle. These operators are hermitian, hence, their eigenvalues are real. A measurement of the observable spin will always yield one of these eigenvalues.
The components of $\vec{\hat{S}}$ do not commute [1]:

$$[\hat{S}_i \hat{S}_j] = i\hbar\epsilon_{ijk}\hat{S}_k \tag{2.1}$$

where ϵ_{ijk} is the Levi-Cevita-Symbol and $\hbar$ the reduced Planck constant. It then follows from Heisenberg's generalised uncertainty relation that it is only possible to measure one component of $\vec{\hat{S}}$ at a time [20]. Moreover, measuring one component disturbs the others by an indefinite amount, as the non-commuting components become indeterminate after measurement [21]. However, the total spin magnitude $\vec{\hat{S}}^2$, defined as $\hat{S}_x^2 + \hat{S}_y^2 + \hat{S}_z^2$, commutes with each component of $\vec{\hat{S}}$, allowing $\vec{\hat{S}}^2$ and the spin projection onto any one axis to be measured simultaneously.
As mentioned above, only specific discrete measurement results are allowed, namely the eigenvalues of the corresponding operators. A measurement of $\vec{\hat{S}}^2$ results in eigenvalues of the form [21]:

$$\vec{\hat{S}}^2|\psi\rangle = s(s+1)\hbar^2|\psi\rangle \tag{2.2}$$

where s is the spin quantum number associated with the eigenstate $|\psi\rangle$. s can take integer or half-integer values, such as:

$$s = 0, \frac{1}{2}, 1, \frac{3}{2}, 2, \frac{5}{2}, \dots \tag{2.3}$$

Each particle has a fixed spin quantum number. Particles with half-integer spin are referred to as fermions (e.g., baryons, leptons, and quarks), while those with integer spin are known as bosons (e.g., mesons and force mediators).
For a given s a measurement of the spin projection onto an axis yields:

$$\hat{S}_i|\psi\rangle = m_s\hbar|\psi\rangle \tag{2.4}$$

where m_s is the magnetic quantum number associated with the spin component along the i-th axis. The possible values of m_s are:

$$m_s = -s, -s+1, \dots, s-1, s \tag{2.5}$$

In quantum mechanics, the state of a system can either be a definite eigenstate of the spin operator, in which case the measurement outcome is deterministic and corresponds to the associated eigenvalue, or it can be a superposition of eigenstates. If the system is in a superposition, the measurement causes the wavefunction to collapse to one of the eigenstates, with the probability of observing a particular eigenvalue given by the square of the amplitude of the corresponding coefficient in the superposition. The general state in superposition can be written as:

$$|\psi\rangle = \sum_{m_s} c_{m_s}|s, m_s\rangle \tag{2.6}$$

where c_{m_s} are the complex coefficients, and the probability of measuring the eigenvalue $m_s\hbar$ is given by $\left|c_{m_s}\right|^2$, the square of the absolute value of the coefficient corresponding to that eigenstate.

2.1.2. Polarised Electron Beams

Spin polarisation describes the extent to which electron spins are aligned in a given ensemble. In an unpolarised electron beam, spins are randomly distributed, while in a polarised beam, they tend to align along a specific direction [15].

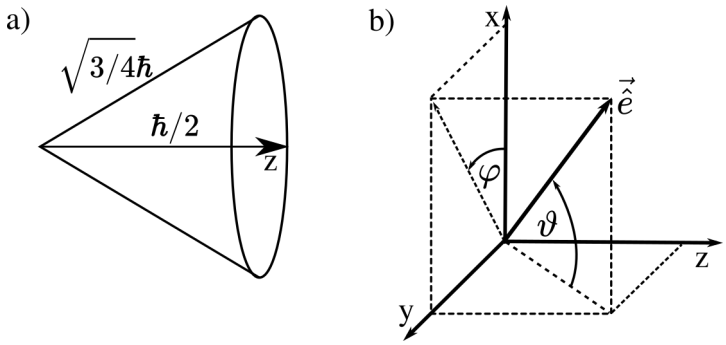

Figure 2.1.: a) spin in z-direction b) spin direction, both adapted from [15]

Electron spin

Electrons are $s = 1/2$ particles. Their total spin angular momentum is given by the eigenvalue equation [19]:

$$\vec{\hat{S}}^2|\psi\rangle = \frac{3}{4}\hbar^2|\psi\rangle. \tag{2.7}$$

The spin component along any chosen axis, such as the z-axis, can take only two possible eigenvalues:

$$\hat{S}_z|\psi\rangle = m_s\hbar = \pm\frac{\hbar}{2}|\psi\rangle \tag{2.8}$$

These correspond to the "spin-up" state $|\uparrow\rangle$ for $m_s = +\frac{1}{2}$ and the "spin-down" state $|\downarrow\rangle$ for $m_s = -\frac{1}{2}$. Due to the commutation relations discussed in the previous section, it is impossible to simultaneously determine all three spin components. Thus, the statement that "the spin points in the z-direction" means only that the z-component is well-defined $\left(\pm\frac{\hbar}{2}\right)$, while the x- and y-components remain indeterminate. Geometrically, this means the spin vector lies on the surface of a conical shell with a total magnitude of $\sqrt{3/4}\hbar$ [15]. A visualisation of this is shown in figure 2.1a).
Mathematically, the spin operators of electrons are represented using the Pauli matrices σ_i:

$$\hat{S}_i = \frac{\hbar}{2}\sigma_i \tag{2.9}$$

with

$$\sigma_x = \begin{pmatrix} 0 & 1 \\ 1 & 0 \end{pmatrix}, \quad \sigma_y = \begin{pmatrix} 0 & -i \\ i & 0 \end{pmatrix}, \quad \sigma_z = \begin{pmatrix} 1 & 0 \\ 0 & -1 \end{pmatrix} \tag{2.10}$$

The spin operators become meaningful when acting on spin states. For electrons, the joint eigenvectors of $\hat{\vec{S}}^2$ and $\hat{S}_z$ are represented as two column matrices, known as spinors [19]:

$$\left|\frac{1}{2}, \frac{1}{2}\right\rangle = |\uparrow\rangle = \begin{pmatrix} 1 \\ 0 \end{pmatrix}, \quad \left|\frac{1}{2}, -\frac{1}{2}\right\rangle = |\downarrow\rangle = \begin{pmatrix} 0 \\ 1 \end{pmatrix} \tag{2.11}$$

A general spin state is given by a superposition of these basis states:

$$\chi = a_1 \begin{pmatrix} 1 \\ 0 \end{pmatrix} + a_2 \begin{pmatrix} 0 \\ 1 \end{pmatrix} = \begin{pmatrix} a_1 \\ a_2 \end{pmatrix} \tag{2.12}$$

where $|a_1|^2$ and $|a_2|^2$ represent the probabilities of measuring the spin in the up or down state, respectively. For a properly normalised state, these coefficients satisfy $|a_1|^2 + |a_2|^2 = 1$. A spin direction in ϑ, φ can be described by the unit vector $\vec{\hat{e}} = \left(\hat{e}_x, \hat{e}_y, \hat{e}_z\right) = (\sin\vartheta\cos\varphi, \sin\vartheta\sin\varphi, \cos\vartheta)$, as illustrated in figure 2.1b).

The Polarisation Vector

As described above, the eigenvalues of the spin operator represent the possible results of individual measurements. Polarisation, however, reflects the average spin direction of a particle ensemble. It is an expectation value [15]. For a pure spin state, i.e. all the spins of an ensemble of electrons have the same general direction of ϑ, φ , this means:

$$\vec{P} = \langle\sigma\rangle = \langle\chi|\sigma|\chi\rangle = \left(a_1^*, a_2^*\right)\sigma \begin{pmatrix} a_1 \\ a_2 \end{pmatrix} = \begin{pmatrix} \sin\vartheta\cos\varphi \\ \sin\vartheta\sin\varphi \\ \cos\vartheta \end{pmatrix} \tag{2.13}$$

The polarisation vector $\vec{P}$ also has the direction of ϑ, φ . The degree of polarisation is given by $\sqrt{P_x^2 + P_y^2 + P_z^2} = 1$ for a normalised, pure state. $\vec{P}$ can be fully determined, provided that measurements of its individual components are performed on separate

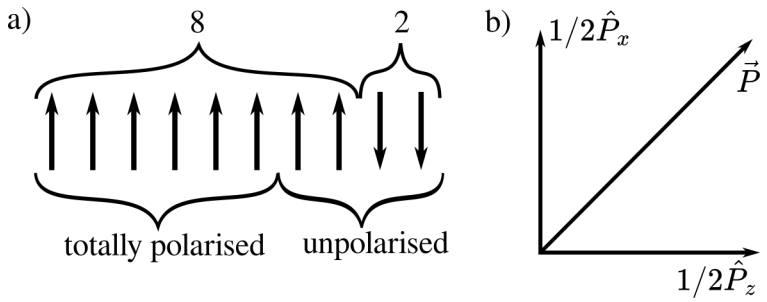

Figure 2.2.: a) Statistical mixture of polarisation states b) superposition of polarisation vectors, both adapted from [15]

particles from an ensemble where all particles can be safely assumed to be in the same state. Partial polarisation is described by the weighted average of individual systems in pure spin states:

$$\vec{P} = \sum_n w^{(n)} \vec{P}^{(n)} = \sum_n w^{(n)} \left\langle \chi^{(n)} \right| \sigma \left| \chi^{(n)} \right\rangle \tag{2.14}$$

with the weighting factor

$$w^{(n)} = \frac{N^{(n)}}{\sum_n N^{(n)}} \tag{2.15}$$

where $N^{(n)}$ is the number of particles in the state $\chi^{(n)}$. The principle of partial polarisation is depicted in figure 2.2a) and that of superposition of polarisation vectors in figure 2.2b).

Scalar Projection of Polarisation

Polarisation is distinguished by the orientation of the spin vectors relative to the beam's direction of motion. For an electron with momentum in z-direction P_x and P_y are called transversal polarisation components. A transversely polarised beam has spin vectors that lie in the plane perpendicular to the beam direction.

This study focuses exclusively on the longitudinal polarisation of electron beams. Here, the spin vectors are aligned either parallel or anti-parallel to the beam's motion. P_z is called the longitudinal polarisation component. In case of a longitudinally polarised beam the polarisation degree then becomes a matter of population imbalance between

the two possible spin states:

$$P_z = \frac{\langle \hat{S}_z \rangle}{S} = \frac{N_\uparrow - N_\downarrow}{N_\uparrow + N_\downarrow} \tag{2.16}$$

where $N_\uparrow$ and $N_\downarrow$ are the populations of electrons with spin-up and spin-down states along the z-axis, respectively. A value of $P_z = 0$ signifies a completely unpolarised electron beam, while $P_z = \pm 1$ signifies a fully polarised beam, with all electrons being either spin-up or spin-down.

A Note on Notation
In the remainder of this work P denotes the polarisation degree in z direction, $\vec{P}$ is the polarisation vector, and $\vec{\xi}$ is the Stokes vector, as defined in GEANT4 (see p. 168 of [24] and section 4.2.4).

2.1.3. Polarisation of Photons

Polarisation has a different meaning for photons than for electrons. This section clarifies the differences between photon spin in the quantum picture and the polarisation of light waves in the classical sense.

Polarisation in the Quantum Picture
Photons are spin-1 bosons and massless particles that always propagate at the speed of light, meaning they do not have a rest frame. Consequently, one considers only the projection of their spin onto their direction of motion, known as helicity. Unlike a massive spin-1 particle, such as the W-boson, which has three possible spin projections ($m_s = -\hbar, 0 + \hbar$), a photon can only exist in two helicity states, $\pm\hbar$ [22].
The two possible helicity states of a single photon correspond to the two circular polarisation eigenstates, right-circular and left-circular. These states are eigenstates of the helicity operator, meaning a photon with definite helicity is always in a circularly polarised quantum state. A general quantum state with superposition coefficients a_1 and a_2 can then take the following forms:

1. **Elliptical Polarisation:** $|a_1| \neq |a_2|$ and both are non-zero.
2. **Circular Polarisation:** One of the coefficients is equal to zero.
3. **Linear Polarisation:** $|a_1| = |a_2|$

Polarisation of Light Waves

In macroscopic light sources, light is generally described as a wave composed of many photons rather than single-photon states. In the classical description, light is an electromagnetic wave, consisting of mutually perpendicular electric and magnetic fields that oscillate perpendicular to both each other and the direction of propagation. Polarisation refers to the orientation of the electric field vector [23]. The possible polarisation states are:

- **Elliptical Polarisation**: The most general case, where the electric field vector rotates around the propagation axis while its magnitude and direction change. Hence, the tip of the vector traces an ellipse.
- **Circular Polarisation**: A special case of elliptical polarisation where the electric field vector rotates in a perfect circle. This occurs when the perpendicular components ($\vec{E}_x$ and $\vec{E}_y$) have equal amplitudes and a phase difference of $\pm 90°$.
- **Linear Polarisation**: The electric field oscillates along a fixed axis perpendicular to the propagation direction, meaning there is no phase difference between the perpendicular components.

Mathematical Description of Light Polarisation

The Stokes parameters provide a modern representation of polarised light, bridging the classical and quantum descriptions. Denoting $E_{0x/y}$ as the amplitudes of the corresponding electric field vector components, ϕ their phase difference, and $\langle\rangle_t$ as time-averaging, the **Stokes vector** is defined as[23]:

$$\vec{\xi} = \begin{pmatrix} \xi_0 \\ \xi_1 \\ \xi_2 \\ \xi_3 \end{pmatrix} = \begin{pmatrix} \left\langle E_{0x}^2 \right\rangle_t + \left\langle E_{0y}^2 \right\rangle_t \\ \left\langle E_{0x}^2 \right\rangle_t - \left\langle E_{0y}^2 \right\rangle_t \\ \left\langle 2E_{0x}E_{0y}\cos\phi \right\rangle_t \\ \left\langle 2E_{0x}E_{0y}\sin\phi \right\rangle_t \end{pmatrix} \tag{2.17}$$

The four components of $\vec{\xi}$ have the following physical interpretations:

- ξ_0: The total intensity of the light.
- ξ_1: Measures the difference between horizontally and vertically polarised light. Positive values indicate more horizontally polarised light, while negative values indicate more vertically polarised light.

- ξ_2: Represents the degree of linear polarisation at $\pm 45°$to the horizontal axis.
- ξ_3: Measures the degree of circular polarisation, which directly corresponds to the photons helicity. Positive values indicate right-circularly polarised light, while negative values indicate left-circularly polarised light.

The Stokes vector definition in GEANT4 (see section 4.2.4) does not use ξ_0.

2.1.4. Helicity, Chirality and the Weak Force

Helicity,[1] is the projection of a particle's spin onto its momentum direction, with the helicity operator being defined as:

$$\vec{\hat{S}} = \vec{\hat{S}} \cdot \frac{\vec{p}}{|\vec{p}|}. \tag{2.18}$$

For a beam of fermions with spin $s = 1/2$, the helicity operator yields +1/2 when the spin is aligned parallel to the momentum direction, and -1/2 when the spin is antiparallel to the momentum.
For massive particles, helicity depends on the reference frame since they move at a finite speed, always below the speed of light. In principle, an observer moving faster than the particle could enter a reference frame where its momentum appears reversed, thereby flipping its helicity. This is precisely the effect of a parity transformation, which inverts the momentum while leaving the spin unchanged.
For massless particles, on the other hand, helicity is the same as **chirality**, a quantum-mechanical property that remains invariant under Lorentz transformations. Chirality is an intrinsic property of fermions that plays a crucial role in their interactions, in particular with respect to the **weak force**. Unlike the strong and electromagnetic forces, which treat left- and right-handed particles symmetrically, the weak interaction violates parity symmetry [27]. This asymmetry arises because the weak force couples exclusively to left-handed fermions and right-handed antifermions.
In collider experiments, this property becomes particularly useful: for highly relativistic particles, helicity effectively corresponds to chirality, which can be exploited for various purposes. For instance, an e^+e^- collider gains several advantages when at least one, or preferably both, beams are polarised [2, 28]. First, since the cross-section of certain interactions depends on the beam polarisation, specific configurations can

[1] This section is largely based on explanations in sections 4.6 and 5.2 of [25] and chapters 5 and 8 of [26]

be chosen to suppress unwanted background or enhance the signal. Second, beam polarisation provides additional observables that enable a more detailed analysis of the chiral properties of processes within and beyond the Standard Model. Finally, by selecting a polarisation configuration where no signal is expected, redundancy measurements can be performed, offering a powerful tool for controlling systematic uncertainties.

2.2. Laser Plasma Acceleration

Ultra-short, high-intensity laser pulses can generate wakefields in gaseous plasmas, producing large-amplitude electric fields that enable the acceleration of charged particles. Not impaired by material breakdown thresholds, plasma accelerators can sustain acceleration gradients of more than 100 GV/m, more than three times greater than conventional rf-accelerators [9]. This capability paves the way for compact, low-cost accelerators with a wide range of future applications.
Laser Plasma Acceleration (LPA) was first proposed by Tajima and Dawson in 1979 [29]. With advancements in laser technology, LPA has become increasingly feasible, leading to the development of various acceleration schemes. This section provides a fundamental overview; for more in-depth information, refer to publications such as [9, 30–32].

Essential Parameters in (Laser) Plasma Acceleration
To understand how LPA works, it is first necessary to clarify key terminology and prerequisites. A widely used definition of **plasma** is:

> "A plasma is a quasineutral gas of charged and neutral particles which exhibits collective behaviour." [33]

In the context of LPA, this definition, in the case of complete ionisation, describes a gas of free electrons and ions whose dynamics are governed by collective electromagnetic interactions.
In the simple case of linear electron motion, when electrons are displaced from the uniform ion background, an electric field arises, acting to restore charge neutrality. Due to their inertia, the electrons overshoot their equilibrium positions, leading to

oscillations at the characteristic frequency [33]:

$$\omega_p = \sqrt{\frac{4\pi n_e e^2}{m_e}} \tag{2.19}$$

where ω_p is the **electron plasma frequency**, n_e is the density of unperturbed electrons, e and m_e are the electron charge and rest mass, respectively [9]. The electric fields arising from electron displacement can be used for plasma-based acceleration. Maximum acceleration occurs when the displacement reaches approximately one plasma wavelength, λ_p [32], where,

$$\lambda_p = \frac{2\pi c}{\omega_p}. \tag{2.20}$$

Still assuming a linear regime, the maximum acceleration gradient can then be expressed as [32]:

$$eE_0 \cong mc^2 \frac{\omega_p}{c} \approx 1 \frac{\text{eV}}{\text{cm}} \cdot \sqrt{n_e}, \tag{2.21}$$

where E_0 is also called the cold non-relativistic wave braking field [34]. From this relation it becomes apparent that the acceleration gradient is directly proportional to the **electron plasma density** n_e. Specifically, to achieve an acceleration gradient of 1 GeV/cm an electron plasma density of $n_e = 10^{18}\text{cm}^{-3}$ is required.
In LPA, laser pulses drive electron displacement. For this to occur efficiently, intense ultrashort laser pulses are required. 'Ultrashort' in this context means that the pulse duration should be approximately equal to or shorter than λ_p. Using the same example as above, this corresponds to λ_p=30 µm and a desirable laser pulse duration of less than 100 fs.
To quantify intensity, a key parameter is the **laser strength parameter** a_0. It is defined as the peak amplitude of the normalised vector potential of the laser field [9]. Here, 'normalisation' refers to expressing the laser field in terms of the momentum it imparts to an electron in a single oscillation, relative to the electrons rest mass, yielding:

$$a_0 = \frac{eE_0}{m_e \omega_0 c} \tag{2.22}$$

where ω_0 is the angular frequency of the laser pulse [30]. a_0 relates to laser peak intensity I_0 with [9]:

$$a_0 = \sqrt{\frac{e^2}{2\pi^2 \epsilon_0 m_e^2 c^5} \lambda_0^2 I_0} \tag{2.23}$$

$$\approx 0.85 \cdot \lambda[\mathrm{m}] \cdot \sqrt{I_0[10^{18}\mathrm{W/cm^2}]}, \tag{2.24}$$

where λ_0 is the central wavelength of the laser pulse. The laser strength parameter determines whether the electron motion in the laser field is linear ($a_0 << 1$) or relativistic ($a_0 >> 1$). As discussed above, efficient LPA requires intense laser pulses, meaning those with $a_0 \gtrsim 1$. Which in the case of a titanium:sapphire laser system ($\lambda_0 = 800\,\mathrm{nm}$) corresponds to pulse intensities on the order of $I_0 \approx 10^{18}\,\mathrm{W/cm^2}$.

Mechanism of LPA in the relativistic regime

Having established the key parameters required for laser-plasma acceleration, the detailed mechanism by which a laser pulse drives a wakefield and accelerates electrons is now examined. Figure 2.3 illustrates this process step by step.

1. The intense ultrashort laser pulse is focused onto a gas target (depicted here as a jet), ionises the gas, and locally creates a plasma (see figure 2.3a)).

2. The gradient of the laser pulse's electromagnetic field energy density gives rise to the ponderomotive force F_p, which acts on charged particles along the laser's path. It can be approximated as [30]:

$$F_p \simeq -\frac{1}{2} mc^2 (\nabla a_0^2) / \sqrt{1 + a_0^2} \tag{2.25}$$

   Due to their high mass, ions remain mostly immobile during the laser pulse, while electrons are pushed radially outward from the laser focus, away from the regions of highest intensity (see figure 2.3b)).

3. Once the laser has passed, Coulomb restoring forces act on the displaced electrons, causing them to oscillate at the plasma frequency ω_p, forming a wave-like structure (see figure 2.3c)). This excited plasma wave, or wakefield, propagates with a phase velocity equal to the laser's group velocity.
   For $a_0 > 1$ the ponderomotive force pushes nearly all electrons away from the axis, forming a spherical bubble initially free of electrons at its centre behind the laser pulse. This is why the relativistic regime is also called the bubble

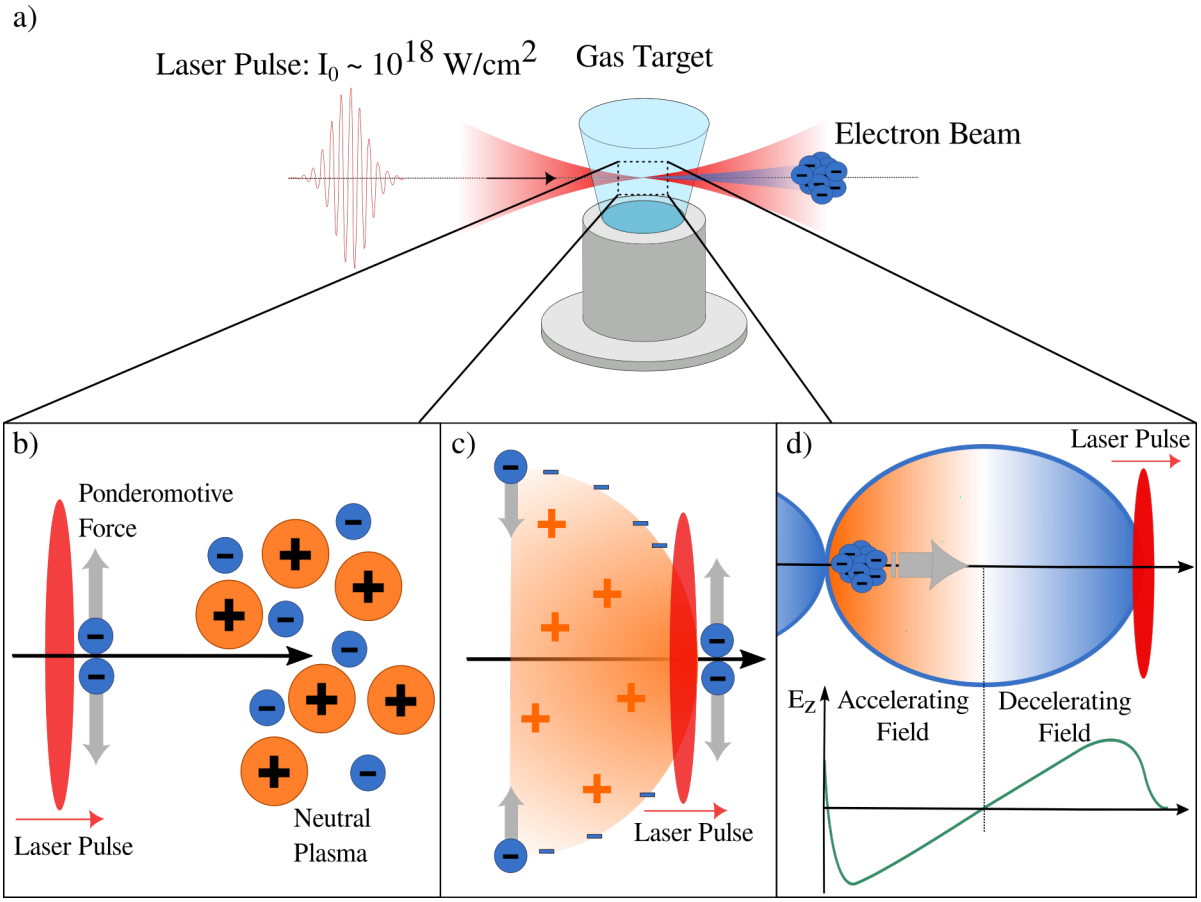

Figure 2.3.: Principle of laser plasma acceleration. a) Relativistically intense laser pulse incident on gas target, locally creating plasma. b) Ponderomotive force pushing electrons radially outward from the highest intensity regions of the laser pulse c) Restoring force acting on electrons, causing them to oscillate and forming a wakefield d) Charge separation in the bubble shaped wakefield causes high electric field gradients. Electrons injected at the back are accelerated.

regime. The displaced electrons continue oscillating around the ions, but their motion quickly becomes incoherent, causing subsequent bubbles to be smaller and smaller. As a result, typically only the first bubble is suitable for acceleration [32].

4. The charge separation generates strong electromagnetic fields. Electrons injected at the correct wave phase, i.e., at the back of the plasma cavity (or bubble), can be efficiently accelerated (see figure 2.3d)). In the nonlinear regime, the amplitude of the plasma wave can exceed the cold non-relativistic wave braking field E_0 [9], leading to extremely high acceleration gradients. In the one-dimensional limit, the maximum electric field amplitude generated by a linear-polarised pulse is given by [35]:

$$E_{\max} = 0.38 a_0^2 \left(1 + \frac{a_0^2}{2}\right)^{-1/2} \sqrt{n_e} \frac{V}{cm} \tag{2.26}$$

Limitations

While the acceleration gradient in an LPA is not limited by material breakdown, there are still fundamental constraints on the maximum energy electrons can gain in a single plasma stage. The most significant limitations arise from dephasing, diffraction, and pump depletion. Dephasing occurs when accelerating electrons gain speed and eventually outrun the accelerating phase of the wakefield, which moves at the group velocity of the laser pulse, slightly less than c. Diffraction limits the interaction length, as a laser beam, tightly focused to several tens of micrometers, naturally spreads out fast as it propagates. Lastly, pump depletion occurs when the laser pulse transfers its energy to the plasma wave; once the pulse is depleted, further acceleration ceases.

2.3. LPA of polarised electron beams using a prepolarised plasma source

Several plasma-based techniques have been suggested for producing polarised electron beams [36], but the most promising approach utilises a prepolarised plasma source in plasma-based accelerators [12, 37]. Using this approach the plasma source is prepared in a way that the free ionised electrons inside have a preferred orientation of spin, before they are finally accelerated by a laser pulse as described in the previous section.

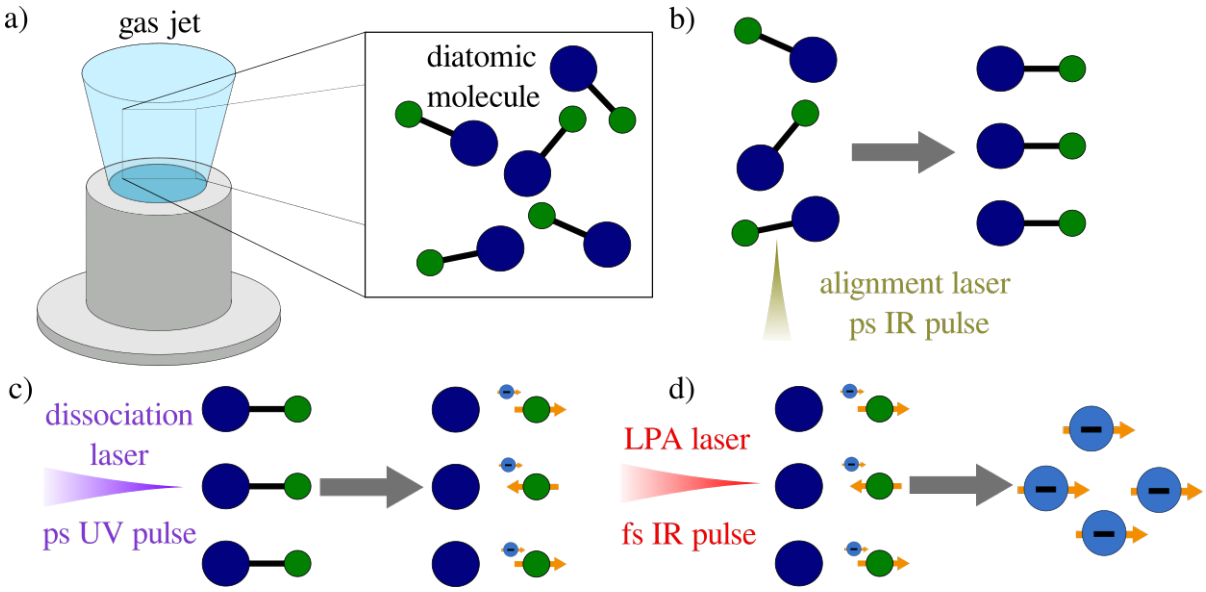

Figure 2.4.: Mechanism of LPA of polarised electron beams using a prepolarised plasma source. a) A target gas of diatomic molecules is chosen b) Molecular bonds are aligned using infrad ps laser-pulse c) Molecules are dissociated using ps UV laser pulse d) Atom ionisation followed by accelratiton of electrons.

One method of doing so is the molecular photo-dissociation of hydrogen halides using a circularly polarised UV laser-pulse [37–44]. The principal working mechanism, as depicted in figure 2.4, can be divided into three steps.

1. **Bond alignment:** The electric field of a linearly polarised infrared (IR) laser pulse is used to align the molecular bonds of diatomic halide molecules [45].

2. **Photo-dissociation:** A circularly polarised UV pulse is directed onto the gas target, parallel to the molecular bond. The molecule absorbs the laser light if the photon energy matches an allowed transition, exciting it into a repulsive state that leads to dissociation. Total angular momentum is conserved during this process. It is first transferred from the laser light to the molecule, and when the molecule dissociates into its atomic fragments, the angular momentum is redistributed between the photofragments. The result are two polarised valence electrons from the hydrogen-halide bond.

3. **Acceleration**: The LPA driver pulse ionises the photofragments while also driving a plasma wakefield. Electrons injected at the correct phase of the wakefield, as described in the previous section, can then be accelerated. Since hyperfine coupling gradually transfers the electron's spin to the nucleus after dissociation

(on a timescale of approximately 350 ps in hydrogen) ionisation must occur on a much shorter timescale [46] to preserve electron polarisation for plasma acceleration.

The choice of target gas

One important consideration for any polarised LPA source employing a prepolarised plasma source is the choice of target gas, as it directly impacts the achievable fraction of polarised electrons and the required wavelength for molecular dissociation. The two valence electrons from the hydrogen-halide bond become polarised, but additional electrons are typically ionised, which dilutes the overall spin alignment and limits the fraction of the theoretically achievable maximum polarisation, P_{max}.

Ideally, one would not use hydrogen halides, but instead pure hydrogen as the target gas, as it has a P_{max} of (near) 100%, since there are no additional electrons with random spin to be ionised. However, the dissociation of H_2 requires laser pulses with wavelengths below 100 nm [47, 48]. Generating such short-wavelength pulses with sufficient intensity remains challenging and is not yet feasible with current laser technology [49].

Using hydrogen halides is a good alternative. Hydrogen fluoride offers the second highest P_{max}, but requires a dissociation laser with a wavelength of less than 150 nm, which is difficult to achieve. Additionally, it forms hydrofluoric acid upon contact with moisture, making it undesirable for use in a laboratory environment.

The next halogen in the periodic table is chlorine. Hydrogen chloride (HCl) has multiple electron levels, and depending on the number of ionised electrons, a maximum electron spin polarisation between 12.5 % and 25 % is feasible. The photodissociation of HCl molecules has been demonstrated at wavelengths around 200 nm [38, 46].

Different proposed schemes

It is not enough to achieve as high an electron spin alignment in the plasma source as possible; the electrons also need to be injected into the correct phase of the plasma wakefield and accelerated, with as little depolarisation as possible. Depolarisation has been shown to mainly occur during the former stage [10]. Various schemes have been investigated using particle in cell simulations and proposed for polarised LPA, including density-down ramp injection [12], self injection [13], the use of Laguerre-Gaussian Laser Beams [11], and colliding pulse injection [14]. A detailed discussion of these schemes is beyond the scope of this thesis. It is sufficient to note that the first three methods come with practical limitations, such as unrealistic density gradients in the precursor gas or limited achievable accelerated charge. The colliding pulse

injection method proposed by Bohlen et al. appears to be the most promising at this time, with simulations – using pure hydrogen as the target gas – resulting in beams with $P > 90\%$, tens of pC charge, low normalised emittance of <1 mm·mrad, and percent level energy spread[2].

2.4. The LEAP Project

LEAP is a project at DESY aimed at experimentally demonstrating laser-plasma acceleration of polarised electron beams for the first time. It will utilise a laser system that has previously demonstrated stable acceleration of electron bunches over several hours [51]. More details about the facility can be found in section 2.5. The project will employ a prepolarised plasma source and use the colliding pulse injection method for plasma acceleration, as proposed by Bohlen et al. in [14]. The conceptual design of LEAP is illustrated in figure 2.5. In total, four laser pulses are required for the process. The first pulse aligns the bonds of HCl, which will be used as the precursor gas. The second pulse dissociates the molecules, and is planned to be generated via fourth-harmonic generation from the fundamental system. Preparatory work on this can be

[2] A 4.4 % energy spread is reasonable for LPAs with polarised beams. For comparison, the ILC electron source is specified to have $\sigma_E/E < 5\%$ with polarisation [8], while LUX@DESY reports $\sim 1\%$ for unpolarised beams. Sub-0.1 % is achievable with energy compression [50]. The influence of beam energy spread on Compton transmission polarimetry is discussed in sections 3.4 and 8.4.2.

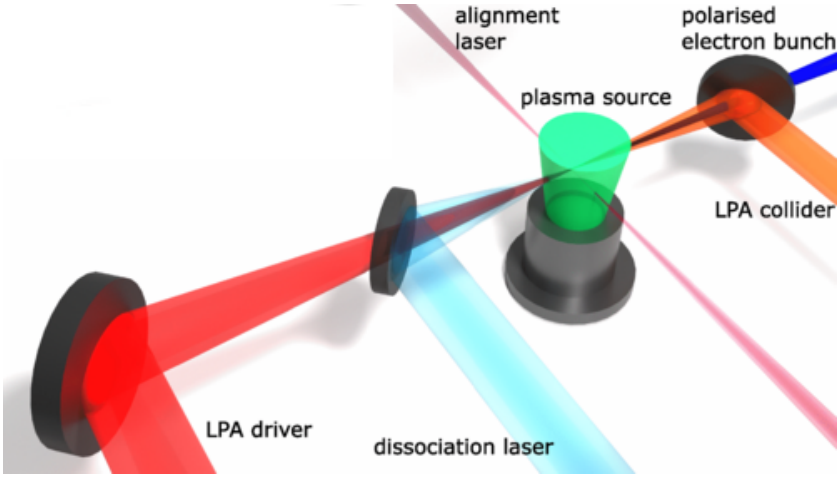

Figure 2.5.: Schematic of the conceptual design anticipated for the LEAP project: LPA employing colliding pulse injection for generating spin-polarised electron beams from a prepolarised plasma source. Drawing adapted from [14].

Beam-Parameter	Expected Value
Polarisation P_{e^-}	$\sim$ 10 %
Bunch energy E_{beam}	30-80 MeV
Bunch charge q	$\sim$ 3 pC
Bunch length τ	$\sim$ 30 fs
repition rate	max. 10 Hz

Table 2.1.: Bunch parameters expected at future LEAP experiments

found in [52]. Finally, two additional pulses are required for ionisation, injection, and acceleration.
The expected beam parameters are summarised in table 2.1. It is important to note that LEAP is a proof-of-principle experiment, and the parameters presented here do not represent the ultimate capabilities of this method and technology. The verification of polarised beams from LPA will be performed using a Compton transmission polarimeter, whose design and commissioning are the main focus of this thesis.

2.5. The FLARE facility

FLARE is a facility at DESY that provides infrastructure for research on laser-plasma accelerators and their applications. LEAP is one of several projects hosted there. The facilitys floor plan is shown in figure 2.6, highlighting the key areas relevant to the accelerator system used for the commissioning work described in section 8: the laser lab, the BOND lab, and the control room.
The **laser lab** houses the facilitys laser systems, including the SPECTRE system a 25 TW titanium:sapphire laser from Amplitude Technologies. It operates at a wavelength of 800 nm, with a maximum repetition rate of 10 Hz and a pulse duration of less than 30 fs.
The laser is propagated to the **BOND** (Beam Optimisation and Novel Diagnostics) **lab**, where it serves as the LPA driver inside the plasma acceleration vacuum chamber. The lab also contains various beam diagnostics for characterising the accelerated electron beams, as discussed in section 2.6. A more detailed description of the SPECTRE system and the accelerator setup can be found in [53], among others.
Data acquisition and control are managed from the **control room**, which oversees the

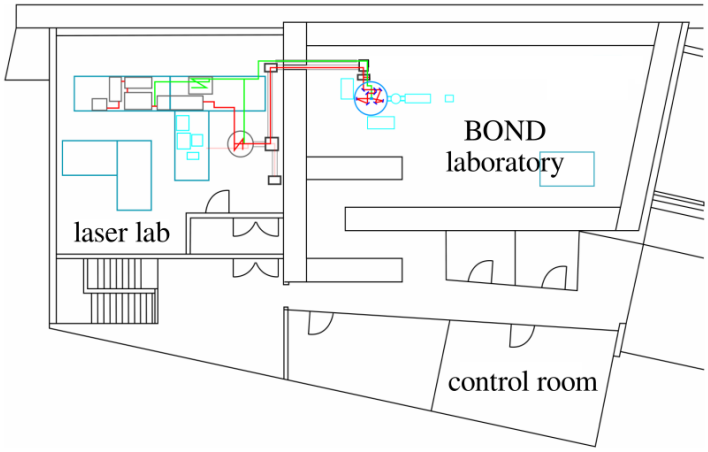

Figure 2.6.: Floorplan of the FLARE facility. Adapted from [53]

accelerator and experimental components. The FLARE facility makes use of DOOCS (Distributed Object-Oriented Control System) [54], a software framework designed for accelerator-based control systems. Each device is accessible via the network and can be monitored and controlled through dedicated applications, with visual interfaces created using jddd (Java DOOCS Data Display) [55].
The FLARE trigger system is synchronised to the master clock of the FLASH accelerator [56, 57], which provides macro pulse numbers. These pulse numbers can later be used to correlate data from different diagnostics.

2.6. Diagnostics for Beam Characterisation

Characterising the properties of a particle beam is not only important for feedback and control but also forms the basis for experimental accuracy, as precise beam parameters are essential for reproducibility and reliable measurements. This section provides an overview of the diagnostics used in the accelerator setup for the commissioning work described in section 8.

2.6.1. DaMon

The DaMon is a diagnostic tool for non-invasive measurement of electron bunch charge [53, 58, 59]. Originally named for its function as a **da**rk current **mon**itor for the

European XFEL, the DaMon is a resonant stainless steel cavity (see Fig. 2.7a) designed to operate in the first transverse magnetic mode (TM01) at a resonant frequency of $f = 1.3\,\mathrm{GHz}$. When an electron beam passes through the cavity, it excites the TM01 mode, generating a voltage described by:

$$U = U_0 \sin(\omega t) e^{-t/\tau} \tag{2.27}$$

where $\omega = 2\pi f$ is the angular frequency and $\tau = Q_L/(\pi f)$ is the decay time. The decay time τ represents how quickly the voltage decays over time, and Q_L is the loaded quality factor of the resonator, which indicates the efficiency of the cavity in storing energy.
The amplitude of this TM01 mode, U_0, is proportional to the beam charge, q. Their relationship is given by:

$$U_0 = qS \tag{2.28}$$

The sensitivity, S, measures how responsive the resonant frequency of a cavity resonator is to changes in certain parameters. Specifically, it is defined as $S = \pi f \sqrt{\frac{Z}{Q_{ext}} \left(\frac{R}{Q}\right)}$, where Z is the line impedance, representing the characteristic impedance of the transmission line, Q_{ext} is the resonator external quality factor related to energy loss due to external coupling mechanisms and $\left(\frac{R}{Q}\right)$ is the normalised shunt impedance, representing the efficiency of the cavity in storing energy relative to its losses and its interaction with charged particles.
By utilising equation 2.28 and knowing all the constants mentioned above one can determine the bunch charge by measuring the amplitude of the TM01 mode. This is independent of the electron beam's position inside the cavity, guaranteeing consistent measurement results no matter where the beam interacts with the cavity fields.
The mode is picked up by two antennas that couple the signal out, directing it to a dedicated electronics unit. This unit filters the signal, converts the amplitude to a logarithmic value, and transmits it to an analogue-to-digital converter (ADC). This process enables the DaMon to detect bunch charges across a dynamic range of seven orders of magnitude, with a minimum detectable charge of approximately 50 fC, limited by the noise in the electronics.

An example ADC trace over time is displayed in figure 2.7b. The peak of this ADC trace, referred to as the DaMon signal for the remainder of this work, can be converted

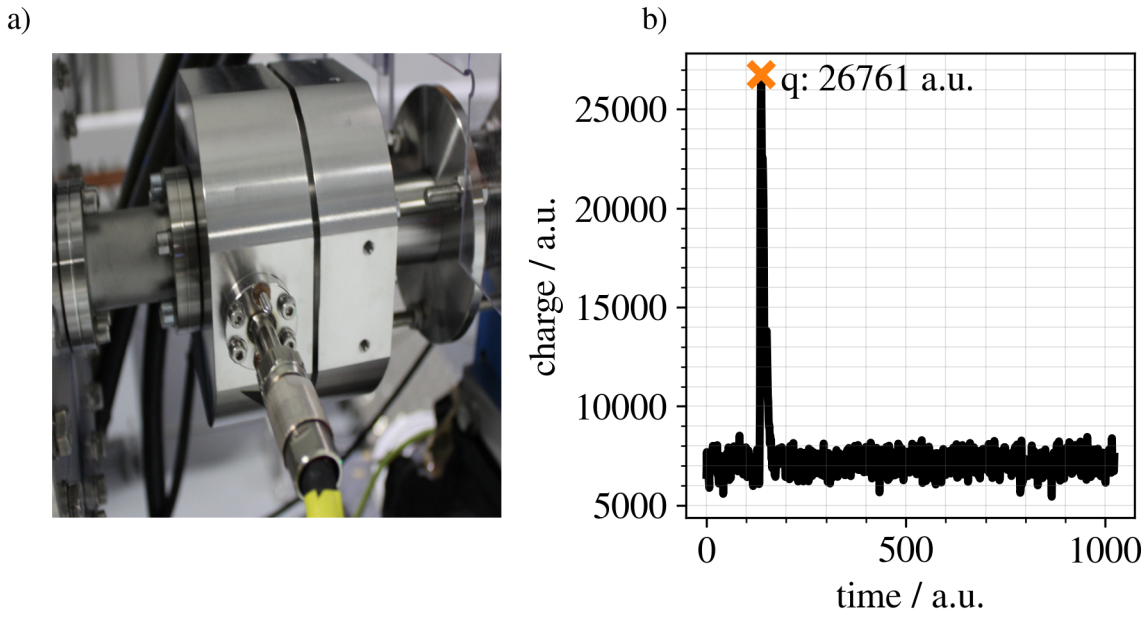

Figure 2.7.: a) Image of the DaMon in the BOND laboratory [53], b) ADC signal recorded by a DaMon charge measurement. Peak marked with cross converts with equation 2.29 to 5.74 pC.

from arbitrary digital units to picocoulombs (pC) using the following formula:

$$q(pC) = p_0 \times 10^{p_1(a.u.)+p_2} \tag{2.29}$$

Where the individual parameters have values of: $p_0 = 9.661 \cdot 10^{-5}$, $p_1 = 5.847 \cdot 10^{-5}$ and $p_2 = 3.209$. The ADC trace is saved for every shot, so that there is a DaMon signal for every shot. These calibration values originate from S. Bohlen, who obtained them through corresponding measurements as part of the work described in [53].

2.6.2. Scintillator Screens

A DRZ-high [60] scintillation screen in combination with a CCD-camera was installed to provide real-time visual feedback and complement the charge diagnostics obtained from the TurboICT and the DaMon (see sections 8.1 and 2.6.1). This screen is used to capture spatial distribution and intensity variations in the electron beam.
"DRZ-high" is the trade name of a type of scintillator screen, distributed by MCI Optonix LLC / Mitsubishi Chemical Incorporated, they contain a layer of the lumines-

cent material gadolinium oxysulfide doped with terbium (Gd_2O_2S:Tb, or Gadox:Tb). This material efficiently converts electron energy into visible light, mostly through fluorescence [61], offering a visual representation of the beam's characteristics.
The principle of operation for the DRZ-high scintillator screen involves three main steps:

1. **Energy Absorption**: As the electron beam passes through the screen, it interacts with the Gadox host lattice. During this interaction, the host lattice absorbs a portion of the electron beam's kinetic energy and transfers it to the terbium ions embedded within the material.

2. **Light Emission**: The energy absorbed by the terbium ions excites them to higher energy levels. As these ions return to their ground state, they release the absorbed energy as visible light through a process called fluorescence. The most significant emission occurs at a wavelength of 545 nm, which appears green.

3. **Fluorescence Capture**: The emitted light is detected by a CCD camera, which captures the intensity and distribution of the fluorescence. This data is used to visualise the electron beam's properties and perform precise charge diagnostics.

DRZ-high screens are composed of powdered Gadox embedded in a transparent binder, layered between a plastic support layer and a PE protective coating. These screens are known for their high light output, with a reported fluorescent efficiency of about 8×10^9 photons/sr/pC, [62],[63]. The decay time of the fluorescence is approximately 1 ms, enabling shot-by-shot measurements at repetition rates up to the kilohertz (kHz) range. While Gadox has a high density of $7.34\,g/cm^3$ and a high average Z, the layer of luminescent material is very thin, only 310 µm [60]. Above a certain threshold energy, the energy loss of the electrons is therefore almost constant [64]. Wu et al. conducted a GEANT4 simulation resulting in a deposited energy of approximately 200 keV per incident electron, independent of the incident electron energy above approximately 10 MeV [63].
This confirms that scintillator screens provide a reliable method for visualizing beam charge distribution. At electron energies of several tens of MeV, the fluorescent light emitted by the scintillator and captured by the CCD camera directly reflects the beam profile. The intensity of the images is proportional to the charge q, calculated using

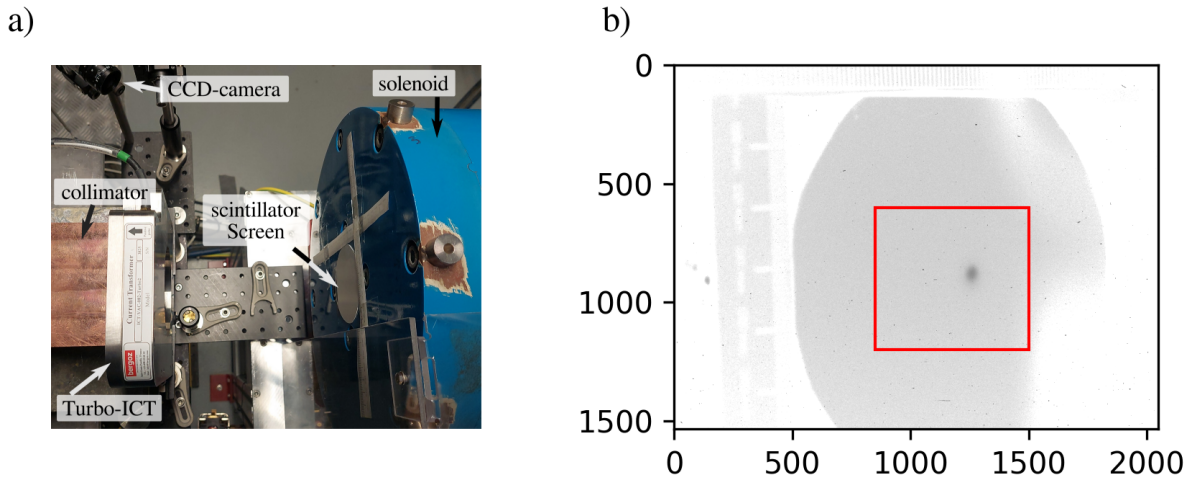

Figure 2.8.: a) Photograph of the DRZ-high scintillator screen and CCD camera as installed in the beamline. b) Camera image of electron beam using a collimator with 1mm diameter. Rectangle marks region of interest(ROI)

the equation:

$$q = \frac{N_{\text{photons}}}{C_s} \tag{2.30}$$

where N_{photons} is the total number of photons emitted by the scintillator into a solid angle of one steradian and C_s is the absolute response of the scintillating screen. This calculation assumes uniformity in the response of the scintillator and takes into account parameters such as the angle between the electron beam and the screen, the effective collection angle, and the light collection efficiency of the optical system.
In this work, the scintillation screen was utilised as a relative charge diagnostic tool rather than an absolute one. To analyse the data, regions of interest (ROIs) were defined in the camera images. An example of an ROI is shown in figure 2.8b, marked by a red rectangle. The scintillation screen signal S_{scint} was then calculated as follows:

$$S_{scint} = \sum N_{c,ROI} - \text{offset} \tag{2.31}$$

where $N_{c,ROI}$ represents the counts in the ROI, quantified as the sum of pixel values. The offset was determined by calculating the mean sum of the pixel values in the ROI for runs conducted without a beam under identical conditions. This approach allows for the subtraction of background noise, ensuring that the signal measurement is more reflective of the actual beam properties.

2.6.3. Dipole Spectrometer

The process planned to be used to measure polarisation, namely Compton scattering, depends on the energy of the incoming electrons (see section 3.1.3). Therefore, it is paramount to accurately determine the energy spectrum of the beam reaching the polarimeter.
The spectrometer installed in the BOND-laboratory utilises the energy-dependent bending radii of electrons in a dipole magnetic field, a common technique for measuring energy spectra in both conventional and plasma-based accelerators. A comprehensive overview of this method is provided by Downer et al. [65].
The dipole spectrometer in the BOND laboratory (schematic shown in figure 2.9a) was recently recommissioned, and a detailed account of this process is documented in the work by C. Varma [66]. The dipole magnet is 500 mm long and the maximum applicable current of 311 A results in a magnetic field amplitude of 0.246 T. The magnetic field is oriented, that the Lorentz-force is deflecting the electrons downwards. Energy dependent bending radii are described by:

$$r_{e^-} = \frac{E_{e^-}}{e_0 B c} \tag{2.32}$$

where E_{e^-} is the electron energy in eV, e_0 is the electron charge, B the magnetic flux density in Tesla and c the speed of light in ms^{-1}. The vacuum chamber inside the dipole magnetic field (50 mm wide, 712 mm long top) has three exit windows, two

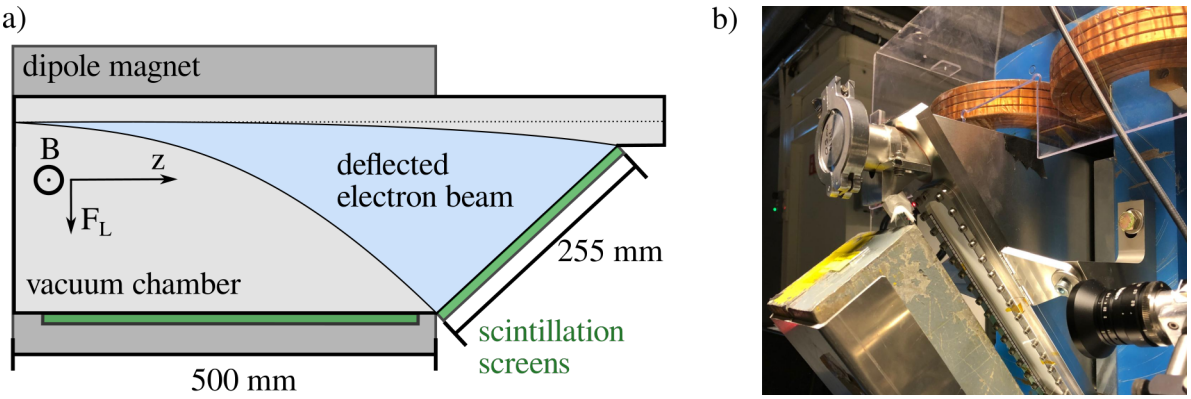

Figure 2.9.: a) Schematic of the dipole electron spectrometer in the BOND laboratory. Original electron propagation in z-direction, magnetic field in x and Lorentz-force F_L acting in y. b) Image of the diagonal DRZ-screen being imaged. During normal operation, the spectrometer setup is covered to protect it from external light sources.

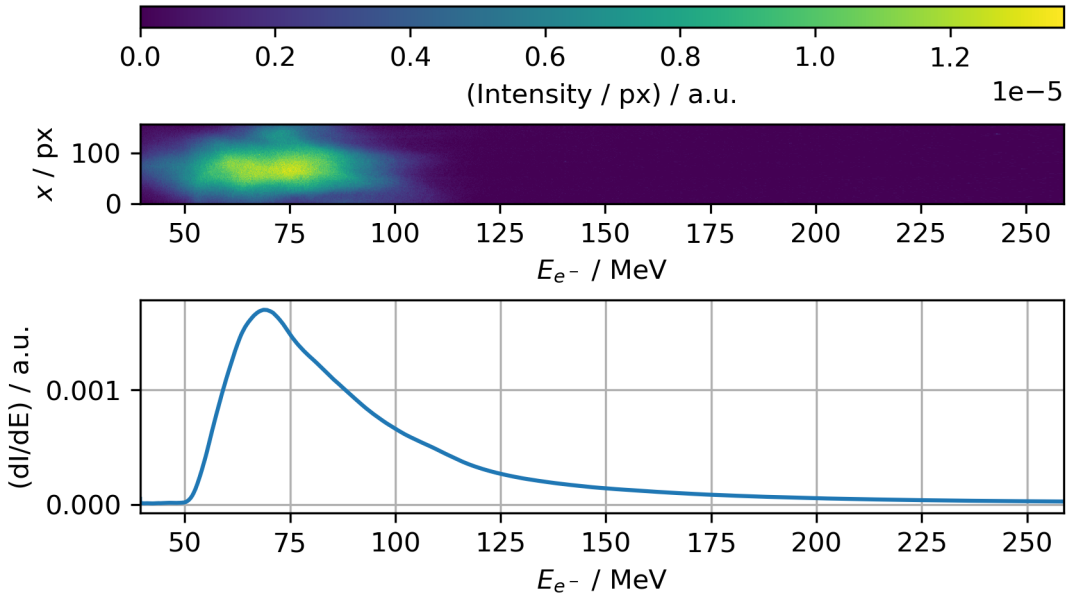

Figure 2.10.: a) Example image of fluorescence caused by electrons deflected onto screen, distortion and intensity corrected, pixel positions translated to energy b) corresponding energy spectrum

with scintillation screens (DRZ high, see section 2.6.2) clamped to it. Low energy electrons are deflected to the one at the bottom, higher energy electrons are deflected to the one mounted in a 140°angle with respect to the beam axis. The fluorescence from the screens is imaged onto CCD-cameras with the aid of mirrors (see figure 2.9b). Finally, the spectral information must then be extracted from the recorded images. The so-called "espec analysis tool", which was developed by Rob Shaloo, was used for this purpose. It uses calibration files to assign corresponding energies to pixel positions, pixel values then correspond to intensity. How this calibration works is described in detail in the work of C. Varma [66], the basic principles are as follows:

1. Pixel positions are translated to accurate positions on the scintillation screen with respect to the electron source. This involves image distortion and intensity corrections. An absolute reference frame is provided by a scale on the flange cover where the screen is mounted.

2. Positions on screen are translated to energy values. For this purpose, detailed magnetic field maps are used and the path of centrally incoming particles is tracked with the space charge tracking package ASTRA [67].

Another important consideration is that, due to the energy-dependent deflection in the magnetic field, pixels correspond to energy ranges of varying widths depending on their position on the screen. To accurately represent the energy spectrum on a linear energy scale, the intensity values must be normalised by the respective bin widths, effectively converting them into differential intensity values, dI/dE. This ensures that the spectral data is correctly interpreted in terms of energy density rather than pixel density. For visualisation and further analysis, the data is then interpolated and rebinned onto a linear energy axis with equal bin widths.
An example of a corrected and energy-calibrated image taken during the LEAP zero polarisation measurement campaign is shown in figure 2.10a), with the corresponding normalised energy spectrum presented in figure 2.10b). The dipole magnet was operated at 180 A.
Although the dipole spectrometer enables precise shot-to-shot measurements, the method is inherently destructive, preventing the electron beam from continuing along the vacuum pipe to the polarimeter. To minimise the energy spread reaching the polarimeter and maintain a more consistent energy profile, the energy-dependent focal lengths of an active plasma lens were employed, in conjunction with a collimator, serving as an energy filter.

2.7. Active Plasma Lenses

An Active Plasma Lens (APL) is a device that focuses charged particles using the azimuthal magnetic fields generated by an externally applied axial current in a plasma. This configuration produces strong, radially symmetric magnetic fields (on the order of kT/m [68]), supporting a compact experimental arrangement.
The development of APL technology has evolved significantly over the years. The first APL was constructed by Panofsky and Baker in 1950 [69]. Subsequent advancements were for example made by van Tilborg et al. [68], who were the first to apply APLs for focusing relativistic laser plasma acceleration (LPA) electron beams.
In electron polarisation measurements, the transmission of bremsstrahlung photons varies with energy, which can affect the accuracy of the polarisation measurement. To minimise this effect, it is important to use a narrow electron-energy spectrum to reduce artificial asymmetries from different beam energies. The spectrometer measurements, as detailed in section 2.6.3, are destructive and, therefore, cannot be conducted on a shot-to-shot basis while using the polarimeter. This is why an APL combined with

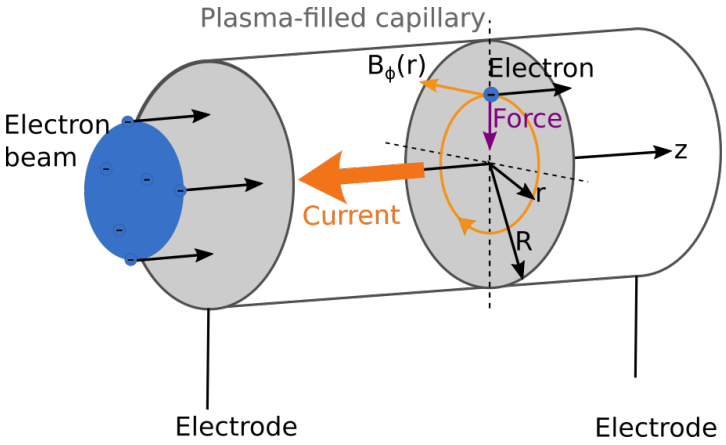

Figure 2.11.: Schematic concept of the focusing force in an APL (adapted from [68])

a collimator was utilised as an energy filter to select the appropriate energy range without requiring destructive measurements. Further details on this approach are provided in section 8.4.2.

The functional principle of active plasma lenses is as follows: An APL consists of a gas-filled capillary with electrodes at both ends (see figure 2.11). When a current is applied, discharge occurs within the thin tube, forming a plasma channel. A current flowing through a straight conductor induces a magnetic field that circulates in concentric circles around the axis of the conductor (azimuthally). By applying Ampère's circuital law:

$$\nabla \times \vec{B} = \mu_0 \vec{J}, \tag{2.33}$$

where $\vec{B}$ is the induced magnetic field, μ_0 is the permeability of free space and $\vec{J}$ is the current density, one can derive the magnetic field within the plasma channel. Assuming an ideal lens with a uniform current density, the resulting magnetic field takes the form:

$$B_\phi = \frac{\mu_0 I_0}{2\pi} \frac{r}{R^2} \tag{2.34}$$

where r is the radial distance from the central axis of the APL in cylindrical coordinates, R is the radius of the capillary, and I_0 the current flowing through the plasma. The magnetic flux density inside the lens therefore increases with distance from the central axis of the lens. Electrons that move through the lens and have transverse motion components experience the Lorentz force and are thus focused. The focusing strength,

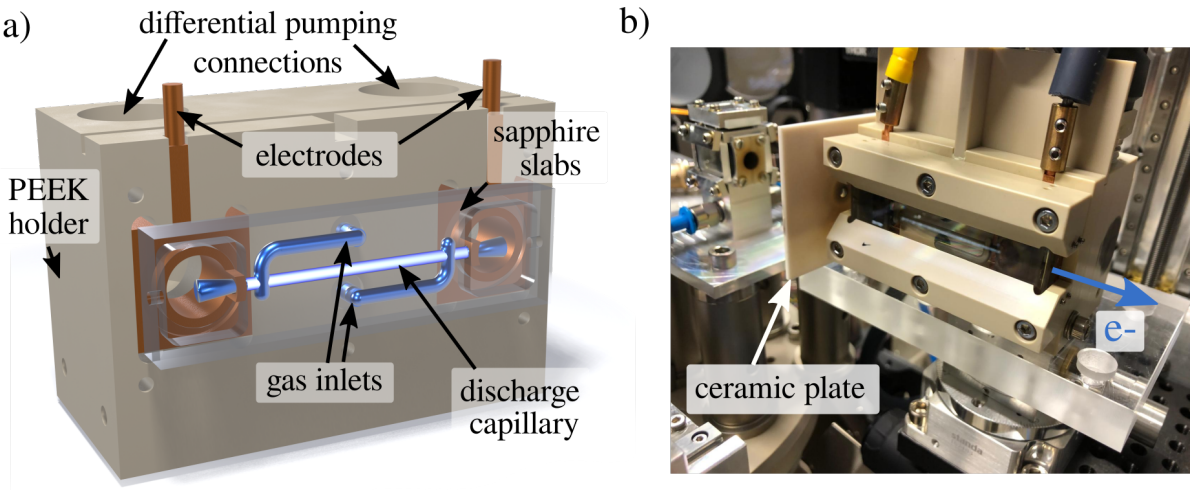

Figure 2.12.: a) CAD-drawing of the APL, adapted from [70] b) Image of the APL inside the interaction chamber

k_{APL}, is given by:

$$k_{APL} = \frac{\partial B_\phi}{\partial r}\frac{e_0 c}{E_{e^-}} = \frac{e_0 c}{E_{e^-}}\frac{\mu_0 I_0}{2\pi R^2} \tag{2.35}$$

and hence not only depends on the discharge current, but also on the energy of the electrons. By adjusting I_0, the location in space where electrons of different energies are focused can be controlled. Under the thin lens approximation, the focal length, f_{APL}, can be approximated by:

$$f_{APL} \approx \frac{1}{k_{APL} L_{APL}} \tag{2.36}$$

with L_{APL} being the length of the capillary.
The APL used in the zero-polarisation measurements with the LEAP polarimeter is depicted in figures 2.12 a) and b). It's design and characterisation are the work of M. Meisel and detailed information can be found in his PhD thesis [70]. Nonetheless, here a short summary: The capillary is constructed from two sapphire slabs, each with grooves drilled into them, resulting in a discharge length L_{APL} of 40 mm and a radius of 1 mm. Two gas inlets provide a uniform gas flow. Argon was chosen as the working gas, because Lindstrøm et al. demonstrated in 2018 that APLs can be made aberration-free, when a heavy gas species is used [71]. Their study showed that using argon produced a linear focusing field that preserves emittance. The gas flow remains steady because of the maximum 10 Hz repetition rate of the laser system. The gas is

differentially pumped through the capillary and its holder. Electrodes are positioned at both ends of the plasma lens. The discharge setup can provide a positive voltage of up to 25 kV, with the anode placed downstream, allowing for the focusing of negatively charged particles. The aforementioned holder of the plasma lens is fabricated out of PEEK, a very durable thermoplastic that can withstand high temperatures and is electrically isolating. Finally, a ceramic plate is mounted at the upstream front of the APL to protect the holder from laser damage and prevent the deposition of soot on optics in the vacuum chamber. The discharge current is measured on the upstream side of the lens using an inductive coil. The resulting signal is attenuated, converted to a digital signal via an analogue-to-digital-converter, ADC, and send to the data acquisition system.

Chapter 3.

Polarimetry

This chapter lays the theoretical foundation for electron polarimetry, providing the necessary framework to understand the simulations and experiments discussed in subsequent chapters. Section 3.1 begins with an overview of photon and electron interactions with matter, followed by a brief introduction to calorimetry in section 3.5. The chapter then explores electron polarisation measurement by scattering (section 3.2), provides an overview of common polarimetry techniques and their applicability to LEAP (section 3.3), and concludes with a discussion of Compton transmission polarimetry (section 3.4).

3.1. Photon and Electron Interactions in Matter

Any particle traversing through matter will interact with it in some way and thus lose energy. The type and probability of interactions depend heavily on each particles unique properties (such as charge, mass, and energy) and the nuclear charge number Z and density of the material it is passing through.
In this work, the interactions of electrons and photons with matter are of particular importance. This section provides a summary of the key interaction mechanisms for these particles, along with additional radiation effects in high-energy regimes that are utilised in this work. Polarised bremsstrahlung and Compton scattering are especially significant for Compton transmission polarimetry and are discussed in detail in sections 3.1.1 and 3.1.3 below. Cherenkov radiation is of importance for the type of calorimeter employed for the LEAP project and is discussed in section 3.1.2. For a more detailed discussion of the here mentioned interaction mechanisms, readers

may consult comprehensive works such as chapter 34 of [72], chapter 2 of [73], or chapters 2 and 3 in [74].

Electrons

Electrons and their antiparticles, positrons, are charged particles with a charge of $q = \mp 1\mathrm{e} \approx \mp 1.6 \times 10^{-19}\,\mathrm{C}$ and a relatively small mass of $m \approx 0.511\mathrm{MeV/c^2}$. As they traverse matter, they lose energy continuously through electromagnetic interactions with atomic electrons and nuclei.

At low energies, electrons and positrons lose energy predominantly through **collisional processes**, where their interactions with atomic electrons cause ionisation and excitation of the material along their path. Other, less dominant processes include:

- Møller scattering: Elastic scattering between two electrons (cf. section 3.3),
- Bhabha scattering: Elastic scattering between an electron and a positron,
- Positron annihilation: Low energy collisions of e^+ and e^- producing two or more photons.

At higher energies, specifically above a material-dependent "critical energy" (E_c), energy loss becomes dominated by radiative processes. In this regime, electrons and positrons primarily lose energy by emitting photons via **bremsstrahlung** (see section 3.1.1).

The stopping power, or the differential energy loss per unit distance, is commonly expressed in units of radiation length (X_0). Radiation length is defined as the mean distance over which an electron's energy decreases by a factor of $1/e$ ($\sim 37\%$) of its initial value due to bremsstrahlung. Figure 3.1a) illustrates the stopping power of electrons in lead as a function of energy, emphasising the transition from collisional to radiative dominance.

The critical energy, at which radiative losses surpass collisional losses, varies with Z. Specifically, higher Z materials have lower E_c values due to their stronger electromagnetic fields, which enhance bremsstrahlung. For example, lead (Z=82) has a critical energy of 7.43 MeV for electrons and 7.16 MeV for positrons. In contrast, for iron (Z=26), the critical energy is 21.68 MeV for electrons and 21.00 MeV for positrons.

Photons

Photons are massless, chargeless particles that interact with matter in discrete events.

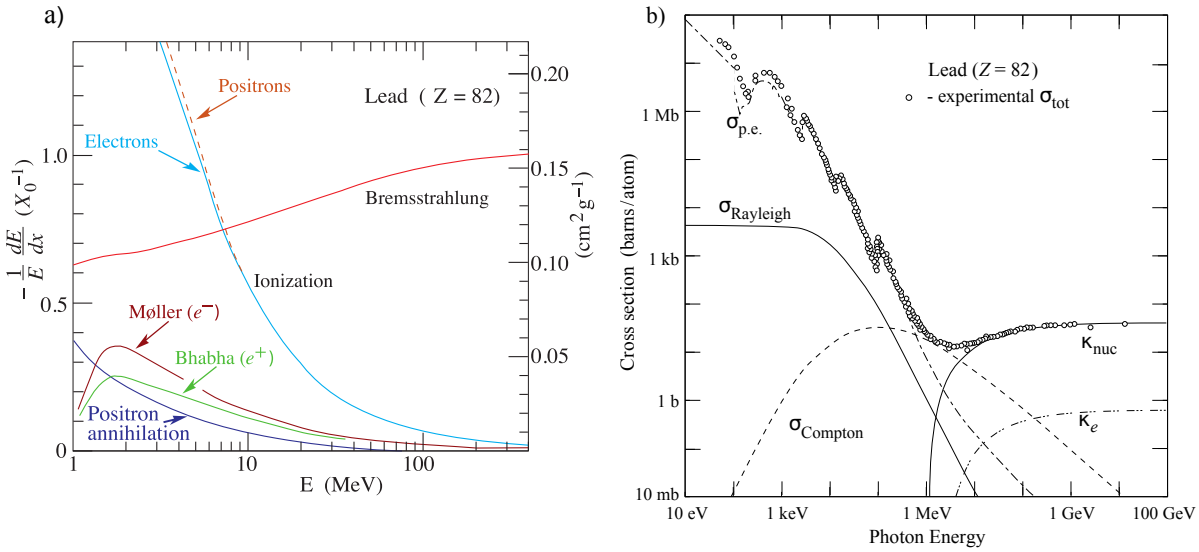

Figure 3.1.: a) Differential energy loss per unit distance (also called stopping power) in units of radiation length of electrons (and positrons) in lead as a function of electron energy in MeV b) Cross-sections of the different photon interaction processes in lead. Both taken directly from [72], with no modifications.

Unlike electrons, whose energy loss is continuous due to cumulative Coulomb interactions, photon interactions occur in distinct processes. The likelihood of each process, quantified by its cross-section, depends on the photons energy and the material's atomic number (Z) and density, as shown in Figure 3.1b). These interactions can be categorized into four primary processes:

1. **Photoelectric Absorption**: At low photon energies, typically between several keV and a few hundred keV, photoelectric absorption is the dominant interaction. In this process, the photon interacts with the atomic electron cloud and transfers all its energy to the atom. This occurs only when the photons energy E_γ exceeds the binding energy E_B of the atomic electron. The atom then emits a photoelectron with kinetic energy $E_{e^-} = E_\gamma - E_B$. The sharp edges visible in the cross-section of photo-absorption $\sigma_{p.e.}$ in figure 3.1b) are known as absorption edges. These correspond to the energy thresholds required to ionise electrons from specific atomic shells.

2. **Rayleigh Scattering**: Coherent Rayleigh scattering occurs when a photon interacts elastically with an atom's electron cloud. The photon neither excites nor ionises the atom, retaining its energy while being deflected in a different direction. The likelihood of Rayleigh scattering decreases with increasing photon energy.

Although it does not dominate at any energy range, it contributes to the overall attenuation of low-energy photons.

3. **Compton Scattering**: At medium photon energies, incoherent Compton scattering (cf. section 3.1.3) dominates. In this process, the photon transfers a portion of its energy to an atomic electron, ejecting the electron and scattering the photon with reduced energy.

4. **Pair Production**: At high energies, ranging from several to tens of MeV, electron-positron pair production becomes the primary interaction process. During this process a photon is converted to an electron positron pair. Pair production can occur only if the photons energy exceeds twice the electron rest mass energy ($2m_e c^2 = 1.022\,\text{MeV}$) and only in the vicinity of a charged, massive object (e.g., a nucleus) that absorbs the excess momentum, ensuring momentum conservation.

When a photon beam passes through a material, the total interaction cross-section, which is the sum of the cross-sections of all individual processes, governs the attenuation of the beam. The number of photons in the beam decreases exponentially as it travels through the material, following the equation for attenuation:

$$I(x) = I_0 e^{-\mu x}, \tag{3.1}$$

where $I(x)$ is the intensity of the photon beam at distance x, I_0 is the initial intensity, and μ is the total attenuation coefficient, which accounts for all the individual interaction processes.

3.1.1. Bremsstrahlung

Bremsstrahlung, occurs when a charged particle emits electromagnetic radiation as a result of a change in velocity due to its interaction with an electromagnetic field. In this work, bremsstrahlung refers specifically to electrons interacting with the Coulomb field of nuclei or, less frequently, other electrons within target materials, with the former being the dominant process.This section examines the process of bremsstrahlung as it pertains to electrons interacting with target nuclei and the associated physical phenomena.

Classical electrodynamics and basic dependencies

In its simplest form, assuming uniform acceleration, bremsstrahlung can be described using classical electrodynamics as the emission of electromagnetic dipole radiation. The radiated power by a single electron changing its velocity, v, is given by the Larmor formula:

$$\frac{dE}{dt} = \frac{2}{3}\frac{e^2}{c^3}\left|\frac{d\vec{v}}{dt}\right|^2 \tag{3.2}$$

When an electron is subjected to Coulomb interactions with an atomic nucleus, the magnitude of the acceleration $\vec{a} = \frac{d\vec{v}}{dt}$ due to the electric field force, $\vec{F_C}$, can be described by the relationship $\vec{F_c} = m_e \cdot \vec{a}$ and

$$|\vec{a}| = -\frac{Ze^2}{m_e b^2} \tag{3.3}$$

where b is the impact parameter , describing the shortest distance between the electrons unperturbed trajectory and the atomic nucleus. A schematic of the process is depicted in figure 3.2a). This expression reveals a quadratic dependency of bremsstrahlung intensity on the target material's atomic number, and an inverse quadratic proportionality on the electrons mass.

$$\frac{dE}{dt} \propto \frac{Z^2}{m_e^2} \tag{3.4}$$

As a result, more massive charged particles (such as pions, kaons, or protons) are much less likely to radiate photons via bremsstrahlung when traversing matter.

Relativistic extension

While the classical description provides useful insights, it becomes incomplete as the electron's speed approaches the speed of light. Relativistic effects fundamentally alter the emission process in two significant ways. The first is relativistic beaming. In the electron's rest frame, bremsstrahlung emission remains isotropic. However, when observed from the lab frame, the emission is concentrated into a narrow cone along the electron's direction of motion. The opening angle of this cone can be approximated

as:

$$\theta_\gamma \approx \frac{mc^2}{E_{e^-}} \tag{3.5}$$

where E_{e^-} is the electron's energy. The second effect is increased energy loss. In the classical case, the radiated power depends on the square of the electrons acceleration. This dependence is amplified in the relativistic case, with the radiated power scaling approximately as γ^4, where γ is the Lorentz factor $\frac{1}{\sqrt{1-\frac{v^2}{c^2}}}$. This results in a much larger energy loss for high-energy electrons. Additionally, the emitted photons tend to carry a greater fraction of the electron's energy, shifting the spectrum to higher photon energies.

Quantum mechanical corrections

The wave-like properties of the particles involved in bremsstrahlung (electrons and photons) require a quantum mechanical treatment of the electron-photon interaction, which is more complex than the classical Coulomb force. In the quantum regime, the interaction is governed by quantum electrodynamics (QED), where photons are emitted in discrete quanta of energy. At high energies, this discrete nature of energy exchange becomes particularly important, and the recoil of the photon, which affects the electron's energy and momentum, must also be taken into account.

Numerous quantum mechanical models have been developed, employing different ansatzes and approximations to account for the intricate nature of bremsstrahlung (a good initial overview is for example given in [75]). They address a variety of phenomena, from individual scattering events to collective effects.

There are two key effects that must be considered in the quantum regime. The first is screening. At high electron energies, the assumption that electrons interact with the full nuclear charge becomes inaccurate. The surrounding electron cloud shields the nucleus, reducing the effective Coulomb field experienced by the bremsstrahlung-emitting electron. This is particularly significant for high Z materials. The second effect is the Landau-Pomeranchuk-Migdal (LPM) effect [76, 77]. This arises from interference between multiple photon emissions by the same electron. At very high energies, this interference reduces the total bremsstrahlung cross-section, as the successive emissions of photons interfere with each other, leading to a decrease in photon production.

Practical Models: The Seltzer-Berger Model

Despite the essential corrections provided by quantum mechanical models, no single

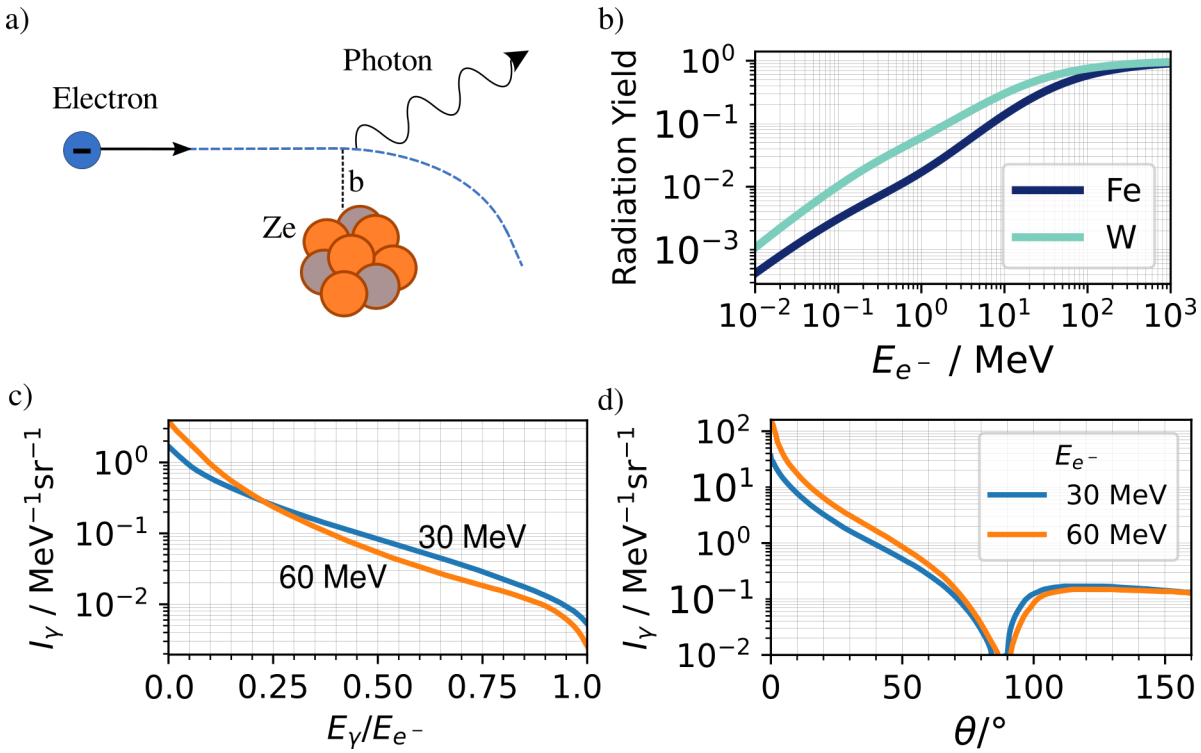

Figure 3.2.: a) Schematic of bremsstrahlung during electron scattering of the Coulomb field of a nucleus. b) Radiation yield, i.e. the fraction of kinetic energy of the primary electron that is converted into bremsstrahlung as it slows down to rest, for iron (Z=26) and tungsten (Z=74). Graph produced by the author, based on data obtained from [78] c) Photon spectra of 30 MeV (blue) and 60 MeV (orange) electron beams incident on a thick tungsten target. Target thickness is twice the electron mean range. Emission angle between 0 and 0.5°. d) Angular dependence of bremsstrahlung emission for the case in c). Graphs c) and d) were digitally extracted and reconstructed using WebPlotDigitizer [79], based on data from [80].

theory encompasses all effects across the entire energy spectrum of bremsstrahlung. Practical approaches, such as the Seltzer-Berger model, address this gap by integrating theoretical insights with experimental data. Seltzer and Berger developed extensive cross-section tables [81] for use in Monte Carlo simulations, covering electron energies from 1 keV to 10 GeV and materials with atomic numbers ranging from 1 to 100. Their model incorporates quantum mechanical effects and remains widely utilised in modern simulation software, such as `Geant4`, particularly for modelling electromagnetic interactions. More information about bremsstrahlung in `Geant4` can be found in section 4.2.4.
Building on this work, the ESTAR database [78] provides detailed electron stopping power and bremsstrahlung cross-section data for a wide range of elements and energy ranges. It serves as a critical resource for both theoretical studies and practical applications in fields such as radiation physics and medical dosimetry.

Example distributions

The following example distributions provide a closer look at the characteristics of bremsstrahlung radiation. Figure 3.2b) shows the radiation yield, i.e., the fraction of the electron's kinetic energy converted into bremsstrahlung as the electron slows to rest, for different electron energies and for materials like iron (Z=26) and tungsten (Z=74). Initially, the radiation yield increases exponentially with energy, but at higher energies, saturation effects reduce the rate of increase. Tungsten, with its higher atomic number, produces a greater radiation yield than iron due to its stronger Coulomb field. A typical bremsstrahlung spectrum is shown in figure 3.2c) for electrons with 30 and 60 MeV initial kinetic energy incident on a tungsten target with a thickness equal to twice the mean range ($r_{0,W}(E_{e^-} = 60\,\text{MeV}) = 0.86\,\text{cm}$, $r_{0,W}(E_{e^-} = 30\,\text{MeV}) = 0.62$ cm [80]). The spectrum is continuous, peaking at low photon energies, with intensity decreasing as photon energy approaches the cutoff energy of the initial electron. The decrease near the cutoff is more pronounced for the 60 MeV electrons compared to the 30 MeV case, due to the increased energy loss at higher electron energies.
Figure 3.2d) illustrates the angular dependence of bremsstrahlung emission for the same scenario. Emission is strongly forward-peaked, with a noticeable dip at 90°. This dip arises from the assumption of an infinitely thick target in the model and would be less prominent in a real-world scenario.

Polarisation transfer

When longitudinally polarised electrons interact with a radiator target, they can produce circularly polarised photons. The efficiency of this polarisation transfer depends

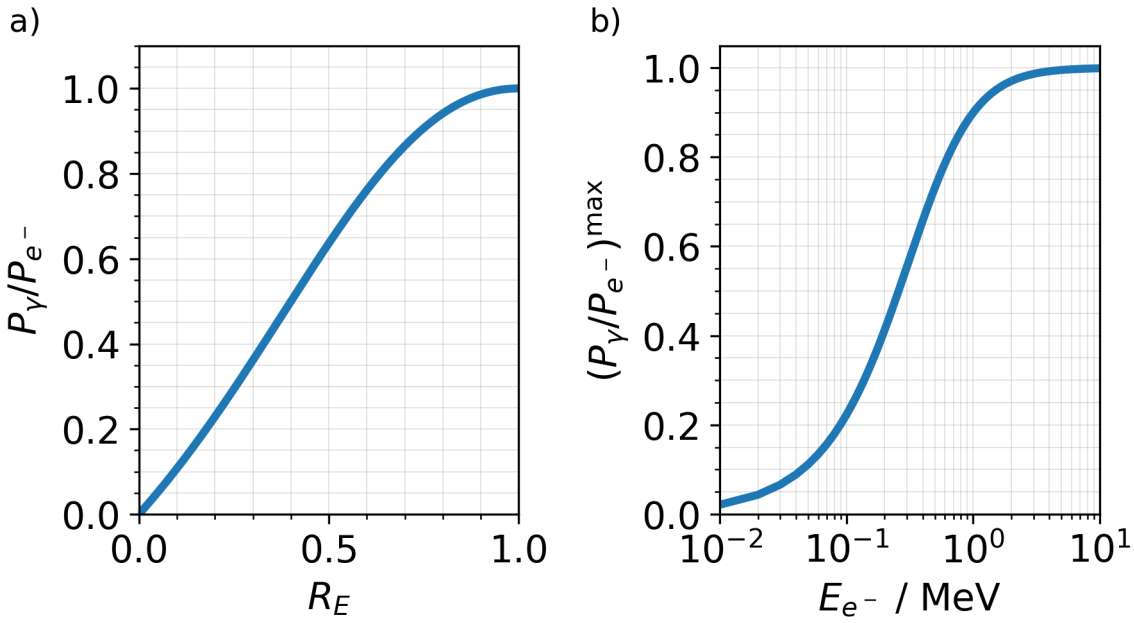

Figure 3.3.: a) Circular polarisation of bremsstrahlung created by longitudinally polarised electron beams. P_γ calculated in the ultrelativistic limit according to equation 3.6. E_{e^-} = 60 MeV b) Efficiency of the Bremsstrahlung polarisation transfer as function of the electron energy according to equation 3.7.

on several factors, including the energy of the particles and the initial polarisation degree of the electron beam, P_{e^-}. In the ultra-relativistic limit, where photon emission is concentrated in the forward direction, the degree of polarisation transfer can be expressed, following Olsen and Maximon [82] and using the notation of Barday et al. [83], as:

$$P_\gamma = R_E \frac{1 + \frac{1}{3}(1 - R_E)}{1 - \frac{2}{3}(1 - R_E) + (1 - R_E)^2} P_{e^-} \tag{3.6}$$

where $R_E = \frac{E_\gamma}{E_{e^-} + m_e c^2}$ is the ratio of the emitted photon energy to the total electron energy. Figure 3.3a) illustrates the polarisation transfer as a function of R_E for 60 MeV electrons. The plot shows that the degree of circular polarisation increases with photon energy, reaching its maximum at high photon energies.
In the short wavelength limit ($R_E \to 1$) and for forward emission (θ_γ=0), the maximum

polarisation transfer can be approximated, as shown by McVoy [84], by:

$$P_{\gamma}^{\max} = \left(1 + \frac{(1-\beta)(E_{e^-} + 2m_e c^2)}{(2-\beta)E_{e^-}}\right)^{-1} P_{e^-} \tag{3.7}$$

Above an electron energy of a few MeV, the polarisation transfer becomes nearly complete. This behaviour is evident from figure 3.3b).

3.1.2. Cherenkov Radiation

Cherenkov radiation is a phenomenon that describes the emission of electromagnetic radiation when a charged particle travels through a dielectric medium at a velocity exceeding the speed of light in that medium. It was first observed experimentally by P. A. Cherenkov in 1934 [85] and later theoretically explained by I. M. Frank and I. Y. Tamm [86]. These contributions were recognised with the Nobel Prize in Physics in 1958.

A simple analogy for this effect is a luminal boom, similar to a sonic boom caused by an object traveling faster than the speed of sound [87]. When a charged particle moves through a dielectric medium with velocity v greater than c_m, the molecules along the particles trajectory become momentarily polarised. The threshold condition for this effect is:

$$v > c_m \equiv \frac{c}{n}, \tag{3.8}$$

where c is the speed of light in a vacuum, n is the refractive index of the medium, and c_m is the speed of light in the medium. Here, 'polarised' refers to dielectric polarisation – the alignment of molecular charges in response to the particles electric field. This should not be confused with the polarisation of electrons or photons, as discussed in section 2.1.

Under normal circumstances, the electromagnetic waves induced by the particle's motion interfere destructively, resulting in no net radiation. However, when the particle's velocity exceeds c_m, the conditions for constructive interference are met. This results in a coherent wavefront forming a cone-shaped pattern of radiation.

The shape of this cone can be understood through a Huygens-type construction of spherical wavefronts, as illustrated in figure 3.4. The opening angle θ of the Cherenkov cone is determined by the relationship between the particle's velocity and the speed of

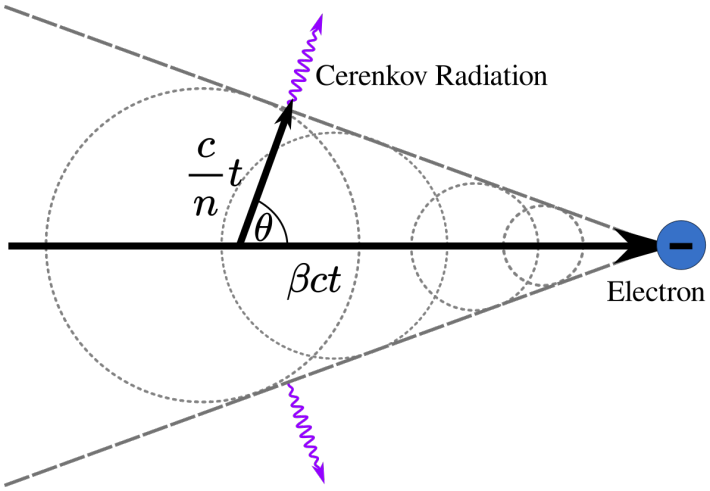

Figure 3.4.: The geometry of Cherenkov radiation for the ideal case without dispersion.

light in the medium. It is given by:

$$\cos\theta = \frac{c_m}{\beta c} = \frac{1}{\beta n}, \tag{3.9}$$

where $\beta = \frac{v}{c}$ is the velocity of the charged particle expressed as a fraction of the speed of light.
The wavelength-dependent energy loss per unit length is given by the Frank-Tamm formula in its wavelength representation:

$$\frac{d^2E}{d\lambda dx} = \frac{2\pi q^2 c}{\lambda^2}\left(1 - \frac{1}{\beta^2 n^2(\lambda)}\right), \tag{3.10}$$

where λ is the wavelength of the emitted radiation, q the charge of the particle and $n(\lambda)$ is the wavelength dependent refractive index of the medium. This relationship indicates that the intensity of the emitted photon spectrum increases at shorter wavelengths, resulting in a characteristic UV-violet to blue dominance of Cherenkov radiation.
The Cherenkov effect plays a role in the operation of the calorimeter used in this work (see section 7.2). High-energy photons interact with the detector material, producing secondary particles that, in turn, generate Cherenkov light, which contributes to the detection process. Additionally, the threshold energy for the Cherenkov effect, which defines the conditions under which radiation is emitted, is essential for the Monte

Carlo simulations described in section 5. This threshold is given by:

$$E_{th} = mc^2 \left(\frac{n}{\sqrt{n^2 - 1}} - 1 \right) \tag{3.11}$$

where m is the particle's mass.

3.1.3. Compton Scattering

Compton scattering is a fundamental interaction mechanism in which a photon undergoes inelastic scattering off a quasi-free electron. This phenomenon, first discovered by A.H. Compton in 1923 [88], provided key experimental evidence for the particle-like behaviour of electromagnetic waves. For this discovery, Compton was awarded the Nobel Prize in Physics in 1927.
As illustrated in figure 3.5a), the fundamental principle of Compton scattering can be understood by considering the interaction between an incoming photon and a quasi-free electron approximated to be at rest. The photon transfers part of its energy to the electron during the scattering process, resulting in a lower photon energy and a change in its propagation direction. The relationship between the initial photon energy E_γ and the scattered photon energy E'_γ is determined by the scattering angle θ, as described below.

$$\frac{E'_\gamma}{E_\gamma} = \frac{1}{1 + \mathcal{E}(1 - \cos\theta)}, \tag{3.12}$$

where $\mathcal{E}$ is the reduced photon energy $\mathcal{E} = \frac{E_\gamma}{m_e c^2}$.

Unpolarised Compton scattering
The differential cross-section, which quantifies the probability of an interaction occurring per unit solid angle, can mathematically be described by the Klein-Nishina-Formula [89]:

$$\frac{d\sigma_{Compton}}{d\Omega} = \frac{r_0^2}{2} \left(\frac{E'_\gamma}{E_\gamma} \right)^2 \left[\frac{E'_\gamma}{E_\gamma} + \frac{E_\gamma}{E'_\gamma} - \sin^2\theta \right], \tag{3.13}$$

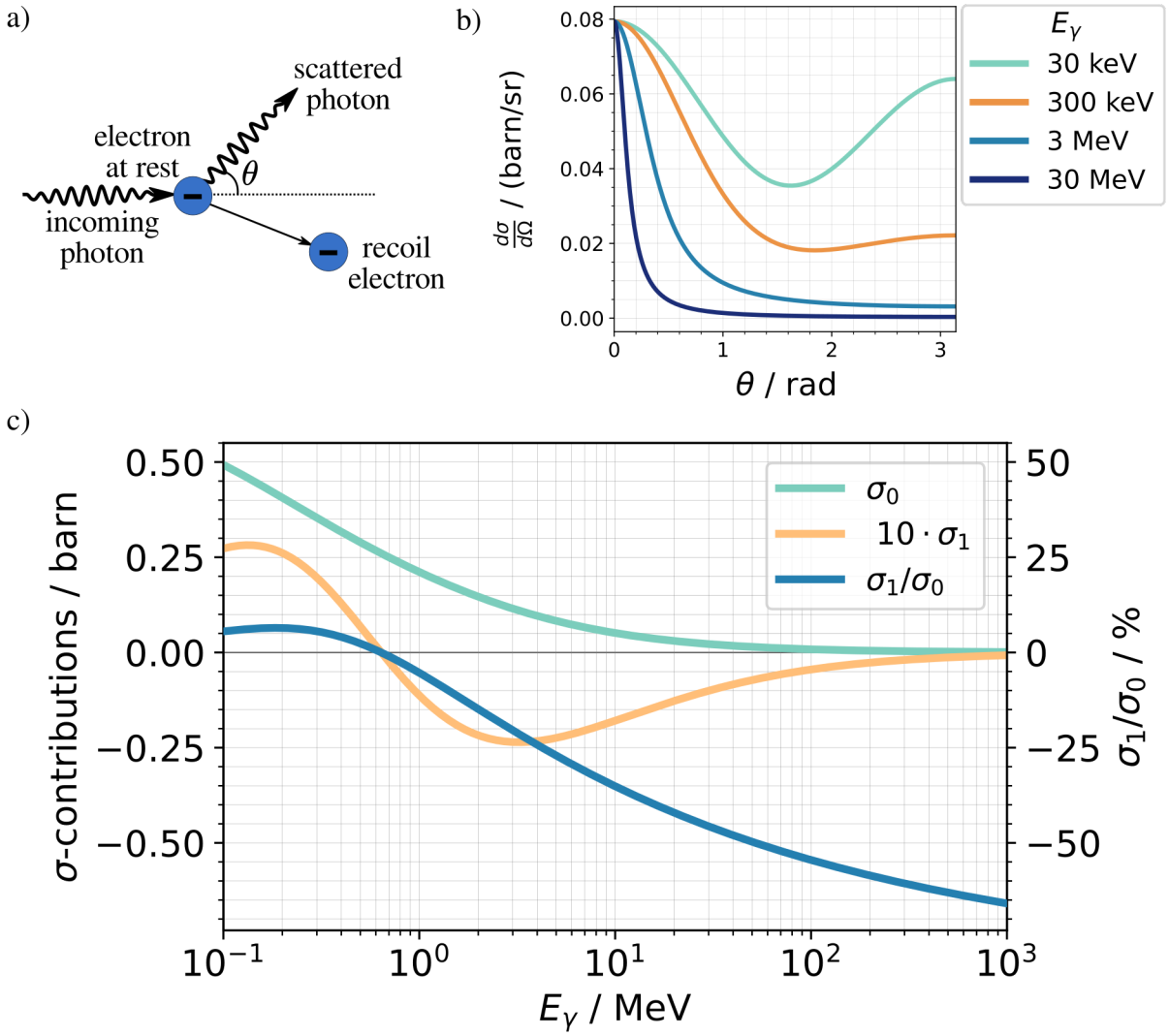

Figure 3.5.: a) Mechanism of Compton scattering. Incoming photon scatters off a quasifree electron approximated as being at rest. The electron recoils and the photon changes propagation direction by an angle of θ b)Unpolarised differential cross-section $\frac{d\sigma}{d\Omega}$ for Compton scattering as a function of azimuthal scattering angle at different photon energies. The angular dependence reflects the Klein-Nishina formula (equ. 3.13). c) Overlay of the polarisation independent (σ_0) and dependent (σ_1) part of the Compton cross-section as a function of photon energy using equations 3.14 and 3.16.

where r_0 describes the classical electron radius given by $r_0 = \frac{e^2}{4\pi\epsilon_0 m_e c^2}$. Figure 3.5b) shows the differential cross-section for photon energies ranging from 30 keV to 30 MeV. It can be observed that as the photon energy E_γ increases, the scattering becomes increasingly forward-peaked, indicating a higher probability of the photon being scattered in the forward direction.
Integrating over all solid angles then yields the total cross-section:

$$\sigma_{Compton} = \frac{\pi r_e^2}{\mathcal{E}} \left\{ \ln(1+2\mathcal{E}) \left[1 - 2\frac{(1+\mathcal{E})}{\mathcal{E}^2} \right] + \frac{1}{2} + \frac{4}{\mathcal{E}} - \frac{1}{2(1+2\mathcal{E})^2} \right\} \tag{3.14}$$

Polarised Compton scattering
In contrast to unpolarised Compton scattering, where the cross-section is independent of the polarisation of the photon and electron, Compton scattering involving polarised particles results in a cross-section that depends on their polarisation states. This dependence is critical for applications such as Compton transmission polarimetry, which is discussed in section 3.4.
The general form of the polarised Compton cross-section can be parametrised as [90]:

$$\sigma_{Compton} = \sigma_0 + P_\gamma P_M \sigma_1, \tag{3.15}$$

where:

- σ_0 is the part of the cross-section that is independent of polarisation as described by the unpolarised case in equation (3.14),
- P_γ is the helicity of the incident Photon (cf. ξ_3 in section 2.1.3),
- P_M is the polarisation degree of target electrons in z-direction (cf. section 2.1.2),
- σ_1 is the polarisation dependent part of the Compton cross-section, which can be written as [90]:

$$\sigma_1 = 2\pi r_0^2 \left[\frac{1+4\mathcal{E}+5\mathcal{E}^2}{\mathcal{E}(1+2\mathcal{E})^2} - \frac{1+\mathcal{E}}{2\mathcal{E}^2} \ln(1+2\mathcal{E}) \right], \tag{3.16}$$

Figure 3.5c) illustrates both σ_0 and σ_1 along with their relation. In the photon energy range of interest for LEAP (order of MeV, with a maximum of tens of MeV), σ_0 is decreasing with increasing E_γ. Meanwhile, σ_1 shows a negative amplitude, peaking

at approximately 3 MeV and then decreasing as E_γ increases. Thus, the ratio of the polarisation-dependent cross-section to the polarisation-independent cross-section decreases with increasing photon energy in the range relevant to LEAP.

3.2. Electron Polarisation Measurement by Scattering

In principle, any well-known, high-rate, and polarisation-dependent process can be used for polarimetry. Electron beam polarisation is typically determined by measuring differences in scattering rates between two different polarisation states. Various targets are employed for this purpose, including some that are themselves polarised. These techniques and their applications are discussed further in section 3.3. For a comprehensive introduction to the topic, C.K. Sinclair provides an excellent overview [91], and the framework presented there has been adapted for the discussion here.
First, it is essential to recall that electron polarisation, relative to a chosen quantisation axis, is defined as the population imbalance between the two possible spin states, spin-up $\uparrow$ and spin down $\downarrow$, as defined in equation (2.16).
When a polarised electron beam interacts with a target, only a fraction of the total scattering probability, S, depends on the spin orientation of the incident electrons (and, when relevant, the polarisation of the target). Using a similar notation as in the previous section, this probability can be divided into a polarisation-independent part, S_0, and a polarisation dependent part, S_1. If the analysing power, $\mathcal{A}$, is defined as the measure of the polarisation-dependent difference in scattering probability, the probability that an electron is scattered onto the detector, depending on spin, can be expressed as follows:

$$S_{\uparrow\downarrow} = S_0 \pm (1 + \mathcal{A}) \tag{3.17}$$

Using equation (2.16) and defining the total number of electrons inside the beam as $N_{e^-,\text{beam}} = N_\uparrow + N_\downarrow$ one then gets the following for the number of spin up, or down, electrons:

$$N_\uparrow = \frac{N_{e^-,\text{beam}}}{2}(1 + P) \quad \text{and} \quad N_\downarrow = \frac{N_{e^-,\text{beam}}}{2}(1 - P) \tag{3.18}$$

If electrons are counted at a specific position relative to the scattering target, the detected rate will be proportional to the number of incident particles and their respective

scattering probabilities, taking into account the contributions from both spin populations. In an experiment where the polarisation direction of the incoming beam can be reversed, the rate R is first measured for a polarisation of $+|P|$ and then for $-|P|$, leading to the following result:

$$\begin{aligned} R_+ &= S_0(1+\mathcal{A})(1+P)\frac{N_{e^-,\text{beam}}}{2} + S_0(1-\mathcal{A})(1-P)\frac{N_{e^-,\text{beam}}}{2} \\ R_- &= S_0(1+\mathcal{A})(1-P)\frac{N_{e^-,\text{beam}}}{2} + S_0(1-\mathcal{A})(1+P)\frac{N_{e^-,\text{beam}}}{2} \end{aligned} \tag{3.19}$$

Combining the two then leads to:

$$\frac{R_+ - R_-}{R_+ + R_-} = \mathcal{A}P, \tag{3.20}$$

where the counting rate difference on the left hand side of the equation is also referred to as asymmetry.
In summary: By measuring the asymmetry in scattering rates between two different polarisation states and knowing the analysing power, the polarisation of an electron beam can be determined.

3.3. Overview of common electron polarisation measurement methods

The LEAP experiment aims to measure the longitudinal polarisation of electrons in the energy range of several tens of MeV (cf. section 2.4). The electron bunches carry approximately 3 pC of charge, with durations on the order of femtoseconds. These parameters result in extremely high instantaneous intensities but a low average current, as the repetition rate is limited to a maximum of 10 Hz.
To determine the most suitable polarisation measurement technique for LEAP, a review of commonly used polarimetry methods is necessary. The most common polarimetry techniques fall into three categories: the scattering of polarised electrons from unpolarised nuclei (Mott scattering), polarised atomic electrons (Møller scattering), or polarised photons (Compton scattering). Each method has unique advantages and limitations that must be evaluated in the context of LEAP's experimental conditions. This section draws heavily on insights from foundational works, including the review article by D. Gaskell et al. [92] and the comprehensive tutorial by C. K. Sinclair [91], to

evaluate polarisation techniques for LEAP.

Mott Scattering

Mott polarimeters exploit the polarisation dependence of the elastic scattering of polarised electrons from the nucleus of a high-Z target [1]. Large-angle Mott scattering occurs when the electron passes very close to the nucleus, where it experiences a strong electric field. Due to relativistic effects, this electric field appears as a magnetic field in the electron's rest frame, interacting with the electron's spin. This spin-orbit interaction modifies the scattering process, introducing a term in the cross-section that depends on the component of the electron's spin perpendicular to the scattering plane. The target is typically a thin foil, and a pair of detectors measures the left-right (or up-down) asymmetry of scattering rates relative to the foil. The analysing power, which is calculated theoretically for single-atom scattering, depends on the energy of the polarised electrons, the Z of the target, and the scattering angle. For real targets, where multiple scattering can occur, thick target values often need to be extrapolated to the single-atom level, typically using experimental data supplemented by simulations. The thickness of the foil depends on the application, ranging from less than 100 nm for keV electron energies to about 1 micron for several MeV. At MeV energies, the analysing power is high, making Mott polarimeters ideal for measuring electron polarisation near the electron source of accelerator-based high-energy physics experiments. In such cases, a precision better than 1 % has been achieved [93, 94].
However, for the tens of MeV electron energies expected at LEAP, Mott polarimeters become impractical. The cross-section drops rapidly at these energies, and the most probable scattering angles approach the direction of the incident beam. Furthermore, the technique is only suitable for measuring transverse polarisation. Spin manipulation would be required to measure the longitudinal polarisation, which is of primary interest for LEAP.

[1] Mott scattering is a form of Coulomb scattering and falls under the category of collisional interactions, as discussed on page 34.

Møller scattering

Møller polarimeters rely on the elastic scattering of polarised electrons from polarised electrons within a target, typically a magnetised foil. The total scattering cross-section depends on the polarisation of the electron beam (P_e) and the target polarisation (P_M), and it can be calculated in leading order quantum electrodynamics. At high energies (above approximately 100 MeV), the analysing power and the scattering probability in the centre-of-mass frame become approximately constant and independent of the energy of the incident electrons. Acceptance uncertainties of the polarimeter may result in $\sim 0.5\%$ relative uncertainties in the analysing power.
In Møller scattering, both the scattered and recoil electrons leave the target with equal energy, each carrying half of the initial electron energy. They scatter at equal and opposite angles, close to 90° in the centre-of-mass frame. Magnetic fields are used to separate the initial beam from the scattering products for detection.
A typical Møller polarimeter setup consists of a magnetised iron foil, collimators, and a spectrometer. The spectrometer selects scattering products within a kinematic range of interest around $\theta \sim 90^\circ$, while avoiding deflection of the primary beam. Two detectors are used to measure both scattering products in coincidence, significantly reducing background compared to single-arm detection. Møller polarimeters are commonly used at energies above approximately 100 MeV and are effective up to several tens of GeV. For example, Jefferson Lab operates multiple polarimeters at beam energies between 850 MeV and 6 GeV, achieving systematic uncertainties below 1% [92].
While there have been Møller scattering measurements in the tens-of-MeV range, such as at MAMI in Mainz [95], using this technique for the LEAP project presents significant challenges. The anticipated LEAP beam parameters (electron bunches with charges in the pC range and femtosecond durations) result in very high peak currents. These conditions could potentially disrupt the target polarisation, hindering accurate measurements.

(Laser-)Compton Polarimetry

(Laser-)Compton polarimetry involves the elastic scattering of a circularly polarised laser pulse from a polarised electron beam, typically in a near head-on collision. In the lab frame, the resulting back-scattered photons are boosted to high energies in the backward direction. The analysing power depends strongly on the electron beam energy and the back-scattered photon energy, with higher electron beam energies and

larger photon energies producing greater asymmetries.
The polarimeter setup depends on whether the backscattered photon, scattered electron, or both are measured. It typically includes a laser system and either a photon detector, a dipole magnet with a segmented electron detector, or both. One major advantage of this technique is its non-destructive nature, eliminating the need for dedicated polarimeter runs. However, since photon targets are not particularly dense, high average-current electron beams or intense laser pulses are desirable.
At a beam energy of 27.6 GeV, the longitudinal and transverse polarimeters at the HERA (Hadron-Electron Ring Accelerator) facility at DESY achieved relative systematic uncertainties of 2.0% and 1.9%, respectively [96]. Similarly, the SLD Compton polarimeter at SLAC achieved a relative systematic uncertainty of 0.7% at an electron beam energy of 45.6 GeV [97]. However, Laser-Compton polarimetry is only efficient at GeV-scale energies, as the asymmetry becomes too small at lower energies, making it unsuitable for the LEAP project.

None of the methods discussed above work well under the expected conditions at LEAP. Therefore, Compton transmission polarimetry was selected as the most appropriate alternative, as explained in the following section.

3.4. Compton Transmission Polarimetry

Compton transmission polarimetry relies on the production of circularly polarised bremsstrahlung as a longitudinally polarised electron beam passes through a suitable converter. The photon polarisation is then measured using transmission asymmetry, which arises from reversing the magnetisation direction of an iron absorber. This straightforward method is well-suited for electron energies in the MeV range [83, 98–106]. The following section will first outline its working principle (cf. section 3.4.1), followed by a discussion of the state of the art (cf. section 3.4.2).

3.4.1. Working Principle

Compton transmission polarimetry relies on a differential measurement, as described in section 3.2. In this technique, photons are first converted into electrons, which then interact with a long, magnetised iron absorber serving as the target. The polarisation-dependent transmission differences between two distinct polarisation states are subse-

quently analysed to determine the polarisation of the electron beam.
Each measurement essentially involves three steps:

1. **Electron-Photon Conversion**: A converter target is typically employed for this purpose. The longitudinally polarised electron beam interacts with the target, producing circularly polarised photons via bremsstrahlung (cf. section 3.1.1). The polarisation transfer, $\frac{P_\gamma}{P_e^-}$, depends on the emission angle θ and the ratio of bremsstrahlung photon energy to the electron beam energy, $\frac{E_\gamma}{E_{e^-,\text{beam}}}$. Assuming forward emission, the polarisation transfer is nearly complete when $E_{e^-,\text{beam}} > 2\,\text{MeV}$ and $\frac{E_\gamma}{E_{e^-,\text{beam}}}$ approaches unity (cf. figure3.3).

2. **Polarisation Dependent Transmission** [107]: The photon beam traverses a polarised iron absorber. The measurement leverages the polarisation dependency of Compton scattering [90]:

$$\sigma_{\text{Compton}} = \sigma_0(E_\gamma) + P_{Fe}P_\gamma(E_\gamma)\sigma_1(E_\gamma) \tag{3.21}$$

   where P_{Fe} is the average longitudinal polarisation of atomic electrons in the absorber. Due to the energy dependence of σ_1 (cf. figure 3.5c)), for photon energies greater than 0.64 MeV, transmission is higher when the photon spin is aligned parallel to the electron spin compared to being antiparallel. The transmission is characterised as [103]:

$$T_\gamma^\pm(E_\gamma, L) = e^{-n_{e^-}^{Fe} L \sigma_{tot}^\pm} = e^{-n_{e^-}^{Fe} L(\sigma_0 + \sigma_{\text{phot}}\sigma_{\text{pair}})} e^{\pm n_{e^-}^{Fe} L \sigma_1} \tag{3.22}$$

   where L is the absorber length, $n_{e^-}^{Fe}$ is its electron number density, "phot." denotes photolectric absorption and "pair" denotes pair production. Respective cross-sections for different photon energies in iron are shown in figure 3.6a). The intensity of radiation passing through the absorber decreases exponentially with its length.
   The ratio of the polarisation-dependent Compton cross-section to the total cross-section (cf. figure 3.6b), which reaches its maximum at 5 MeV, indicates that the efficiency of Compton transmission polarimetry is highest at photon energies of a few MeV. However, as highlighted in orange, the expected photon energies for LEAP are significantly higher. The implications of this are analysed in chapter 6.

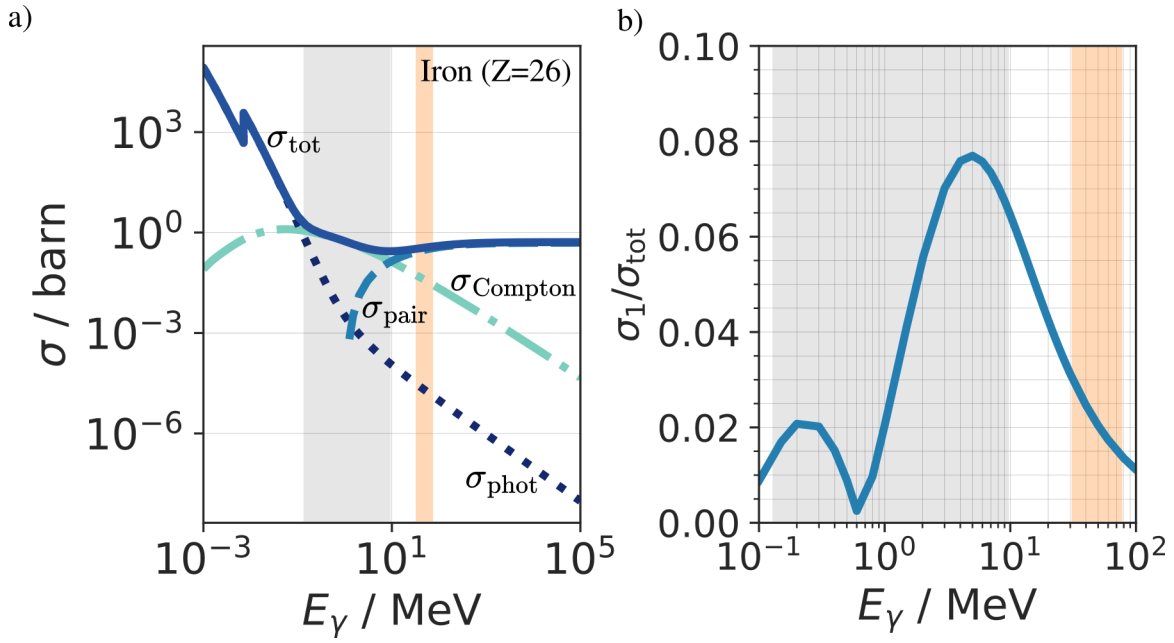

Figure 3.6.: a) Most relevant photon interaction cross-sections for iron. The photon energy region where Compton scattering is the dominant process is highlighted in grey, while the expected energy region for LEAP is highlighted in orange. Cross section data retrieved from [108] b) Ratio of the polarisation-dependent Compton cross-section (according to equ. 3.14) to the total cross-section as a function of photon energy for iron, with highlights matching those in a).

3. **Photon Detection**: The rate of photons transmitted through the iron absorber is measured by detecting the energy deposited by the transmitted particles in a calorimeter (cf. section 3.5).

Of course, two different polarisation states are required for a differential measurement. In principle, it does not matter whether you change the direction (the sign) of P_{e^-} or P_{Fe}. The latter is easier for now because it is related to the applied mean longitudinal magnetic field and its polarisation state is easy to change. The relation is as follows [103]:

$$P_{Fe} = \frac{\langle M_s \rangle}{n_e^{Fe} \mu_B} = 0.03727 \langle B - B_0 \rangle \tag{3.23}$$

where μ_B is the Bohr magneton of $9.272 \times 10^{-24}\,\mathrm{J/T}$ and M_s is the dominant spin part of the total magnetisation M.

$$M_s = \frac{2(g' - 1)M}{g'} \tag{3.24}$$

$$M = \frac{B - B_0}{\mu_0} \tag{3.25}$$

μ_0 is the vacuum permeability of $4\pi \times 10^{-7}\,\mathrm{Tm/A}$, g' is the magneto-mechanical ratio of 1.919 ± 0.002 and the ratio M_s/M is also referred to as spin fraction. Whether the alignment of P_{e^-} and P_{Fe} is parallel or antiparallel can therefore be changed by supplying the solenoid that magnetises the absorber with a current of different polarity.

Asymmetry and analysing power

The result of several measurements of the transmitted photon energy sums in both polarisation configurations are two different energy distributions from the mean of which an **asymmetry** can be calculated:

$$\delta = \frac{\langle E_P \rangle - \langle E_{AP} \rangle}{\langle E_P \rangle + \langle E_{AP} \rangle} \tag{3.26}$$

In order to avoid sign confusion, a notation has been adopted in which P represents parallel polarisation and AP represents antiparallel polarisation. To simplify this notation further, the angle bracket is omitted in the following. The statistical uncertainty of the asymmetry is given by:

$$\begin{aligned}
\Delta\delta &= \sqrt{\left(\frac{\partial\delta}{\partial E_{AP}}\Delta E_{AP}\right)^2 + \left(\frac{\partial\delta}{\partial E_P}\Delta E_P\right)^2} \\
&= \sqrt{\left(\frac{2E_P}{(E_{AP}+E_P)^2}\Delta E_{AP}\right)^2 + \left(\frac{-2E_{AP}}{(E_{AP}+E_P)^2}\Delta E_P\right)^2} \\
&= \frac{2}{(E_{AP}+E_P)^2}\sqrt{(E_P\Delta E_{AP})^2 + (E_{AP}\Delta E_P)^2} \\
&= \frac{2E_{AP}E_P}{(E_{AP}+E_P)^2}\sqrt{\left(\frac{\Delta E_{AP}}{E_{AP}}\right)^2 + \left(\frac{\Delta E_P}{E_P}\right)^2}
\end{aligned} \tag{3.27}$$

where ΔE_i is the statistical uncertainty on the mean of the energy sums.

$$\Delta E_i = \frac{\sigma_{E_i}}{\sqrt{N}} \tag{3.28}$$

σ_{E_i} is the standard deviation of the transmitted photon energy sum distribution and N the number of measurements.
The **analysing power** can be found via simulation (cf. chapter 5) and is defined as:

$$\mathcal{A} = \delta(P_{e^-} = 1, P_{Fe} = 1) \tag{3.29}$$

Its statistical precision is the same as that of the asymmetry, with the difference that N is the number of simulations. σ_{E_i}/E_i in this case depends on the number of simulated particles. Because of available computing power one usually simulates fewer particles than are realistically present in an LPA accelerated electron bunch. The effects of this are explained in section 6.7.
In the end, knowing the measured asymmetry δ_m as well as the iron core polarisation P_{Fe}, one can obtain the electron polarisation P_{e^-} with:

$$P_{e^-} = \frac{\delta_m}{P_{Fe}\mathcal{A}} \tag{3.30}$$

False Asymmetries

In a real experiment, the measured signal is unfortunately not only subject to changes due to polarisation differences. It is made up of several components and if these not only fluctuate uniformly around a mean value, but are subject to trends across changes in magnetic field direction, false asymmetries occur. These constitute systematic uncertainties on the measured asymmetry that need to be accounted for.

3.4.2. State of the Art

Early experiments using a magnetised iron absorber to determine photon polarisation, and, by extension, with a bremsstrahlung converter to determine electron polarisation, were already conducted in the 1950s [90, 107, 109, 110]. Advances in technology and the integration of polarisation modelling in Monte Carlo codes such as `Geant4`, have paved the way for a wide range of modern Compton transmission polarimetry

Experiment / facility	e^- / e^+	energy / MeV	$\mathcal{A} \cdot P_{Fe}$/%	P / %
Mainz parity violation exp. [98]	e^-	300	0.002	44.9 ± 1.8 (43.8 ± 1.8)
A4 @ Mami [100, 101]	e^-	570, 854	0.012, 0.008	N/A
MIT Bates [102]	e^-	20, 200	1.7, 0.8	40 ± 2 @ 20 MeV
E166 @ SLAC [103, 104]	e^+	4.5-7.5	1.04-1.17 ± 0.03	80 $\pm$(8-12)
Mami [83]	e^-	3.5	N/A	N/A
PEPPo @ JLab [105, 106]	e^-, e^+	3.1-6.3	$\sim$0.7 - 1.4	43 ± 6.5 ± 1.1 - $82.2 \pm 2.7 \pm 1.3$
JLAB [99]	e^-	5,7	1.28 ± 0.08 (exp), 1.24 ± 0.01 (sim) @ 7 MeV	37.7 ± 2.3

Table 3.1.: Overview of Compton Transmission Polarimeters. The two different values for the measured polarisation at the Mainz parity violation experiment are the mean values for the two different runs. The objective of the polarimeter presented in [83] was precise asymmetry measurement rather than absolute polarisation, achieving $\Delta\delta/\delta < 0.2\,\%$. N/A signifies "not applicable".

measurements. An overview of these experiments is provided in table 3.1.
Most measurements were conducted in the electron energy range where the ratio of the polarisation-dependent Compton cross-section to the total cross-section is highest, approximately 4-8 MeV, with some experiments extending even to energies of several hundred MeV. The effective analysing power ($\mathcal{A} \cdot P_{Fe}$) is typically on the order of 1 % or lower, with relative measurement errors on the polarisation ranging from about 4 % to 16 %.
As shown in equation (3.30), determining the effective analysing power with high precision is crucial for accurate polarisation measurements. Two approaches are commonly used:

1. One approach involves using another polarimeter to calibrate the system. By employing electron beams with a known degree of polarisation, the Compton transmission asymmetry can be measured and the effective analysing power subsequently calculated. This technique is employed in experiments at MAMI, where Barday et al. [83] use a Mott polarimeter, and the A4 [100, 101] experiment employs a Møller polarimeter.

2. Alternatively, if the absorber polarisation is known, e.g., through simulations with OPERA3D [111], Monte Carlo simulations can be used to calculate the analysing power. This method was employed in the E166 experiment [103] and will also be used in this work (cf. section 8.8).

Experiments at Jefferson Lab [99, 106] employed both approaches, yielding consistent effective analysing powers. This agreement highlights a well-understood beamline and validates the implementation of polarisation in `Geant4` simulations.
A comprehensive understanding of Compton transmission polarimetry measurements requires addressing various sources of systematic uncertainty that can influence the results. Commonly reported sources include energy calibration, background correction, detector linearity, electronics noise, and non-statistical fluctuations in the particle beam. Additionally, simulation and analysis methods can introduce systematic uncertainties. A useful strategy to mitigate uncertainties related to the measured asymmetry is to alternate not only the polarity of the absorber but also that of the incident particle beam.
Overall, Compton Transmission Polarimetry is considered a well-suited method for measuring the polarisation of electrons (and positrons) in the MeV range. These polarimeters are relatively simple, as they do not require spin manipulation to measure

longitudinal electron polarisation, and they can easily withstand large beam currents when equipped with appropriate absorbers.

3.5. A very brief introduction to calorimetry

A calorimeter, in high-energy physics, is a detector that measures the energy of particles through their total absorption within a block of matter (cf. section 3.1). This work focuses exclusively on electromagnetic calorimeters and draws on established literature [74, 112, 113] and lectures [114]. In the context of Compton transmission polarimetry (cf. section 3.4), a calorimeter is used to measure differences in photon transmission through magnetised absorbers.
Generally, the operational principle of calorimeters can be divided into four stages, which are outlined here with reference to the lead glass calorimeter developed for the LEAP project (for more details, see section 7.2):

1. **Particle-Matter Interaction – Shower Initiation**: The incident particle interacts with the calorimeter material, creating a cascade of secondary particles (a shower) and depositing its energy.

2. **Signal Conversion**: The deposited energy is converted into a detectable signal, such as visible light or an electrical signal. For example, in the case of the lead glass calorimeter, charged particles produced by the shower generate Cherenkov radiation (cf. section 3.1.2) as long as their energy exceeds the emission threshold.

3. **Data Acquisition**:The resulting signal is captured and processed into a digitised format. In the case of the LEAP calorimeter, photomultiplier tubes detect the Cherenkov light and convert it into an electrical signal, which is then digitised and recorded by the data acquisition system for further analysis.

4. **Calibration and reconstruction**: The collected data is used to infer particle information through calibration and reconstruction techniques.

Electromagnetic Showers
Electromagnetic showers form the basis of energy deposition in calorimeters, enabling the measurement of high-energy particles. When a high-energy particle, such as an electron or photon, interacts with the calorimeter material, it initiates a cascade of secondary particles. This cascade is driven primarily by two processes: pair production

for photons and bremsstrahlung for electrons and positrons.
The number of particles in the shower grows approximately proportional to the initial energy E_0. In a simple model, the particle count roughly doubles with each radiation length X_0, which is the average distance over which a high-energy electron loses $1/e$ of its energy or a photon undergoes pair production.
As the shower develops, the energy of secondary particles decreases. Once the critical energy E_c, the point at which ionisation losses dominate over radiation losses, is reached, the particles are gradually stopped or absorbed. The depth at which the shower reaches its maximum intensity depends on the ratio of the initial energy to the critical energy and is approximately proportional to $\ln(E_0/E_c)$.
The lateral extent of the shower is characterised by the Molière radius, which contains approximately 90 % of the shower energy. This radius depends on the material properties, including the radiation length and atomic number Z.

Energy resolution
A key metric for characterising a calorimeter is its energy resolution. For a calorimeter with a linear energy response, the resolution is commonly expressed as:

$$\frac{\sigma_E}{E} = \frac{a}{\sqrt{E}} \oplus \frac{b}{E} \oplus c \tag{3.31}$$

Here, σ_E represents the standard deviation of the measured energy, and E is the particles energy. The resolution is defined by three components added in quadrature: the stochastic term, the noise term, and the constant term.
The first component, $\frac{a}{\sqrt{E}}$, is the stochastic term, which arises from intrinsic fluctuations in the shower development process. These fluctuations are governed by Poisson statistics, reflecting uncertainties in the number of secondary particles produced. The effect of this term diminishes with increasing energy, as higher-energy showers involve a larger number of particles, reducing relative fluctuations.
The second component, $\frac{b}{E}$, is the noise term. It accounts for electronic noise in the readout chain and pulse pileup, the latter occurring when signals from multiple events overlap. This term is most significant at low energies, where it dominates over other sources of uncertainty.
Finally, the constant term, c, arises from factors unrelated to the energy of the incident particle. These factors include variations in detector response due to imperfections in construction, calibration errors, and energy leakage from the calorimeter. While the amount of leakage depends on the energy of the incident particle, the additional

relative width in the measured energy distribution caused by leakage remains effectively constant across energies. This term sets a lower bound on the achievable resolution at high energies.

Calorimeter Types

There are two general types of calorimeters: homogeneous and sampling calorimeters. In **homogeneous calorimeters**, both shower development and signal collection occur within a single material. Their primary advantage is that all deposited energy is collected, resulting in excellent energy resolution and linearity. However, their segmentation is limited, in particular in the longitudinal direction.

In contrast, **sampling calorimeters** consist of two different materials: an absorber for shower development and an active medium for signal collection. Only the energy deposited in the active material is collected, meaning the shower is sampled. These calorimeters are typically more cost-effective, as absorber materials are generally less expensive than active ones. They also allow for easy longitudinal and transverse segmentation, and if a dense absorber material is chosen, they can be made highly compact. However, their energy resolution is lower compared to homogeneous calorimeters. The stochastic term in the energy resolution (cf. equation (3.31)) is larger because only a fraction of the total charge is collected in the active material, leading to sampling fluctuations.

Chapter 4.

Computational essentials

Computer-aided methods are indispensable tools for addressing complex problems in physics, from analyzing intricate data sets to performing detailed simulations. This chapter explores three key computational techniques. It begins with Monte Carlo methods, which are fundamental for modeling and understanding complex probabilistic systems. Next, it covers GEANT4, a versatile toolkit for simulating the passage of particles through matter. Finally, it examines the batch computing processes employed at DESY, which are essential for managing large-scale computations efficiently.

4.1. Monte Carlo Methods

Monte Carlo (MC) simulation is a computational technique that makes use of stochastic methods to solve a wide range of mathematical and statistical problems. Using MC methods one first sets up a mathematical model to represent a system or process in reality [115]. Then one uses repeated random sampling of this model until the target variables can be approximated and one can obtain statistical estimates [116].
MC methods were used long before computers existed. They had their beginnings in the 18th century with the Buffon-Laplace needle experiment, which is described very clearly by Dunn and Shultis in [117]. Another great example of analog MC is Enrico Fermi using statistical sampling methods to investigate the slowing down of neutrons in the 1930s. However, he was still dependent on mechanical calculators. It was not until the middle of the 20th century, with the advent of digital computers, that MC simulation became a practical and increasingly widely used tool. The first corresponding computation models were developed during the work on the nuclear

weapons programme. In 1949 Nicholas Metropolis and Stanislaw Ulam published a paper called "The Monte Carlo Method" [118]. Allegedly, Metropolis, knowing Ulam's fondness for games of chance, coined the name Monte Carlo based on the city famous for the casino of the same name in Monaco.
Since then, MC methods have been continuously developed and numerous applications have emerged.
One of those is particle physics. As MC simulations excel at modelling probabilistic processes, they are eminently well suited to investigate the paths of particles in matter determined by stochastic interactions such as scattering and absorption. Furthermore, many physical systems are so complex that analytical methods are no alternative at all. Another advantage of MC methods is that they make it possible to test hypotheses using relatively inexpensive simulations before carrying out experiments, some of which consume a lot of resources and assume huge scales.

4.1.1. Core principles of MC methods

As mentioned above, a mathematical prediction model is formulated for a MC simulation, which is then fed with independent variables that follow a certain probability distribution. Repeated random sampling can then be used to infer real-world population characteristics from the simulated sample data. In this section, the individual building blocks and steps required for the most basic applications are explained.
Repeated random sampling would not be possible without a random number generator (RNG), which creates random values (RVs) uniformly distributed between 0 and 1, denoted here as λ. Since computers operate based on predictable algorithms, they cannot create true random numbers [119]. Instead, they generate **pseudo-random numbers**, which are sequences of numbers that appear random but are generated by deterministic processes.
The probability of occurrence of a continuous random variable can be defined by a function called the **probability density function** (PDF). The PDF specifies the likelihood of a random sample x_i taking on a specific value x within a small interval dx. Mathematically, $p(x)dx$ represents the probability that x_i lies within dx around x [117]. Unlike discrete probabilities, the PDF represents a density; the actual probability is obtained by integrating the PDF over an interval.
A direct measure of probability is given by the **cumulative distribution function** (CDF), which provides the probability that a random variable X will take a value less

than or equal to x. It can be written as:

$$P(x) \equiv \int_{x_{min}}^{x} p(x')dx' \Leftrightarrow \frac{dP(x)}{dx} = p(x) \tag{4.1}$$

Discrete distributions can be described by adjustments, such as replacing the integrals with sums, but for the sake of simplicity, I will focus on continuous distributions here. One simple method to generate x from λ is the inverse transform method. This method allows us to transform a uniformly distributed random variable λ into a random variable x with a desired distribution by using the inverse of the CDF. Random variables of x can be generated using the following sampling formula:

$$x = P^{-1}(\lambda) \tag{4.2}$$

This method is particularly useful because it provides a straightforward way to generate samples from any distribution, given its CDF and its inverse.
The Monte Carlo Method uses random samples to approximate the expected values of a function. Given a function $f(x)$ and the distribution $p(x)$ the expected value is

$$\langle f \rangle = \int f(x)p(x)dx \tag{4.3}$$

If X_i are random variables drawn from $p(x)$ the Monte Carlo estimator for the expected value is:

$$\overline{f} \equiv \frac{1}{N}\sum_{i=1}^{N} f(X_i) \tag{4.4}$$

The **law of large numbers** (LLN) now states that

$$\lim_{N\to\infty} \overline{f} = \langle f \rangle \tag{4.5}$$

Meaning that in the limit of infinity the sample mean $\overline{f}$ will tend to the population mean, or true expected mean $\langle f \rangle$, which is a deterministic number not a random variable [120]. In other words: The Monte Carlo estimations become more and more accurate as more samples are used. The LLN thus represents one of two most important principles of MC calculations.
The other is the so called **Central Limit Theorem**. It states that the sum of N independent and identically distributed random variables, each having finite variance, is

distributed in the limit of $N \to \infty$, according to a Gaussian distribution, regardless of the underlying PDFs [121]. Which means that $\overline{f}$, assuming that N is sufficiently large, follows a normal distribution:

$$p(\overline{f}) = \frac{1}{\sigma_f \sqrt{2\pi}} \exp - \frac{(\overline{f} - \langle f \rangle)^2}{2\sigma_f^2} \tag{4.6}$$

This distribution is centered around the true expected value $\langle f \rangle$ with the true standard deviation σ_f. The error in the Monte Carlo estimate is the standard error $\sigma_f / \sqrt{N}$. Based on the LLN, σ_f can be approximated with the sample standard deviation.
In the context of particle tracking, the core principles of Monte Carlo simulation can be concisely outlined as follows: Random sampling is used, for instance, to generate initial positions and energies of particles from known distributions. It is also used to sample scattering angles at interaction points or energy losses. By tracking a particle through multiple interactions and accumulating a quantity of interest, such as deposited energy, the Monte Carlo Estimator can estimate the average quantity by averaging the results from all particles. According to the law of large numbers, simulating more particles increases the likelihood that the average will approximate the true value. Additionally, the central limit theorem suggests that as the number of particles increases, the distribution of the average result will tend to be normal. This Gaussian distribution is advantageous because it simplifies the calculation of confidence intervals and supports robust uncertainty analysis, making it easier to interpret the results and quantify the reliability of the estimates.

4.1.2. Challenges and Limitations

MC simulations are an excellent tool for making predictions about reality and serve as an important complement to both experimental and theoretical approaches. However, they come with several challenges and limitations.
One significant limitation is the need to balance the accuracy of the simulation with the available computational resources [122]. Simulations demanding extensive CPU time or exceeding memory limits of the available machines are impractical. The statistical uncertainty decreases inversely with the square root of the number of simulated events, necessitating a large number of simulations for high precision. It is up to the researcher to decide the desired level of accuracy, considering that the law of large numbers and the central limit theorem are valid only in the limit as the number of simulations

approaches infinity. Additionally, decisions must be made regarding how closely the model should mimic reality and when to accept approximations that simplify the model and reduce computational complexity.
In addition to the statistical uncertainty of a simulation, simulations also suffer from numerical inaccuracies, which arise from the finite precision of numerical values. Truncation and round off errors will always happen.
Furthermore, the quality of model input parameters play an important role. An example from particle tracking: Does the energy distribution of the incoming particles correspond to the real events of interest? Is the spectrum perhaps undersampled, leading to the loss of certain features?
Similarly, high-quality (pseudo-) random number generators are crucial. The random numbers should be independent, follow the expected distribution of a truly random sequence, and have a very long period before repeating [119].
Finally, every simulation is accompanied with the need for verification and validation [123]. Verification involves procedures to ensure the code runs without errors, while validation compares simulation results with experimental data from the modeled system. When complete experimental replication is impractical, validation of partial aspects becomes crucial, allowing for comparison of simulation results with tested components or subsystems.

4.2. GEANT4

A toolkit that makes use of MC methods is GEANT4 [124–126], a free software package to create simulations of the passage of particles through matter [127, 128].
It's development began in 1994, when a large international collaboration of physicist programmers and software engineers united their efforts to write a detector simulation program which had the functionality and flexibility necessary to meet the requirements of the next generation of subatomic physics experiments. They redesigned a major CERN software package (GEANT3, based on FORTRAN) for an object-oriented environment based on C++ and in 1998 the first production release was delivered.
Since then the community of developers and users has grown and nowadays GEANT4 is used for a wide range of applications from high energy, nuclear and accelerator physics, to medical and space science.
The toolkit includes all aspects of the simulation process:

- The creation of a model of the geometry of the system one is interested in and the associated materials,
- the tracking of particles through the defined model,
- the application of physics processes for electromagnetic, strong and weak interactions of particles in matter over an energy range from milli-eV to TeV,
- the recording of selected information to generate detector responses,
- the visualization of geometry and tracks,
- and the analysis of data.

To build a specific application the user chooses from the different available models and tools and implements code in GEANT4 user action classes.

4.2.1. Fundamental components

There are three mandatory classes a user has to provide in a GEANT4 simulation. The **Detector Construction** sets the environment, the **Physics List** contains the models that describe the physics used and the **Primary Generator Action** determines the particle sources. The subsequent portion of this section delineates these elementary components.

Detector Geometry: The detector construction is the representation of the geometrical elements of the simulation, but also contains their materials, electronic properties and visualization properties.
GEANT4 uses a hierarchy of volume classes. The so called "solid" describes the shape and size of a geometry. The "logical volume" holds information about it's material, sensitivity, whether it contains electromagnetic fields, it's visualisation properties, the mother-daughter relationship of nested volumes and more. The physical volume is the geometry's actual placement and contains information about it's position and rotation.

Physics List [129]: A collection of physical models that can be used to describe the particles to be simulated and their interaction with matter at different energies [130]. During an event loop the physics list provides information to the run manager when which physics process is needed.

There are many different models that describe the same interactions. The algorithms differ in terms of accuracy, applicability and computing time. Depending on the application, the developer must decide what level of detail they need and how much time they want to sacrifice for it, as well as which models are really necessary for the application and its energy range.
GEANT4 contains seven major categories of physics processes: electromagnetic, hadronic, decay, photolepton-hadron, optical, parametrisation and transportation. There are standard reference physics lists which contain a comprehensive set for standard use cases. The GEANT4 Physics Lists Guide [24] provides an overview of the different lists and their areas of application.

Primary Generator Action: This class arranges the way primary particles are generated. The user can choose between the primary generator classes that actually create the particles during a simulation run. The two most common are the Particle Gun and the General Particle Source (GPS). The gun is a simpler tool. It generates a number of particles of a certain type with a given momentum and position These values do not follow a distribution. All particles have the same kinematics. This is different when using the general particle source. It allows the specifications of the spectral, spatial and angular distribution of the primary source particles.

Additionally, there are **optional user actions** that provide further customization and control over the simulation at various stages. These actions are encapsulated in virtual classes, each with methods that can be overridden by the user. Each method in these classes has an empty default implementation, enabling users to inherit from these classes and implement only the methods they need [131]. These capabilities are commonly utilized to gather data during event handling, including each step, and at the start and end of tracks, events, and runs.

4.2.2. Key stages of a simulation

The largest unit of simulation is a **run**. It consists of a set of events under the same conditions, meaning that detector geometry and physics processes used stay the same within. Changes can be made in between runs, a state also called run break. Every run has two phases. First, initialization, where detector geometry, sensitive detectors, particles, and physics processes are constructed, then, the event loop. Similar to a real-life experiment, the loop starts with the command Beam On and is followed by a

series of events [132].
An **event** starts with the generation of primary particles, continues with the simulation of all subsequent interactions and processes and ends when all particle tracks have been processed. Multiple primary particles can be created within an event and the tracks to be processed include those of secondary particles. In order to make statistical estimates of unknown variables based on repeated random sampling, in other words, to be able to portray the randomness and variability of the physical processes in the simulated system, it is necessary to simulate a large number of events or runs without the parameters changing in between (see equation 4.5).
As a particle moves along a trajectory through and interacts with the simulation geometry it passes through different points of space at different times. A **track** in GEANT4 is the state of the particle at one of those. The corresponding class keeps static information like particle identity, mass and charge, as well as current information like position, momentum and energy.
The smallest unit of simulation is a **step**. It is the difference between two of those above mentioned points in space and time. The corresponding class stores transient information including the two endpoints.
Individual actions can be performed by the user during each of these individual steps through the optional user action classes. A summary of the interaction of the main programme and the Geant4 kernel is depicted in Figure 4.1.
At the step level, the simulation operates as follows: Random numbers are generated for each active physics process based on the appropriate probability density function, and the physical interaction lengths are computed. The process with the shortest interaction length is identified. If it is an exclusive process, it is executed alone. If not, corresponding actions for other active processes are also invoked. Particle information, steps, and tracks are updated accordingly. If the process occurs within a sensitive logical volume, particle hits are generated.

4.2.3. Runtime Simulation Control

GEANT4 can operate in interactive mode, allowing users to adjust simulation parameters and issue commands in real-time via a command-line interface or graphical user interface (GUI), or in batch mode, where simulation parameters and command sequences are predefined in **macro files**. The latter allow for an automation of the simulation process without the need of user interaction. Macros are ASCII files and

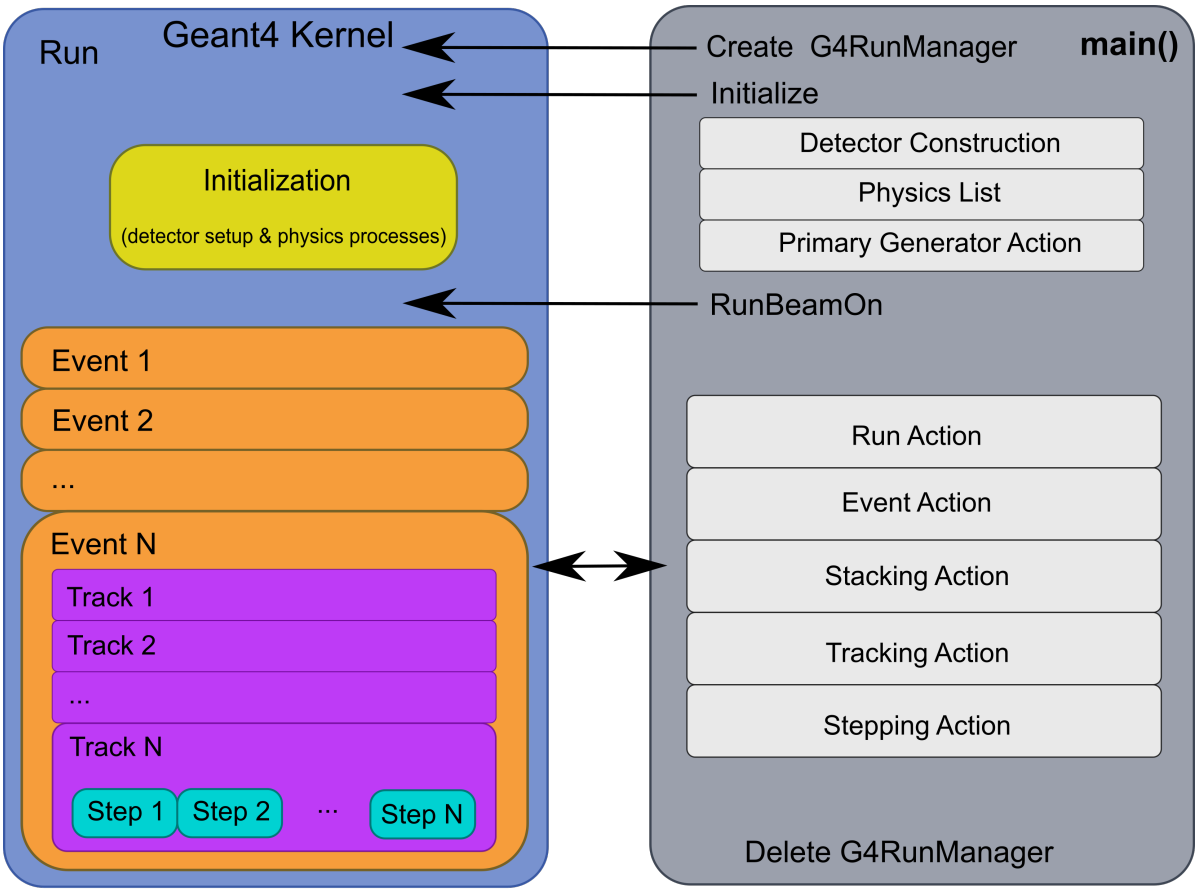

adapted from I.Hrivnacova and P. Gumplinger, Geant4 Tutorial for ED MIPEGE 2013

Figure 4.1.: Schematic of the GEANT4 application work flow. The main program initializes the GEANT4 Kernel and interacts with it. Run initialization is followed by an event loop. User-defined components, such as detector construction, physics list, and action classes, enable interaction.

usually have a '.mac' ending [133].
GEANT4 has various built-in UI commands, each roughly corresponding to a specific GEANT4 category such as control, geometry, tracking, particle, run, or (physics) process. A comprehensive list of these commands can be found in the GEANT4 Application Developer Guide [131]. It is also possible for the user to define their own UI commands. This is done with the help of **messenger classes**.

4.2.4. Polarisation in GEANT4

With the electromagnetic polarisation extension, polarised particles and materials and their interaction were added to GEANT4 [134]. The available processes are Bhabha/Møller scattering, positron annihilation, Compton scattering, pair creation, and bremsstrahlung.
The idea behind the extension is that each particle is assigned a polarisation vector, the Stokes vector $\vec{\xi}$ [135], and to then track the mean polarisation from one interaction to another. How this vector is defined is displayed in table 4.1.
Important to note is that the there noted directions are in the particle reference frame. A 100 % longitudinally polarised electron beam would have $\vec{\xi} = (0, 0, \pm 1)$, where ± 1 corresponds to spin parallel or antiparallel to particle momentum [134].

Initial beam particles can be given a polarisation state using set methods in the macro file. To simulate polarised media, a Stokes vector is assigned to their physical volumes during detector construction. To do this, their logical volume must be made known to the polarisation manager. As soon as this is the case, $\vec{\xi}$ can also be changed with the help of the macro. Here, the world volume is used as reference frame. Polarised bremsstrahlung in `Geant4` is based on unpolarised cross-sections, with the primary modification being the assignment of polarisation vectors to the final state particles.

Table 4.1.: Definition of the Stokes vector in the EM polarisation library. Positive z being the direction of beam propagation.

	Photons	**Electrons**
ξ_1	linear polarisation	polarisation in x direction
ξ_2	linear polarisation but $\pi/4$ to right	polarisation in y direction
ξ_3	circular polarisation	polarisation in z direction

The standard unpolarised model used is the Seltzer-Berger model (cf. section 3.1.1). For electron energies below 1 GeV, cross-sections are evaluated using dedicated parameterisations, while for energies above 1 GeV, analytical values are used. The Landau-Pomeranchuk-Migdal effect, which reduces bremsstrahlung in dense materials at high energies, is implemented.
For Compton scattering, the effects of polarisation on the total cross section, mean free path, and the distribution of final state particles are included. Polarisation vectors are assigned to the scattered photon and the ejected electron. The electrons in the material are assumed to be free and at rest, neglecting atomic binding effects.

4.3. Batch Computing at DESY

In order to cover a wide range of parameters efficiently and manage dependencies between simulations, tasks are often categorized into batches and submitted as jobs to a computing cluster.
DESY is accommodating the National Analysis Facility, or NAF for short, a computer complex providing analysis infrastructure for particle physicists in Germany [136]. In simple terms, it can be said that it is a network of computers, also known as worker nodes, which work together as a single system. The NAF features a large batch farm called BIRD. A subsystem optimized for handling a large number of independent tasks that don't require user input, also called batch jobs. It runs on HTCondor [137], which manages the queue of jobs and assigns them to available worker nodes.

Chapter 5.

LEAP_SIMS - a simulation framework

LEAP_SIMS [138] is a framework developed as part of this thesis for conducting various simulation studies of the LEAP polarimeter. At its heart is the GEANT4 application, which simulates the passage of particles through the diagnostic system and, if desired, the beam line. It is described in more detail in sections 5.1 to 5.4. However, in order to carry out a large number of studies, further components and work steps are required. They are displayed in figure 5.1.
Each simulation begins by modifying the configuration file to include the necessary components and parameters. To ensure a comprehensive range of simulations within

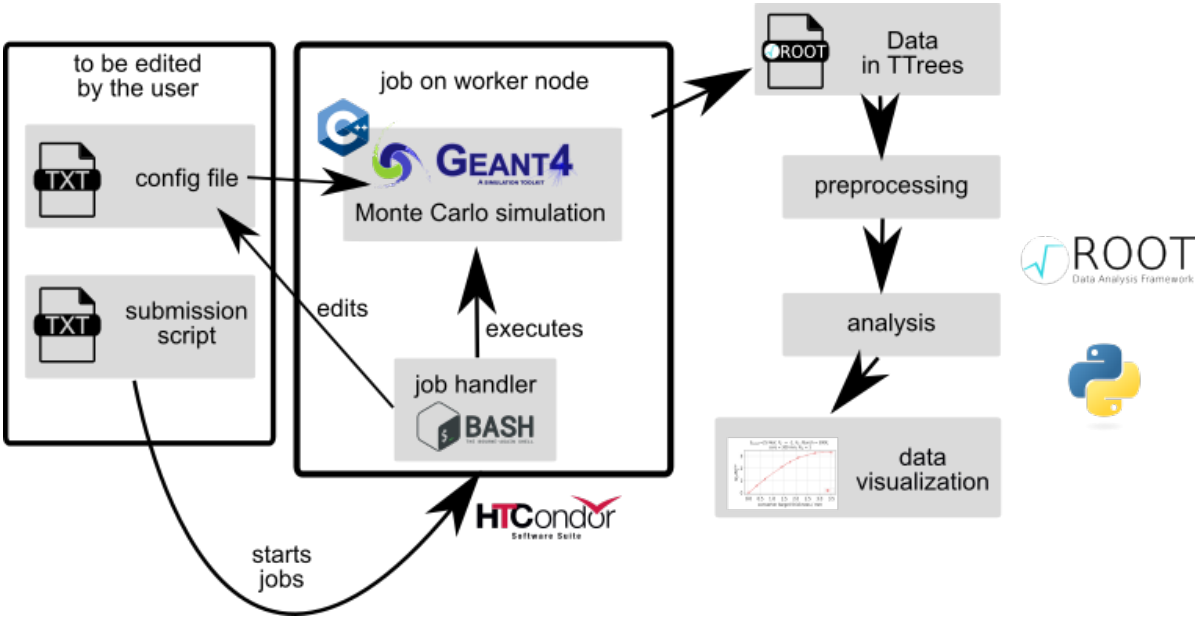

Figure 5.1.: Schematic of the workflow in LEAP_SIMS

a reasonable time frame, the simulation campaigns are divided into manageable segments and submitted as jobs to a computing cluster (see section 4.3). To submit LEAP_SIMS jobs, a submission script is required, allowing specification of the number of jobs and the varying input parameters. For instance, if investigating the effect of different electron energies on the polarimeter, one would list these energies in the submission script. To achieve a desired level of statistical accuracy, each job would be repeated a specified number of times.
Considering then a job on a single worker node, a bash script uses the input parameters to edit the configuration file and executes the GEANT4 application. The output of the simulation is saved in ROOT-files. ROOT is an Object Oriented framework for large scale data analysis [139]. It was created having the enormous amounts of data produced by high energy physics experiments in mind. ROOT-files are therefore optimised for saving and accessing those, ensuring both the integrity and accessibility of the generated data. Inside the ROOT-files the data is organised in TTrees, a tree-like data structure, enabling fast access of hierarchical data sets. As every worker node produces it's own output files, files containing simulation results for the same set of parameters are merged. Part of this data pre-processing is also the recording of the simulated parameter sets and the corresponding file names in a database. The next step is then the analysis of the generated data sets. PYTHON and ROOT were used to write packages which can be used to perform the most common analyses. One example is the determination of the analysing power (see section 5.5). Last but not least, LEAP_SIMS also includes python packages that can be used to create the standard figures that appear in this work.

5.1. GEANT4 application setup and working principle

Many different aspects of the polarimeter and its tests have to be simulated. Therefore, the GEANT4 application is designed with a focus on user-friendliness, leveraging a modular architecture that allows for dynamic creation of components based on a configuration file, ensuring both flexibility and ease of use.
The entry point of the LEAP_SIMS G4-application is the main() program. Upon execution, the configuration file is read, and based on its content, necessary structures are prepared and variables declared. This process addresses questions such as: Which components of the diagnostic system should be included? Which elements should aggregate information? What data structures are required to store the simulation output?

What types of particle beams need to be simulated? Additionally, this information is used to dynamically generate a macro to influence run-time behaviour.
Then, an object of the AnaConfigManager class is constructed using an instance of the ConfigReader, initialising it with the necessary configuration settings for the analysis. The class acts as central management hub for configuring and controlling the analysis and data output aspects of the GEANT4 simulation. A comprehensive list of all classes can be found in appendix A. It offers more detailed information about the input and the methods contained within.
Next, an instance of the G4 run manager class is generated. It controls the flow of the program and manages the event loop(s) [131]. Now the three mandatory initialisation classes as well as the user action classes can be instantiated and set in the run manager. The initialisation of the run manager constitutes the initial setup of the simulation. The detector geometry, sensitive detectors, particles, and physics processes are constructed (see section 5.2) and cross-section tables are calculated.

Finally, main() processes the macro mentioned above, or, if it was started with the visualisation flag, starts a user interface session.
The content of the macro depends on the settings in the configuration file, but the basic procedure is always the same. First, random seeds are set. The engine generating those pseudo random numbers uses seeds as staring points [140]. In the case of LEAP_SIMS two integers are used. From the same seed, or set of seeds, the random number generator always generates the same sequence of random numbers. To model the polarimeter performance accurately, a large number of statistically independent simulations is needed. As previously mentioned, these simulations are submitted as jobs to a computing cluster. One option is to submit a single job per parameter set containing thousands of runs, but this approach results in long computation times. Instead, it is more efficient to submit many small jobs, each containing a single run(-pair), as they are easier for the scheduler to accommodate and reduce overall computation time. However, without setting a random seed, each job would use the same seed and produce identical results, leading to a lack of statistical independence. Therefore, the LEAP_SIMS job handler (see Fig. 5.1) generates different random seeds for every job and edits the configuration file accordingly. Using the Unix time, number of seconds since 00:00:00 UTC on 1. January 1970, is a good starting point, but multiple jobs may be created at the same time. Therefore, the first random seed in LEAP_SIMS is the Unix time plus the job-ID and the second is the Unix time plus the process-ID of the current shell. This guarantees that whenever the simulation is started, a unique sequence of random numbers is produced.

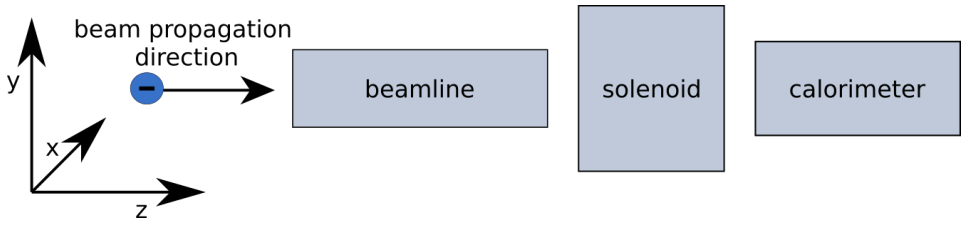

Figure 5.2.: Modules of the LEAP_SIMS detector geometry

Once statistical independence of the simulation is confirmed, the next step is to reinitialise the run using the `run/initialize` command. This command typically allows for dynamic adjustments to accommodate changes in simulation parameters. In the case of LEAP_SIMS, it establishes a specific initialisation state required for the polarisation manager, ensuring that the simulation environment is properly set up for polarisation calculations, even if no changes to geometry or materials are made.
Next, the details of the particle source are configured. This means that particle type, the number of particles per event, spot size, divergence, direction, and energy are set. The particles can be mono-energetic, or there can be a Gaussian or user defined distribution.
Finally, the polarisation (-direction) of either the particles or the solenoid core can be specified before a run, the event-loop, is started. If one is interested in asymmetries it is important to simulate both polarisation direction configurations, parallel and anti-parallel.

5.2. Upon Initialisation

As mentioned in the previous section, during run initialisation detector geometry, sensitive detectors, particles, and physics processes are constructed. In the following these will be explained in more detail.

5.2.1. Detector Geometry

LEAP_SIMS is designed to be highly modular. Therefore, the simulation setup is divided into several parts, which can be switched on and off independently of each other using the configuration file. The general layout of the geometry is displayed in figure 5.2. Possible geometry modules that can be placed are the beam line, the

polarimeter-solenoid, and the polarimeter-calorimeter. The user can choose between two different beam line options: One representing the beam telescope at the DESY II test beam (see [141] and section 7.2.3), the other portraying the setup of the zero polarisation measurements at the FLARE facility (see section 8.1). The solenoid can either be of a more generic type as for example used in the design study in chapter 6, or be of the exact dimensions used in the zero-polarisation measurement (examples in chapter 8.8). Several sub-components can be switched on and off as desired and likewise the magnetic field of the solenoid. Details of specific simulation setups are consistently provided in the sections where they are conducted. The calorimeter can either be a single lead glass crystal, a set of nine crystals stacked in a three by three grid, or nine crystals surrounded by an aluminium housing. All the individual components are contained in the enclosing world volume. This can be made out of air, as it would in an actual experiment, or vacuum. An example configuration file is included in appendix B.

5.2.2. Sensitive Detectors

Sensitive detectors (SDs) are geometrical components in GEANT4 that are designated to collect information about the particles passing through them. They do so by generating data structures called hit objects, filled with the information collected from each step of the particle's movement as it traverses through or interacts with the detector [131]. The application developer can determine which data is collected and whether there are any additional conditions.
There are two different types of SDs used in LEAP_SIMS. The most commonly used are virtual volumes with ideal detectors. Those are thin, 1 mm thick, volumes out of the same material as their surrounding, which register information about every particle passing through their front as long as their z-momentum is positive. The latter condition is a measure to prevent back-scattered particles from being registered. The user can decide whether they want to collect aggregated data or record the information of each individual step. In the following this will be referred to as summary or detailed output mode. In the former, the sum of the total energy and number of passing particles are returned for all particles, photons and electrons. In the latter, information about the particle definition, it's total energy, position, vertex position, momentum direction, polarisation, track- and parent-ID is gathered for every pre-step point. Regardless of the output mode, the energy spectrum and the energy-

weighted beam profile are aggregated and presented as histograms in each of the virtual SDs. The energy-weighted beam profile represents the spatial distribution of incident particles at the plane of virtual detection, with each region weighted by the total energy sum per unit area. Fixed histogram limits can be set for the beam profile, requiring the user to specify only the number of bins in the configuration file. The situation is different with the energy spectra. The lower limit is always set to 0 MeV, while the upper limit is determined by the maximum energy of the bremsstrahlung spectrum, which corresponds to the highest energy emitted by the particle source. To ensure comparability across different runs, the user specifies the bin width in the configuration file.
The crystals of the calorimeter constitute an exception. They are the second type of SD used in LEAP_SIMS. In the end, it is of utmost interest to obtain, through our simulations, a parameter that is proportional to our detector response. The LEAP calorimeter is a Cherenkov calorimeter (see section 7.2): photons generated by the Cherenkov effect propagate through the crystal and are registered by photomultiplier tubes (PMTs). Simulating optical photons in `Geant4` is very complex and computationally intensive. Therefore, in LEAP_SIMS, we use the deposited energy of charged particles above the Cherenkov threshold in lead glass as a first approximation. Specifically, if the total energy of charged particles exceeds 642.43 keV, their deposited energy is accumulated and output at the end of the run. Details on this topic can be found in the work of Felix Stehr [52].
If the user wants to follow the shower development, they have to set an extra parameter in the configuration file to true, as it results in a very large amount of data output. Regardless of type, every SD in LEAP_SIMS can be switched on and off individually. Their volume will be placed if the geometrical component they belong to is switched on, and they will record data according to what is specified in the configuration file.

5.2.3. Physics Processes

LEAP_SIMS utilises a modular physics list, where individual modules are compiled into a list tailored for the application. First, all types of particles are created. Then, transportation is added. Depending on whether polarisation is enabled in the configuration file, either a custom polarised electromagnetic physics list is added or the standard module for electromagnetic physics, `G4EmStandardPhysics` [134], is used. The custom LEAP_SIMS module includes support for polarised particles and materials.

Specifically, it incorporates the following polarised processes along with multiple scattering: polarised photo-electric effect, Compton scattering, γ-conversion, ionisation, bremsstrahlung, and positron annihilation.
One of the key trade-offs in simulations is balancing accuracy with simulation time. This involves not only considerations like the number of simulated input particles for statistical robustness but also the selection of included processes, the precision of employed models, and the transitions between them.
For example, simulating optical photons can be computationally intensive, which is why they are not included by default in LEAP_SIMS. However, if optical photon analysis is required for the calorimeter crystal(s), an optional module can be activated via the configuration file.
To improve the accuracy of energy deposition while maintaining reasonable simulation times, the energy loss `StepFunction` in `Geant4` was adjusted (cf. "Particle Transport" in [134]). In `Geant4`, the energy loss of charged particles can be treated in two ways: as a continuous process, where the mean energy loss is calculated over each step, or as discrete events involving the production of secondary particles. The `StepFunction` determines when continuous energy loss is assumed and when discrete events are considered. The energy loss fraction (also known as `dRoverRange`) sets the threshold for this transition. In LEAP_SIMS, the default value of 0.2 is used, meaning that if a particle loses less than 20 % of its energy in a step, the loss is treated as continuous. Another key parameter is the minimum step length (`finalRange`), which defines the smallest step a particle can take. In LEAP_SIMS, this has been reduced from 1 mm to 0.01 mm. While this increases the number of steps and thus simulation time, it also enhances accuracy in critical regions, such as boundary surfaces of the calorimeter.

5.3. During a run

As soon as the initialization phase of the simulation is complete, i.e., the geometry of the simulation environment and its materials, the particle source, and all required physical processes have been defined, a run can be started. This happens via the `/run/beamOn` command in the macro.
At the beginning of the run action, a ROOT output file is created, and TTrees and histograms are booked according to the configuration file. In this context, 'booking' means that memory is allocated, and the tree or histogram structure is defined. Every activated sensitive volume gets its own tree, with an additional tree for the metadata

of the configuration file. The histograms store energy spectra and energy-weighted beam profiles.
The framework supports two summary modes: summary mode for events and summary mode for runs. These modes control how data is accumulated and stored during the simulation.

- Summary mode for events: Accumulates information during an event and writes it at the end of each event.
- Summary mode for runs: Accumulates information over the entire run and writes it at the end of the run.

The distinction is important because different simulation setups require different modes. In cases where single-particle events are used, many events per run together constitute a single bunch. In contrast, multi-particle events may represent an entire bunch within a single event. To ensure compatibility with different configurations - particularly to maintain the proper functioning of the General Particle Source (GPS)summary mode for runs is the default. This mode will simply be referred to as 'summary mode' in the following text.
During execution, the begin-of-event action resets accumulables if 'summary mode for events' is enabled. Each event starts with primary particle generation according to the GPS definitions in the configuration file. These primaries and their secondaries are tracked step by step as they interact with the geometry. Sensitive detectors either write data directly to TTrees in detailed mode or accumulate information in summary mode while filling histograms. An event ends once all particles have either exited the simulation volume or been stopped.
If 'summary mode for runs' is active, accumulated data is written to the TTrees only at the end of each event. Finally, after all events are processed, the end-of-run action writes all TTrees and histograms to the output file and closes it.
A summary of what happens during an event loop is shown in figure 5.3.

5.4. Key Configurations

There are a couple of configurations, sometimes sets of them, that are used repeatedly throughout the thesis. While a complete list of parameters is provided in the example configuration file in appendix B, this section highlights some frequently used ones,

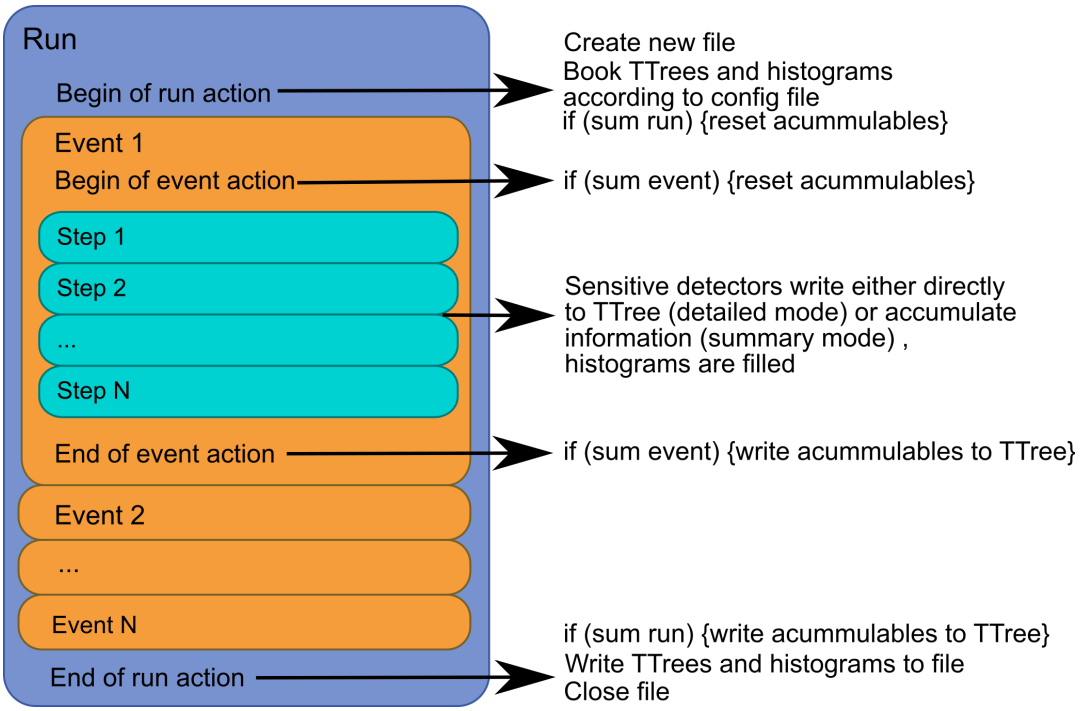

Figure 5.3.: Schematic of actions during an event loop

providing context and additional definitions.

Run types in the simulation

Depending on the analysis, it is sometimes necessary to simulate individual runs or run pairs.The parameter `Run:type` can be used for this.

- **Asymmetry runs**: A simulation consists of a run pair with opposite polarisation configurations.
- **Single runs**: A simulation consists of a single run.

Composition of a simulated electron bunch

In reality, if everything goes well, one electron bunch is accelerated with each laser shot. The composition of such a bunch in the simulation is as follows:

- 1 run with `Nevents = 500000` (default)
- `GPS:nBunch = 1`
- `Output:mode` can be set to `detailed` or `sumRun`

Polarisation configuration of bunch pairs
The polarisation configurations of the aforementioned bunch pairs can be described as:

- **Parallel**: $\xi_{\mathrm{Fe}} \uparrow\uparrow \xi_{\mathrm{e}^-}$, the polarisation vectors of the electrons inside the iron core and the bunch electrons are identical. $\vec{\xi} = (0, 0, 1)$
- **Anti-parallel**: $\xi_{\mathrm{Fe}} \uparrow\downarrow \xi_{\mathrm{e}^-}$, the polarisation vectors of the electrons inside the iron core and the bunch electrons have opposite directions. $\vec{\xi} = (0, 0, \pm 1)$

Achieving different polarisation configurations for asymmetry runs
When `Run:type asymmetry` is selected, multiple ways to achieve different polarisation configurations are available. These configurations can be adjusted using the `Run:flip` parameter.

- **Source configuration**: 2 runs, $\xi_{3,\mathrm{Fe}}$ stays as initially defined, ξ_{3,e^-} switches signs
- **Core configuration**: 2 runs, ξ_{3,e^-} stays as initially defined, $\xi_{3,\mathrm{Fe}}$ and B_{Fe} switch signs

Unfortunately, assigning both a magnetic field and a polarisation to a logical volume simultaneously did not work. Since polarisation is not defined in the presence of a magnetic field, the default setting disables the magnetic field when studying polarisation effects. Conversely, to examine the effect of the magnetic field on particle trajectories, polarisation must be set to zero (see sections 8.6.3 and 8.5 for an example). Resolving this limitation, allowing for the concurrent assignment of both properties, should therefore be considered an important task for future work to enhance the accuracy and versatility of the simulation framework.
Different electron beam types
Various electron beam types/forms are used in the simulation studies of this thesis, the following is an overview of some of the possible terms.

- **Point Source**:
  ```
  GPS:posType = Beam
  GPS:spotSize = 0.0 mm
  GPS:divergence = 0.0 rad
  ```
  A highly localized beam with no initial divergence, representing an idealised point-like source.

- **Flat Top Beam**:
  `GPS:posType = Plane`
  `GPS:spotSize = radius of disk in mm`
  A beam with a uniform intensity distribution across a circular cross-section.

- **Gaussian Beam**:
  `GPS:posType = Beam`
  `GPS:spotSize =` $\sigma_x = \sigma_y$
  `GPS:divergence =` σ_θ
  A beam with a spatial intensity profile following a Gaussian distribution.

- **Pencil Beam**:
  `GPS:divergence = 0.0 rad`
  A narrow, collimated beam with no divergence.

5.5. Algorithm for analysing power calculations

The simulation and calculation of the analysing power ($\mathcal{A}$) is an essential part of the development of the polarimeter, as it enables to quantify the diagnostics' ability to measure the transmission asymmetry, detailed in section 3.4. The details of the calculation of $\mathcal{A}$ are therefore described below.
In summary mode, the LEAP_SIMS GEANT4 application returns the total amount of energy E_{trans} and the number of particles transmitted. Usually, at least 1000 runs are carried out per configuration and polarisation direction. For every parameter set this results in a distribution of E_{trans} which is processed as follows: A ROOT-histogram is configured with a default setting of 100 bins within a range of ± 5 standard deviations around the array mean. This bin range was chosen so that, assuming an almost normal distribution, the majority of the values in the data set are accounted for and efficiently distributed across the bins. At the same time, this approach prevents rare outliers from distorting the overall analysis. The bin width is calculated as the histogram range divided by the number of bins. Then, each E_{trans} value is evaluated, and if it is greater than zero, that value is entered into the histogram. If the histogram mean is greater than the histogram RMS, a Gaussian is fitted to the histogram using ROOT's fit function. In the following, $\langle E^i_{\text{trans}} \rangle$ represents the mean of the fit, with 'i' indicating the polarisation configuration, either parallel (P) or anti-parallel (AP). The analysing power is derived using equations 3.26 and 3.29. The associated error is determined

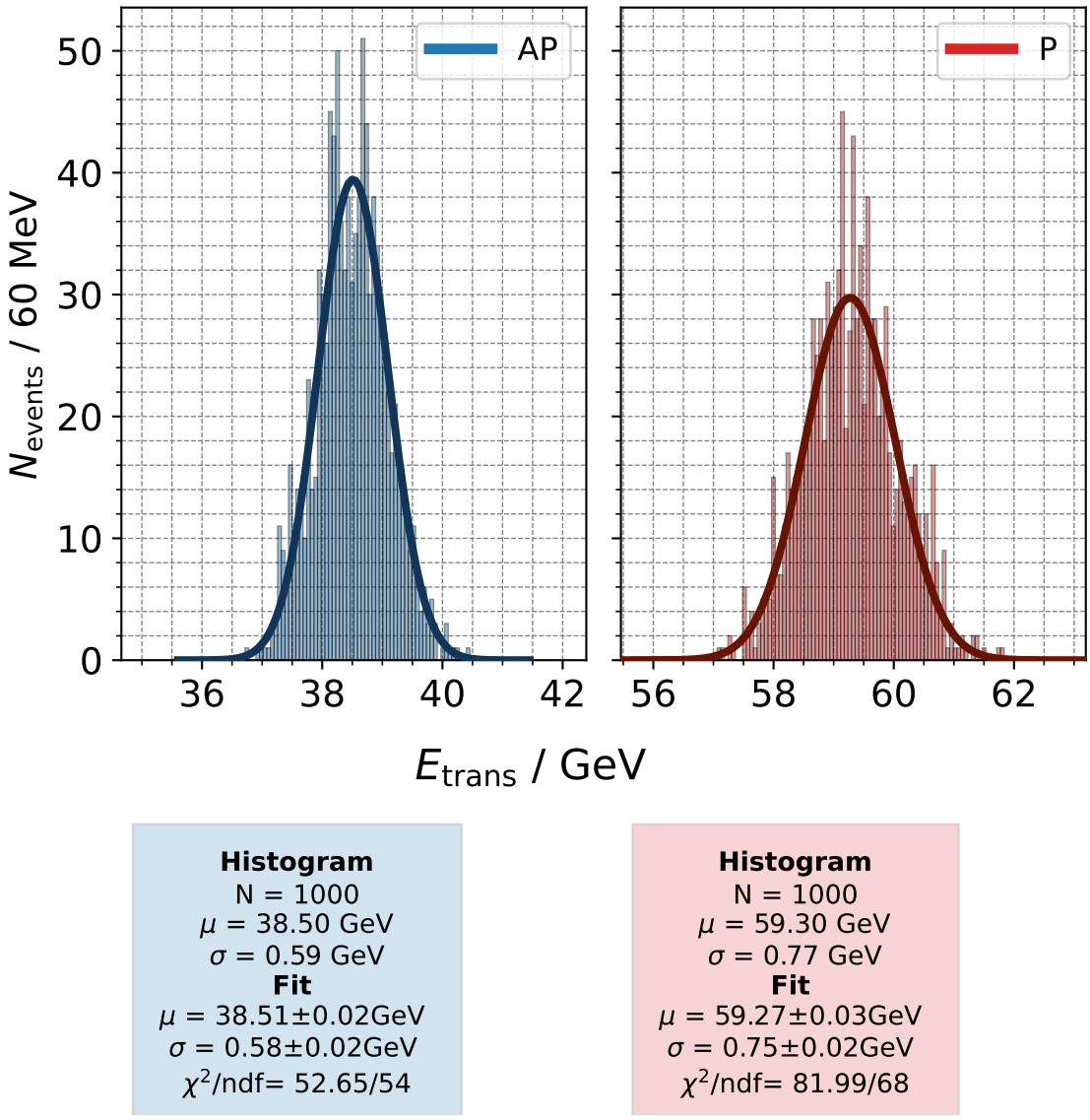

Figure 5.4.: Distributions of total transmitted energies for parallel (P) and anti-parallel polarisation configuration (AP). Histogram represents simulation results, solid line a ROOT-Gaussian-fit in a $5\,\sigma$ range around the histogram mean. AP: $\xi_{e^-} = (0,0,-1)$, $\xi_{\mathrm{Fe}} = (0,0,1)$. P: $\xi_{e^-} = (0,0,1) = \xi_{\mathrm{Fe}}$. Simulation in solenoid configuration. Details can be found in section 6. $E_{\mathrm{beam}} = 30\,\mathrm{MeV}$, core length of 150 mm, 1.75 mm thick converter target, $5 \cdot 10^5$ electrons per bunch.

from equation 3.27, which incorporates the standard deviation (σ) of the fit and the count of histogram entries in its calculation. If an extrapolation, e.g. to the full bunch intensity expected at LEAP, is applied to the errors of the measured asymmetry (as discussed in section 6.7), this will be explicitly stated.

Figure 5.4 shows an example of E_{trans} distributions for parallel and anti-parallel polari-

sation. To ensure comparability of the distributions, the bin width was standardised to 60 MeV, diverging from the approach of determining the number of bins as previously described. Using the equations specified above, the means and standard deviations of the example's fits result in an analysing power of 21.25 ± 0.03 %.
The fraction of transmitted particles and the sum of transmitted energy depend on the energy of the electrons in the original beam (E_{beam}) and the thickness of the iron core. Especially at low energies and or very long solenoid cores it is therefore extremely important to decide when too little energy is transmitted to fit the distribution with a Gaussian and calculate an analysing power. Figure 5.5 illustrates the importance of comparing the histogram's mean to its RMS as a prerequisite for fitting a Gaussian distribution. This comparison is crucial in determining the suitability of a Gaussian fit for the observed data distribution. The simulation setup mirrors that of the previously discussed example, with the exception of E_{beam} values. In scenario a), the standard case is depicted, where the mean of the total transmitted energy, $\langle E_{\text{trans}} \rangle$, is significantly greater than zero, resulting in an almost normal distribution of E_{trans}. On the other hand, in scenario b) the mean of the distribution is only marginally greater than zero, with a portion of its tail truncated at zero. Despite this, the distribution can still be appropriately fitted with a Gaussian, as the mean is greater than the RMS value. Finally, in scenario c) $\langle E_{\text{trans}} \rangle$ falls below the RMS value, resulting in substantial truncation of the distribution to the extent that a Gaussian fit is no longer representative of the observed data. The dashed line in the figure serves solely to highlight this discrepancy. Under these conditions, the algorithm identifies the parameter set as unsuitable for analysis, consequently returning NaN (Not a Number) values for both the analysing power and its statistical error.
To conclude: LEAP_SIMS includes a robust algorithm for the calculation of the analysing power and it's associated statistical error. It was designed to handle a wide parameter range, is capable of handling outliers and accommodates fringe cases.

5.6. Code Validation and Verification

When using simulation results, it is crucial to ensure their reliability. This involves two key processes: verification and validation. Verification ensures that the code is free from bugs or logical errors, while validation confirms that the system accurately models the real-world phenomena it is designed to simulate. Ensuring accuracy of LEAP_SIMS is particularly important, as its results are used to inform decisions about

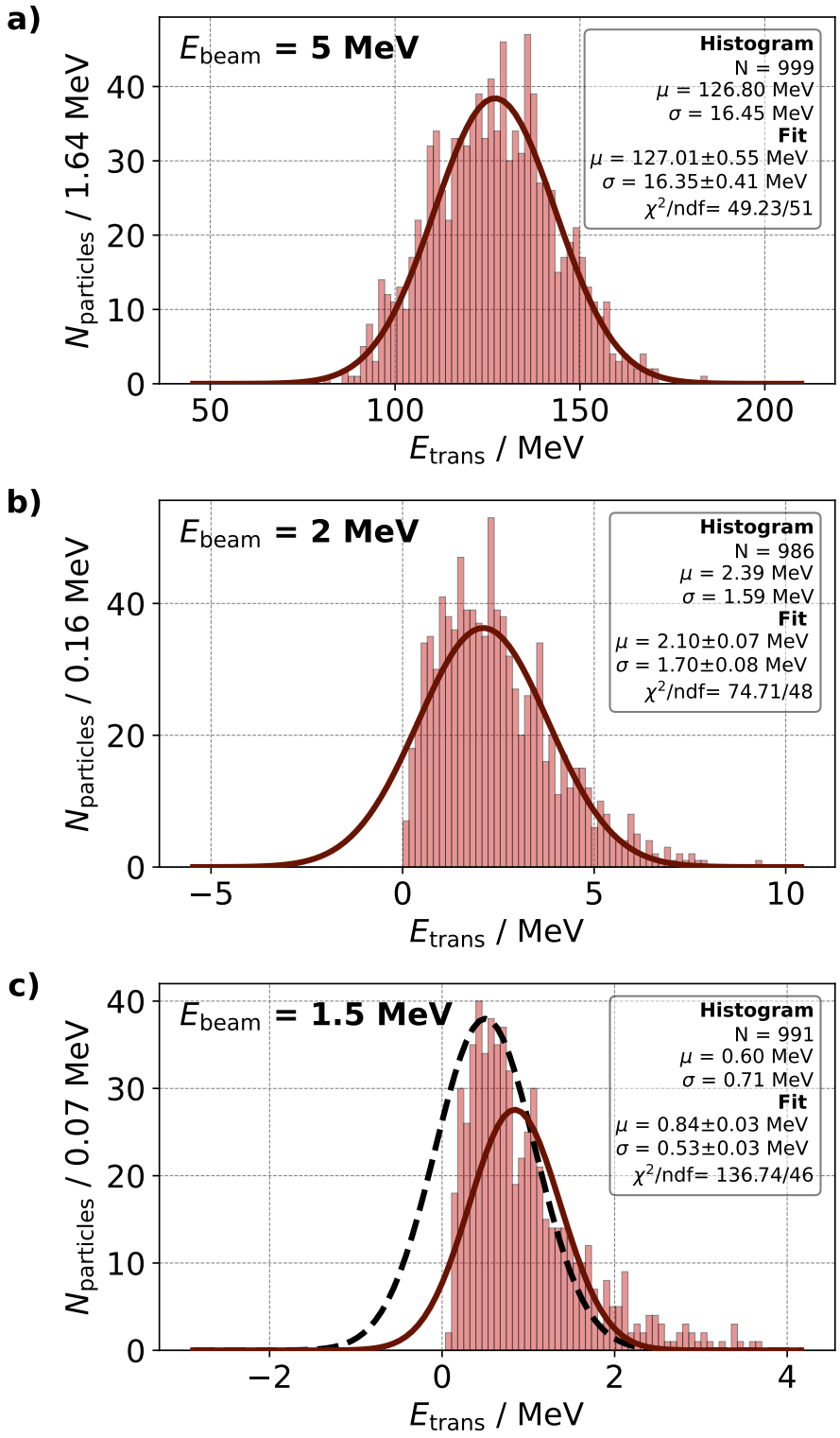

Figure 5.5.: Distributions of total transmitted energies in the parallel polarisation configuration for different initial electron beam energies. a) $\langle E_{\text{trans}} \rangle \gg 0$. Standard case. b) Fringe case, but $\langle E_{\text{trans}} \rangle > \sigma_{E_{trans}}$. Histogram is still being fitted. c) $\langle E_{\text{trans}} \rangle < \sigma_{E_{trans}}$. Algorithm rejects data point. Gaussian can not be fitted to histogram data.

the polarimeter hardware that will be purchased and constructed. These results also play a vital role in determining the polarimeter's analysing power, which is crucial for assessing electron polarisation. Incorrect simulation outcomes can lead to misleading conclusions and ultimately affect the reliability of experimental results.
The Geant4 toolkit itself has undergone thorough validation, driven by both the developer collaboration and its user community. Its components are continuously tested and refined across various application fields, with simulation results compared against real-world data. Detailed information on the physics models used and their applicability can be found in the Geant4 Physics Reference Manual [134]. For LEAP_SIMS, this means that the primary focus is on verification, ensuring no logical errors have been introduced during the implementation of the Geant4 components. This goes beyond simply confirming that the code compiles, runs smoothly, and saves results correctly; it also involves conducting additional tests to ensure the correctness and consistency of the simulation outputs. Some sample tests are documented below.

5.6.1. Geometry Verification

In a Geant4 simulation, accurate verification of the programmed detector geometry against intended simulation parameters is crucial. Several common sources of error were identified and addressed during the development phase of LEAP_SIMS.

Geometry Placement and Assigned Physics An initial method for verifying detector geometry involves using the LEAP_SIMS visualisation display (see figure 5.6). This provides a macroscopic overview to ensure correct volume placement. Examining the event displays for a small number of simulated particles also allows verification of material assignments and physics configurations. For instance, in figure 5.6b), where 10 electrons with an energy of 30 MeV are incident onto the polarimeter magnet from a distance of 2m, it is evident that switching the world material from vacuum to air is successful, as scattering in air causes a broadening of the particle profile. Similarly, the magnetic field of the solenoid can be tested by setting extreme values and observing the helical motion of charged particles with an XY-momentum component. All components implemented in LEAP_SIMS were visually inspected to confirm correct placement and functionality.

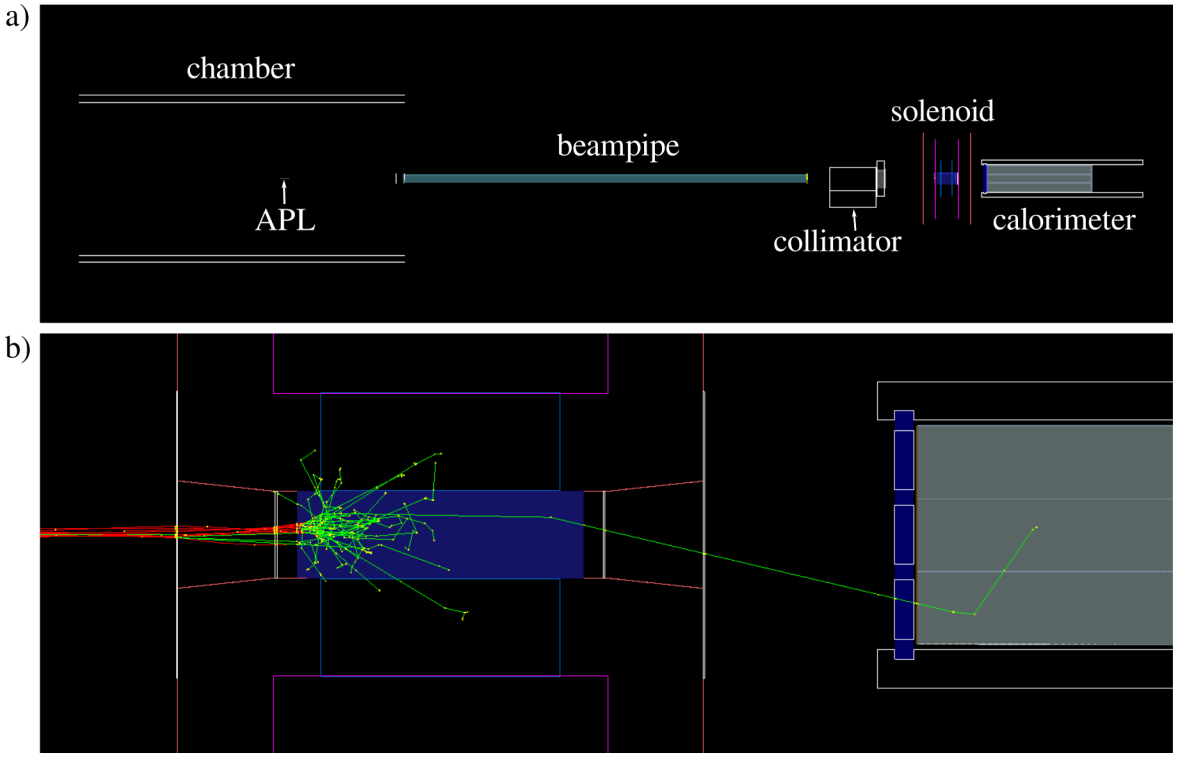

Figure 5.6.: LEAP_SIMS visualisation displays. a) Correct geometry placement including beamline. b) Event display of 10 electrons with an energy of 30 MeV incident onto the solenoid from a distance of 2 m. Beamline and magnetic fields are switched off, and the world material is set to air.

Overlapping Volumes Although visual inspection is effective for macroscopic positioning, detecting overlapping volumes by eye can be challenging, especially when dealing with numerous levels or small volumes. Overlapping volumes create undefined spatial regions, where it is unclear which physics parameters apply. Such ambiguities may lead to simulation errors, as the choice of volume depends on particle direction. To address this, the built-in `Geant4` function `geometry/test/run` was employed in interactive mode. This analysis confirmed that no overlapping volumes were present in LEAP_SIMS.

5.6.2. Memory Footprint Verification

Memory leaks occur when a program allocates memory, but does not properly free it after use. Over time this can lead to excessive memory usage, performance issues and even crashes. Proper memory management is therefore key to ensure a programs efficiency and stability.
The memory footprint of LEAP_SIMS was analysed using `Valgrind` [142], a programming tool for memory debugging, memory leak detection, and profiling. While small memory leaks were identified (approximately 5,538 bytes in 71 blocks), these issues were not addressed at this stage of development and are planned for resolution in future work. The leaks do not appear to significantly impact the overall performance of the simulation. To further investigate the effect of particle count on memory usage, `Massif`, `Valgrinds` heap profiler, was employed to track memory consumption at different particle counts. Simulations with 10 and 10,000 particles yielded very similar peak memory usage: 27.21 MB for 10 particles and 27.75 MB for 10,000 particles, indicating that memory usage does not significantly scale with the number of particles. This suggests that the memory leaks are not related to per-particle data accumulation. While addressing these leaks remains a priority for future optimisation, their minimal impact on memory usage ensures that the simulation can scale effectively without substantial memory overhead at this stage.

5.6.3. Polarised Bremsstrahlung

To evaluate the functionality of polarised bremsstrahlung, the following test was performed (see figure 5.7a): Two simulation runs were conducted, each consisting of a bunch of 1000 electrons, where each electron had an energy of 30 MeV. The electrons

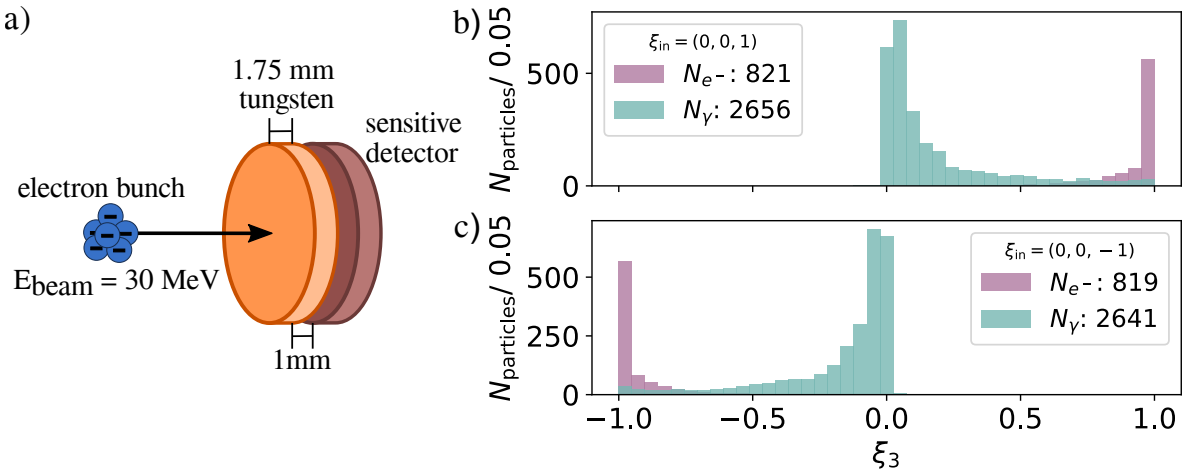

Figure 5.7.: a) Simulation setup: 1000 electrons incident on a tungsten target with 50 mm diameter followed by a sensitive detector. b) ξ_3 for detected γ-rays and primaries. ξ of incident beam is (0 , 0, 1) c) same as b) but with $\xi_{in,3}$ = -1

were assigned a polarisation vector $\xi = (0, 0, \pm 1)$ and propagated in the z-direction through a vacuum before striking a 1.75 mm thick tungsten target. The diameter of the latter was 50 mm. A sensitive detector volume (see section 5.2.2) was placed 1 mm behind the target.

As described in the section on polarisation transfer in section 3.1.1, one would expect a longitudinally polarised electron beam with $\xi_{in,3}$ = 1 to cause right-handed circularly polarised bremsstrahlung. Similarly one would expect, left-handed circularly polarised bremsstrahlung at a $\xi_{in,3}$ of -1. This is exactly what one can see in the results shown in figures 5.7 b and c. The electron beams are transferring their polarisation to the photons. And since a maximum degree of circular photon polarisation is to be expected at high photon energies, the number of detected particles decreases with increasing polarisation, similar to the way the energy of a bremsstrahlung spectrum behaves.

Chapter 6.

Design Studies

As highlighted in chapter 3, Compton transmission polarimetry is a useful technique for measuring the polarisation of electrons with expected energies in the range of a few 10 MeV to a few 100 MeV. Similar diagnostics which have been utilised at previous experiments were optimised for partly very different conditions than in the LEAP project. Examples are particle energies of only a few MeV [83, 103] or a few hundred [101]. Therefore, to find out the ideal design for the LEAP polarimeter, a Monte Carlo design study was performed with the help of GEANT4. Details about the programmed framework named LEAP_SIMS can be found in chapter 5.
This chapter will describe the influence of the individual components of the polarimeter on its analysing power and what conclusions can be drawn with regard to future measurements.

6.1. The simulation setup

For the design study LEAP_SIMS (refer to chapter 5) was used with only the polarimeter-solenoid geometry module placed (see section 5.2.1). Therefore, the geometry included a particle gun and the solenoid depicted in figure 6.1. They where placed 2 m apart, initially in vacuum. For initial parameters a solenoid as used in the positron line of the E166 experiment was assumed [103]. The magnet itself was simulated to consist of an iron yoke, copper coils, or rather a tube of copper, a central iron core and a conversion target. Two idealised detector layers were used (see section 5.2.2). The first was placed directly behind the converter target, the second was placed 10 mm behind the iron core. Exact dimensions of the individual components and exact geometry details

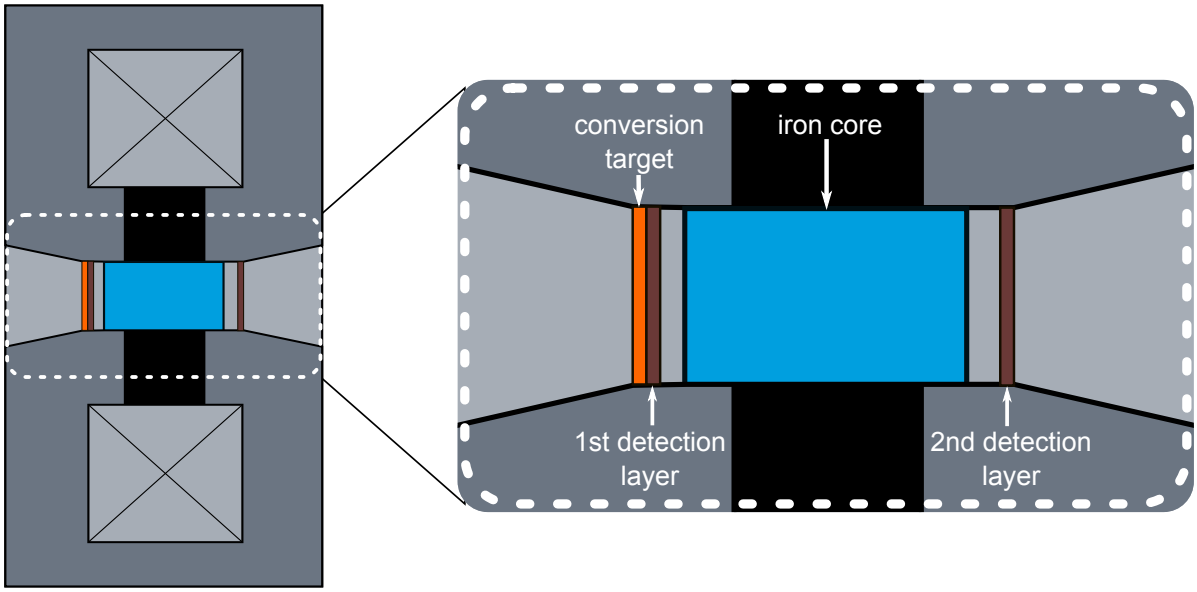

Figure 6.1.: Schematic of the solenoid used for the design study. The iron yoke is coloured in grey, the lead shielding in black and the copper coils are situated in the Xed out areas.

Table 6.1.: Overview of default simulation parameters

parameter	explanation	default value
E_{beam}	energy of electrons inside the accelerated electron beam	25 MeV
N_{e^-} / Bunch	number of electrons simulated per bunch	500000
P_{e^-}	polarisation of the accelerated electrons	± 1
P_{Fe}	polarisation of the iron core electrons	1

can be taken from the following sections and the technical drawings in appendix C. Simulations were performed in both detailed and summary output modes.

Table 6.1 provides an overview of the default simulation parameters used in this study. In a future LEAP experiment, polarised electron beams are anticipated to have energies in the range of several tens of MeV. For the purposes of this study, an initial energy of 25 MeV was selected. The expected electron bunch charge is approximately 3 pC. However, simulating 1.9×10^7 particles repeatedly is computationally expensive; therefore, a reduced value of 5×10^5 particles per simulated bunch was chosen as the default. In this study, the analysing power is the parameter to be optimised.

Consequently, the polarisation of the accelerated electron beam (P_{e^-}) and the iron core (P_{Fe}) were both set to 1. It is important to note, however, that for the prediction of asymmetries to be measured (cf. section 6.7), the realistic values of polarisation will likely be closer to 10 % for P_{e^-} and 7 % for P_{Fe}. The maximum electron spin polarisation in iron is $\pm 8.19\%$ [103].

6.2. The Converter Target

Since the converter target is a disk in the opening of the solenoid, there are four parameters that can be varied: Its radius, thickness, material, and the distance to the iron core. The radius of the converter target is fixed by the magnet aperture and was set to the same value as in the E166 experiment, namely 25 mm. The distance between the conversion target and the iron core was also assumed at the beginning as in experiment E166. It amounts to 12.5 mm. This leaves the ideal thickness and material for this configuration to be determined.
The emitted bremsstrahlung is proportional to the the square of the nuclear charge number (see section 3.1.1). A high conversion rate is desirable and therefore, the bremsstrahlung conversion target was simulated to be out of the high Z material tungsten (Z=74).
The thicker the target, the more energy the passing electrons can deposit and therefore the more bremsstrahlung is emitted. On the other hand, the probability of photon attenuation increases with the target thickness. Now the optimal thickness shall be determined by simulation. It was varied ranging between 0.1 and 1 times the radiation length of Tungsten, which is 3.5 mm [72].
First, individual bunches were simulated and the data of each electron passing the virtual detector planes was stored (see section 5.1). Figure 6.2 shows the mean number of photons produced per electron incident on the converter target, i.e. the total number of photons detected in the first detection layer divided by the number of electrons shot by the particle gun. With 500000 simulated particles, the here assumed errors of $\frac{1}{\sqrt{N_{e^-}}} = 0.0014$ are too small to be visibly discernible in the plot. The number of photons leaving the target saturates at a converter target thickness of about 0.7 times the radiation length.

However, the number of emitted photons, i.e. the conversion rate, is not the only parameter to be considered. For the polarisation measurement the circular polarisation

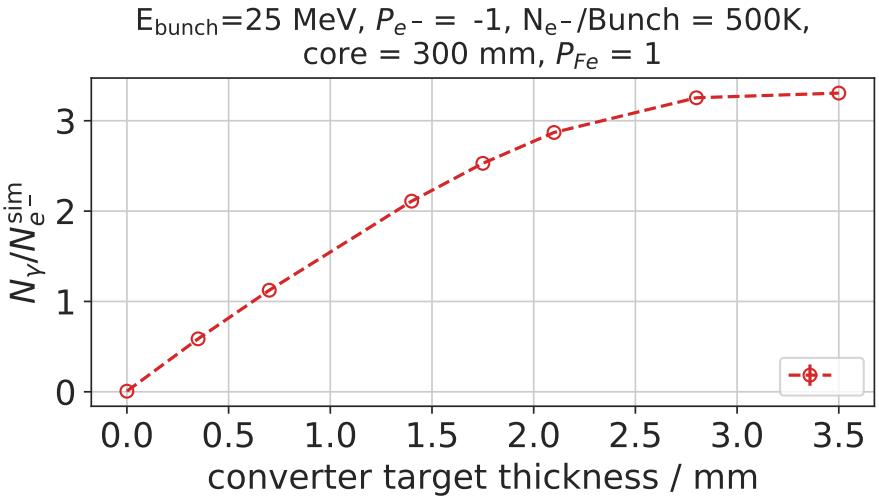

Figure 6.2.: Mean number of photons produced per electron incident on converter target simulated for different target thicknesses.

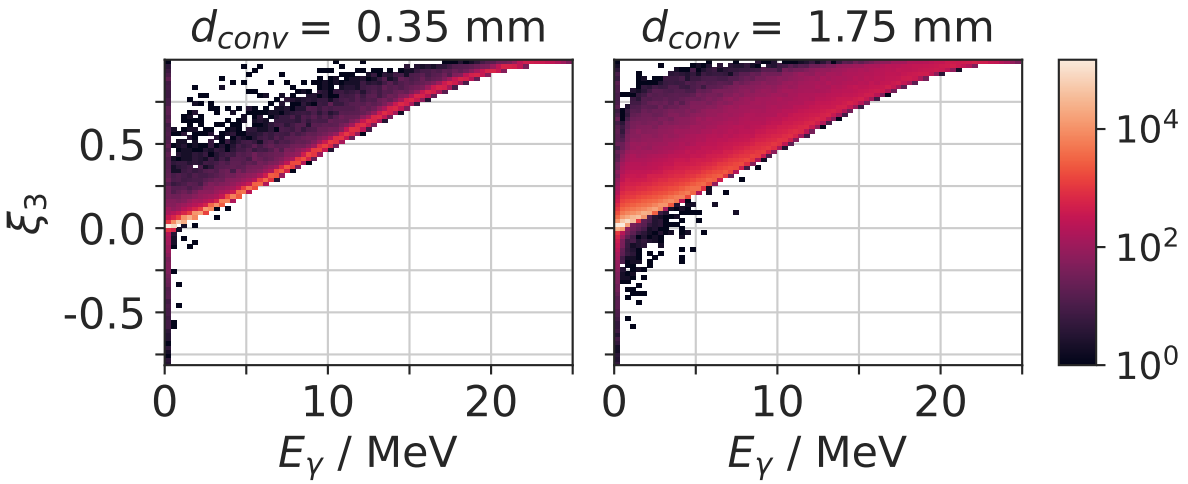

Figure 6.3.: Distribution of circular polarisation component, ξ_3, and gamma ray energy, E_γ for two different converter target thicknesses. $E_{\text{bunch}} = 25\text{MeV}, P_{e^-} = -1$

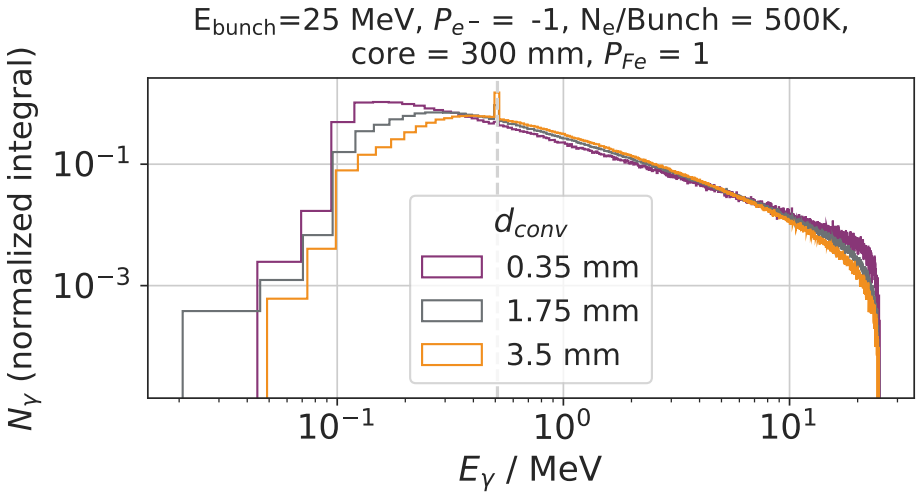

Figure 6.4.: Gamma ray spectrum behind the converter target for different converter target thicknesses.

of the produced photons, the third element of the stokes vector, is of utmost importance. The circular photon polarisation ξ_3 is proportional to the degree of electron polarisation $|\xi|$ (cf. section 3.1.1). If one considers this, it becomes evident that the photons with higher energies are most important. As for example below 1 MeV a lot of photons are polarised in the other direction. This is illustrated in figure 6.3, which depicts the circular polarisation versus the energy of detected photons for two different converter target thicknesses.

The bremsstrahlung spectra for different converter target thicknesses are presented in figure 6.4. From this data one can see, that there are relatively more high-energy photons with thinner targets.

In the end it is the polarimeter's analysing power and the statistical error that is to be optimised. It was found to slightly decrease with target thickness from 49.5 ± 0.6 % at 0.35 mm to 48.7 ± 0.7 % at 3.5 mm with the relative error increasing (see figure 6.5). This shows that the overall effect of a change in target thickness on the analysing power is relatively small. In fact, simulations with and without converter target show that the effects on the analysing power are negligible (see table 6.2). The iron core itself serves as a bremsstrahlung converter. More about the change of the analysing power with the length of the iron absorber can be found in the next section.

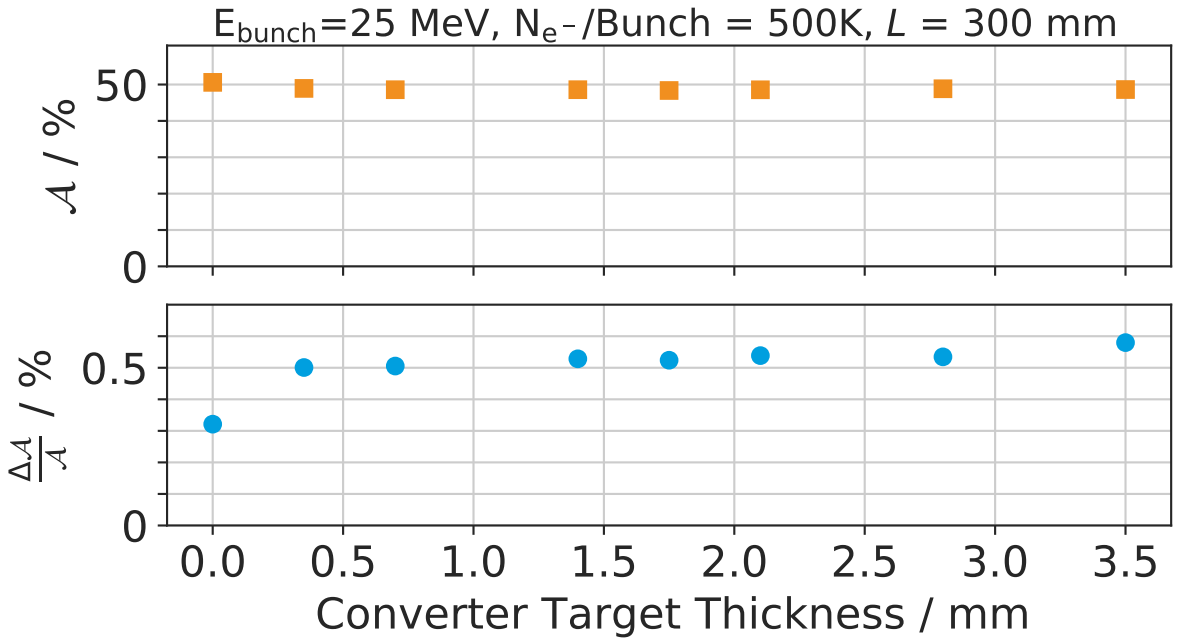

Figure 6.5.: (top) Analysing power $\mathcal{A}$ vs converter target thickness d_{conv}. Statistical error bars are included; however, they are not visually discernible due to their small magnitude. (bottom) relative error of analysing power vs converter target thickness.

6.3. The Iron Absorber

The absorber is a rod making up most of the centre of the solenoid. It should consist of a ferromagnetic material that exhibits a high electron spin polarisation during saturation magnetisation (cf. section 3.4). Iron was chosen because its properties are well known [143] and it is inexpensive compared to other materials. As in the previous section for the converter target, the absorber's radius depends on the aperture of the solenoid and was initially assumed to be 2.5 cm. This leaves it's length L as a free parameter to be studied. According to equations (3.26) and (3.22) the analysing power

Table 6.2.: Analysing Power $\mathcal{A}$ for different core thicknesses without converter target and with a converter target thickness d_{conv} of 1.75 mm and an E_{bunch} of 25 MeV

core thickness / mm	$\mathcal{A}$ (d_{conv}= 0 mm) / %	$\mathcal{A}$ (d_{conv}= 1.75 mm) / %
75	11.33 ± 0.01	10.83 ± 0.01
150	24.61 ± 0.02	22.93 ± 0.02
300	50.6 ± 0.2	48.5 ± 0.2

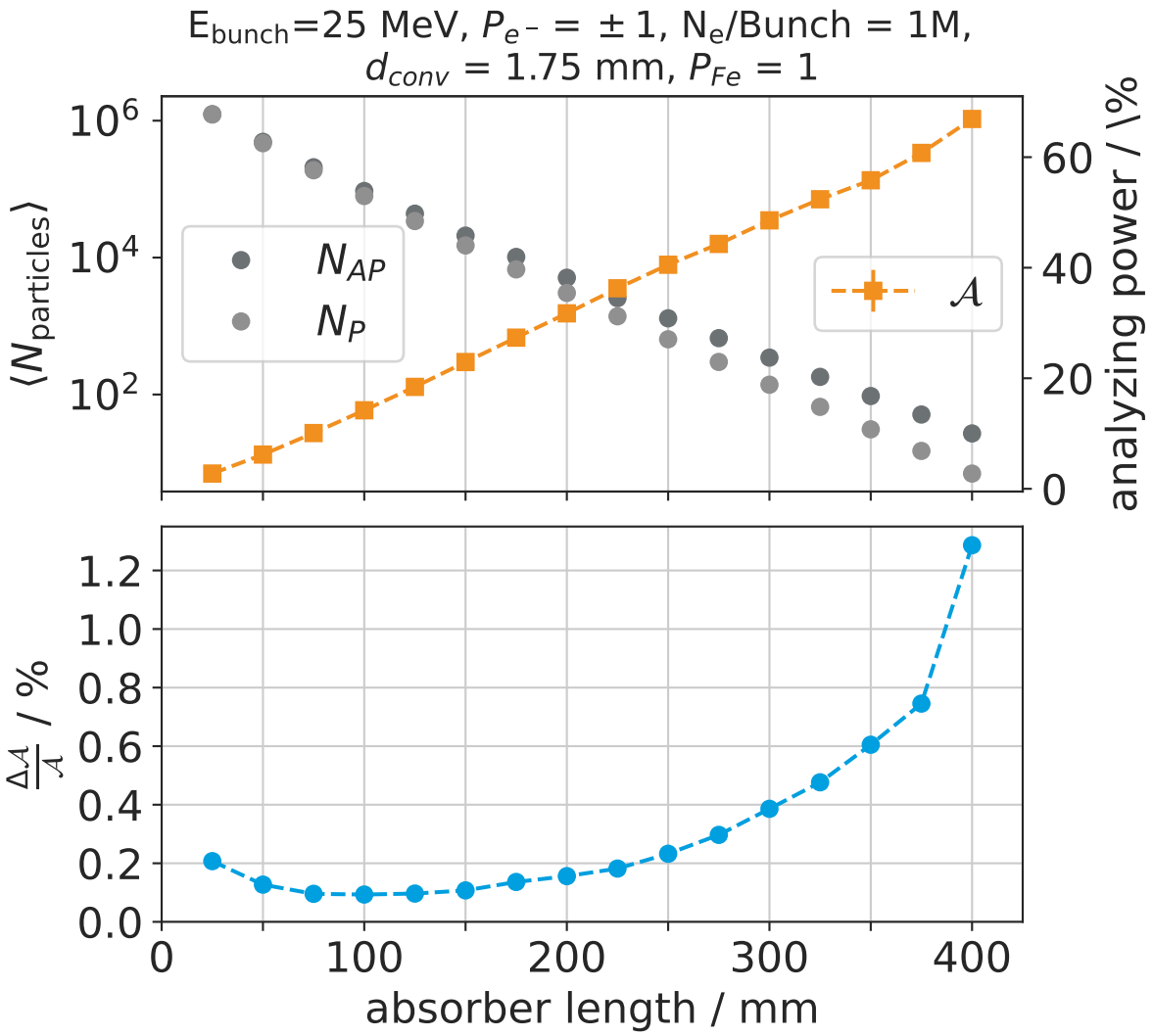

Figure 6.6.: (top) Average number of transmitted photons for parallel and anti-parallel polarisation directions, and analysing power plotted against absorber length. (bottom) Relative statistical error of analysing power plotted against absorber length for different number of shots.

$\mathcal{A}$ is expected to increase linearly with absorber length and the beam intensity should decrease exponentially. The top of figure 6.6 shows the simulation results which confirm this pattern with $\mathcal{A}$ increasing linearly from $2.8 \pm 0\,\%$ at 25 mm core length to $66.9 \pm 0.9\,\%$ and the number of transmitted photons decreasing exponentially with an average of 1.2×10^6 photons with 25 mm absorber length and an average of 7 photons at 400 mm.

The relative error of the analysing power for different core thicknesses is displayed in the bottom of Fig. 6.6. It is minimal at 100 mm core length. The caveat is that the

analysing power at this length is only $14.2 \pm 0.01\%$, which means that according to equation 3.30, one would, with a P_{e^-} of 10 % and a P_{Fe} of 7 % , need to measure an asymmetry of only 0.1 %. While the statistical uncertainty in the MC simulation can, in principle, be reduced arbitrarily by increasing the number of simulated events, here it serves as a proxy for the expected statistical uncertainty of an actual measurement. The simulation was performed using 1 million particles, corresponding to a bunch charge of less than 0.2 pC, which is significantly lower than the bunch charge of 3 pC that is expected at a future LEAP experiment. Hence, the number of photons transmitted through the absorber is not the limiting factor for $\frac{\Delta\mathcal{A}}{\mathcal{A}}$ and it makes sense to increase L to increase $\mathcal{A}$. For example, if one wanted to have to measure an asymmetry of 1 % an iron core of approximately 300 mm were necessary.

6.4. The electron beam energy

An integral part of transmission polarimetry is the Compton scattering of the bremsstrahlung-photons inside the iron absorber (see section 3.1.3). The cross-section of this interaction, and thus also rate and asymmetry, depend on the energy of the initial electrons (cf. figure 3.5).
At the time this design study was carried out the details of how the prepolarised electrons would be accelerated and in particular the injection method into an LPA were still under investigation. Injection method, the gas that is used and the pressure it has, laser parameters like energy and pulse duration, all this has an influence on the energy of the accelerated electrons (cf. chapter 2). As mentioned before, a bunch energy of some 10 MeV is expected. However, the investigation of the effect of E_{bunch} on the analysing power and the relative statistical measurement error could point to a direction in which the accelerator development can be targeted.
Fig. 6.7 shows the analysing power $\mathcal{A}$ against the energy of the electrons in the simulated bunches for different core length. In the expected energy range $\mathcal{A}$ decreases with E_{bunch} because the cross section for Compton scattering does. $\mathcal{A}$ is 48.6 ± 0.2 % at 25 MeV and reduces to 24.07 ± 0.07 % at 80 MeV, using an iron core of 300 mm length. However, it is less dependent on E_{beam} at higher values. The statistical error decreases with energy, because the transmission probability increases. The rate decreasing with energy is also the reason why some lower energies where excluded for longer cores. See section 5.5 for more information on the algorithm and used criteria.
These simulations were carried out with mono-energetic particle beams, which

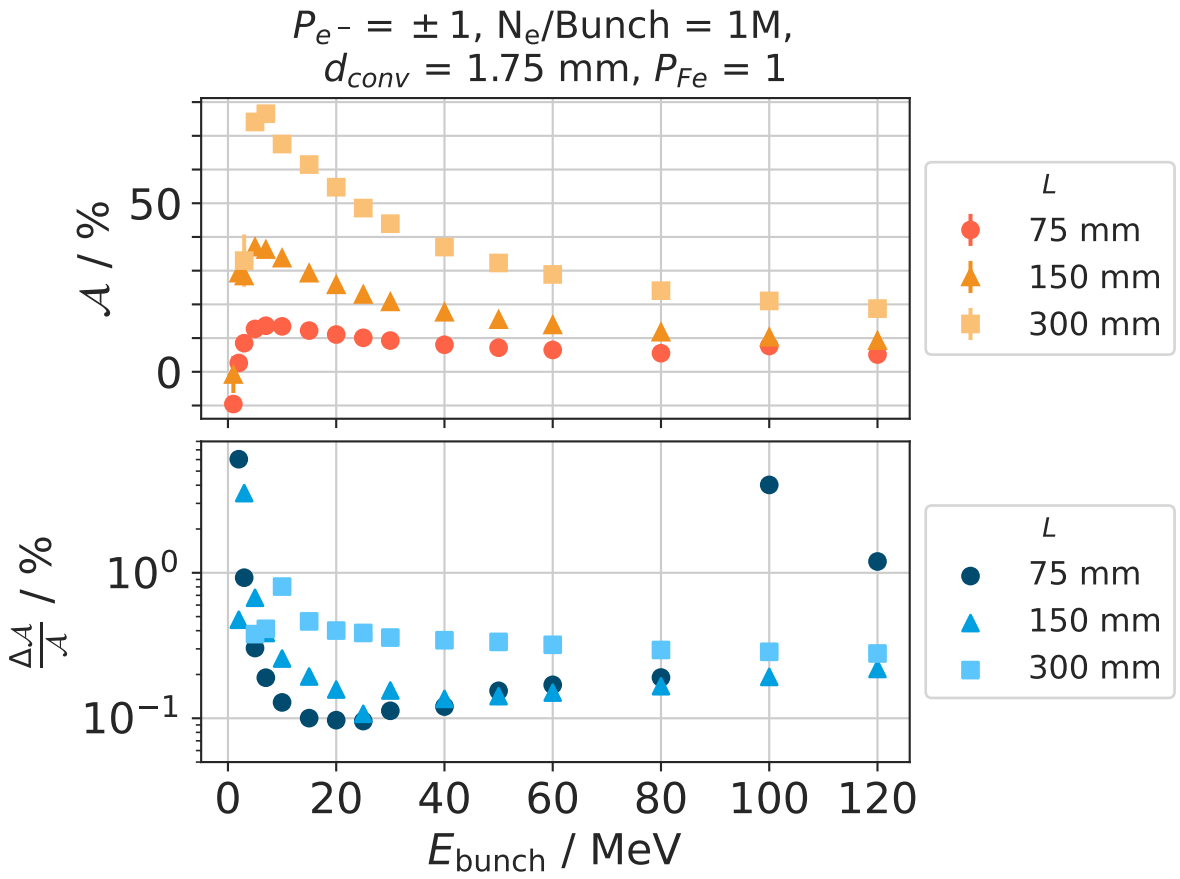

Figure 6.7.: (top) Analysing power $\mathcal{A}$ as a function of electron bunch energy E_{bunch} for different absorber lengths. Statistical error bars are included; however, they are not visually discernible due to their small magnitude. (bottom) Relative statistical error of the analysing power as a function of electron bunch energy for different absorber lengths. The outliers at high energies are likely due to an insufficient number of simulated particles.

of course do not exist in reality. The effect of the energy distribution of a beam is addressed when determining the analysing power of the LEAP polarimeter in section 8.8.2.

6.5. Separation of Electrons

To investigate whether separating the forward scattered gamma rays and secondary electrons increases the analysing power, solenoid simulations with detailed output (cf. section 5.4) were carried out.
The polarisation of the electron beam as well as that of the iron core electrons were set to 100%. A mono-energetic point beam of 25 MeV was used. d_{conv} was 1.75 mm and L was 150 mm. To increase computing performance, jobs were submitted in batches of 1×10^5 electrons and afterwards the results of 20 of them stitched together leading to the results of 49 runs of 2×10^6 particles being shot. Those results were then in the subsequent analysis filtered for their PDG-ID (see chapter 45 of [72]).
First the analysing power was computed for different particle species (see Fig. 6.8). It was found that if no particle separation is performed, the analysing power is 22.884 ± 0.003 %. For photons alone, it is 15.957 ± 0.003 %, while for electrons, it reaches $\mathcal{A} = 84.054 \pm 0.036$ % – more than three and a half times higher than in the

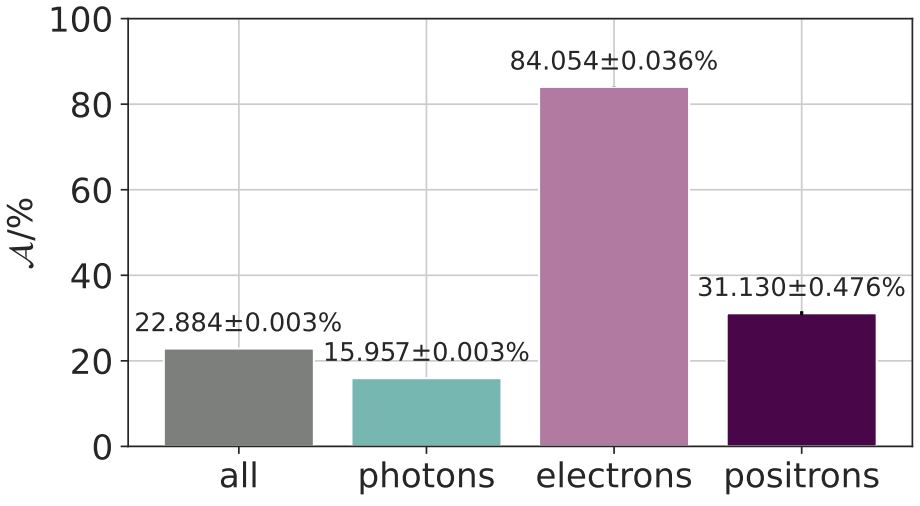

Figure 6.8.: Analysing power for different particle species. N_{sim} = 2M, E_{e^-} = 25 MeV, P_{e^-} = 1, d_{conv} = 1.75 mm, L= 150 mm

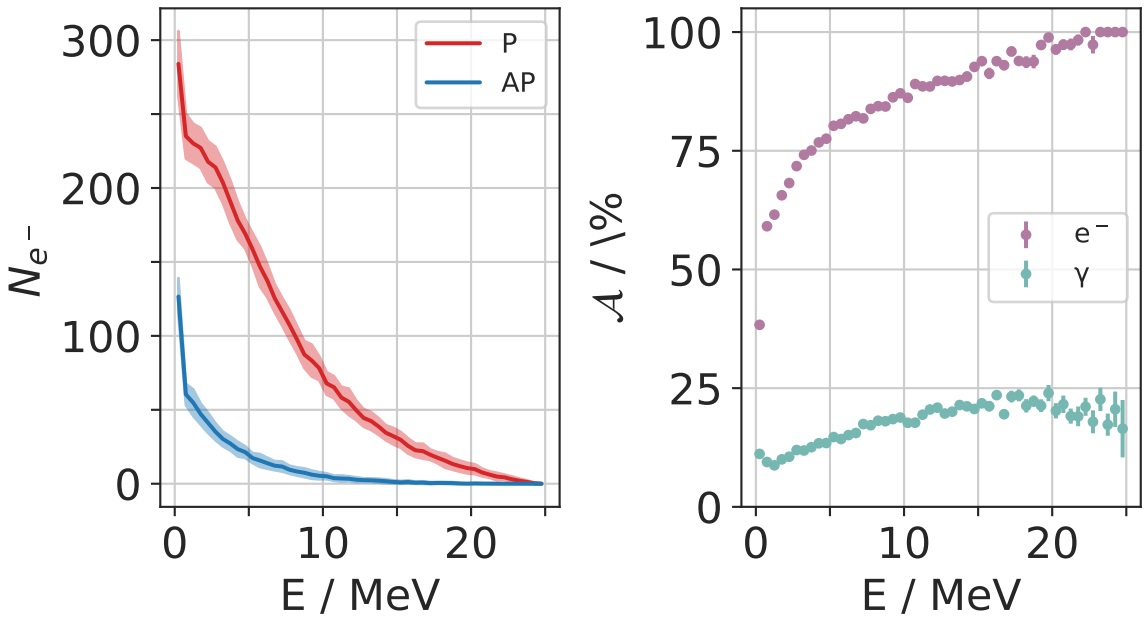

Figure 6.9.: (left) spectra of transmitted electrons for parallel and antiparallel polarisation configuration averaged over 49 bunches, (right) average analysing power per energy bin for electrons and photons

case without separation.

A separation of the electrons thus seems advisable, albeit for reasons different from those initially assumed. If this effect were to be exploited in a future experiment, it would first need to be established whether the observed high analysing power is an artifact of the GEANT simulation or a real physical phenomenon, as well as to what extent the polarisation of the incoming electrons remains linearly proportional to the measured asymmetry of the secondary electrons. While a detailed investigation of this effect is beyond the scope of this thesis, a potential approach for future measurements would be to place a dipole magnet behind the solenoid and position an additional electron detector at the corresponding deflection angle, enabling energy-resolved asymmetry measurements. As a first step toward this, this study examines the energy spectra of the detectable electrons and the associated analysing power for the relevant energy ranges. This analysis was performed using the filtered data discussed above and is presented in figure 6.9.

$\mathcal{A}$ was found to increase with energy, exceeding 80 % at 5 MeV for electrons. At least for the tested electron beam energy, the increase in bremsstrahlung polarisation transfer, $\frac{P_\gamma}{P_{e^-}}$, with the photon energy fraction $\frac{E_\gamma}{E_{\text{beam}}+m_e c^2}$ appears to outweigh the decrease in

the polarisation-dependent part of the Compton cross-section, $|\sigma_1|$, with increasing photon energy E_γ (cf. section 3.1). However, especially for a parallel polarisation configuration, this coincides with rates of only a few tens of electrons or fewer, which has to be taken into account when designing a diagnostic to detect them. Nevertheless, should the project be continued at a future point in time, a detailed investigation would be highly valuable – especially at high E_{beam}, given the low analysing power of photons in this regime.

6.6. Conclusions for real measurements

Before drawing conclusions, it is important to recapitulate the expected beam parameters for the real measurements. Bunch charges of approximately 3 pC, corresponding to $\sim 1.9 \times 10^7$ electrons, and electron bunch energies, E_{beam}, in the range of several tens of MeV are anticipated. The longitudinal beam polarisation is expected to be around 10%.

It was found that, within this expected energy range, a high-Z bremsstrahlung converter target in front of the solenoid's iron core is unnecessary, as the core itself serves as the converter.

Furthermore, with the thickness of the iron core, L_B, held constant, the analysing power, $\mathcal{A}$, decreases as the electron beam energy, E_{beam}, increases. This is because the cross section for Compton scattering decreases with higher energies. Given the high bunch charges and beam energy, the experiment operates at the higher end of the energy spectrum typically used in Compton transmission polarimetry, resulting in a lower analysing power. However, transmission rates are not a limiting factor. As a result, a longer core can be used without significantly increasing the statistical error on the analysing power due to low transmission rates.

A solenoid, previously used as a photon analyser in the E166 experiment [103], is available for use. It has a core length of 150 mm, with additional details provided in section 7.1. According to the data in table 6.2, its use under the specified conditions would result in an analysing power of $\mathcal{A} = 24.61 \pm 0.02\,\%$, indicating its suitability for Compton transmission polarimetry in the context of LEAP.

To increase the analysing power and thereby achieve larger, more easily measurable asymmetries, a solenoid with a longer iron core could be used. For instance, a core length L_B of 300 mm would result in an analysing power of $\mathcal{A} = 50.6 \pm 0.2\,\%$. However, achieving more precise optimisation requires a better understanding of the beam

parameters, which necessitates further progress in the accelerator design.
Additionally, the use of a dipole to separate the electrons from the photons may enhance the $\mathcal{A}$ further, although this approach requires additional investigation.
While simulations described in this chapter can provide a valuable first insight, it is important to recognise that the current models assume an idealised beam, environment, and detector. Therefore, the results should be interpreted with caution until more realistic conditions are incorporated. A first extrapolation to measurable asymmetries can be found in the next section.

6.7. Calorimeter Requirements

Simulations of the type conducted in this design study, involving an idealised electron beam and a diagnostic in a vacuum environment, can be used to narrow down the calorimeter requirements for the polarimeter utilising the E166-photon analyser solenoid (cf. section 7.1). To do this, however, it is first necessary to extrapolate from the previously simulated analysing power to the predicted measurable asymmetry.
The simulations assumed a solenoid without converter target, having a core length of 150 mm. A point-like pencil beam (cf. section 5.4) was modelled, consisting of 5×10^5 electrons per bunch, each with an energy of 30 MeV. The energy sums detected by an idealised detector positioned behind the core were used for the subsequent analysis, which proceeds as follows:

1. **The analysing power**: By definition, the analysing power corresponds to the asymmetry at full polarisation, so simulations were conducted with $P_{Fe} = 100\,\%$ and $P_{e^-} = \pm 100\,\%$. The energy sum distributions, used for asymmetry calculations following the algorithm in section 5.5, are well separated. Specifically, 2000 simulations per polarisation configuration produced distributions with a fit mean, $\langle E_{\text{trans}} \rangle$, of 46.54 ± 0.01 GeV and a standard deviation, σ, of 0.62 ± 0.01 GeV for the antiparallel polarisation configuration and a mean of 68.6 ± 0.02 GeV with σ of 0.79 ± 0.02 GeV for the parallel polarisation configuration, refer to figure 6.10a).

2. **Corrected beam and core polarisation**: For the measured polarisation, the actual iron core polarisation ($P_{\text{Fe}} = 7.23\,\%$) and the expected beam polarisation ($P_{e^-} = 10\,\%$) must be taken into account. Accordingly, the simulation was repeated with these settings, and the results are shown in figure 6.10b). The distribution means

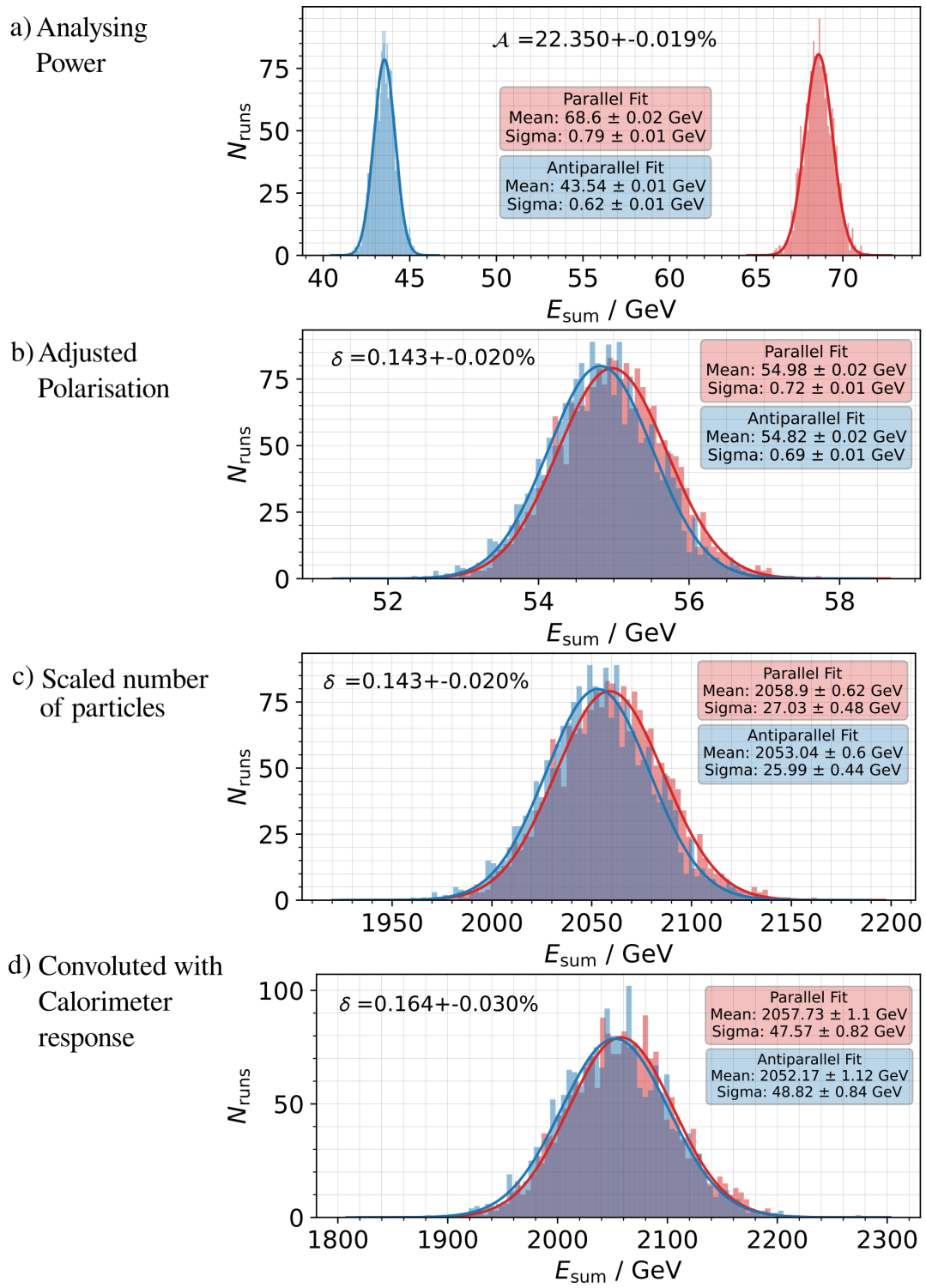

Figure 6.10.: a) Simulated analysing power. 30 MeV , monoenergetic point source, $P_{Fe} = 100\,\%$ and $P_{e^-} = 100\,\%$. b) Simulated results with $P_{Fe} = 7.23\,\%$ and $P_{e^-} = 10\,\%$. c) histogram from b) scaled to 3 pC bunch charge. d) Histogram from c) convoluted with Gaussian response function, that represents a 2 % energy resolution of the calorimeter.

($\langle E_{\text{trans}} \rangle_{AP} = 54.82 \pm 0.02\,\text{GeV}$ and $\langle E_{\text{trans}} \rangle_{P} = 54.98 \pm 0.02\,\text{GeV}$) are noticeably closer together.

3. **Bunch charge scaling**: Simulated bunches contain $N_{e^-,sim} = 5 \times 10^5$ electrons, which is less than the expected bunch charge of 3 pC, corresponding to $N_{e^-,exp} = 1.87 \times 10^7$ electrons. Therefore, the distribution mean and standard deviation must be scaled. The scaling is done as follows:

$$\langle E_{\text{trans}} \rangle_i^{\text{exp}} = f \cdot \langle E_{\text{trans}} \rangle_i^{\text{sim}} \tag{6.1}$$

$$\sigma_i^{\text{exp}} = \sigma_i^{\text{sim}} \cdot \sqrt{f} \tag{6.2}$$

Here, i represents the respective polarisation configuration, "sim" indicates the simulated values, "exp" refers to the expected values at the experiment, and f is the scaling factor, defined as:

$$f = \frac{N_{e^-,exp}}{N_{e^-,sim}} \tag{6.3}$$

In figure 6.10c), this scaling is applied to all individual entries from figure 6.10b) using the factor f. This results in means of $\langle E_{\text{trans}} \rangle_{AP} = 2053.04 \pm 0.6\,\text{GeV}$ and $\langle E_{\text{trans}} \rangle_{P} = 2058.9 \pm 0.62\,\text{GeV}$, and standard deviations of $\sigma_{AP} = 25.99 \pm 0.44\,\text{GeV}$ and $\sigma_P = 27.03 \pm 0.48\,\text{GeV}$.

4. **The calorimeter response**: While the simulations use ideal detectors that provide perfect measurements, real detectors exhibit a response function that causes broadening of the measured signal compared to the true value. Mathematically, this can be described as the convolution of the true signal and the detector response. For simplicity, the calorimeter response is assumed to be Gaussian, centred at zero. The convolution of two Gaussians results in another Gaussian, where the mean remains unchanged, but the standard deviation of the measured signal is given by:

$$\sigma_i^{\text{measured}} = \sqrt{\left(\sigma_i^{\text{exp}}\right)^2 + \left(\sigma_{\text{calo}}\right)^2} \tag{6.4}$$

Here, σ_{calo} represents the absolute precision of the calorimeter energy measurement. In figure 6.10d) a simple Monte Carlo approach was used, adding random

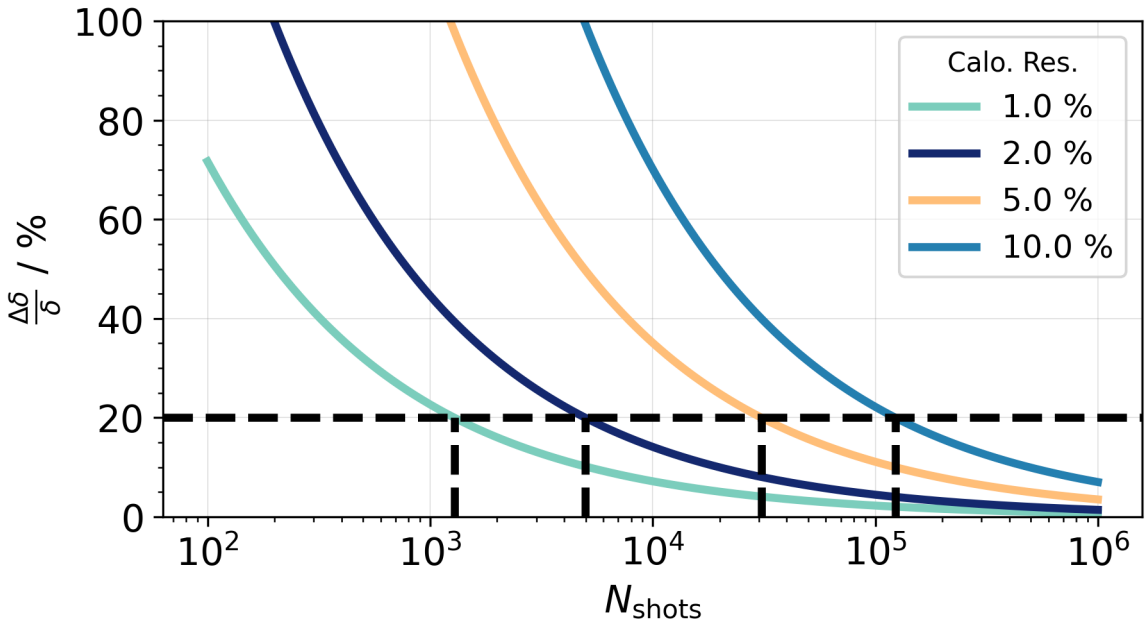

Figure 6.11.: Relative statistical uncertainty of predicted measurable asymmetry for different number of shots and calorimeter resolutions.

Gaussian noise to the histogram shown in figure 6.10c). Using a relative calorimeter precision of 2 %, the standard deviations increase to $\sigma_{AP} = 49.39 \pm 0.88\,\text{GeV}$ and $\sigma_P = 48.93 \pm 0.83\,\text{GeV}$.

In figure 6.10, it was assumed that the number of simulated bunches is the same as the number of shots in the actual experiment. However, this need not be the case. Consequently, the following error can be applied to the transmitted energy sum when calculating the asymmetry:

$$\Delta\langle E_{\text{trans}}\rangle_i = \frac{\sigma_i^{\text{measured}}}{N_{\text{shots}}/2} \tag{6.5}$$

Here, N_{shots}, is the total number of shots, combining both polarisation configurations. Note, that a higher number of shots does not decrease the widths of the energy distributions, just the precision with which they are sampled.
Using equations (3.26) and (3.27), the relative precision of the measured asymmetry can be calculated for different numbers of shots and calorimeter resolutions, as shown in figure 6.11. Achieving a relative precision of 20 % with calorimeter resolutions greater than 5 % requires tens of thousands of shots. This is currently impractical, given

that the accelerator can only operate at a few Hertz. In contrast, with a calorimeter resolution of 2 %, only about 5000 shots are needed, which corresponds to a measuring time of approximately 42 minutes when operating the accelerator at 2 Hz. At a 1 % calorimeter resolution, the required number of shots decreases further to about 1300, reducing the measurement time to 11 minutes.
These considerations highlight key requirements for the calorimeter design. Firstly, as shown in figure 6.10d), with a bunch charge of 3 pC and electron energies in the range of a few tens of MeV, the energy sums transmitted through the solenoid core reach a scale of several TeV. Therefore, the calorimeter must be capable of measuring such large energy deposits without saturating. Secondly, based on the results in figure 6.11, and considering that it is really the total error budget for the energy distribution that must remain below 2 %, it is evident that the calorimeter must achieve an energy resolution better than 2 %, which suggests the use of a crystal calorimeter.

Chapter 7.

The LEAP polarimeter

Guided by the results of the preceding design study, a polarimeter was constructed, as shown in figure 7.1. It consists a solenoid (cf. section7.1) and a calorimeter (cf. section 7.2). Since an additional high-Z converter in front of the solenoid core was found to provide no significant benefit in terms of analysing power (cf. section 6.2), it was omitted.

7.1. Solenoid

For the solenoid of the LEAP polarimeter, a magnet was selected that had previously been used as a photon analyser in the E166 experiment [103]. A detailed technical drawing and a table listing the relevant specifications are provided in the appendix (see Appendix C). Figure 7.2 offers a visual representation, including a) a schematic sketch highlighting the key dimensions and components of the solenoid, and b) a photograph of the solenoid as it appears in the BOND laboratory (cf. section 2.5).

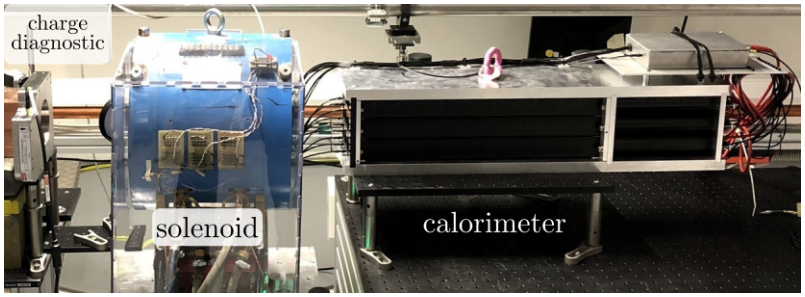

Figure 7.1.: The LEAP-polarimeter.

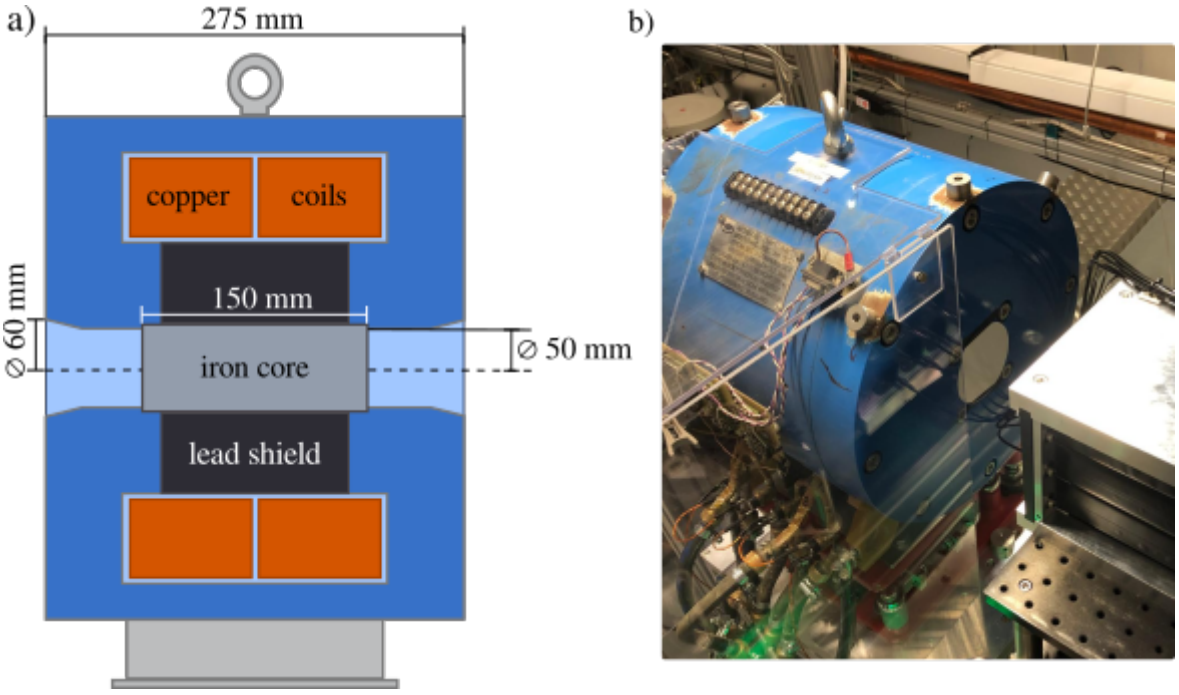

Figure 7.2.: The LEAP-solenoid: a) Schematic of key components. b) Photograph of downstream end of the solenoid in the BOND-laboratory.

The solenoid core is made of iron and has a length of $L_{\text{core}} = 150\,\text{mm}$. During the experiment, the solenoid current was cycled between +60 A and -60 A, with each target value being maintained for 5 minutes before switching. The transition between these values took approximately 12.5 s. This cycle of holding and switching was repeated continuously throughout the experiment.

Due to constraints in time, budget, and available personnel, certain measurements were not conducted as part of this study. Specifically, magnetic flux measurements taken during the E166 experiments using pickup coils indicated a central magnetic field of $B_z^{\text{max}} = 2.165\,\text{T}$ with a relative measurement error of 1%, and the average magnetic field $\langle B_z \rangle = 2.040\,\text{T}$ was modelled with Opera-2D [111] for the axial case over the full length of 150 mm. It was assumed that these values remain unchanged. According to equation 3.23, P_{Fe} is proportional to $\langle B - B_0 \rangle$, which leads to the calculated polarisation of the electrons in the iron core of $P_{Fe} = 0.0723 \pm 0.0015$, resulting in a relative error of 2.01%. While these assumptions are based on the values reported in [103], future work should include direct measurements and independent simulations to validate these assumptions and ensure the accuracy of the results.

7.2. Calorimeter

Measuring transmission variations caused by bremsstrahlung from the solenoid's iron-core is a key part of the polarisation analysis. An energy resolution of $\frac{\sigma_E}{E} < 2\%$ is required (cf. section 6.7), and to meet this requirement, a homogeneous lead-glass calorimeter is used in the LEAP polarimeter. The design and testing of the calorimeter were primarily developed by F. Stehr. For a more detailed description, please refer to his work [52]. This section summarises the calorimeter's operating principles, components, calibration procedure, signal definition, and its setup in the BOND laboratory (cf. section,2.5).

7.2.1. Key Components and their Operational Principles

To better understand the functionality of the LEAP calorimeter, this section provides a detailed overview of its key components, their working principles, and interactions. Figure 7.3a) presents a schematic of the system, illustrating the arrangement of the major elements, while figures 7.3b) and c) show photographs of the actual setup.

Radiator Components
In this calorimeter, TF1 lead glass is used as the radiator material. Material composition and properties of TF1 are listed in tables 7.1a) and b). The primary mechanism for optical light generation is the Cherenkov effect (c.f. section 3.1.2), scintillation is minimal.
Nine lead glass blocks with a dimension of 38x38x450 mm are stacked in a 3 x 3 grid. Each block is wrapped in reflective aluminium-coated Mylar foil to enhance light collection by reflecting emitted photons back into the glass or towards the photo-detector. An additional layer of black vinyl tape is applied to ensure light tightness, thereby preventing external light from interfering with the measurement of Cherenkov photons.

The Photodetectors
XP1911-UVA photomultiplier tubes (PMTs) [146] are used as photon detectors in the system, converting light into electrical signals. These PMTs have a cylindrical shape with an active area diameter of 15 mm. Their quantum efficiency peaks in the ultraviolet (UV) range, which is well-suited for detecting Cherenkov light. Before

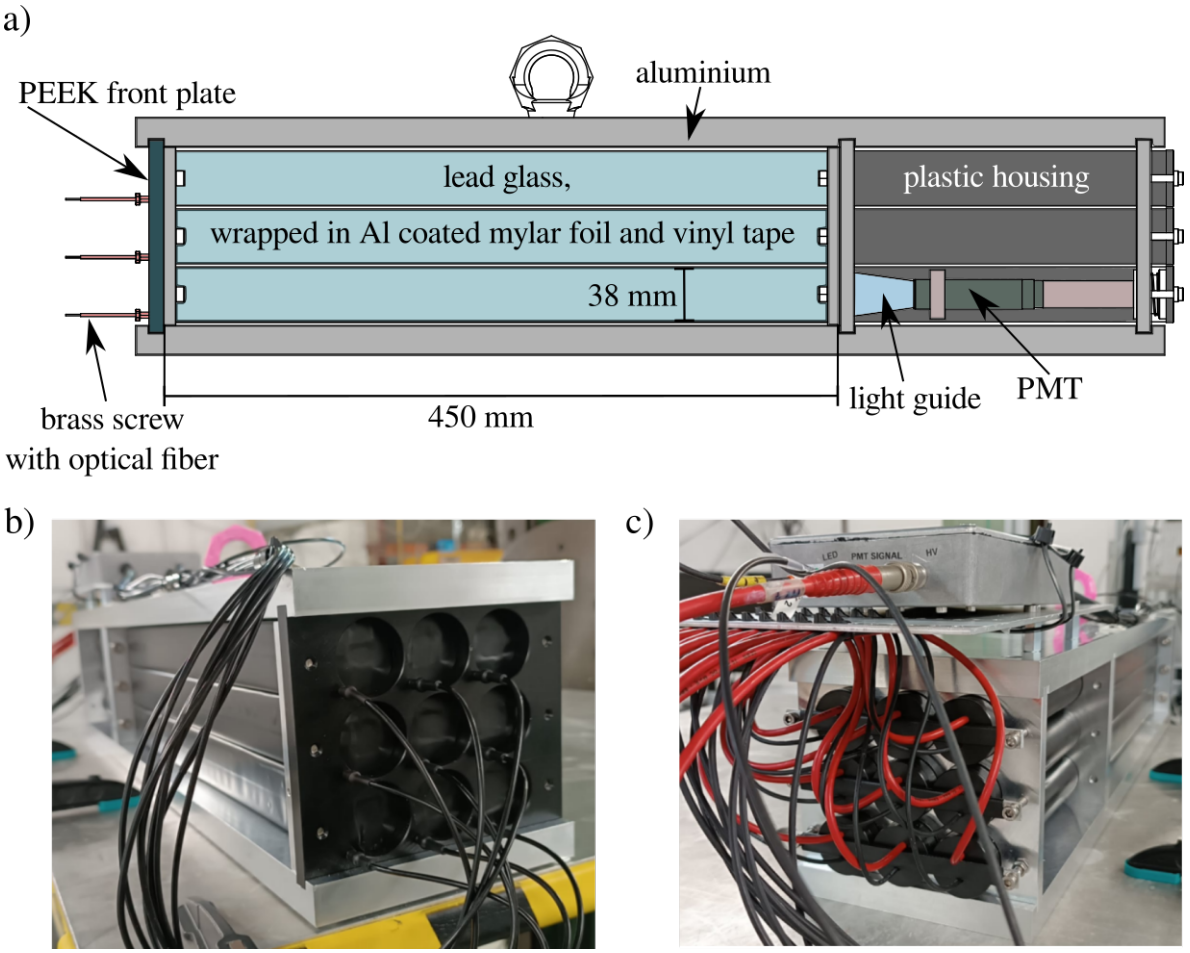

Figure 7.3.: The LEAP-calorimeter : a) Schematic of key components. b) Photograph of front view. c) Photograph of back view.

Table 7.1.: Material properties and composition of TF1 lead glass

a) Composition of TF1 [144]

Compound	PbO	SiO_2	K_2O	AsO_3
Percentage / %	51.2	41.3	7	0.5

b) Parameters of TF1 [145]

Parameter	X_0 / cm	R_m / cm	E_{crit} / MeV	n	ρ / g cm^{-3}
Value	2.74	3.7	15	1.647	3.86

installation, LED tests were performed to verify the functionality and gain linearity of the PMTs, and to select nine units with similar performance characteristics. Conically shaped plexiglass light guides are used to enhance optical coupling between the lead glass blocks and the PMTs. These guides are glued to the entrance windows of the PMTs. Each PMT-light-guide assembly is housed within a plastic tube and securely clamped against a glass block, eliminating the need for optical grease.

The Housing

The nine photo-detection-modules are secured in an aluminium frame. Two plates (160 mm wide, 20 mm thick and 693 mm long) form the base and top of the structure. Aluminium inserts hold everything in place. However, the front plate is made of PEEK plastic to have less dense material in front of the radiator. Nine holes with a diameter of 37 mm are supposed to allow as many gamma rays as possible to pass through.

The Gain Monitoring System

Each glass block in the calorimeter has additional holes in the bottom right-hand corner of its front panel. These holes accommodate brass screws that hold optical fibers in place. The fibers are bundled and connected to a UV LED, which is driven by an Arduino-based pulse controller. This system provides gain monitoring by periodically delivering a consistent amount of light to the detector. Any variation in the detectors response indicates a change in gain.

The Voltage Supply

The PMTs require a high voltage for operation, typically in the range of 1000 to 1350 V (the specific voltage used in the experiment is discussed in section 8.2.2). To supply this voltage, the SY127 high-voltage (HV) system from CAEN [147], equipped with three A100 positive high-voltage modules, was used. The PMTs were connected to the power supply via SHV cables and connectors. The control module of the HV system was connected to a PC through an RS232 cable, using a serial adapter for interfacing. A control software was written that utilizes the pySerial library [148] to communicate with the high-voltage system. Among other things this software sets the V_{set} (set voltage) and retrieves and monitors V_{set} and V_{read} (read voltage) values allowing for control and monitoring of the PMT operating conditions. Calibration of the HV modules was done via multimeter.

The Signal Chain

The PMT signals from the LEAP calorimeter are transmitted via LEMO cables and processed by a Charge-to-Digital Converter (QDC) unit, specifically a VME module of

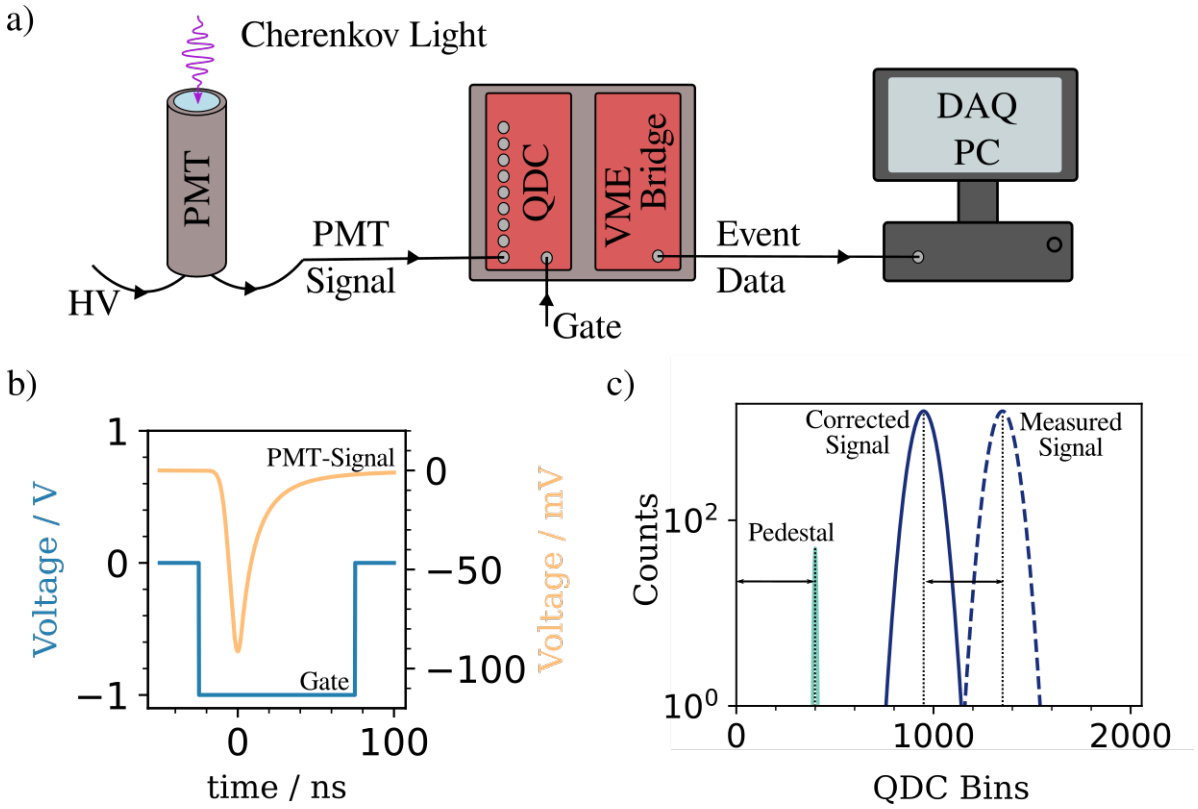

Figure 7.4.: Calorimeter signal management: a) Schematic of the signal chain, b) Illustrative representation of PMT and gate signals incident to QDC, and c) Measured and pedestal corrected QDC signals. Note that the plotted data is not derived from actual measurements but is generated for conceptual demonstration purposes.

type V965 from C.A.E.N. [149]. The QDC requires a gate signal to determine when data is recorded. For the zero-polarisation measurements, the FLARE trigger system was employed for the polarimeter. Further details are provided in section 2.5. At this stage, it is sufficient to note that the system provides a TTL signal synchronised with the laser, with the delay adjustable via control software. The gate signal for the QDC must conform to the NIM standard and match the duration of the PMT signal (see section 8.2.1 and the paragraph below), necessitating the use of NIM modules for signal conversion and extension. Once the QDC receives its gate signal, the event data is transferred via the VME-PCI Optical Link bridge (Model V2718 from C.A.E.N. [150]), which communicates this data to a PC through a fiber optic connection to a PCIe card (PCI Express CONET2 Controller A3818 from C.A.E.N. [151]). A schematic that summarises this signal chain is displayed in figure 7.4a).

7.2.2. The QDC Signal

The digitised QDC signals form the basis for calculating the measured asymmetry, making them crucial for the polarisation measurements. Therefore, a detailed examination of these signals is necessary.
The QDC has 16 input channels, the calorimeter PMTs using 9 of them, and one gate input common to all of them. As shown in figure 7.4b), when the gate signal is at a logical 1 (high = -1 V), the QDC begins integrating the incident charge signal. This integration process continues as long as the gate remains high, accumulating the charge over this period. Once the gate signal returns to logical 0 (low $\approx$ 0 V), the QDC stops integrating and holds the final integrated value, which corresponds to the total charge collected during the gate's active period. The integrated charge signals are then converted into voltage levels by QAC (Charge to Amplitude Conversion) sections. The LEAP QDC employs a dual-range QAC system, utilizing either a 1x or 8x gain setting. For the zero polarisation measurement, the high-range 8x QAC section was consistently selected , which provides a broader dynamic range at the expense of slightly lower resolution. After conversion, these voltage levels are then multiplexed, i.e. combined into a single stream, before being processed by two fast 12-bit ADC modules. This setup results in a final resolution where each of the 4096 bins corresponds to 200 fC.
Having explained the operation of the QDC, it is essential to consider the impact of the baseline offset, known as the pedestal. Even if no input signal is present, a small current flows, which is integrated during the gate period and thus forms the pedestal. As a result, the measured value for each event does not correspond to the true integrated charge, but to the sum of the true and baseline values. To obtain the true value, the pedestal must therefore be subtracted (cf. figure 7.4c). This subtraction is achieved by performing measurements with no signal present, allowing the baseline to be determined and subsequently removed. This process increases comparability across channels, with a consistent baseline, and can also account for fluctuations due to external influences through regular background measurements (see section 8.3).

7.2.3. Response Calibration and Energy Resolution Studies

The asymmetries expected to be measured in a future LEAP polarisation run are on the order of per mille (see Figure 6.10, where an asymmetry of $0.14 \pm 0.02\%$ is predicted

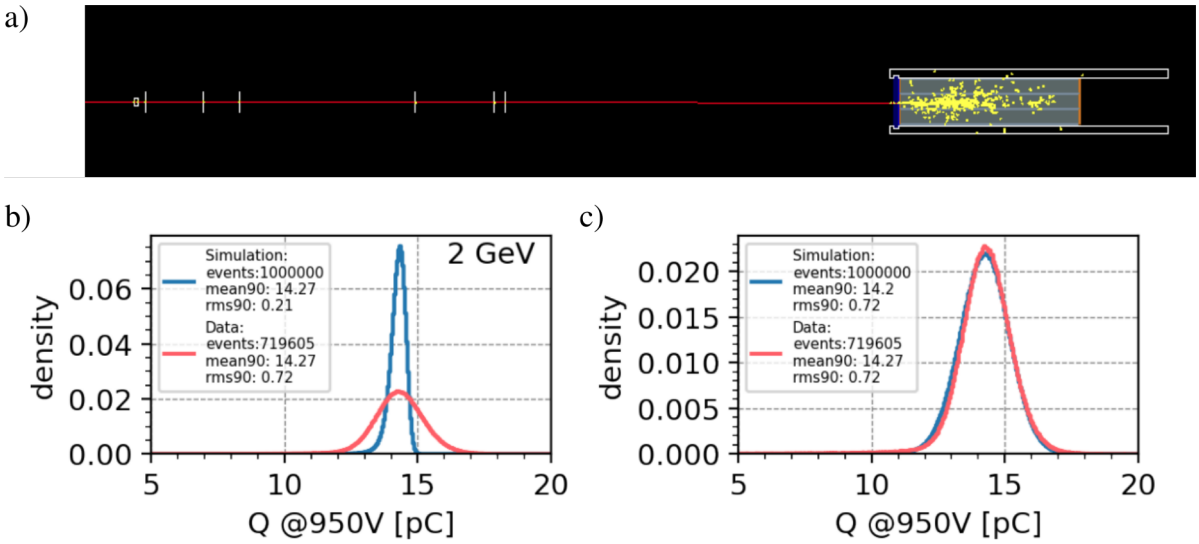

Figure 7.5.: Comparison of calorimeter test beam results with simulation. Panels reproduced from [52]. a) LEAP_SIMS-simulation geometry. Scintillator trigger fingers, simulated as 10 mm thick cubes of plastic scintillator, six telescope planes simulated as 0.5 mm thick silicon disc and the calorimeter. b) Calibrated calorimeter signal summed up over all glass blocks, Q, compared to translated simulated distribution. c) Q compared with simulation results that have been broadened and then translated

for 30 MeV electrons). Therefore, it is crucial to measure energy differences with the highest possible precision. To ensure this, the response of the calorimeter was characterised through a test beam study at the DESYII test beam [152].
The calorimeter was irradiated with single electrons with energies ranging from 1 to 5.6 GeV. The PMT-voltages were varied between 700 and 1200 V. For both scans, each glass-block-PMT unit was individually positioned at the beam centre to ensure consistent measurements.
Since each unit has a slightly different response, the same measurements were performed for all units. By comparing their results, a cross-calibration was carried out to account for these variations. Additionally, the linearity of the calorimeter response with respect to the incoming electron energy was verified. To this end, the mean of the QDC signal $\langle Q \rangle$ was fitted as a function of E_{beam}, and within statistical uncertainties, all measured values were found to be consistent with a linear relationship, with deviations from the fit of less than 1%.

Comparison with Simulation

To validate the test beam results, LEAP_SIMS-simulations were conducted, where

single electrons with energies between 1 and 5.6 GeV were directed at the calorimeter. The test beam setup was replicated by setting `beamLineStatus` to 2, as shown in figure 7.5a).
To relate the measured charge Q to the simulated deposited energy of charged particles with energy above the Cherenkov threshold E_{ct}, the mean values of the measured and simulated distributions were compared and fitted to derive a conversion function. However, this approach alone proved insufficient for inferring measured values from simulation results, as the simulation does not account for effects such as statistical fluctuations in the Cherenkov process, the quantum efficiency of the PMTs, or electronic noise in the readout chain. As a result, the measured signal is significantly broader than the simulated one (cf. figure 7.5b)).
To replicate these effects, a digitisation function was derived from a comparison between data and Monte Carlo simulations, incorporating additional smearing and scaling [52]. An example of the transformed simulated calorimeter response is shown in figure 7.5c) for an electron energy of 2 GeV. The transformed simulated distribution (blue) exhibits good agreement with the measured distribution (red).

Energy Resolution
Using the test beam energy scan and transformed LEAP_SIMS simulations, it is possible to determine the calorimeter's energy resolution for the energy sums expected at LEAP in the TeV range. A visual representation of this analysis can be found in figure 7.6. The plot presents the energy resolution ($\frac{\sigma}{E}$) of the calorimeter as a function of the beam energy E_{beam} of the incident particles (black circles). To model this behaviour, the data was fitted using the standard energy resolution function described in equation 3.31 (red line). The fit has been extrapolated to the TeV beam energies expected in LEAP measurements (c.f. section 6.6), where only the energy-independent constant term remains relevant.
Yet, LEAP_SIMS simulations reveal a critical limitation: for individual high-energy electrons, a point is reached where not all of the total energy is deposited in the lead glass blocks, resulting in energy leakage through the back of the detector. As a result, the energy resolution worsens, contradicting the naive extrapolation.
Fortunately, when considering a large number of low-energy particles that collectively carry a high total energy – such as in a real experimental scenario – the resolution improves with increasing E_{beam}. In this case, the simulation results (blue star) and the extrapolated data show good agreement.
Moreover, at a confidence level greater than 99.7 % , the energy resolution of the LEAP

calorimeter is expected to be better than 2 % at the anticipated beam energy sums for LEAP, which matches the requirements derived in section 6.7.

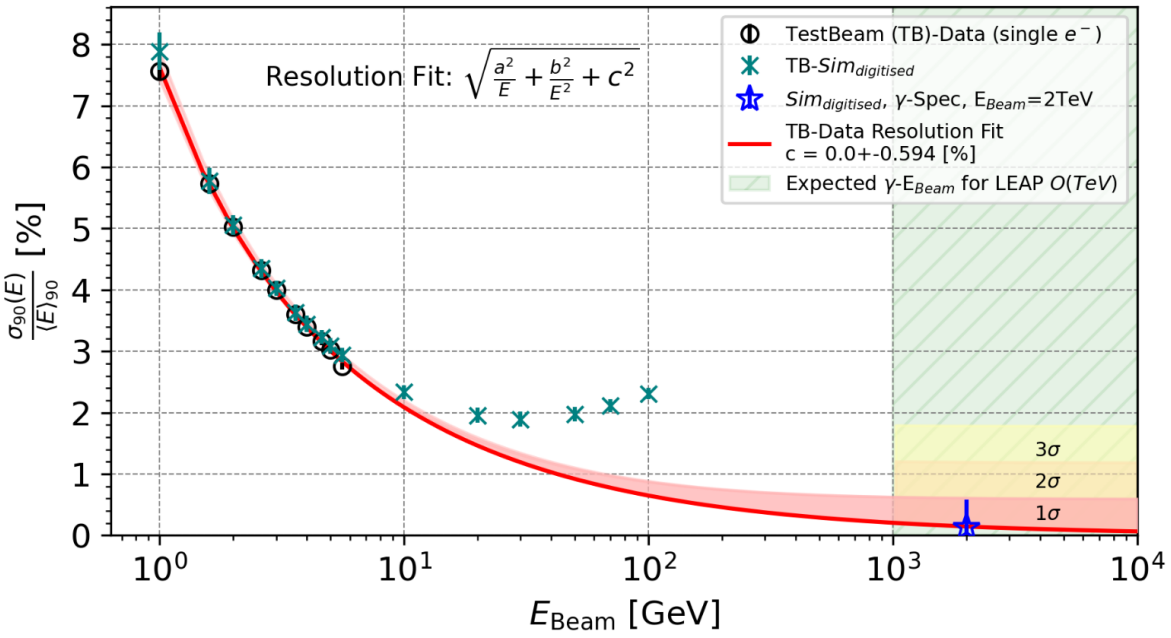

Figure 7.6.: Extrapolation of calorimeter energy resolution to the TeV energy regime expected at LEAP. Test beam data shown as black circles, simulated single electron results shown as teal crosses, and simulated energy resolution resulting from a 30 MeV electron spectrum shown as blue star. Fit to test beam data energy resolution shown in red, has been extrapolated to TeV energy. Reproduced from [52]

Chapter 8.

Commissioning of the LEAP polarimeter

The commissioning of a newly assembled diagnostic system is a critical step in ensuring its reliability and functionality under experimental conditions. Before it can be used for precise measurements, the system must be thoroughly tested to validate its performance and identify potential limitations. For the LEAP polarimeter, this process is particularly important given the absence of a polarised electron beam with a known polarisation for direct calibration.
To address this challenge, a polarisation measurement was conducted using the unpolarised laser-plasma-accelerated electron beam. This "zero measurement" serves as a controlled test to evaluate the polarimeter's behaviour under conditions where no polarisation is expected. The goals of this measurement are threefold:

1. **Validation of functionality:** Do all the subsystems of the polarimeter work together seamlessly, and does the experimental procedure need adaptation?
2. **Identification of systematic errors:** Are there biases in the measurement setup that could mimic a false polarisation signal?
3. **Baseline accuracy check:** How accurately can the LEAP polarimeter measure zero polarisation, and what is the magnitude of the associated uncertainty?

By addressing these questions, the zero measurement provides essential insights into the polarimeter's performance and lays the groundwork for future polarisation measurements with a polarised beam.
This chapter begins by detailing the measurement setup (section 8.1) and describing the measurement procedure (sections 8.3 and 8.2). This is followed by the characteri-

sation of the beam parameters (sections 8.4 and 8.6) and simulations of the expected polarimeter signal (section 8.5). Finally, the measured asymmetry (section 8.7) and analysing power (section 8.8) are evaluated to assess the polarimeters overall performance (section 8.9).

8.1. Setup

The experimental setup for the commissioning of the LEAP polarimeter is displayed in figure 8.1. The LPA laser beam, displayed in red, is guided into the plasma acceleration chamber, a vacuum chamber with a diameter of 1.4 m that houses the setup for the electron source. There it is focused with an off-axis parabolic mirror (3" diameter, dielectric coating, 500 mm focal length) onto a gas target, specifically a gas cell (also referred to as plasma cell), rather than a gas jet, where gas is expelled through a nozzle. The cell contains a helium-nitrogen mixture, following the setup outlined in [66].
Electrons are accelerated (cf. section 2.2), and the electron beam is focused using an active plasma lens (APL), which captures the electron beam, reducing beam jitter and enhancing pointing (cf. section 2.7). The optimisation and operation of the accelerator were managed by domain experts; therefore, only key aspects are discussed here.
Once the beam exits the main chamber it traverses the DaMon, a diagnostic to measure the accelerated charge (cf. section 2.6.1), before entering the auxiliary chamber. Inside this chamber, a scintillation screen, mounted on a motorised stage, can be positioned in the beam path to image the resulting fluorescent light for beam profile measurements. The electron beam's energy spectrum can be determined with the aid of a dipole magnet spectrometer (cf. section 2.6.3). When the dipole is activated, it diverts the electrons away from the downstream diagnostics, requiring a choice between spectral measurements or data collection from the polarimeter.
A copper collimator with a diameter of 1 mm is placed behind the exit window of the beam pipe (300 μm thick, made of aluminium). The collimator not only reduces the amount of charge incident onto the solenoid core (the necessity of which is explained in section 8.2.2), but also, in combination with the APL, acts as energy filter (section 8.4.2).
A current transformer (ICT-VAC-082-Turbo2 from Bergoz [153], short: TurboICT) was mounted behind the collimator with the intention to provide absolute shot-to-shot measurement of the charge incident on the polarimeter. However, the amount of charge that made it through the collimator was so close to the lower detection limit of 50 fC that the signal-to-noise ratio, slightly reduced by additional noise from the APL,

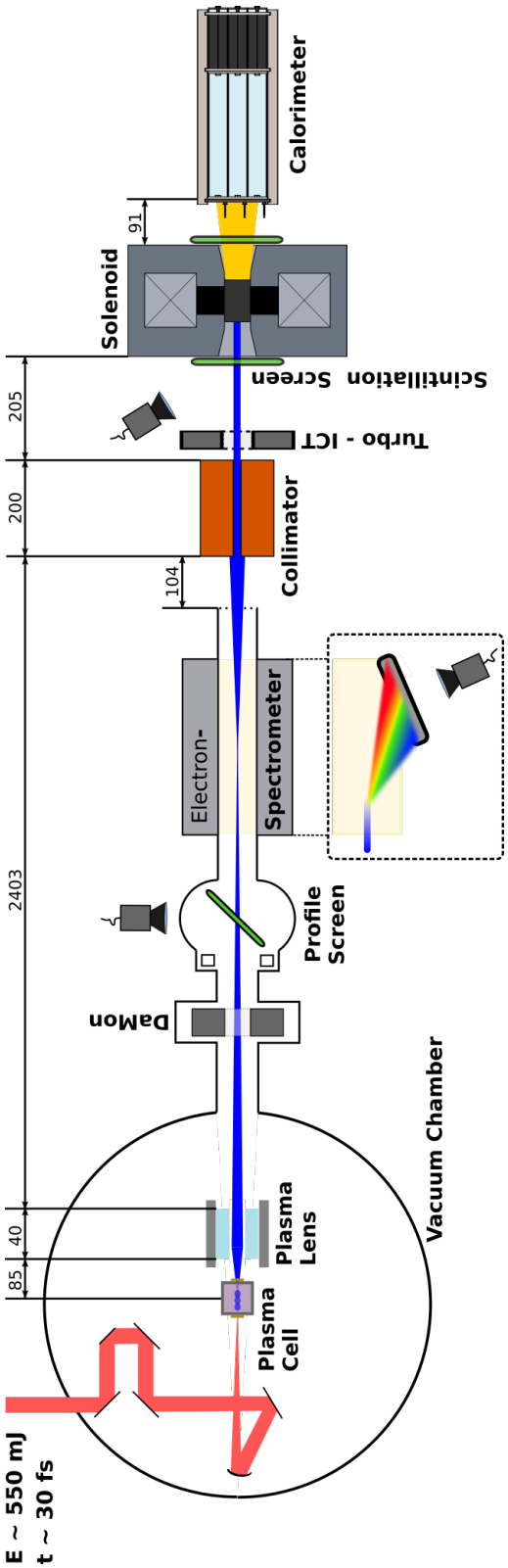

Figure 8.1.: Sketch of the experimental setup for the commissioning of the LEAP polarimeter. Distances in mm. Image credit: F.Stehr

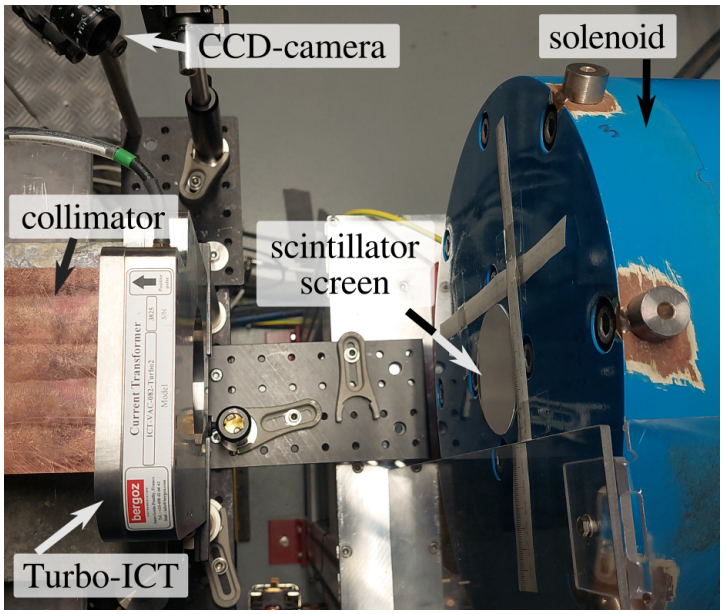

Figure 8.2.: Setup in front of the polarimeter-solenoid.From left to right: Copper collimator with 1mm diameter, Turbo-ICT, scintillator screen imaged by CCD-camera and solenoid magnet. Scales and screens are directly mounted to the solenoid front.

was too small for reliable measurements to be made. Therefore, for absolute charge measurement, only the DaMon measurement taken before the collimator could be used.

Two scintillating screens, each with a radius of 3 inches (76.2 mm) were used for relative charge measurement (cf. section 2.6.2). One was mounted in front of the solenoid entrance (cf. figure 8.2), one at the solenoid exit. Both screens were imaged onto CCD-cameras for charge and beam spot diagnostic. During the experiment, the camera aimed at the exit screen did not detect any fluorescent light, so the following discussion refers exclusively to the screen at the entrance.

The polarimeter was placed 205 mm behind the plasma cell, thus approximately 2.9 m behind the plasma cell. It consists of a solenoid with iron core (cf. section 7.1) and a Cherenkov calorimeter (cf. section 7.2).

All diagnostics and experimental components needed for the zero polarisation measurements and requiring control were integrated as far as possible into the DOOCS based FLARE control and DAQ systems (cf. section 2.5). The DaMon, the profile screen system, the APL and the electron spectrometer were part of it anyway. The cameras monitoring the scintillation screens, the QDC, as well as the power supply of the solenoid have been integrated as part of this work. To drive the solenoid current flow in the rectangular pattern described in section 7.1, Taskomat software [154] was

used, which can be interfaced with via jddd panels.
Unlike the other components, the supply voltage of the PMTs is not integrated into the DOOCS-based control system. Instead, it is controlled separately using a custom Python-based GUI (see section 7.2). Nevertheless, the supply voltage data is still recorded by the FLARE-DAQ during the run. Extracted data is saved in hdf5 file format.

8.2. Pre-Run Adjustments and Verifications

Before commencing data collection, several pre-run adjustments and verifications were performed to ensure the accuracy and reliability of the experimental setup. These adjustments focused on three key areas: the timing of the PMT signal, the linearity of the PMT response, and considerations regarding electromagnetic pulse noise caused by the APL.

8.2.1. QDC Gate

The calorimeter QDC (Charge-to-Digital Converter) operates by integrating input signals during a specified gate period (see section 7.2). It is crucial that the input signal is fully within this gate period and that the gate length is appropriately chosen to ensure that the entire signal is captured without truncation.
The delay of the QDC trigger relative to the laser, and consequently to the acceleration of the electrons, can be adjusted using a jddd panel. The gate length is set using the NIM logic as described in section 7.2. To ensure proper synchronisation between the gate and the PMT signal, both were connected to an oscilloscope, allowing for simultaneous observation of their relationship with the incoming electrons.
The gate period was adjusted to 100 ns. An example oscilloscope display is shown in figure 8.3.

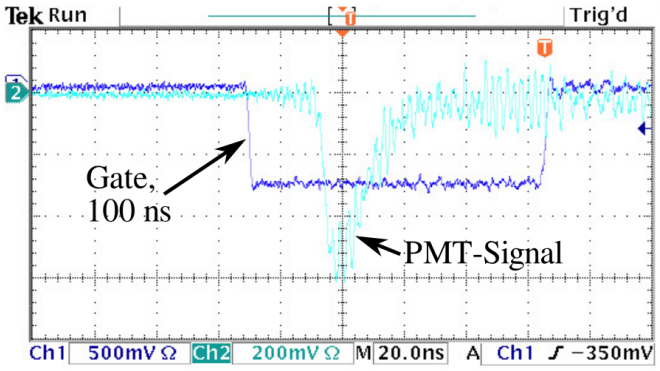

Figure 8.3.: Cropped oscilloscope display. PMT-signal generated by an electron bunch shown in light-blue, QDC-gate-signal shown in dark blue.

8.2.2. Optimizing the PMT Response: Saturation Prevention Measures

To ensure accurate and reliable measurements, it was necessary to prevent the PMTs from saturating. Saturation can occur when an excessive amount of particles reaches the calorimeter, producing more Cherenkov light than the PMTs' dynamic range can handle, which leads to a non-linear response. Maintaining a linear response is crucial because a direct proportionality between the PMT-signal and the amount of input light enhances the accuracy, reliability, and interpretability of measurements.
To assess the PMT response, it is necessary to vary the intensity of the incoming light. In our case, the natural charge variation of the electron beams accelerated by the LPA provides this variation. By examining the correlation between the QDC signal q_{QDC} and the scintillation screen signal S_{scint}, one can determine if the PMT is operating linearly. A strong linear correlation indicates that the PMTs are not saturating and are functioning within their optimal dynamic range.
A brief test run of 15 min using the initial PMT voltage of 550 V and a 15 mm collimator clearly indicated signs of saturation, demonstrating that the PMTs were operating outside their linear range.
Now there are two possibilities how to address the situation:

1. **Reduction of collimator diameter**: This reduces the charge incident on the polarimeter and hence the light reaching the PMT, preventing the input signal from reaching saturation levels. However, a smaller collimator diameter increases

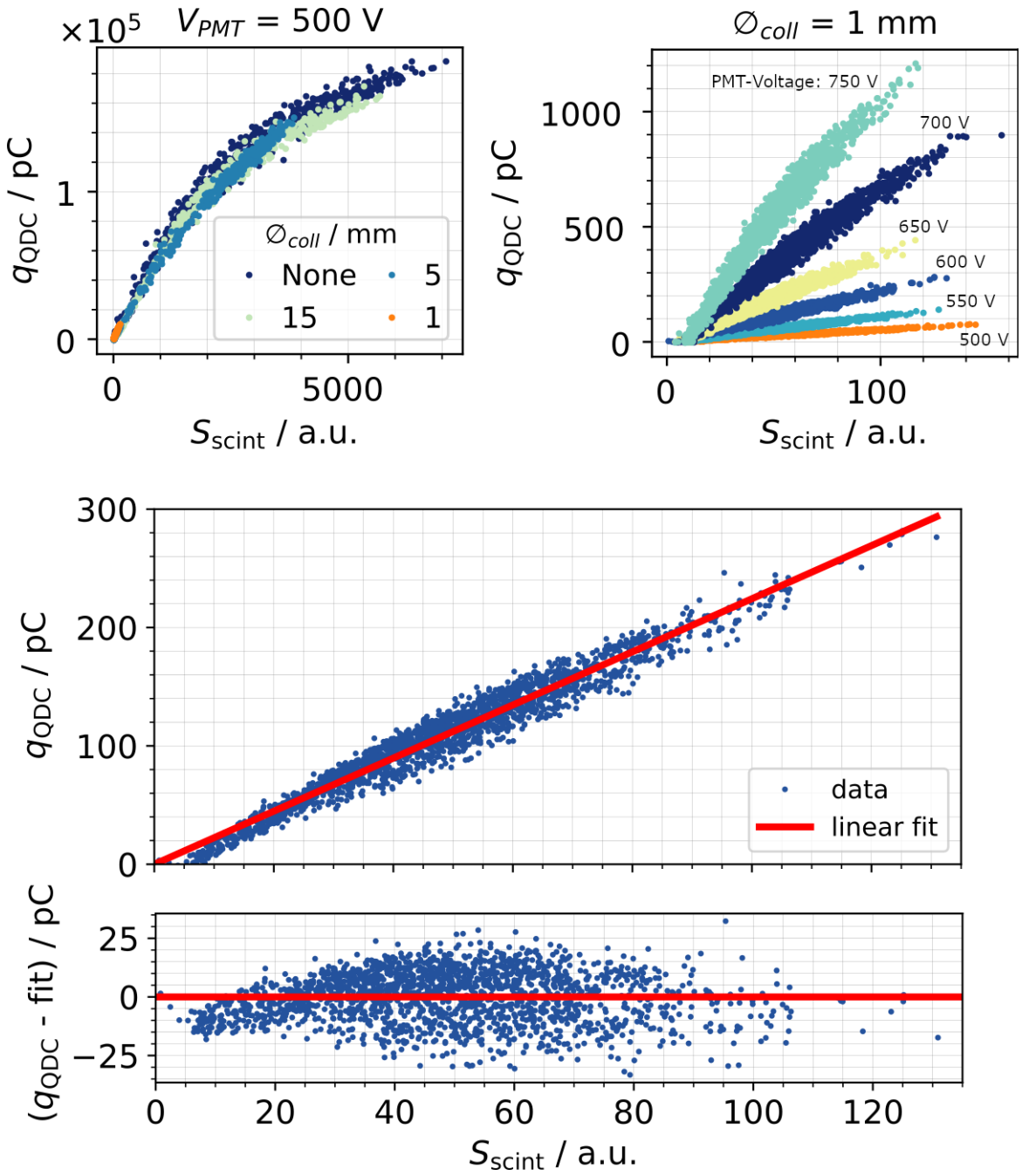

Figure 8.4.: PMT-linearity measurements. a) Scan of different collimator diameters at a PMT-Voltage V_{PMT} of 500 V. b) Scan of different PMT-voltages for a collimator diameter of 1 mm c) Response for 600 V and 1 mm diameter. Linear fit with forced intercept of 0 for visualization purposes. d) Corresponding residual. For typical beam parameters see section 8.4

the difficulty of aligning the electron beam with the polarimeter, as the electrons must pass precisely through the narrower opening.[1]

2. **Reduction of PMT operating voltage**: Lowering the operating voltage reduces the PMT's gain, thereby decreasing the output signal for a given amount of incident light. This helps keep the PMT response within its linear range but may reduce the signal strength and dynamic range.

In the following, a series of short runs, each lasting approximately 10 to 15 minutes, was conducted. The PMT voltage was varied for each collimator size, as adjusting the voltage did not require realignment of the system. Collimators with diameters of 15 mm, 5 mm, and 1 mm were used. The effect of reducing the collimator size is shown in figure 8.4a. Here it becomes visible that lowering the collimator diameter from 15 mm to 5 mm reduces the charge incident on the polarimeter, but not enough, so that even at 500 V the PMTs are saturating. Reducing the the collimator size to 1 mm significantly reduces the charge so that q_{qdc} is reduced from hundreds of thousands of pC to charges on the order of 100 pC.
To utilise the dynamic range of the QDC, while still maintaining a linear PMT response, a PMT operating voltage scan between 500 V and 750 V was performed. The results of which are presented in figure 8.4b. At higher energies, increased voltages still exhibited signs of saturation, leading to the decision to operate the PMTs at 600 V.
The results using V_{PMT} of 600 V and a collimator diameter of 1 mm are presented in more detail in figure 8.4c. A red fit line is included to visualise the linearity of the data points. A linear regression was performed using the least squares method, with the line constrained to pass through the origin, as theoretically, zero input should correspond to zero output. The R^2 value of 0.95 indicates that 95% of the variance in the output signal is explained by the input signal. This high R^2 suggests a strong linear relationship between the variables.
Residuals were plotted (see figure 8.4d) to further assess the fit. The residuals were overall symmetric, indicating no significant bias in the fit. However, the baseline values observed around 7 a.u. in the scintillation signal suggest a visibility threshold in the scintillator's response rather than nonlinearity in the PMTs.

[1] A reduction of the collimator size also has the advantage of reducing the spectral width. Further details can be found on page 136.

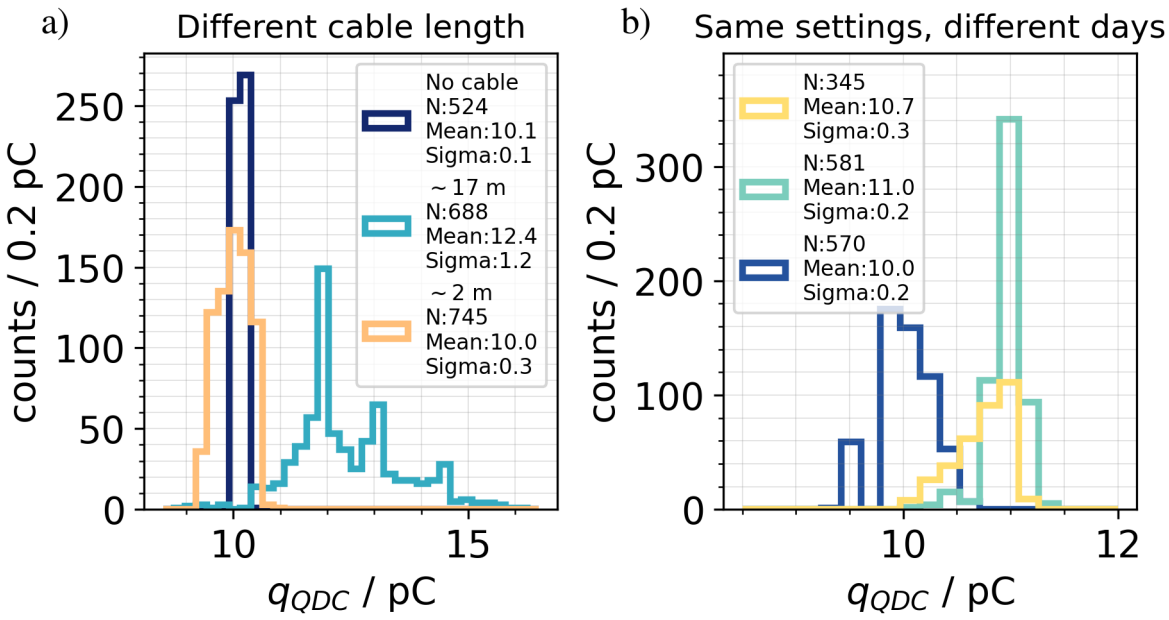

Figure 8.5.: QDC pedestal measurements. a) for consecutive runs with different cable length. $V_{APL} = 16\,\text{kV}$. b) for same settings on different campaign days. $V_{APL} = 20\,\text{kV}$, cable length of 2 m.

8.2.3. Assessment of EMP effects on the QDC

The laser plasma acceleration of electrons and the discharge units of the active plasma lens are sources of electromagnetic pulses (EMPs) that can cause electronic noise in the diagnostic equipment used [64, 65, 155].
While the DaMon, for example, has been shown to work well in the immediate vicinity of the APL [156] , the same behaviour is not clearly established for the polarimeter. Therefore, an assessment is important.
One key consideration in this assessment is the performance of the QDC in the presence of EMP noise. Notably, variations in the pedestal width of the QDC have been observed, potentially indicating a sensitivity to electromagnetic interference. The long cable rolls connecting the calorimeter with the QDC, originally used as signal delay, were suspected to act as antenna, picking up the EMP and potentially amplifying it. Figure 8.5a illustrates the influence of cable length on the QDC pedestal connected to the central calorimeter channel. Measurements were taken with no accelerated electrons, a plasma lens voltage of 16 kV, and QDC configurations with cable lengths of 17 m, 2 m, and no connecting cables. The 17 m long cables were

causing a pedestal shift from a mean of 10.1 pC to 12.4 pC and a standard deviation increase from 0.1 to 1.2 pC. Reducing the cable length to 2 m lead to a recorded pedestal mean of 10 pC and a standard deviation of 0.3 pC.
Shortening the cable length has reduced the influence of EMP noise, though it has not completely eliminated it. Nonetheless, the pedestal widths remain relatively narrow and are still influenced by other factors. External conditions, such as temperature fluctuations and the stability of the power supply, also affect both the mean value and the shape of the pedestal. Therefore, conducting pedestal measurements before each data run is essential for accurate correction. This is illustrated in figure 8.5b, which shows the pedestal for a 2 m cable length and 20 kV APL voltage on different days.

8.3. Operation Procedure

During the experimental campaign described in this chapter there were three different run types taken:

a) **Data runs:** The main type of run with the aim to gather polarimeter data. The primary run 50379, focused on measuring the zero-polarisation of the accelerated electrons, was conducted with APL voltage of 20 kV and solenoid current of $\pm$ 60 A switching polarity every 5 min. Additional, shorter runs were carried out at APL voltages of 16, 18, and 24 kV to complement the main run. To validate the influence of the solenoid on the measurements, additional control runs were performed with the solenoid turned off.

b) **Pedestal runs**: These are short runs conducted with the laser blocked, preventing the acceleration of electrons. For each data run, a corresponding pedestal run is performed under identical settings to ensure accurate subtraction of baseline values from the QDC measurements (see section 7.2).This includes the operation of the plasma lens. Scintillator-screen images taken during these type of runs are likewise used for background subtraction (see section 2.6.2).

c) **Electron spectrometer runs**: These types of runs, conducted at the beginning and end of each campaign day, as well as in regular intervals between longer data runs, serve the purpose of characterising the energy spectra of the accelerated

electron bunches. Due to the destructive nature of the measurement simultaneous data runs are not possible. More details are described in section 2.6.3.

The laser was operated at 2 Hz to ensure stable performance and reduce wear on system components. The solenoid current polarity interval of 5 minutes was chosen as a compromise between obtaining sufficient statistical data and accounting for the expected temporal variations in the parameters of the accelerated electron beam.
A comprehensive run-overview is attached in appendix D.

8.4. Beam Parameters

Compton transmission polarimetry is based on the relative comparison of several measurements. To ensure that any observed asymmetries originate from the degree of polarisation of the electron beams rather than fluctuations in beam parameters, these parameters must be characterised with high precision. A key example is the dependence of analysing power on beam energy (cf. section 6.4), which underscores the importance of precise beam diagnostics. This allows for error estimation, corrections for temporal variations, and the development of accurate simulations. In the following sections, beam parameters that are relevant for polarisation measurement are determined. Primarily for the longest and most stable measurement: Run 50379. In this run an APL voltage of 20 kV was applied. If necessary, other runs are used for comparison.

8.4.1. Incident charge

There are two diagnostics that measure the charge in front of the polarimeter:

a) the DaMon (cf. section 2.6.1) that measures the absolute charge that is accelerated, q_{DaMon},

and

b) the Scintillation screen setup (cf. section 2.6.2) which, with the integrated signal S_{scint}, gives relative information about the charge that makes it through the collimator.

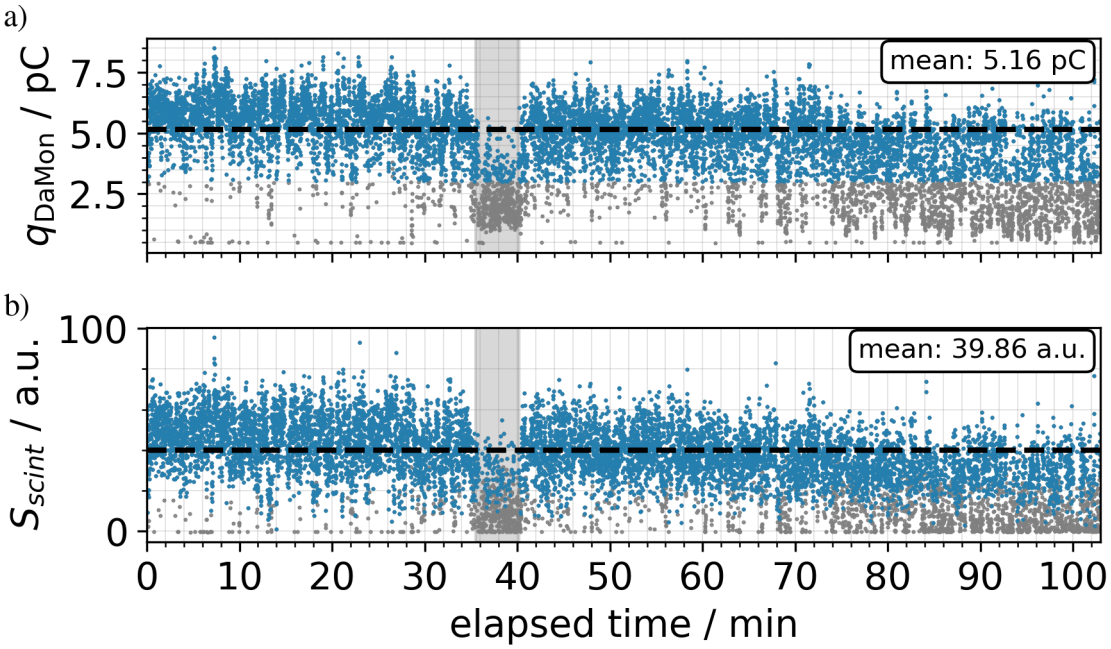

Figure 8.6.: a) charge recorded by the DaMon for run 50379 b) Scintillation screen signal recorded during the same run. Grey points mark shots with a DaMon charge below 3 pC or with a negative scintillation screen signal. The greyed out area marks a period of low laser energy. The dashed line marks the mean of the data with cut applied. The number of shots N=11791 before the cut and 9239 after.

Figure 8.6 shows how the measured charge for both diagnostics changes over time during run 50379. The results from both diagnostics demonstrate similar behaviour, with significant shot-to-shot fluctuations and a general decrease in the average charge over time. During a period of slightly more than 4 minutes, the charge accelerated and the charge detected by the screen both decreased, corresponding to a period of reduced laser energy. This interval is indicated by a grey background in the figure. Examining the correlation between the two data sets (see figure 8.7) reveals the following:
Firstly, in the histogram displaying the DaMon data there are about 70 entries in the baseline bin around 0.5 pC, while the S_{Scint}-histogram contains over 600 entries in the baseline bin at zero. This indicates a non-negligible amount of over 500 shots where charge is accelerated but fails to pass through the collimator even with APL on. Such results suggest a degree of pointing instability, which also explains at least part of the width of the correlation distribution in the joint plot.
Secondly, if the low-energy tail of the distribution is also taken into account, the correlation is not linear. One might even assume that there are several populations. This behaviour, which also can be explained by the pointing instability, was also observed in other runs with collimator and a 3 pC DaMon cut was established. This data was greyed out in figure 8.6 as well as figure 8.7. After this cut, it can be seen that the distribution of S_{scint} even becomes approximately Gaussian.
The average charge measured with the DaMon, $\langle q_{\mathrm{DaMon}} \rangle$, is now 5.2 pC with a standard deviation of $\sigma_{\mathrm{DaMon}} = 1.0$ pC. This leads to a relative width of the distribution of 19.8 %.
The average scintillation screen signal $\langle S_{Scint} \rangle$ is 40 a.u. with a standard deviation of $\sigma_{Scint} = 13$ a.u.. The relative width here is 32.6 %.
A comparison with other runs (cf. figure 8.8) shows that $\langle q_{\mathrm{DaMon}} \rangle$ is fluctuating between 4.6 and 6.8 pC and $\langle S_{scint} \rangle$ between 19 and 57 a.u.. The ratio between the two charge measurements shows that runs 50282 and 50379 were particularly well aligned. Note, that even for the same plasma lens settings the mean accelerated charge measured with the DaMon during different times of the campaign varies between 4.6 and 6.8 pC.
The combined analysis of DaMon and scintillator screen measurements demonstrates that beam jitter from pointing instabilities, coupled with the small 1 mm collimator diameter, leads to fluctuations in the fraction of accelerated charge reaching the polarimeter. Additionally, the APL's energy-dependent focusing further contributes to the variation in transmitted charge, as different energy components of the beam are focused to different extents (for a more detailed discussion of the energy-dependent

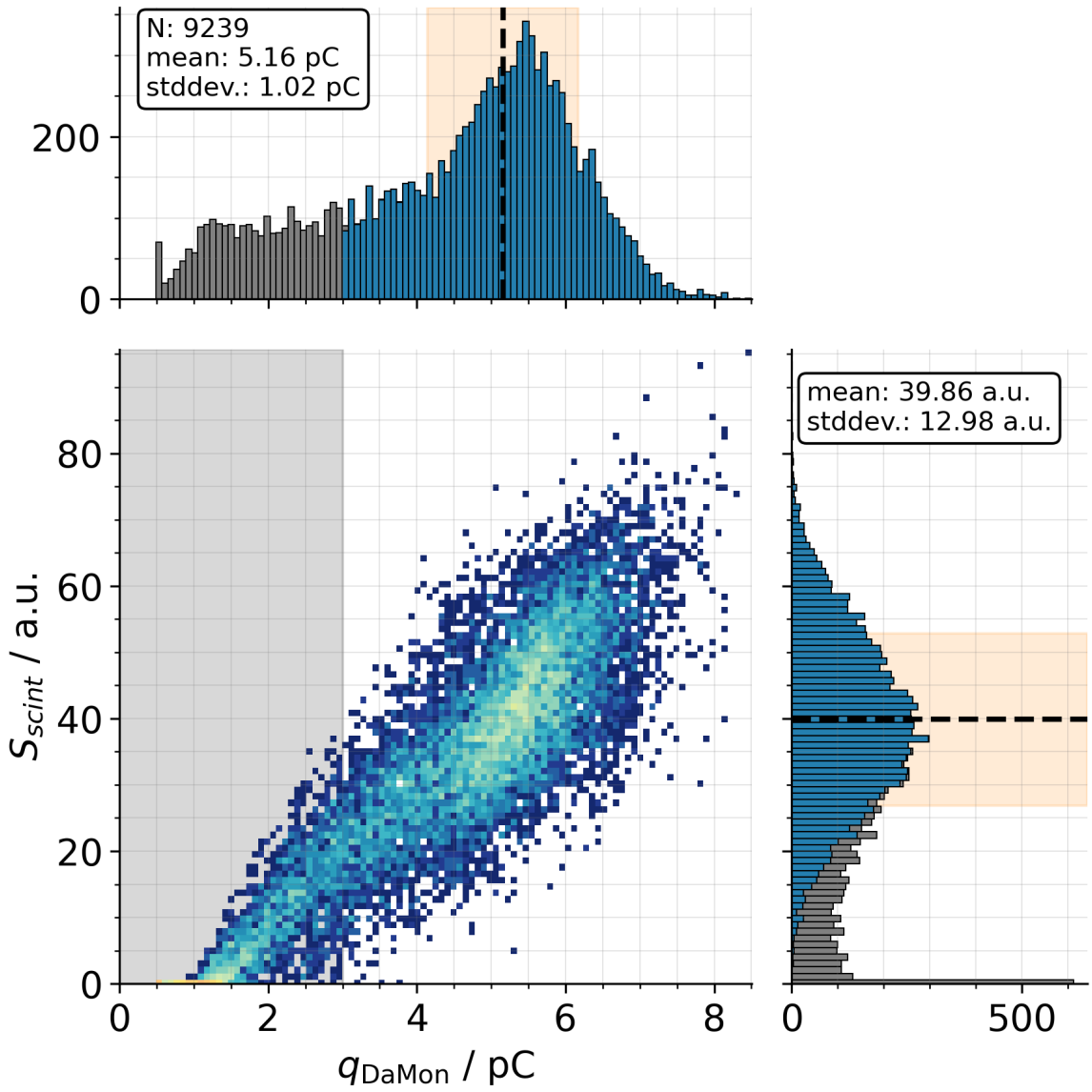

Figure 8.7.: Correlation of charge measured by the DaMon, q_{DaMon}, and scintillator signal, S_{scint}, during run 50379 and projections onto the axes. Greyed out areas have $q_{\mathrm{DaMon}} < 3\,\mathrm{pC}$. Statistic boxes refer to data with cut applied. Dashed lines mark means. Orange highlighted background signifies the standard deviation.

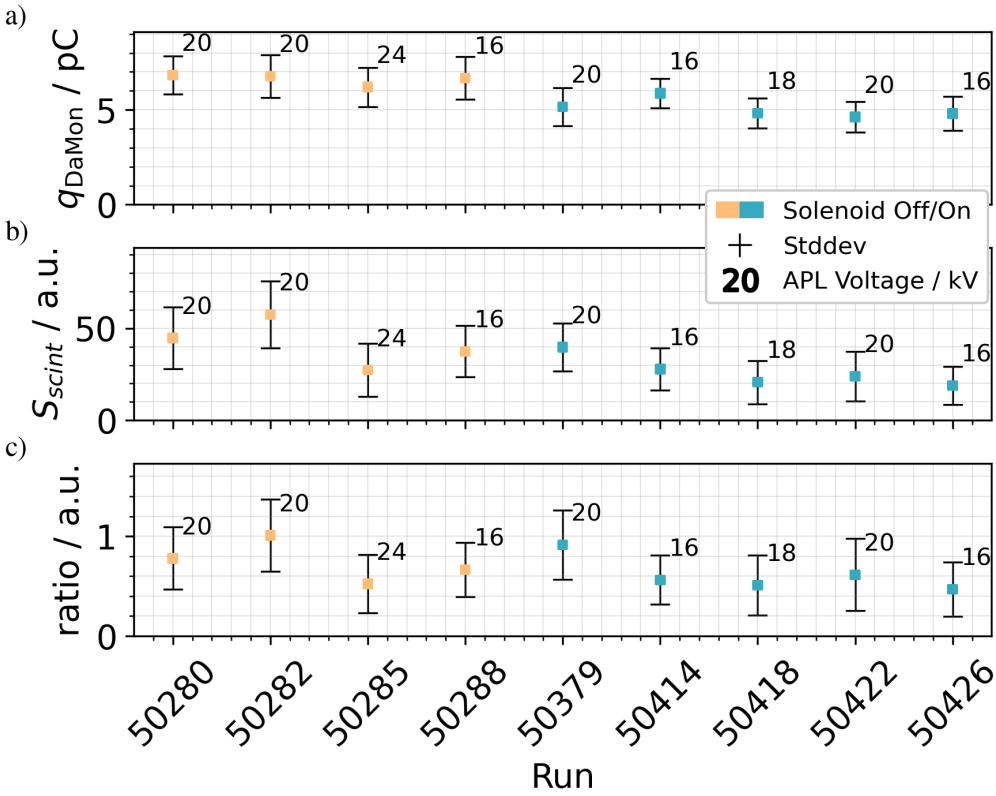

Figure 8.8.: Mean charge for different runs measured with a) the DaMon and b) the scintillator screen setup. c) Ratio of normalised S_{scint} / q_{DaMon}. Orange markers denote, that the solenoid was switched off, blue markers denote that the current was ramped in the usual pattern (see section 7.1). Numbers next to the markers are the applied APL voltages.

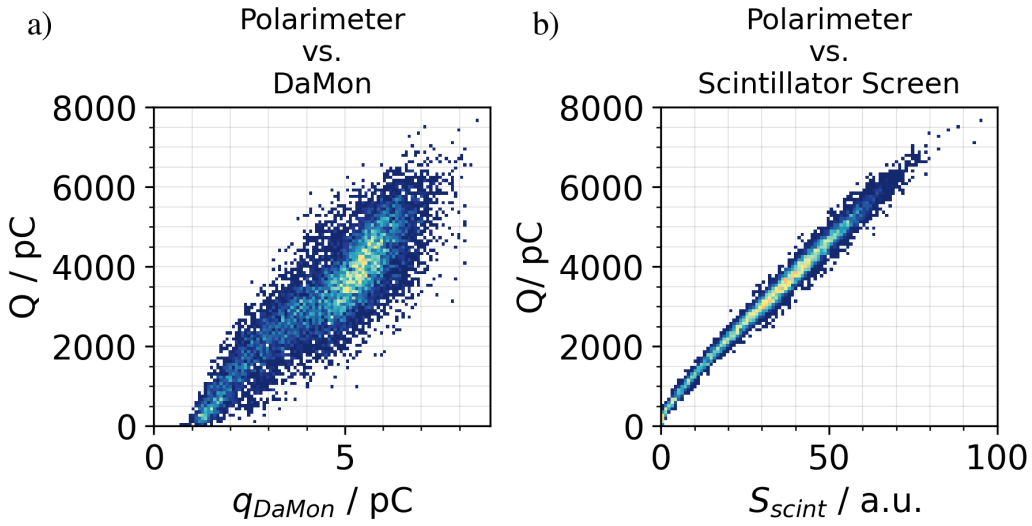

Figure 8.9.: Correlation of charge measurements by a) the DaMon and b) the scintillator screen setup with the QDC signal.

effects, see page 136 ff.). The absolute charge measurement using the DaMon can serve as an indicator of whether sufficient charge has been accelerated, but not as a measure of the charge incident on the solenoid. This is especially apparent when comparing the correlation between the DaMon and scintillator signals with the QDC signal in figure 8.9. It is clear that the correlation between Q and S_{scint} is significantly stronger than the correlation between Q and q_{DaMon}. The data points in the Q vs. S_{scint} plot demonstrate a distinct positive linear trend, while the Q vs. q_{DaMon} plot shows a more scattered distribution of data points, indicating a weaker relationship between these variables. Thus, it is preferable to use the scintillator screen signal for charge correction (see section 8.6.1).

8.4.2. Energy

Since both the bremsstrahlung conversion and the transmission of the photons through the iron core are energy-dependent (cf. chapter 3), and thus also the analysing strength and the asymmetry to be measured (cf. e.g. section 6.4), it is important to characterise the energy of the incoming electron beams precisely. In the following section, the electron spectra produced by the laser plasma accelerator will be examined first. Subsequently, the use of an active plasma lens in combination with a collimator as an

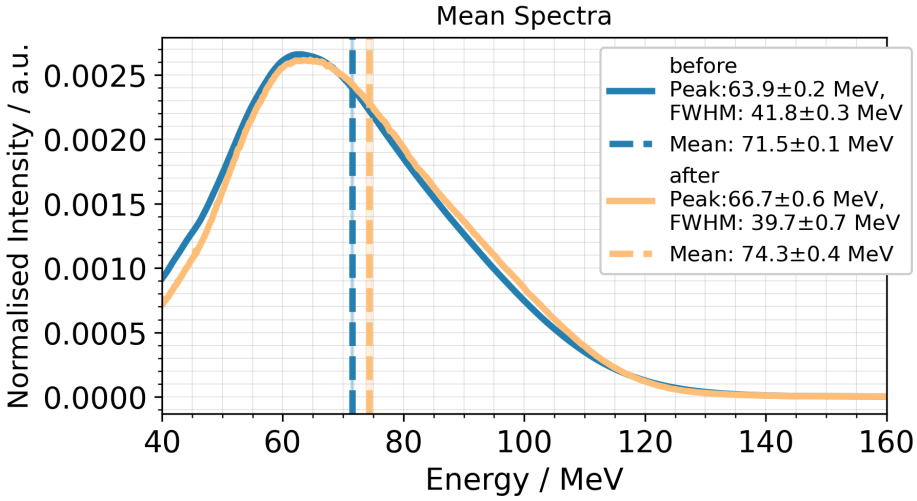

Figure 8.10.: Average energy spectra of accelerated electrons before and after the long data run.

energy filter will be evaluated.
A detailed energy study was carried out by Felix Stehr. The author of this work has used the spectra pre-analysed by him and analysis scripts written by him. For a more detailed consideration of energy diagnostics, in particular the use of the plasma lens as an energy filter, please refer to his work [52].

Electron Spectra from Laser Plasma Acceleration

Due to the destructive nature of the dipole spectrometer measurements, the exact spectra of the electrons that reached the polarimeter during the data run remain unknown. However, electron spectrometer measurements were performed immediately before and after each data run, providing a basis for assessment.
Figure 8.10 shows the average spectra of spectrometer runs 50377 (taken until 2.5 min before the long data run 50379) and 50383 (started 1.5 min after the long data run). The spectra were interpolated onto linear axes (cf. section 2.6.3) and normalised by dividing by the spectral intensity, defined as the sum of all counts. This normalisation was applied to focus on the spectral shape rather than the quantity of accelerated charge, which is the primary interest in this analysis. Average spectrum here means average intensity per pixel.
The comparison of pre- and post-data-run spectra reveals an increase in mean energy from 71.52 ± 0.14 MeV to 74.28 ± 0.44 MeV. Since the spectra are non-Gaussian, both the peak energy and full width at half maximum (FWHM) were analysed, following

standard practices in plasma acceleration research. The peak with the maximum prominence was selected, with a minimum prominence threshold of 100 and a minimum width of 10 to exclude noise and hot pixels. The spectrum before the data run exhibits a peak energy of 63.88 ± 0.23 MeV with a FWHM of 41.79 ± 0.33 MeV, while the post-data run spectrum peaks at 66.71 ± 11.2 MeV with a FWHM of 39.70 ± 0.75 MeV.
The standard deviation of the mean increased from 3.65 MeV before the run to 6.85 MeV after the run, indicating an increase in statistical fluctuations and suggesting a decreasing stability in the electron energy spectra during run 50379. However, this says nothing about shot-to-shot fluctuations, let alone about spectral differences between different measurement periods determined by the solenoid current.
To find out how the energy of the accelerated electrons behaves over a longer period of time, a spectrometer run of 33 min length has been conducted (run number 50281). At this point shot to shot changes and their mean are described. More on the interval analysis can be found in section 8.6.2.
An examination of the individual spectral images reveals several instances where electrons were either accelerated at very low energies or where the electron beam had poor alignment. If the electron beam enters the dipole magnetic field at an angle or off-center, it distorts the resulting spectral image. Therefore, in addition to the 3 pC DaMon cut (cf. section 8.4.1) a $2 \cdot 10^6$ a.u. spectral integral cut has been applied. This is visualised in the histogram of spectral integrals in figure 8.11a), where excluded data has been drawn in grey. From initially 3386 shots 347 were excluded.
Selected individual spectra (data of every hundredth shot) as well as the average spectrum is displayed in figure 8.11b). On average the spectra have a mean of 73.11 ± 0.06 MeV, a peak of 66.48 ± 0.10 MeV and a FWHM of 46.47 ± 0.12 MeV. It is evident that the shape of individual spectra deviates significantly from the mean in certain cases, which is important because the high-energy tails have a considerable influence. This is particularly relevant since the analysing power does not decrease linearly with electron energy.
The means and standard deviations of the electron energy spectra over time are represented in figure 8.11c), along with the average mean as an overlaid line. The data reveals fluctuations around the mean, with no discernible overall trend. An estimation of the spectra of the electrons reaching the polarimeter has yet to be provided.

APL and Collimator as Energy Filter

An active plasma lens (APL) has a focusing strength that depends on both the energy

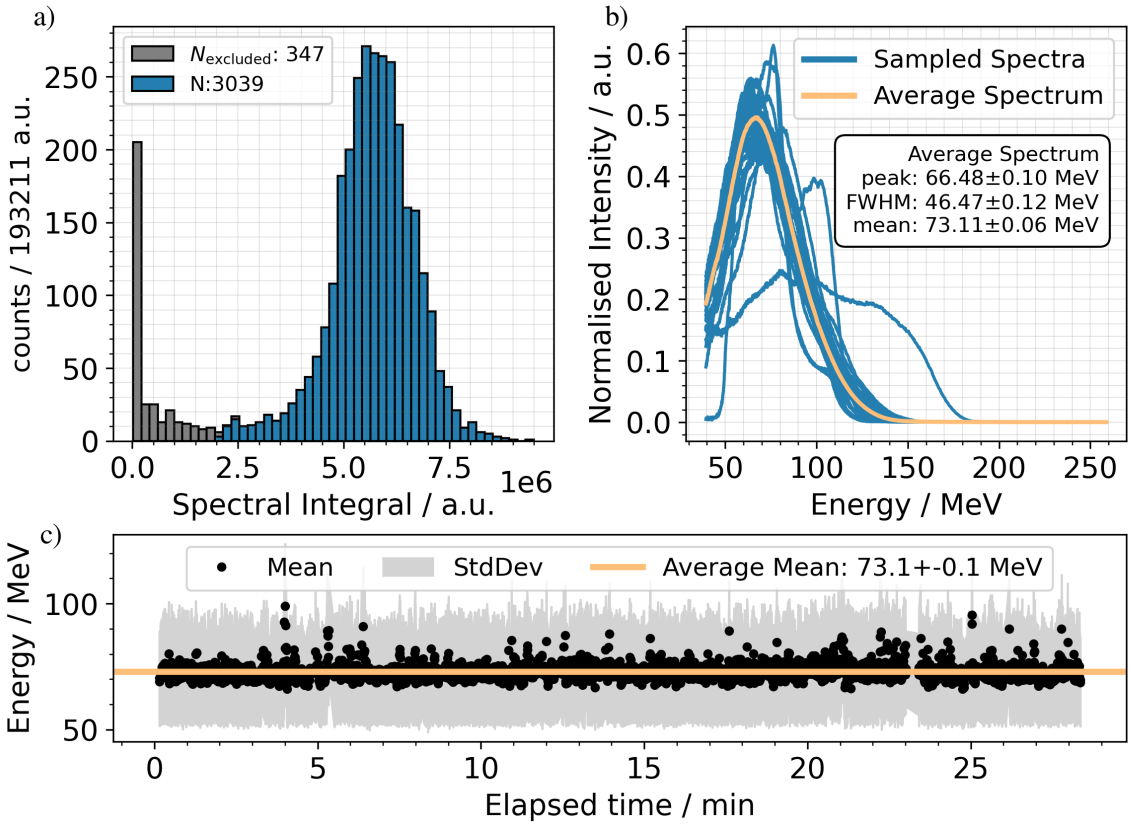

Figure 8.11.: a) Spectral integral during electron spectrometer measurement, run 50281. Events that are excluded because of an accelerated charge below 3 pC, or a spectral integral below $2 \cdot 10^6$ a.u., are greyed out. b) corresponding single energy spectra and average energy spectrum c) mean energy and standard deviation over time

of the incident charged particles and the discharge current set (see section 2.7). This implies that, for a given APL current, electrons of different energies will be focused to different points along the beamline or will exhibit varying beam sizes at the same location. Consequently, by adjusting the APL current, one can control which electrons pass through the collimator more effectively, allowing the APL-collimator combination to act as an energy filter.
The resulting electron spectra behind the collimator are expected to be both narrower and more stable, improving the quality of the beam for downstream polarisation measurement.
The process of calculating the transmitted electron spectra is divided into five points, which are summarised below. A more detailed description can be found in [52].

1. **Determining the current from the plasma lens voltage**: The plasma lens voltage is set during the experiment, while the discharge current, essential for calculating the focusing power, is measured by an inductive coil. The coil's signal is sent to an ADC for processing. By knowing the output of the coil and measuring the attenuation [52], the average current during a run can be calculated. Figure 8.12a) illustrates the average discharge current for different voltages. Notably, for the long data run 50379, the measured current was 423 ± 3 A for a set voltage of 20 kV.

2. **Focusing strength of the APL**: An electron spectrometer measurement taken with the APL switched on and the discharge current being scanned can determine the energy that is in focus at the spectrometer position. The intensity profile observed on the spectrometer screen resembles a butterfly, with the narrowest point indicating the energy that is focused.

3. **Beam propagation**: Knowing the initial parameters of an electron beam allows for analytical calculations to determine its behaviour along the beam axis. This analysis assumes an initial angular divergence characterised by the Twiss parameter α_0(describing the beam's focusing properties) of 0 and a normalised emittance of 1 µm. Using linear transport matrix calculations, the evolution of the beam's state is analysed, where the matrix elements for the drift depend solely on the drift length, while those for the plasma lens are influenced by lens length and focusing strength. To understand how the beam width changes along the path, beam envelope equations are utilised.

Table 8.1.: Set APL voltage and corresponding measured current and data of transmitted spectra. Note the significantly smaller statistical error compared to measurements without the APL, indicating improved stability and precision with the plasma lens in place.

Set U_{APL}	I_{APL} / A	Peak / MeV	FWHM / MeV	Mean / MeV
16	337 ± 3	68.31 ± 0.01	5.536 ± 0.003	72.46 ± 0.03
18	381 ± 3	77.15 ± 0.01	7.005 ± 0.004	78.91 ± 0.02
20	423 ± 3	84.544 ± 0.004	8.52 ± 0.01	84.17 ± 0.03
24	509 ± 4	94.680 ± 0.005	10.89 ± 0.03	90.55 ± 0.03

4. **Transfer probability through the collimator**: Once the beam width has been determined as a function of the energy of the individual electrons and the plasma lens current ($\sigma(E_{e^-}, I_{\mathrm{APl}})$) , it is possible to determine what proportion of the electron beam is transmitted through the collimator. Assuming a radially symmetric, Gaussian beam profile and a negligible divergence over the length of the collimator, the transmission probability, T, can be described as :

$$T(\sigma, r) = \frac{\int_{-\infty}^{\infty} f(x) \cdot \exp(-\frac{x^2}{2\sigma^2}) dx}{\int_{-\infty}^{\infty} \cdot \exp(-\frac{x^2}{2\sigma^2}) dx} \tag{8.1}$$

where $f(x)$ is defined as:

$$f(x) = \begin{cases} 1 & -r \leq x \leq r \\ 0 & \text{else} \end{cases} \tag{8.2}$$

5. **Transmitted spectra**: Finally, the transmitted spectra can be calculated by multiplying the intensity of the measured energy spectra by the transmission probability corresponding to each energy.

The result of this procedure are energy spectra that depend on the plasma lens current. The average spectrum from figure 8.11b, after applying the transmission functions corresponding to various set APL voltages, is shown in figure 8.12b and table 8.1. For the main run with a 20 kV setting, the spectrum peaks at 84.6 MeV with a full width at half maximum (FWHM) of 8.5 MeV. The transmission peak, determined by APL focusing, increases by nearly 20 MeV compared to values without the plasma lens. Additionally,

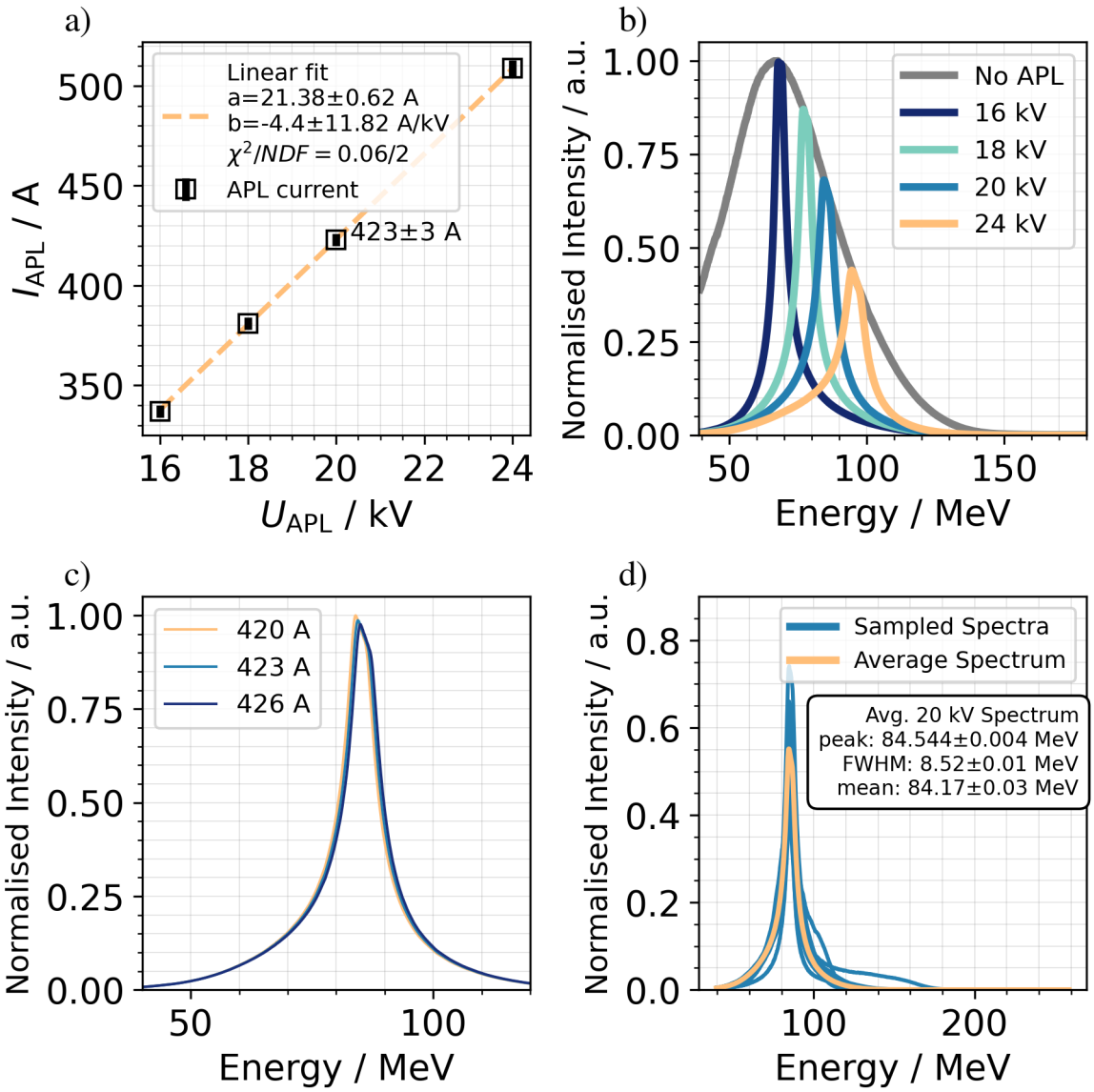

Figure 8.12.: a) Measured APL currents corresponding to set APL voltages b) Predicted spectra of beam passing through the collimator for different APL voltages. Grey envelope corresponds to average 20 kV spectrum from figure 8.11b. c) Effect of current fluctuations on 20 kV average spectrum. d) Sampled individual shots from run 50281 with 20 kV transmission function applied (same as in figure 8.11b), as well as average spectrum.

the FWHM is drastically reduced, making the average spectrum approximately 5.5 times narrower. The statistical error is an order of magnitude smaller, enhancing the reliability of these measurements.
The effects of fluctuations in the APL discharge current by ± 3 A are shown in figure 8.12c. The peak energy varies between 84.2 and 85.1 MeV, while the FWHM fluctuates between 8.5 and 8.6 MeV.
If the 20 kV transfer function is applied not only to the average spectrum from the electron spectrometer run 50281 but also to each individual recorded spectrum, it becomes evident that some isolated shots have spectra with different shapes, such as a pronounced long high-energy tail. This is visualised in figure 8.12d.
While these calculated spectra cannot fully reproduce the electron energy spectra from the long data run 50379, they provide a good indication of how the spectral shape evolves over time and of the impact of fluctuations in the plasma lens current.

8.4.3. Spot Size and Divergence

To be able to correctly simulate the experimental conditions for the determination of the analysing power (cf. section 8.8), it is also important to know how the electron beam propagates in space. Thus, in this section beam size and divergence will be determined with the help of the scintillation screen placed in front of the solenoid.
First, the conversion factor from pixel values to mm was calculated with the aid of mm-scales mounted on the top and to the side of the screen. This resulted in a conversion factor of approximately 0.039 mm/pixel.
The next step is to find out where the centre of the beam was within the region of interest, ROI. Since the camera is positioned at an angle to the scintillator screen in the x-z plane, the beam profile images are distorted in the x direction. Therefore, only y-line-profiles were used for the analysis. A Gaussian fit was applied to each y-line-profile for every x position in the ROI, and the x-pixel where the amplitude of the Gaussian fit was highest was identified. This process was repeated for a hundred different shots to obtain an average pixel position for the beam center. An example of this procedure is shown in figure 8.13. Figure 8.13a) shows the ROI of an image for a random shot during run 50379. The blue line marks the y-line-profile where a gaussian fit yields highest amplitude at pixel 55, which turned also out to be the average. In figure 8.13b) the corresponding line-profile with fit is displayed. It yielded a width of $\sigma_y = 0.720 \pm 0.004$ mm.

A Gaussian fit can now be applied to all y-line-profiles at the beam center position for all shots with $q_{\mathrm{DaMon}} > 3\,\mathrm{pC}$, allowing for a comparison of the results. It was found that for a meaningful comparison further data cuts have to be applied. Shots where charge is accelerated, but does not make it properly through the collimator, have to be excluded. Therefore only shots were considered where:

- the amplitude of the Gaussian fit applied to the central y-line-profile is above zero
- no value of the line-profile is greater than three times the mean amplitude
- the standard deviations of the fit result is positive and within three sigma of the mean standard deviation. A negative standard deviation can only result from fitting artefacts and suggests a failed fit.

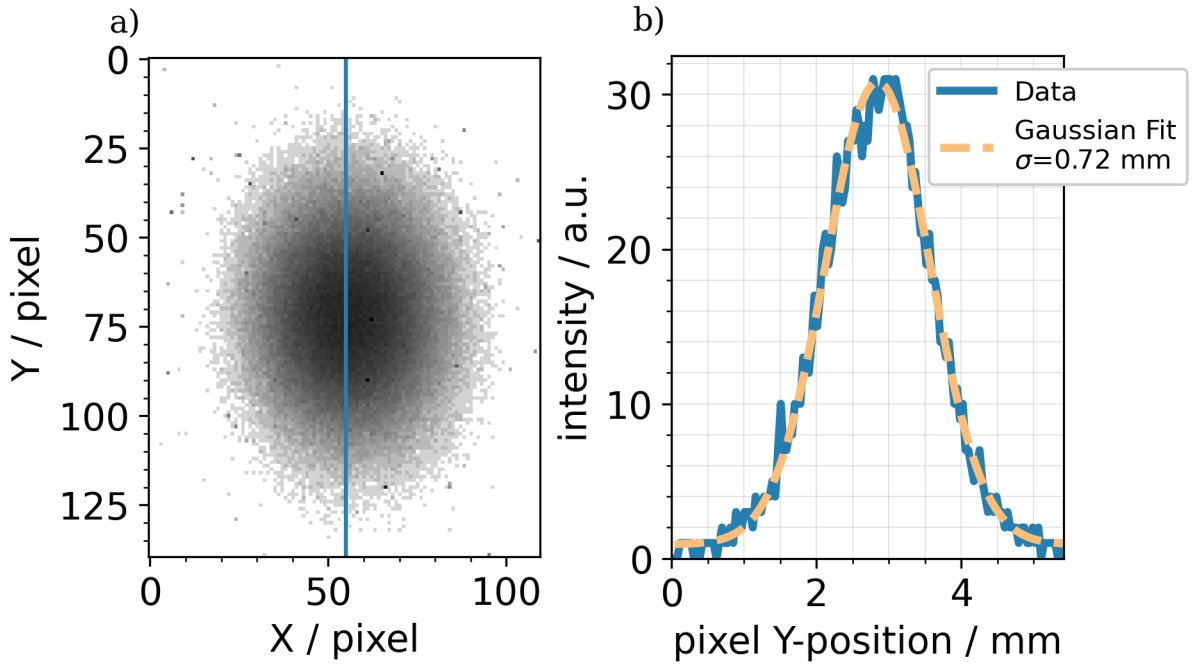

Figure 8.13.: a) ROI of the scintillator screen image. The blue line marks the y-line profile, corresponding to the vertical slice where the Gaussian fit yields the highest amplitude. b) Corresponding line-profile with Gaussian fit. Fit result: Amplitude: 29.9 ± 013 a.u., mean: 2.847 ± 0.003 mm, sigma: 0.720 ± 0.004 mm, offset: 0.91 ± 0.08 a.u.. The x-axis in b) represents the position in millimetres, obtained by converting pixel indices using a calibration factor of 0.039 mm/pixel.

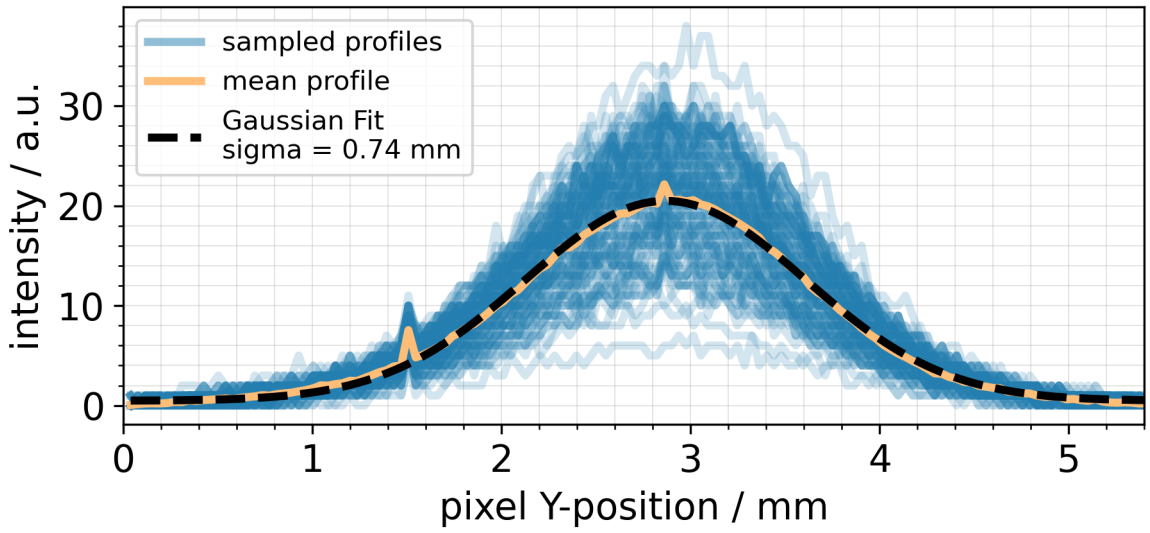

Figure 8.14.: Sample of line profiles at x-pixel 55 (every 100th shot shown) in blue. Mean profile in orange, Gaussian fit with dashed line. Spikes in the mean profile indicate damaged pixels.

- the offset of the fit result is within three sigma of the mean offset. Due to background subtraction this value should be zero, but due to minor intensity fluctuations between pixels this is not exactly true.

Figure 8.14 shows every 100th line profile, together with the mean profile and Gaussian fit applied to it. The result was a width of $\sigma_y = 0.74\,\text{mm}$.
The results of the individual shots are shown in figure 8.15. Figure 8.15a) shows how σ_y behaves over time and figure 8.15b) shows the distribution of the widths in a histogram. The mean width was found to be $\langle\sigma_y\rangle = 0.74 \pm 0.02\,\text{mm}$, which coincides with the result obtained from the Gaussian fit to the average spectrum. As the statistical error corresponds to the size of about half a pixel, it can be said that due to collimator and APL the fluctuations in beam size are rather small.
The comparison with other runs (cf. figure 8.16) shows a slight difference in spot size with APL voltage. The mean spot size for 20 kV is $0.74 \pm 0.01\,\text{mm}$, while for 16 kV it is $0.80 \pm 0.02\,\text{mm}$. For 18 kV and 24 kV, the measured spot sizes are $0.76 \pm 0.07\,\text{mm}$ and $0.77 \pm 0.05\,\text{mm}$, respectively. However, due to the shorter run times for these settings, the statistical uncertainties are significantly larger, making a precise comparison difficult. The divergence θ can then be calculated using the spot sizes at the collimator, $\sigma_{y,col} = 0.5\,\text{mm}$, and at the scintillator screen, $\sigma_{y,scint} = 0.74 \pm 0.02\,\text{mm}$, as well as the

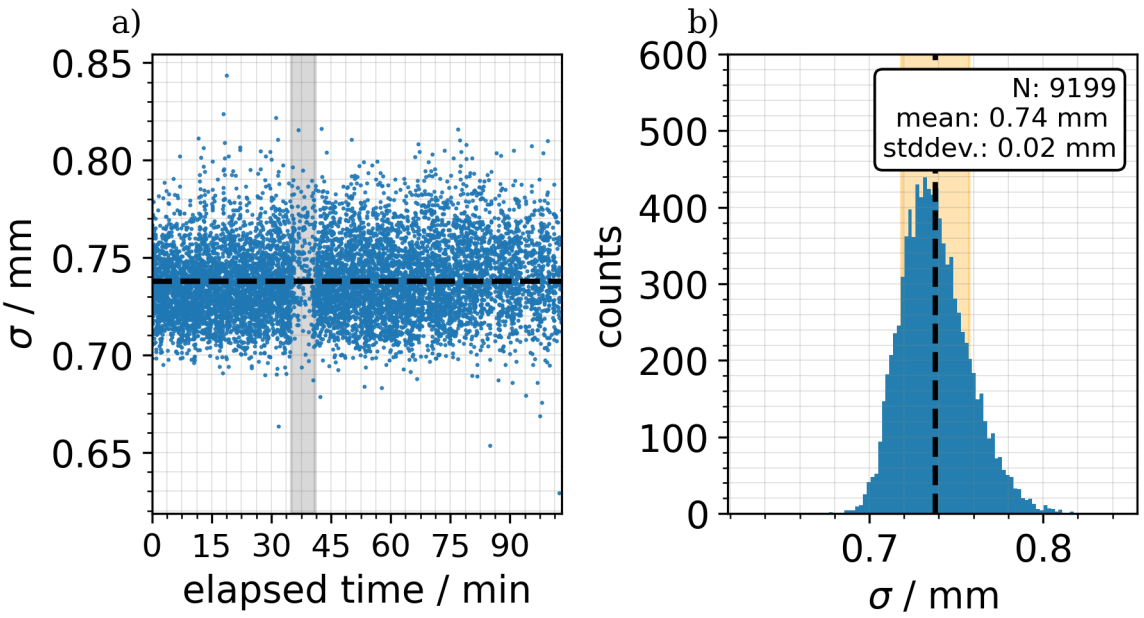

Figure 8.15.: a) Width resulting from Gaussian fits to beam profiles for every shot, greyed out area marks period of low laser energy b) Corresponding distribution of beam width

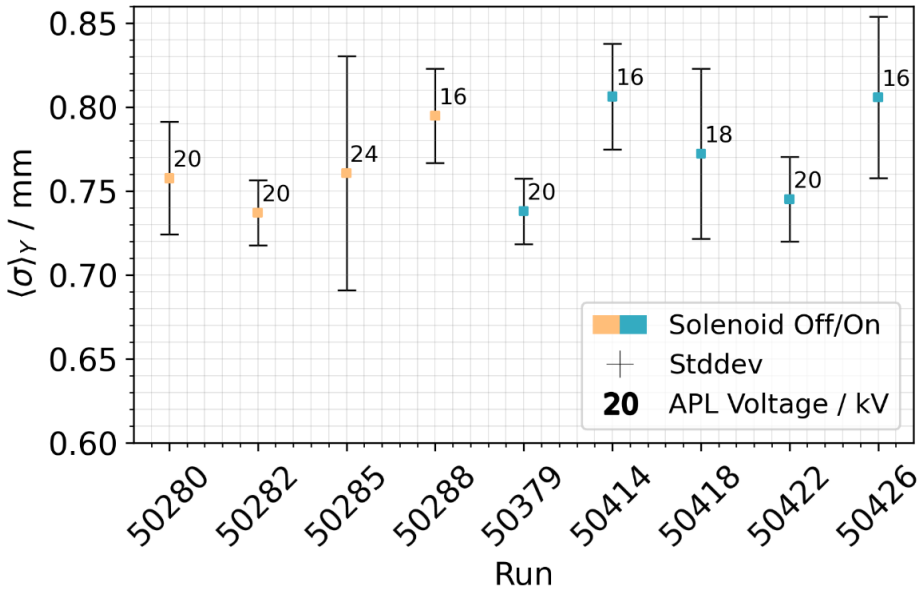

Figure 8.16.: Mean spot size for different runs

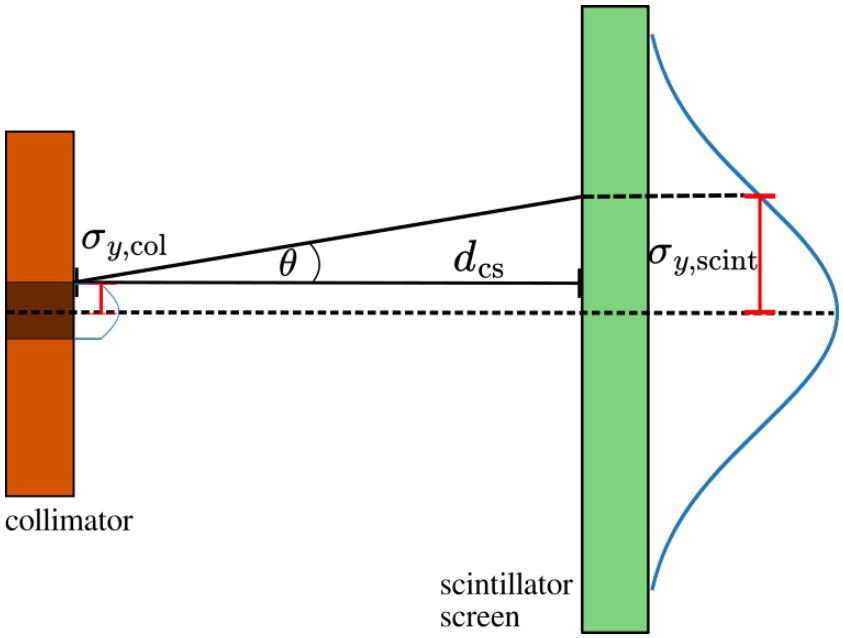

Figure 8.17.: Schematic representation of divergence calculation

distance between those points, $d_{cs} = 205 \pm 2\,\mathrm{mm}$. Their relation is given as

$$\theta = \arctan\left(\frac{\sigma_{y,scint} - \sigma_{y,col}}{d_{cs}}\right) \tag{8.3}$$

and the associated error is

$$\Delta\theta = \frac{1}{d_{cs} \cdot (b^2 + 1)} \cdot \sqrt{(\Delta\sigma_{y,scint})^2 + b^2(\Delta d_{cs})^2} \tag{8.4}$$

where b is $\frac{\sigma_{y,scint} - \sigma_{y,col}}{d_{cs}}$. A schematic is displayed in figure 8.17. Using the formulas above the resulting divergence for an APL voltage of 20 kV is then $\theta = 1.17 \pm 0.10\,\mathrm{mrad}$.

8.5. Expected Polarimeter Signal

Using the beam parameters determined in section 8.4, the calorimeter calibration performed by F. Stehr (cf. [52] and section 7.2.3) and LEAP_SIMS (cf. section 5), simulations were conducted to predict expected calorimeter readings, i.e. the expected polarimeter signal. The input parameters used for the simulation are presented in table 8.2. Note that polarisation of particles and materials was switched off and the magnetic field

Table 8.2.: Central values used to simulate the expected polarimeter signal

simulation parameter	value	simulation parameter	value
run type	single	divergence	0.067 °
core length	150 mm	calo. position in x/y	(0,0) mm
converter thickness	0 mm	distance to polarimeter	91 mm
energy	20 kV spectrum	polarimeter rotation	0 °
gun position	(0,0,-1) mm	$P_{e^-/Fe}$	0
spot size	0.74 mm	B_z	2.04 T

switched on to account for its effect on electron motion. 5×10^5 electrons were simulated per bunch. The detector geometry includes the solenoid and the calorimeter placed in air, as visualised in figure 5.6b). The particle gun was positioned 1 mm downstream of the front scintillator screen.

The simulation tracks the incident electrons and possibly resulting secondaries until they loose all their kinetic energy. To assess the effect of the solenoid core on the beam, the energy spectrum and spatial distribution of electrons reaching the calorimeter front are examined in figure 8.18.
Panel a) presents the energy spectrum, averaged over 3932 bunches. The spectrum exhibits the characteristic shape of bremsstrahlung radiation, with the number of detected particles decreasing as energy increases. A small plateau appears near the peak of the incident spectrum, followed by a gradual decline between 100 and 175 MeV. For an initial beam of 5×10^5 electrons, an average of 79×10^4 photons ultimately reach the calorimeter, corresponding to an average total energy of 520.03 ± 0.05 GeV.
Panel b) shows the corresponding energy-weighted beam profile. Approximately 40% of the incident signal is expected to be deposited in the central glass block, which has an area of 38×38 mm. The spatial distribution has a FWHM of about 19 mm.
To estimate the expected calorimeter signal, the energy deposited by charged particles above the Cherenkov threshold in lead, denoted as E_{ct} (cf. section 5.2.2), is first considered. Figure 8.19a) shows the distribution of E_{ct}, summed over all nine glass blocks per simulated bunch. The distribution has a mean of 363.5 GeV, a standard deviation of 2.4 GeV and hence a relative with of 0.7%.
The simulation assumes a fixed number of electrons per bunch. To emulate shot-

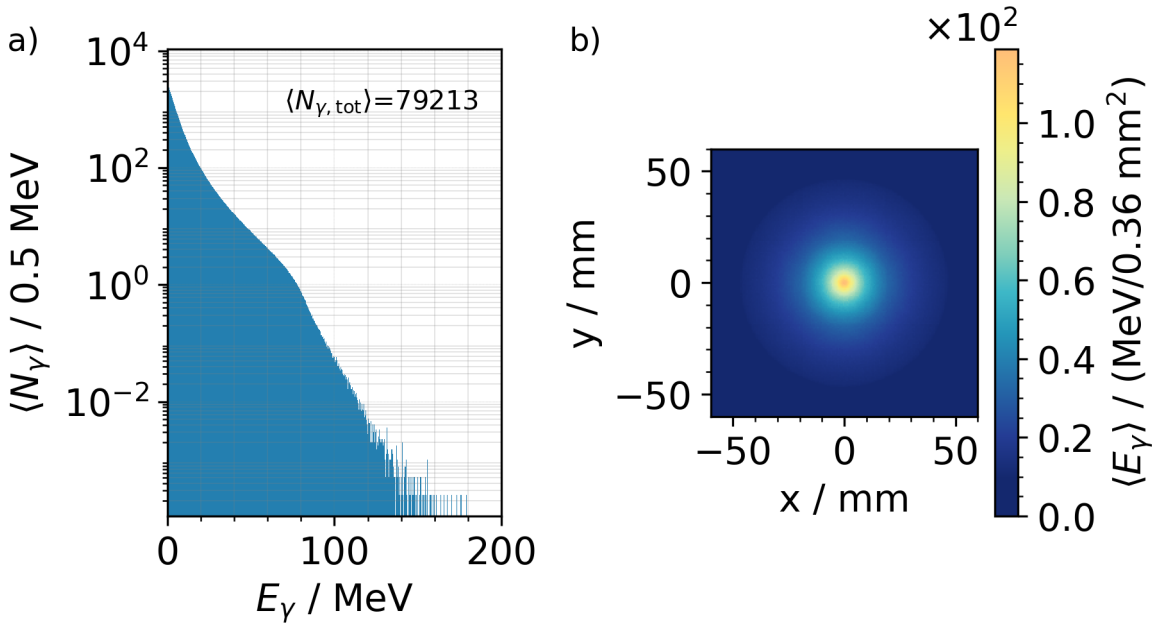

Figure 8.18.: a) Simulated energy spectrum of particles incident on the calorimeter front, averaged over 3932 bunches. 5×10^5 electrons per bunch were sent into the solenoid. Parameter overview in table table 8.2. b) Corresponding energy weighted beam profile.

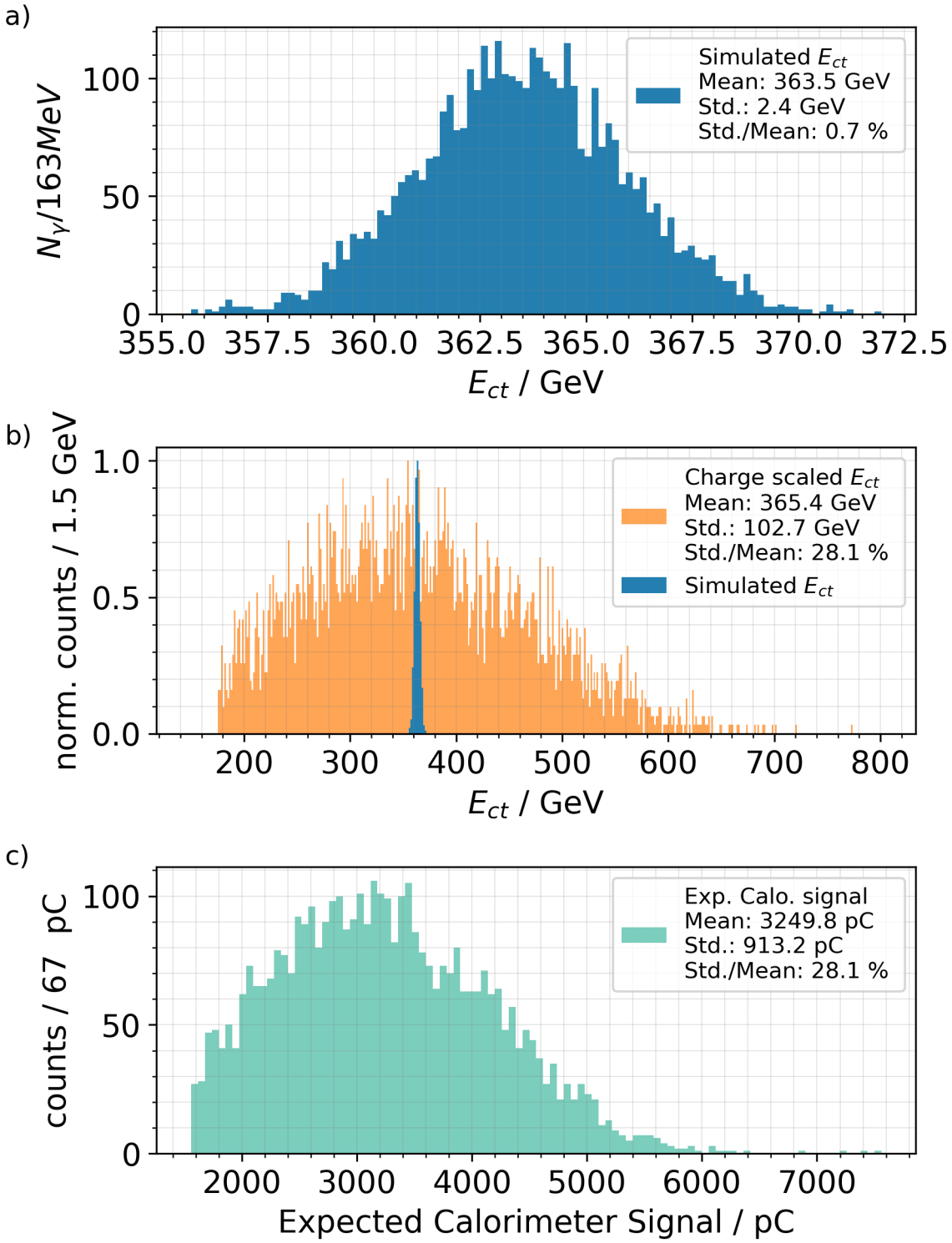

Figure 8.19.: a) Distribution of deposited energy of charged particles above the Cherenkov threshold in all lead glass blocks. b) Width of signal scaled with scintillator screen charge measurement c) Expected calorimeter signal converted using function derived from test-beam calibration

to-shot fluctuations of the beam charge, the individual histogram entries are scaled by a randomly sampled factor from the measured $S_{\text{scint}}/\langle S_{\text{scint}}\rangle$ distribution, which provides a relative measure of the incident charge on the solenoid core during the measurement (cf. section 8.4.1). The comparison is depicted in figure 8.19b). With this fluctuation model applied, the mean of the distribution shifts to 366 GeV with a standard deviation of 103 GeV, resulting in a relative width of 28.2%.
Finally, the expected calorimeter signal is computed using the calibration function derived from the calorimeter test beam (cf. section 7.2.3 and [52]), which converts E_{ct} into fully digitized calorimeter values in pC. Applying this function results in a distribution with a mean of 3256 pC, a standard deviation of 920 pC and a relative width of 28.2 %.
The simulated number of 5×10^5 electrons corresponds to a charge of approximately 0.08 pC. The mean value of the expected calorimeter signal must still be scaled according to the actual number of particles that pass through the collimator. However, since the scintillation screen is not calibrated, absolute values cannot be determined.
Assuming that 1% of the average 5.16 pC passes through the collimator, the expected calorimeter signal has a mean of approximately 2100 pC with a standard deviation of about 600 pC. For 2% transmission, the mean increases to 4200 pC with a standard deviation of 1200 pC, while for 5% transmission, a mean of 10500 pC with a standard deviation of 3000 pC is expected. A comparison of these expected values with the measured calorimeter signal is presented in section 8.6.1.

8.6. Interval Analysis

From the beam parameter analysis in section 8.4, it became evident that beam parameters can fluctuate significantly from shot to shot, and that overarching trends, such as a decrease in average charge over the course of a run, may arise. If these changes do not occur symmetrically across both solenoid current directions, they can introduce false asymmetries δ_{fake}.
The aim of the analysis in this section is to investigate whether any δ_{fake} have influenced the zero-polarisation measurement and to assess their magnitude.
Charge variations can be corrected using the scintillator data, up to the accuracy of the charge measurement (see section 8.6.1). However, shot-to-shot energy information was unavailable during the polarimeter run. Thus, key remaining questions include: How does the energy of the accelerated electrons evolve over the 5-minute intervals in

which the solenoid is operated (see section 8.6.2)? Furthermore, are there additional changes linked to the solenoid current direction that we must account for (see section 8.6.3)? Finally, how should the results of this section inform the further analysis leading to the determination of electron beam polarisation (see section 8.6.4)?

8.6.1. Charge Corrections

From the analysis of the beam parameters in section 8.4.1, it is evident that there are considerable shot-to-shot charge fluctuations and a decrease in accelerated charge over time. What happens when the charge is examined within 5-minute intervals of the solenoid current? Are the changes in charge unequal across solenoid current directions, potentially leading to false asymmetries?
The scintillator screen setup provides a measure of the charge reaching the polarimeter. Figure 8.20a) shows the time-averaged values for individual intervals $\langle S_{scint} \rangle$, where fluctuations between 32.0 ± 0.5 a.u. and 49.8 ± 0.5 a.u. are observed. A general decrease in these values is also evident over time. If the mean charge is calculated separately for positive solenoid current, $\langle S_{scint} \rangle^{+} = 41.6 \pm 0.2$ MeV, and negative solenoid current, $\langle S_{scint} \rangle^{-} = 41.2 \pm 0.2$ MeV, and the asymmetry is determined, a false asymmetry $\delta_{\text{scint,false}}$ of 0.4 ± 0.3 % arises.
$\delta_{\text{scint,false}}$ may not be significantly different from zero at the 2σ-level, but still poses a huge problem for the measurement of asymmetries caused by polarisation δ_{pol}. With the expected δ_{pol} on the permille level, an uncertainty of $\pm 0.3\%$ would completely dominate the measurement. Furthermore, it remains unclear whether this effect arises solely from statistical charge fluctuations or if systematic measurement effects contribute, which would not be mitigated by increasing the data sample.
However, because the charge can be measured on a shot-to-shot basis during data runs with the scintillator screen, it is possible to normalise the polarimeter signal with respect to the charge, effectively addressing any charge-induced false asymmetries, up to the resolution of the screen.
For relative charge correction, it is sufficient to divide Q by S_{scint}. However, to maintain consistency in charge units - particularly when comparing simulated and measured data - it is necessary to scale Q by the ratio of the scintillator screen signal, averaged over the run, to the current signal. This accounts for fluctuations around the mean.

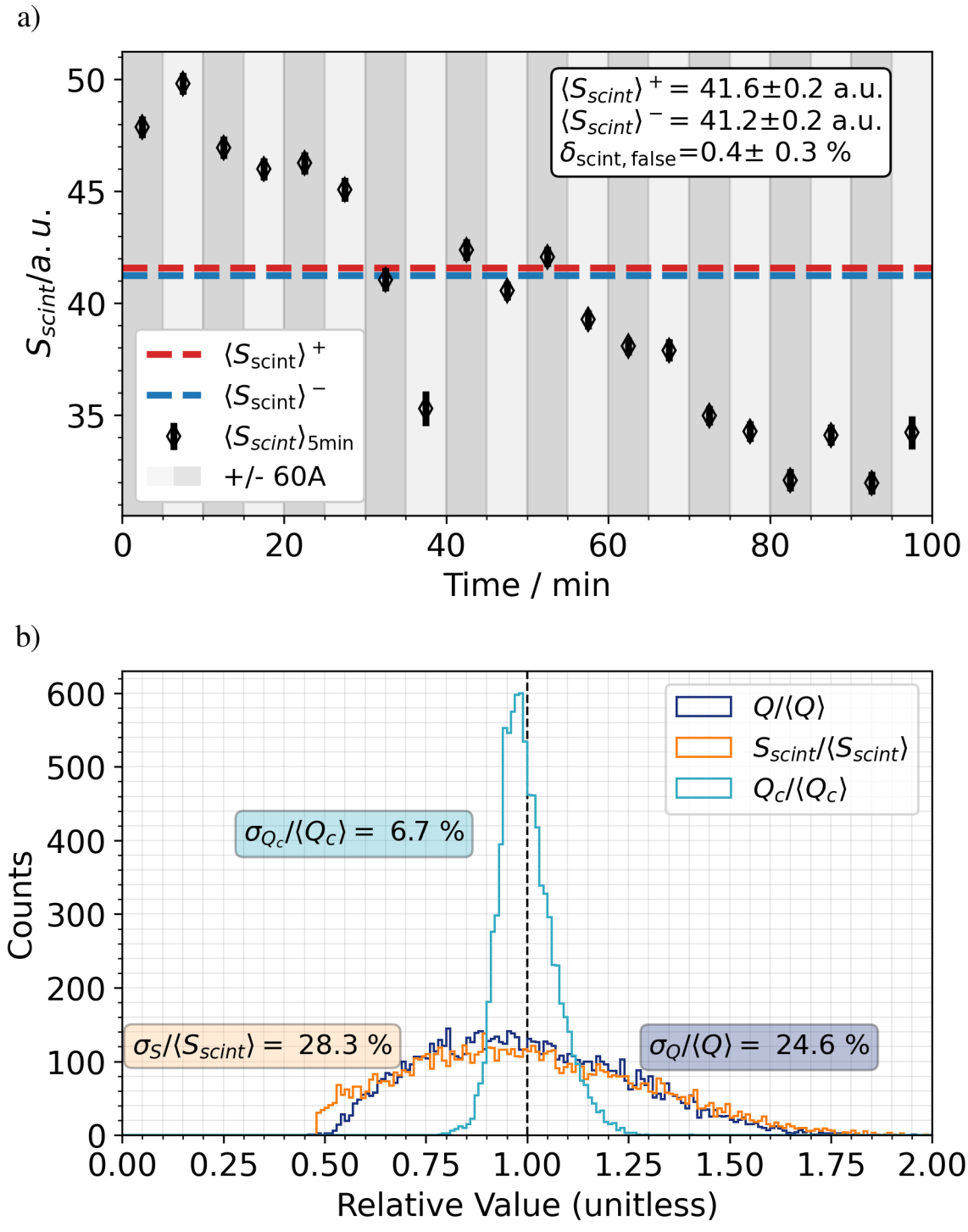

Figure 8.20.: a) Scintillator screen signal S_{scint} averaged over the solenoid current periods. Mean over positive and negative currents lead to a false asymmetry of $\delta_{\text{scint,false}} = 0.4 \pm 0.3\%$. For clarity, the y-axis has been truncated, highlighting the variation and associated error bars. b) Histograms of relative values of scintillator screen signal S_{scint}, polarimeter signal Q and the corrected polarimeter signal Q_c. N = 8683, bin width = 0.01.

The corrected QDC signal Q_c can be expressed as:

$$Q_c = \frac{Q}{S_{scint}/\langle S_{scint}\rangle} \tag{8.5}$$

If this correction is applied, the relative width of the polarimeter signal is significantly reduced. Figure 8.20b) displays histograms of unitless relative values for the polarimeter/QDC signal Q, the scintillator screen charge measurement S_{scint}, and the corrected polarimeter signal Q_c. The initial relative widths are $\sigma_S/\langle S_{scint}\rangle = 28.3\%$ and $\sigma_Q/\langle Q\rangle$=24.6%, while the correction reduces $\sigma_{Q_c}/\langle Q_c\rangle$ to 6.7 %. As a result, the relative width has been nearly quartered. It should be noted that for this analysis, in comparison to the previous sections, not only the DaMon cut at 3 pC was set, but also a scintillator cut at 20 a.u.. The reason for this is the non-proportionality between Q and S_{scint} below that value, as visible in figure 8.4c) and d).
Before determining the measured asymmetry δ_m with Q_c (c.f. section 8.7), it is important to understand the effect of the correction on the polarimeter signal. What uncertainties are associated with this correction? To do this, it is necessary to take a closer look at the individual components:

The scintillator signal is exclusively a function of the charge, meaning its value is directly related to the amount of charge interacting with the scintillator material (cf. section 2.6.2). The width of the distribution $S_{scint}(q)$ is influenced by both the true charge distribution q and the response function of the scintillator screen setup.

The polarimeter signal is a function not only of the charge of the accelerated electron beam but also of its energy. The sums of energies from the electrons transmitted through the solenoid and detected by the calorimeter are central to this measurement. Additionally, the detector response of the polarimeter is energy-dependent.

If the charge correction is carried out and its influence is eliminated, the residual width of the corrected signal σ_{Q_c} still depends on:

- the width of the energy distribution due to fluctuations in electron energy σE_{e^-}
- the response function of the polarimeter, i.e. the combination of solenoid and calorimeter
- the uncertainty of the scintillator screen charge measurement ΔS_{scint}

Having established the necessity of a correction and identified the components that continue to contribute to the width of the corrected signal, the next step is to estimate

the magnitude of these contributions. One method that can be used for this is the comparison between simulation (cf. section 8.5) and measurement.
A good impression of the response function of the polarimeter can be gained by applying the E_{ct}-to-Q-transfer function, described on page 116, to the simulation results shown in figure 8.19. This represents the response to an electron beam with no charge variation, using the 20 kV energy spectrum. A comparison with Q_c is presented in figure 8.21. The relative width of the simulated detector response, 0.74 %, is found to be significantly narrower than the 6.68 % residual width of Q_c, particularly when uncertainties are combined quadratically. This suggests that neither the resolution of the calorimeter nor the physical processes within the solenoid are the dominant contributors to the residual width.
Additionally, in [52], a comparison between the measured polarimeter signal and the scintillator screen signal revealed that $\sigma_S/\langle S_{scint}\rangle$ is not only larger than $\sigma_Q/\langle Q\rangle$ on average (as shown in figure 8.20), but that this is consistently the case across all intervals. Since S_{scint} depends solely on the charge, while Q depends on both charge and energy, the opposite trend would be expected. This suggests that the accuracy of the charge measurement plays a significant role in the residual width of Q_c, having a much greater influence than fluctuations in E_{e^-}.
If it is assumed that the detector response of the polarimeter and the fluctuations in the energy of the electrons play a minor role, then the following applies:

$$\frac{\Delta S_{scint}}{\langle S_{scint}\rangle} \approx \sqrt{\left(\frac{\sigma_{S_{scint}}}{\langle S_{scint}\rangle}\right)^2 - \left(\frac{\sigma_Q}{\langle Q\rangle}\right)^2} \approx 14\% \tag{8.6}$$

where ΔS_{scint} corresponds to the measurement error of the scintillator screen, while $\sigma_{S_{scint}}$ denotes the width of the charge distribution obtained from the scintillator screen measurement. Given the assumptions made, this value should be approximately equal to the relative width of the corrected polarimeter signal, $\sigma_{Q_c}/\langle Q_c\rangle = 6.7\,\%$, but it is more than twice as high. One possible explanation for this discrepancy is an anti-correlation between beam charge and energy fluctuations. This warrants further investigation, particularly since Simon Bohlen et al. observed a positive correlation in a previous study conducted with the same accelerator and a similar setup [51]. Nonetheless, given the limited statistical precision, the values are sufficiently comparable to suggest that the charge correction's effectiveness is strongly influenced by the accuracy of the charge measurement taken immediately before the solenoid. Finally, a sanity check can be performed by comparing the measured Q with the simulated, expected results from figure 8.19c). This comparison is shown

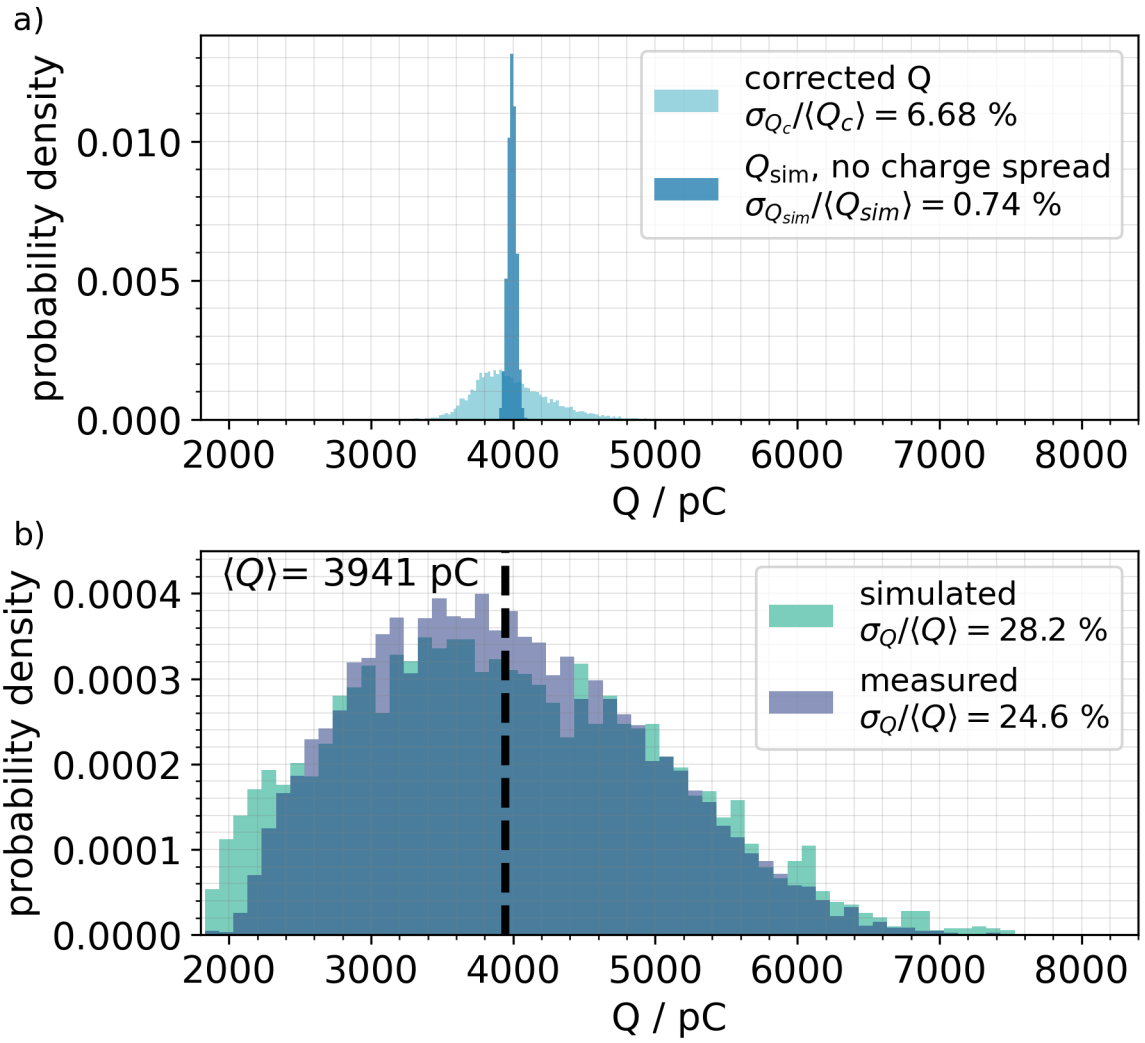

Figure 8.21.: Comparison between LEAP_SIMS simulations and measurement results: a) Simulation result without charge scaling translated to QDC signal (cf. section 8.5) compared to corrected charge signal, Q_c. b) Simulated estimate and measured result of Q_c.

in figure 8.21b). The measured distribution has a mean value of $\langle Q \rangle = 3941\,\text{pC}$ and a standard deviation of 970 pC. Scaling the central value of the simulation to this measurement, the translation factor suggests that a total of 0.096 pC, i.e. approximately 2 % of the incident charge, passes through the collimator. The relative width of the simulated signal, at 28.2 %, is broader than the measured width of 24.6 %. This again confirms that signal broadening due to interaction processes in the solenoid is negligible compared to fluctuations in the incident charge. Furthermore, this comparison yields no discernible difference from the comparison between S_{scint} and Q in figure 8.20b).

8.6.2. Energy Variation During Intervals

To estimate the behaviour of the energy of accelerated electron beams over an extended period, the spectrometer data from run 50281, with an APL voltage of 20 kV, was divided into artificial time intervals mimicking the 5-minute intervals used in solenoid current reversal during the polarimeter runs. The electron energy spectra were then averaged for each time interval.
The mean energy of the electrons that would have been transmitted through the collimator in the absence of deflection by the spectrometers magnetic field is estimated by applying a calculated transfer function (cf. section 8.4.2) to the measured energy distribution. This yields a value of $\langle E_{trans} \rangle = 84.17 \pm 0.03\,\text{MeV}$. Figure 8.22a) presents a direct comparison between the mean energy spectrum of the accelerated electrons and that of the transmitted electrons. The mean energy of the accelerated electrons is measured to be $\langle E_{acc} \rangle = 73.11 \pm 0.06\,\text{MeV}$. The deviations from these mean values over 5-minute time intervals are illustrated in figure 8.22b).
It can be observed that the interval values exhibit significant fluctuations. The mean energies of the accelerated electron spectra vary between $72.84 \pm 0.18\,\text{MeV}$ and $73.81 \pm 0.16\,\text{MeV}$, while the mean energies of the transmitted electron spectra range between $84.05 \pm 0.06\,\text{MeV}$ and $84.39 \pm 0.06\,\text{MeV}$.
The maximum difference in the mean transmitted spectra amounts to $0.34 \pm 0.08\,\text{MeV}$.
To estimate the impact on false asymmetries, dedicated simulations are required. By performing simulations similar to those described in section 8.5, but replacing the fixed spectrum with the measured spectra corresponding to intervals 4 and 5 from figure 8.22, and assuming a constant charge of 0.096 pC (cf. section 8.6.1), the resulting

signals are processed through the E_{ct}-to-Q transfer function. The simulated mean Q-values are found to be 3907 pC and 3939 pC, both with a standard deviation of 29 pC. This **would have led to false asymmetries of $\delta_{E,false} \approx -0.403 \pm 0.008$ %** during the polarimeter data runs.

It should be noted that the uncertainty quoted for the false asymmetry reflects only the Monte Carlo statistical error and does not account for additional uncertainties in the energy analysis. The application of the APL transfer function introduces further assumptions, as the beam energy cannot be measured simultaneously with the energy deposited in the calorimeter. Nevertheless, the order of magnitude of the result appears reasonable and is comparable to the false asymmetry observed due to charge fluctuations (cf. section 8.6.1). This strongly suggests that energy fluctuations also have a significant impact on the zero polarisation measurement and must be considered in its interpretation.

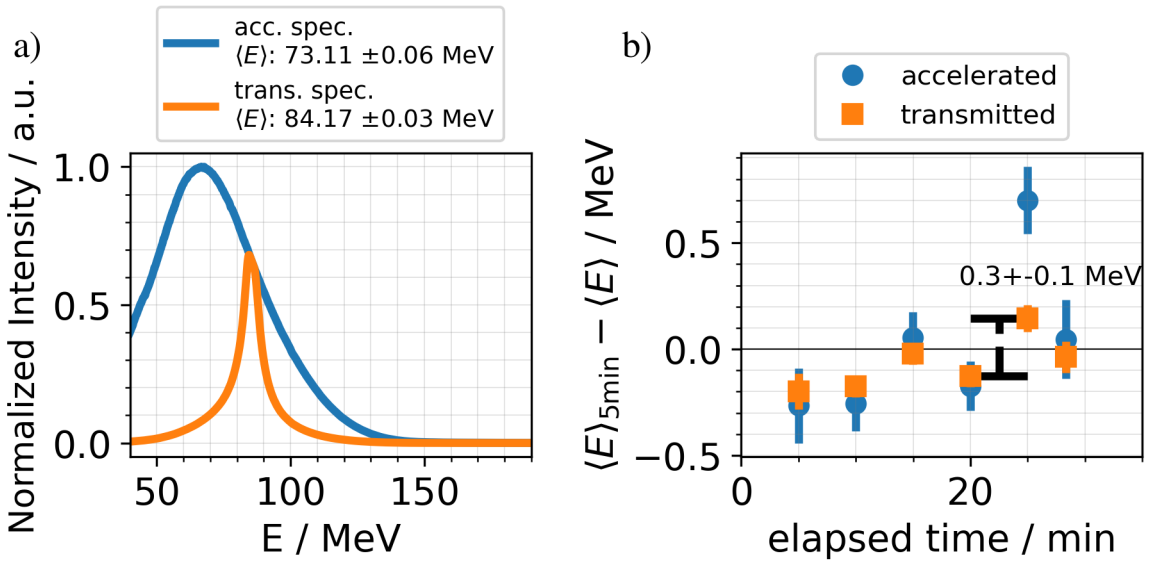

Figure 8.22.: a) Average spectra of accelerated electrons and estimated spectra of electrons that would have been transmitted through the collimator during run 50281. b) Mean energy of the average spectra during 5 min intervals minus the respective run-mean displayed in a).

8.6.3. Signal Distribution Across Calorimeter Channels During Solenoid Current Reversal

An analysis of the distribution of Q across the individual calorimeter channels revealed that it varies with changes in the solenoid current polarity. This is illustrated in figure 8.23a), which shows the normalised interval mean of individual channels relative to the mean of the total signal from all channels, for various solenoid current intervals recorded during extended data run 50379. Several key observations can be drawn from the plot:

1. The mean interval values vary systematically with the solenoid current. Under negative solenoid current, the signal in the top-centre channel (Channel 1) increases, while the signal in the bottom-centre channel (Channel 7) decreases. The signals in the centre-left (Channel 3) and centre-right (Channel 5) channels remain approximately equal, within error margins. Under positive solenoid current, the values for Channels 1 and 7 are closer to each other, while those for Channels 3 and 5 show a greater divergence.

2. Absolute variations in response to different solenoid currents are on the order of 1% for Channels 1 and 7, and around 0.2 % for Channels 3 and 5.

3. The signals from Channels 1, 3, and 5 oscillate around a mean value of approximately 12%, whereas Channel 7 oscillates around a mean of approximately 10.8 %.

To verify that these patterns were not coincidental, additional runs were analysed, as shown in figure 8.23b). Runs conducted with the solenoid deactivated (zero current) were also examined. Here, the data was averaged over 5-minute periods based on the number of shots. Additional observations include:

4. With the solenoid off, the individual channel values show no oscillatory behaviour.

5. The mean values of Channels 1 and 7 with the solenoid off (1: 11.91 ± 0.06 %, 7: 10.90 ± 0.05 %) closely match the mean values across all intervals with the solenoid on (1: 12.00 ± 0.07 %, 7: 10.74 ± 0.06 %).

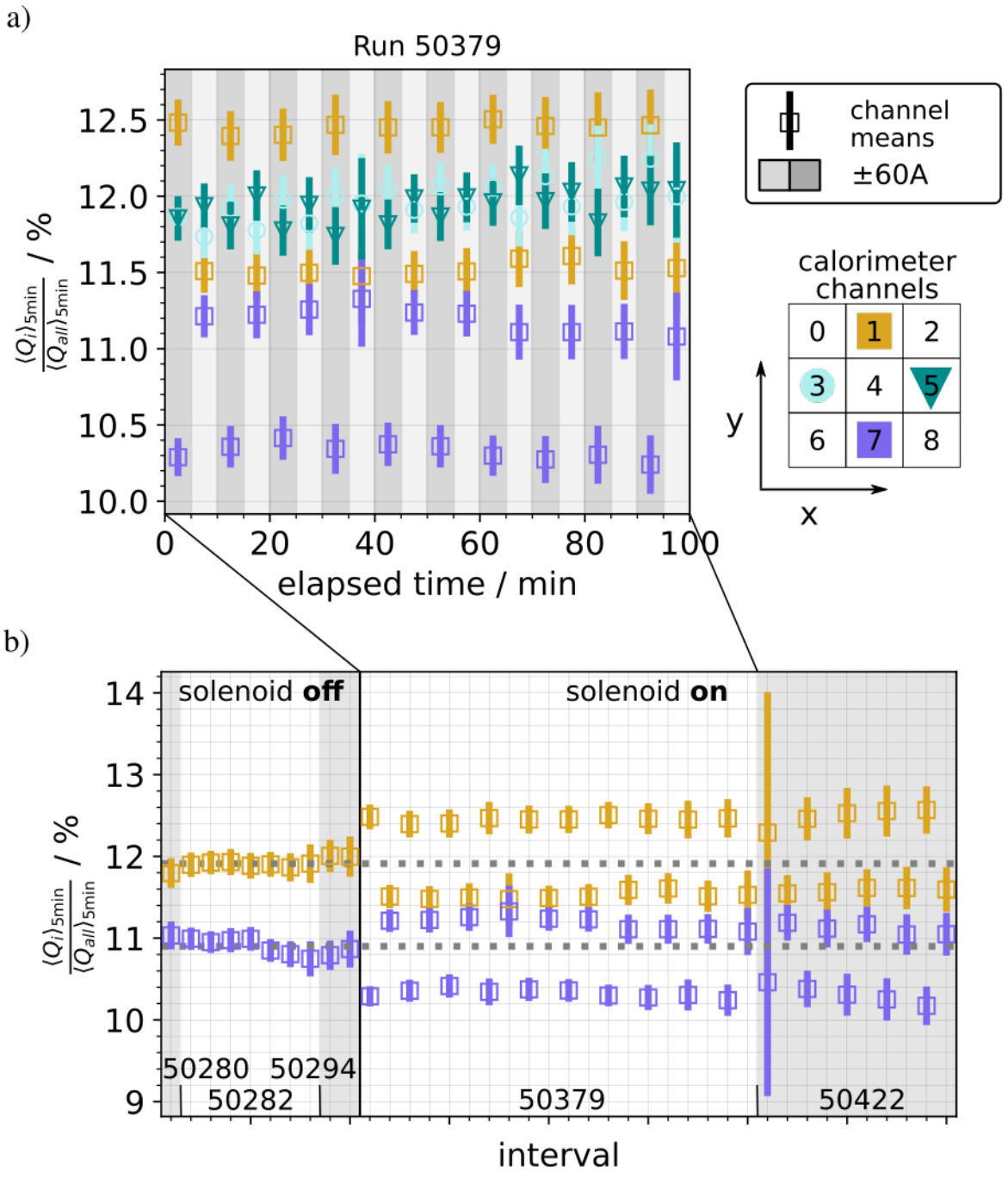

Figure 8.23.: Interval means of calorimeter channels normalised by total sum. a) Centre-top, bottom, left and right glass blocks for the different intervals of run 50379, different background colours illustrate solenoid current. b) Centre-top and bottom calorimeter channels for different runs with solenoid off and on. Different background colour emphasises different runs. Dotted lines illustrate the means of solenoid off runs: Channel 1: 11.9 %, Channel 7: 10.9 %. For clarity, the y-axes have been truncated, highlighting the variation and associated error bars. The first interval during run 50422 contains a low number of shots, this is considered when calculating the weighted average.

6. The differences between runs are comparable to the fluctuations observed within individual runs, provided that only intervals with the same solenoid current setting are compared.

These findings suggest that the changes in the polarimeter signal amplitude distribution across individual channels are indeed influenced by the solenoid current reversal, and thus may introduce variations unrelated to the polarisation of the incident electron beam.
There are two main reasons why this effect could occur. First, stray magnetic fields might be influencing the photomultiplier tubes (PMTs). Second, the magnetic field may be affecting the trajectory of electrons incident on the solenoid core in an unexpected way. If the first scenario were true, the magnetic field near the PMTs would be strong enough to alter the path of photo-electrons within the PMT. This alteration would depend on the PMT's orientation relative to the magnetic field, potentially changing the proportion of photo-electrons that reach the first dynode [157]. However, the PMTs were installed without specific attention to dynode orientation relative to the magnetic field. This would mean that any pattern in signal variation caused by the magnetic field's effect on the dynode orientation would be coincidental rather than consistent. Given that the rear end of the calorimeter is over 50 cm from the solenoid and that the PMTs are shielded, the second explanation seems more likely.
To investigate whether a rotational misalignment of the solenoid might be contributing to the observed effects - potentially introducing transverse magnetic field components that alter the trajectory of incident electrons - simulations were conducted. The solenoid magnet was aligned within the experimental area using a laser diode to mark the beam path. Although the exact rotation of the solenoid is unknown, it is assumed to be small. A 5-degree rotation, which would be visually noticeable, was simulated to determine whether even a minor rotation could yield effects with comparable behaviour and magnitude to those observed experimentally. Figure 8.24 presents results for a) a rotation around the x-axis and b) a rotation around the y-axis. The simulation parameters were set according to the values in table 8.3, with the exception that polarisation was set to zero and the solenoid field alternated between ± 2.04 T.
The simulation shows that a 5 °-rotation around the x-axis produces significant differences between the top and bottom glass blocks, with channel 1 receiving over 4 % more of the signal than channel 7. This result supports the conclusion that the observed effect described in Observation 2 (specifically, the difference in signal between Channels 1 and 7) may be due to a slight misalignment, either from the calorimeter being positioned too low, a slight tilt in the solenoid, or a combination of both. However, it

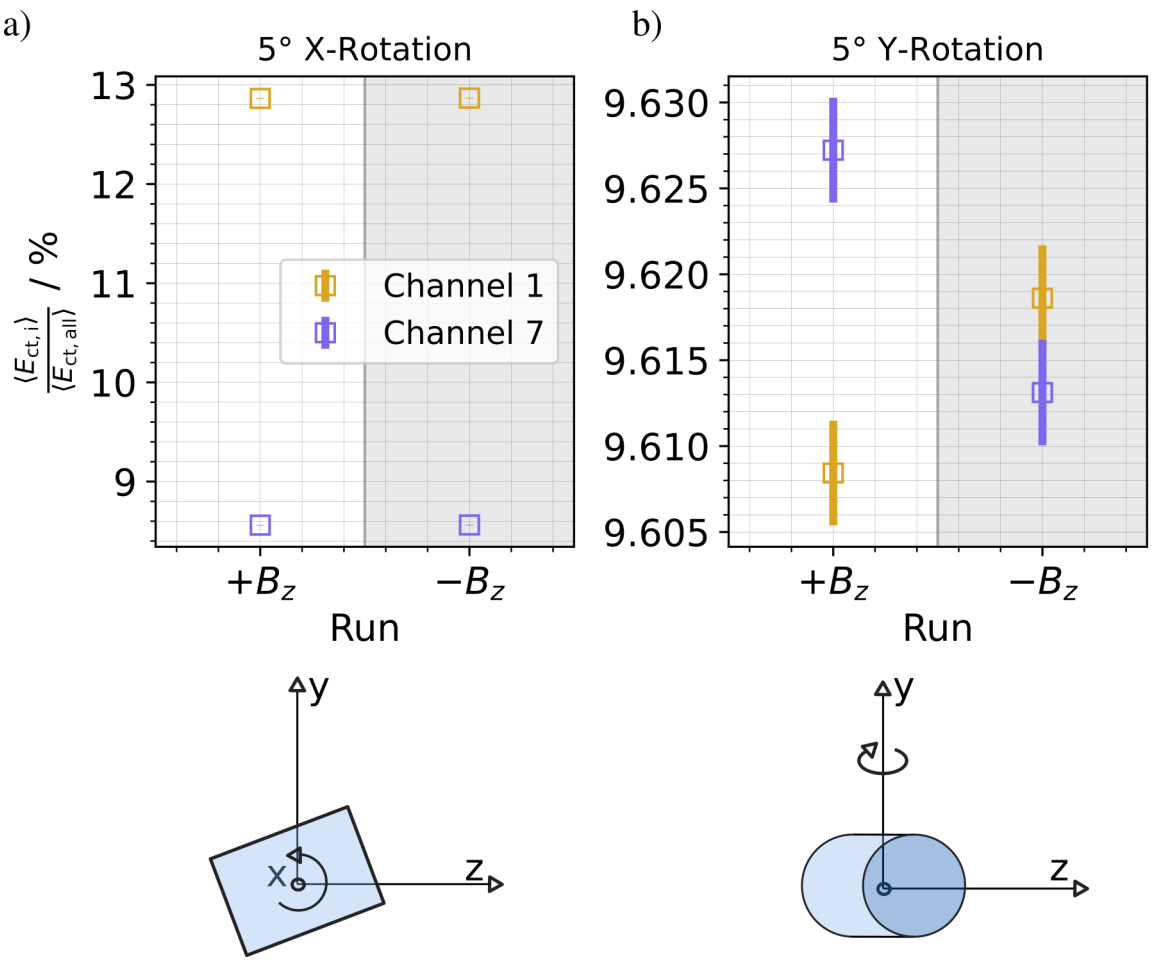

Figure 8.24.: Mean energy deposited by particles above the Cherenkov threshold for individual calorimeter glass blocks $\langle E_{ct,i}\rangle$ normalised by the mean sum of all. Same settings as in table 8.3 with the exception that polarisation was set to zero and the solenoid field alternated between ± 2.04 T. a) The solenoid was rotated by 5 °around the x-axis, b) the solenoid was rotated by 5 °around the y-axis. For clarity, the y-axes have been truncated, highlighting the variation and associated error bars.

does not explain the change with solenoid current reversal described in observation 1. A rotation around the y-axis produces slight changes in signal amplitude with magnetic field reversal. Although the signal in the centre-top channel remains higher with a negative B-field, the variations are only around 0.01 %, an order of magnitude too small to account for the observed oscillations in signal distribution with solenoid current reversal. This suggests that a rotation around the y-axis is unlikely to be the sole cause of these oscillations, suggesting instead a combination of multiple contributing factors.
The simulations assumed an ideal B-field; However, the actual magnetic field may contain imperfections that could contribute to the observed oscillations. For future, more precise measurements, it would be beneficial to measure the solenoid B-field directly if feasible. Alternatively, simulating a more realistic field using suitable software could help account for these imperfections. Additionally, the alignment of both the magnet and the calorimeter should be re-evaluated.
Since no oscillating behaviour of Q_c is observed (see section 8.7), it is reasonable to conclude that the calorimeter front is sufficiently large to capture the majority of the signal, despite fluctuations in beam positions. Any uncertainties arising from misalignment of the beams as they exit the solenoid and interact with the calorimeter are addressed by considering the x/y-position of the calorimeter when determining the analysing power (cf. section 8.8).

8.6.4. Implications for Further Analysis

Shot-to-shot fluctuations of the beam parameters described in section 8.4 follow distributions around mean values, which can be considered as uncertainties in the input parameters of the simulation when determining the analysing power (see section 8.8). However, as noted in this section, these considerations do not account for overarching trends over time. Such asymmetric changes introduce uncertainties in the measured asymmetry (see section 8.7). While the influence of the charge can be corrected, the accuracy of the charge measurement must also be taken into account. In the current setup, the energy remains unknown during a run, and its influence can therefore only be estimated.

8.7. The measured Asymmetry

With the preliminary work completed by accounting for input parameters (see section 8.4) and performing the charge correction (see section 8.6.1), the measured asymmetry of the corrected polarimeter signal, δ_{Q_c}, can now be calculated.
The charge-corrected, shot-to-shot data, is represented by grey dots in figure 8.25a). Here, an associated positive current of +60 A is indicated by a light background, while a negative current of -60 A is represented by a dark background.
The analysis proceeds in two stages. In the first stage, the data is divided into two subsets corresponding to the positive and negative current cycles over the runs duration. For each subset, the mean and standard error of the mean (SEM) are calculated, resulting in values of $\langle Q_c \rangle^- = 4011 \pm 4\,\text{pC}$ and $\langle Q_c \rangle^+ = 3973 \pm 4\,\text{pC}$, with distributions shown in figure 8.25c. The run asymmetry and associated error are calculated according to

$$\delta_{Q_c} = \frac{\langle Q_c \rangle^+ - \langle Q_c \rangle^-}{\langle Q_c \rangle^+ + \langle Q_c \rangle^-} \tag{8.7}$$

and

$$\Delta\delta_{Q_c} = \frac{2\langle Q_c \rangle^+ \langle Q_c \rangle^-}{(\langle Q_c \rangle^+ + \langle Q_c \rangle^-)^2} \sqrt{\left(\frac{SE_{\langle Q_c \rangle^+}}{\langle Q_c \rangle^+}\right)^2 + \left(\frac{SE_{\langle Q_c \rangle^-}}{\langle Q_c \rangle^-}\right)^2}, \tag{8.8}$$

yielding a result of $\delta_{Q_c} = -0.48 \pm 0.07\,\%$.
In the second stage, data is examined over sequential intervals to capture temporal evolution. For each interval, the mean and its associated standard error are calculated, as illustrated by the red and blue square markers in figure 8.25a). Paired intervals (representing consecutive positive and negative current cycles) are then used to calculate asymmetry values, as depicted in figure 8.25b), allowing observation of the time-dependent behaviour of asymmetry. Values varied within the range of $-1.63 \pm 0.32\,\%$ to $0.29 \pm 0.29\,\%$, indicating fluctuations throughout the observed period. The maximum deviation corresponding to the period of low laser energy already described in section 8.4.1. If the values during that period are excluded, the mean measured asymmetry is still $\delta_{Q_c} = -0.44 \pm 0.07\,\%$
Furthermore, looking at the interval results in figure 8.25b), it appears that the values up to minute 70 fluctuate around a different mean value than after that. It is not possible to say exactly what happened without analysing the laser and accelerator

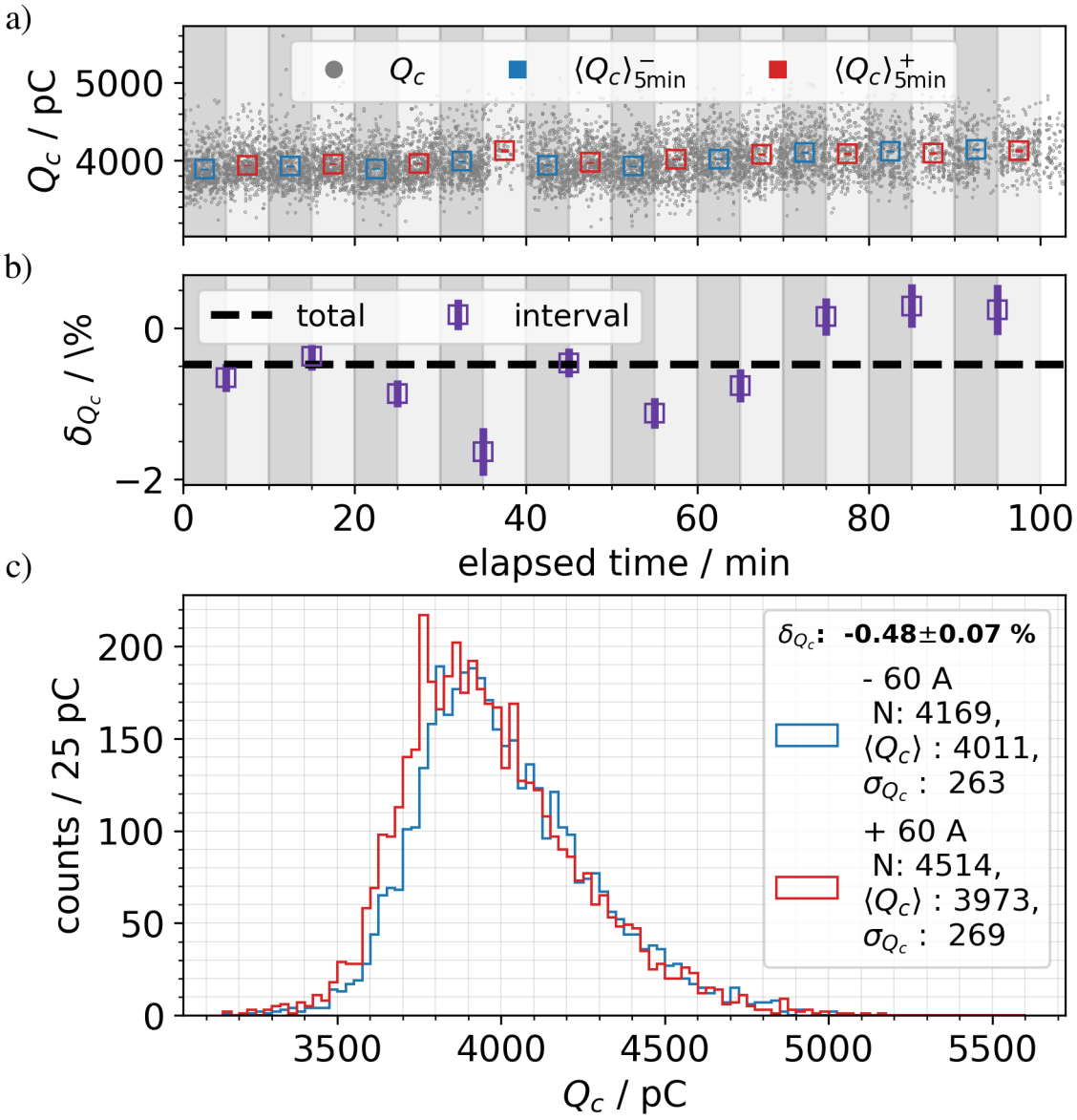

Figure 8.25.: a) Charge corrected polarimeter signal for individual shots (grey dots) and averaged over solenoid current intervals (displayed in blue for -60A and red for +60 A) over time b) Asymmetry calculated for interval pairs (violet squares) and calculated using all data divided into two groups c) Distributions of charge corrected polarimeter data of run 50379 with negative (blue) and positive (red) solenoid current. Averaging over the whole run leads to an asymmetry of $\delta_{Q_c} = -0.48 \pm 0.07\,\%$

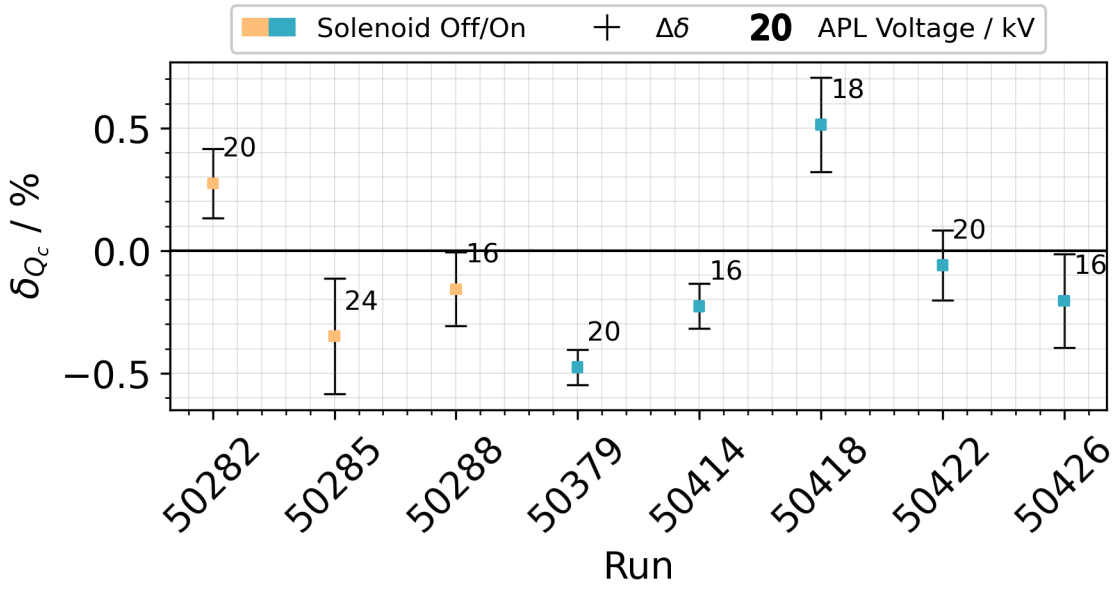

Figure 8.26.: Asymmetry of corrected polarimeter signal for different runs

parameters in detail. However, this would go beyond the scope of this work.
To better understand these results of measured asymmetry and assess their consistency, additional runs were analysed, including those with the solenoid turned off to determine whether it is one of the primary sources of systematic uncertainty contributing to non-zero asymmetry. The results are shown in figure 8.26.
For these 'solenoid off' runs, shot numbers were used to assign time-based intervals, with each interval incrementing every 5 minutes. Each shot was assigned to an interval, where even-indexed intervals correspond to positive current values, and odd-indexed intervals to negative. Regardless of the solenoid setting, only runs longer than 10 minutes, i.e., those containing at least one interval pair, were analysed to calculate an asymmetry.
Run 50282, which shares all settings with the primary long run (50379) except for the solenoid configuration, yields an asymmetry of $\delta_{Q_c} = 0.28 \pm 0.14\,\%$. Similarly, run 50422, conducted with identical settings to run 50379, results in asymmetry of $\delta_{Q_c} = -0.06 \pm 0.14\,\%$.
When all plasma lens voltages are considered, the asymmetry values range from $-0.48 \pm 0.07\,\%$ in run 50379 at 20 kV to $0.51 \pm 0.14\,\%$ in run 50418 at 18 kV. No clear trend in asymmetry is observed as a function of plasma lens current.
The measured asymmetries vary in both positive and negative directions around zero, indicating that the mean values do not consistently favour one direction. At a 3σ confi-

dence level, most runs are consistent with zero. However, the run with the highest statistics deviates from zero by approximately 7σ. Fluctuations between positive and negative values remain even when the solenoid is off, ruling out any contributions from the solenoids magnetic field or unintended beam polarisation. Additionally, because charge correction has been applied, variations in beam charge cannot be the source of this asymmetry, with only the accuracy of the charge measurement itself contributing to the overall uncertainty. The most likely source of this non-zero asymmetry is thus attributed to false asymmetries arising from drifts in the energy spectrum of the accelerated electron beams, a possibility supported by the findings in section 8.6.2, which indicate that such drifts could indeed reach this magnitude.
Placing this in the context of the expected asymmetries due to polarisation ($\delta_{\text{pol}} \approx 1.5‰$) derived in section 6.7, it can be concluded that these fluctuations, resulting from false asymmetries, are substantial and would mask the true signal in a polarisation measurement. Thus, the beam energy spread and fluctuations need to be significantly reduced before any polarisation can be measured.

8.8. The Analysing Power

As explained in section 3.4.1, the analysing power quantifies the expected asymmetry in the polarimeter's response to a fully polarised electron beam, in absence of fake asymmetries. Its accurate determination is essential for reliably translating measured asymmetry to beam polarisation.
Simulations were used to determine both the central value of the analysing power and its associated uncertainties. These uncertainties stem from several sources that must be carefully assessed to ensure reliability. The primary sources include statistical fluctuations due to finite sample size, systematic effects related to real-world variability in beam parameters and setup, and nonlinear correction factors applied to simulate calorimeter measurements from deposited energy above the Cherenkov threshold. The following sections provide an in-depth analysis of these factors, beginning with the determination of the central value and its statistical error.

Table 8.3.: Central values used for analysing power analysis

simulation parameter	value	simulation parameter	value
switch	core	divergence	0.067 °
core length	150 mm	calo. position in x/y	(0,0) mm
converter thickness	0 mm	distance to polarimeter	91 mm
energy	20 kV spectrum	polarimeter rotation	0 °
gun position	(0,0,-1) mm	P_{e^-}	1
spot size	0.74 mm	P_{Fe}	1

8.8.1. Central Value and Statistical Uncertainty of the Analysing Power

The analysing power is determined with the aid of LEAP_SIMS simulations. The framework is described in chapter 5, with key configurations being described in section 5.4 and the algorithm for analysing power detailed in section 5.5.

Input parameters were selected to closely match the actual conditions during the zero polarisation measurement. The `Run:type` was set to "asymmetry". To maintain consistency with the fully polarised conditions required to assess analysing power, the polarisation of both the incoming electrons and the solenoids iron core are set to 100 %. The core polarity is flipped for parallel and anti-parallel polarisation conditions. A Gaussian beam profile is assumed. The other input parameters are derived from the results of the beam parameter analysis (see section 8.4) and direct physical measurements of the setups spatial dimensions. An overview of the simulation parameters is provided in table 8.3. The input spectrum, the average displayed in figure 8.12d), was used in the range between 39.42-190 MeV with a bin width of 0.15 MeV. Details on the handling of the spectra can be found in section 8.8.2.

Simulation results: A total of 16104 simulations, each involving $5 \cdot 10^5$ particles[2], were conducted for both parallel (P) and anti-parallel (AP) polarization configurations. This resulted in the distributions of deposited energy of charged particles above the Cherenkov threshold in lead glass, E_{ct}, as shown in figure 8.27. Gaussian fits applied to these distributions yielded mean values of $E_{ct,AP} = 302.31 \pm 0.02$ GeV and

[2]The comparison between charge-corrected polarimeter data and simulations suggests that on average approximately 6×10^5 electrons were incident on the polarimeter front during run 50379 (cf. section 8.6.1), leading to a scaling factor of 1.2 (cf. equation 6.3)

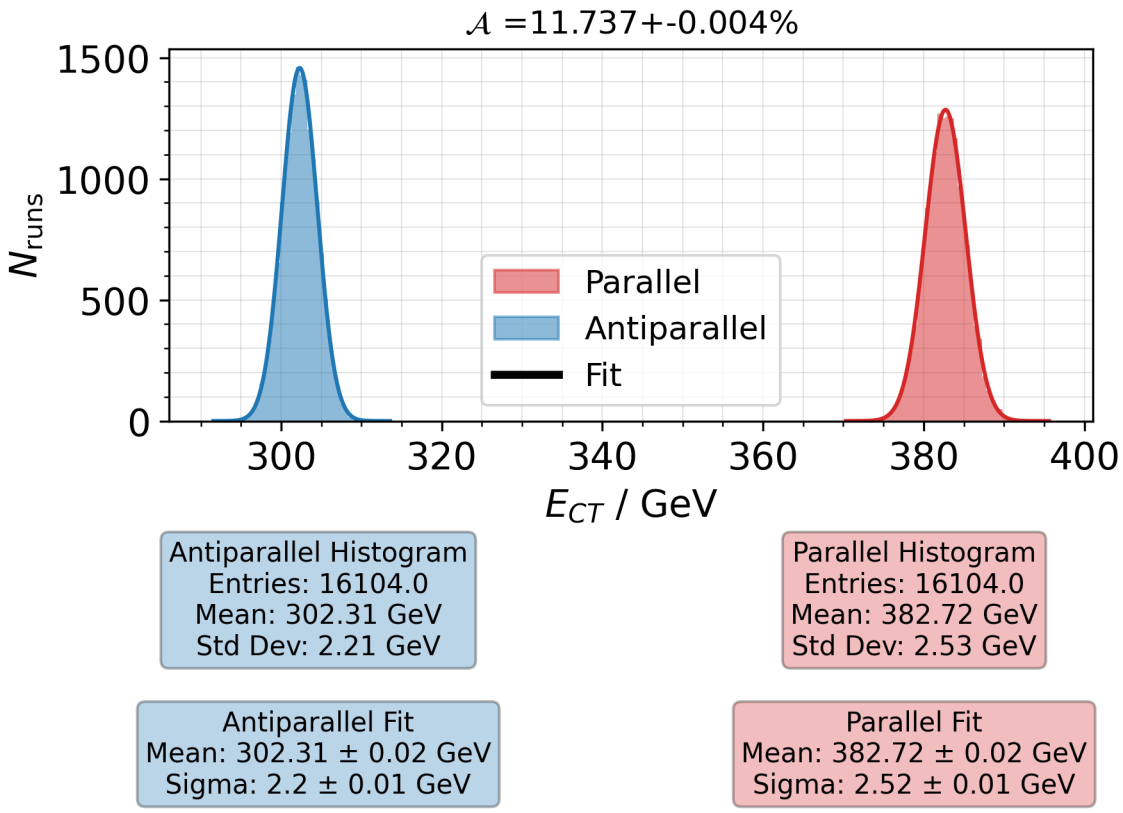

Figure 8.27.: Simulated E_{ct} distributions for both, parallel and antiparallel, polarisation configurations. 1×10^5 electrons were simulated per bunch.

$E_{ct,P} = 382.72 \pm 0.02\,\text{GeV}$. Using equations 3.26 and 3.27 leads to a **central value of the analysing power of $\mathcal{A} = 11.737 \pm 0.004\%$**.
The statistical error in the analysing power calculation has two main contributions: the width of the E_{ct} distributions and the total number of simulated particles, which is determined by the number of conducted simulations and the number of particles per simulation. The widths of the E_{ct} distributions reflect both intrinsic statistical fluctuations within the defined input beam parameters and additional variability due to the probabilistic nature of the interaction processes, which are governed by interaction cross-sections. To obtain the error in the analysing power, the statistical errors of $E_{ct,P}$ and $E_{ct,AP}$ are each divided by the square root of the number of simulation runs to calculate their standard errors of the mean (SEM). These SEM values are then propagated to estimate the overall statistical error in the analysing power. The number of simulation runs was therefore chosen to make this propagated Monte Carlo statistical uncertainty an order of magnitude smaller than the anticipated systematic errors.

8.8.2. The Electron Spectrum and Its Sampling Technique

As already discussed in section 8.4.2, the energy of the electrons plays a crucial role in the accuracy of Compton transmission polarimetry. Several factors contribute to the systematic uncertainty in this regard:

- The peak of the spectrum transmitted through the collimator varies with the plasma lens current (cf. figure 8.12).
- The electron spectral shape varies from shot to shot due to fluctuations in the laser-plasma acceleration process. These variations are further influenced by beam jitter: since the APLs focusing is energy-dependent, small pointing fluctuations result in different energy components being preferentially transmitted or blocked by the collimator, modifying the observed spectrum.
- The method used to bin and process the discrete spectral data introduces uncertainties, as it relies on a discrete representation of otherwise continuous information.

The first item will be addressed in the following section, while the latter two will be addressed here in a combined approach.
Figure 8.12d shows that the shape of the spectrum transmitted through the collimator

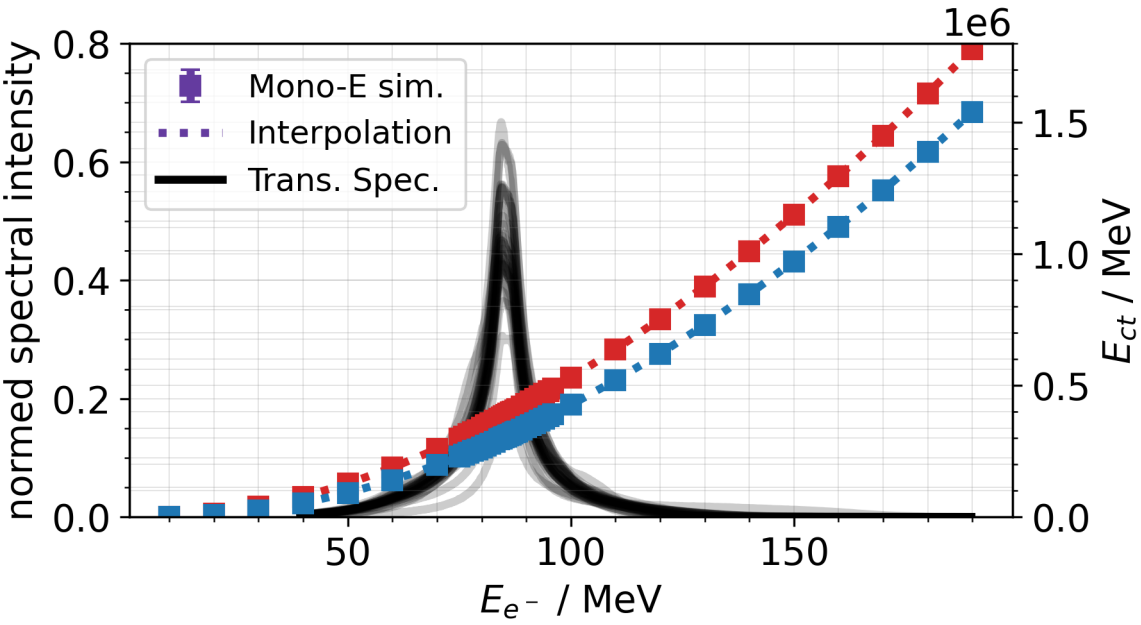

Figure 8.28.: Selected spectra transmitted through collimator, with I_{APL} = 423 A displayed as grey lines. Simulated deposited energy above Cherenkov-threshold E_{ct} for both polarisation configurations shown as square markers. Red for parallel, blue for anti-parallel. Dashed lines show interpolated values that match the sample points of the measured spectra.

can vary considerably from shot to shot, which sometimes leads to long high-energy tails. Since the polarisation-dependent component of the Compton scattering cross section is nonlinear with respect to energy (see fig. 3.5), these variations could impact the analysing power. This influence is illustrated in figure 6.7 of chapter 6, where monoenergetic electron beams were simulated to assess how varying electron energies affect the analysing power. The results indicate that the analysing power decreases with higher energy, although less strongly for higher energies.

One approach to account for the effect of the incident electron spectrum shape on $\mathcal{A}$ involves using all spectra measured in run 50281, with the plasma lens transmission function applied, as shown partially in figure 8.12d. These spectra could then be used as inputs for the simulation. However, given the large number of spectra, this is computationally very intensive. A more efficient approach involves simulating the polarimeter response for monoenergetic beams across the relevant energy range and then approximating the results for any electron spectrum of interest by applying appropriate spectral weighting.

The spectral weighting algorithm can be applied either to a single spectrum, yielding

two mean E_{ct} values for asymmetry calculation, or to multiple spectra, resulting in two distributions of mean E_{ct} values. In the latter case, asymmetries must be computed from the means of these distributions. The detailed method proceeds as follows, with step 5 being required only when multiple spectra are considered:

1. **Obtain transmission spectra**: Obtain the spectra transmitted through the collimator as described in section 8.4.2, along with the input spectrum used in the previously described `GEANT4` simulations. The APL-spectra are shown as grey lines in figure 8.28.

2. **Simulate polarimeter response**: Simulate E_{ct}, the polarimeter response, for monoenergetic electron beams with with incident energies $E_{e^-,\text{in}}$ spanning 40-190 MeV, covering both polarisation configurations (parallel and anti-parallel). Due to high-energy tails present in some spectra, the energy range is extended beyond that used in the `GEANT4` simulation, which only considers the average spectrum. Simulations are performed in increments of 10 MeV over 10-190 MeV, 1 MeV increments over 75-96 MeV, and 0.5 MeV increments from 84 to 88 MeV. Theses values are shown in red for parallel and in blue for antiparallel polarisation configuration in figure 8.28.

3. **Interpolate the E_{ct} values**: Interpolate the simulated E_{ct} values to obtain a corresponding E_{ct} value for each $E_{e^-,\text{in}}$. Linear interpolation is applied, calculated as follows:

$$E_{ct,interp.} = E_{ct,1} + \frac{E_{ct,2} - E_{ct,1}}{E_{e^-,\text{sim2}} - E_{e^-,\text{sim1}}}(E_{e^-,\text{sim1}} - E_{e^-,\text{in}}) \tag{8.9}$$

   where $E_{e^-,\text{sim}}$ denotes simulated beam energies, and indices 1 and 2 specify the values between which interpolation occurs. Associated statistical uncertainties are also propagated, with:

$$\Delta E_{ct,interp.} = \sqrt{\left(\frac{E_{e^-,\text{sim2}} - E_{e^-,\text{in}}}{E_{e^-,\text{sim2}} - E_{e^-,\text{sim1}}}\right)^2 (\Delta E_{ct,1})^2 + \left(\frac{E_{e^-,\text{in}} - E_{e^-,\text{sim1}}}{E_{e^-,\text{sim2}} - E_{e^-,\text{sim1}}}\right)^2 (\Delta E_{ct,2})^2} \tag{8.10}$$

   The interpolated values of E_{ct} are shown as dashed lines in figure 8.28.

4. **Compute weighted average(s)**: The weighted average of E_{ct} is calculated using the spectral intensity I, as weight:

$$\langle E_{ct} \rangle = \frac{\sum_{i=1}^{N} I_i \cdot E_{ct,i}}{\sum_{i=1}^{N} I_i} \tag{8.11}$$

   where N is the number of points at which the spectrum was sampled. The uncertainty in the weighted average is propagated as follows:

$$\Delta\langle E_{ct} \rangle = \sqrt{\sum_{i=1}^{N} \left(\frac{I_i}{\sum_{j=1}^{N} I_j} \right)^2 (\Delta E_{ct,i})^2 + \sum_{i=1}^{N} \left(\frac{E_{ct,i} - \langle E_{ct} \rangle}{\sum_{j=1}^{N} I_j} \right)^2 (\Delta I_i)^2} \tag{8.12}$$

5. (For multiple spectra only) **Obtain the E_{ct} distributions and their means:** These are calculated as described in section 5.5 for both polarisation configurations.

6. **Calculate the Asymmetry**: Again, the analysing power is the asymmetry for 100% polarisation.

First, it is important to compare the here described approach with the approach that was used to simulate the central value above. For this the same spectrum provided as an input parameter to `GEANT4` was analysed. Due to the limited number of histogram bins, the spectrums energy range was restricted to 40-150 MeV, with a bin width of 0.25 MeV. Using the weighted average approach yields a value of 11.724 ± 0.001 %, compared to $\mathcal{A}_0 = 11.737 \pm 0.004$ % from `GEANT4` sampling from the beam energy histogram. The discrepancy between these values is attributable to differences in data handling.These differences likely stem from the methods used to sample the energy spectrum. According to the `GEANT4` source code [158], the user-defined differential energy spectrum (up to 1024 bins) is converted into a normalised cumulative distribution function (CDF). For each particle, a random number r between 0 and 1 is generated, representing a position on the CDF (cf. inverse transform method in section 4.1.1). The corresponding energy bin is identified, and the exact energy is determined via linear interpolation between bin edges, ensuring smooth transitions and a continuous-like spectrum. While limited by double-precision floating-point accuracy (step size $\sim 10^{-16}$), this discretisation is negligible, making the energies effectively continuous. In the weighted average approach, there is no explicit bin limit. However,

the accuracy of the measured spectrum is constrained by the resolution of the electron spectrometer camera (see section 2.6.3). Instead of simulating every individual particle, transmitted energies from pre-simulated monoenergetic electron beams are linearly interpolated. While theoretically an unlimited number of monoenergetic simulations can be performed, the accuracy remains limited by the discretisation of the input spectrum.

While the weighted average approach is highly efficient for analysing multiple spectra, provided monoenergetic simulation data is available, `GEANT4` sampling from the beam energy histogram produces a quasi-continuous spectrum, making it a closer representation of a real spectrum. Thus, the `GEANT4` sampling is used to determine the central value of the analysing power. However, for computational efficiency, spectral weighting is applied to evaluate the relative impact of beam energy spectrum variations and the associated systematic uncertainty on this central value. For the final error assessment, see section 8.8.5.

Due to the occasionally occurring high-energy tails, the energy limits of the incident electron spectrum were extended from 40-150 MeV to 40-190 MeV. For consistency, the number of bins in the linearised measured spectra was kept constant, resulting in a bin width of 0.085 MeV. This approach yielded a computed analysing power of 11.723 ± 0.002 %. The slightly lower central value is likely due to increased contributions from high-energy values (cf. figure 3.3). In a test comparing bin widths from 0.05 to 1 MeV, the central value remained stable while the statistical error increased from 0.002 % to 0.007 %.

Using all spectra, estimated based on data from run 50281 as if transmitted through the collimator, results in an average analysing power of 11.739 ± 0.039 %. Due to fluctuations in the energy spectrum, the statistical error increases by an order of magnitude, and additional 'shots' would be required to achieve the same precision as previously obtained using only the average spectrum. The systematic error attributable to spectral fluctuations, reflected in the change of the calculated central value, is hence statistically insignificant. Thus, changes in the central value of the spectrum (see fig. 8.30) represent a significantly larger source of systematic error in the analysing power than the fluctuations in the shape of the spectra.

To further investigate the effect of the spectral shape, a Gaussian input spectrum with the same central value and FWHM as the average spectrum in figure 8.30 was analysed using the weighted average method. As shown in figure 8.29, this primarily eliminates the asymmetric tails of the spectrum. The resulting analysing power is 11.884 ± 0.001%, representing a 1.4 % shift in the central value compared to the previously mentioned

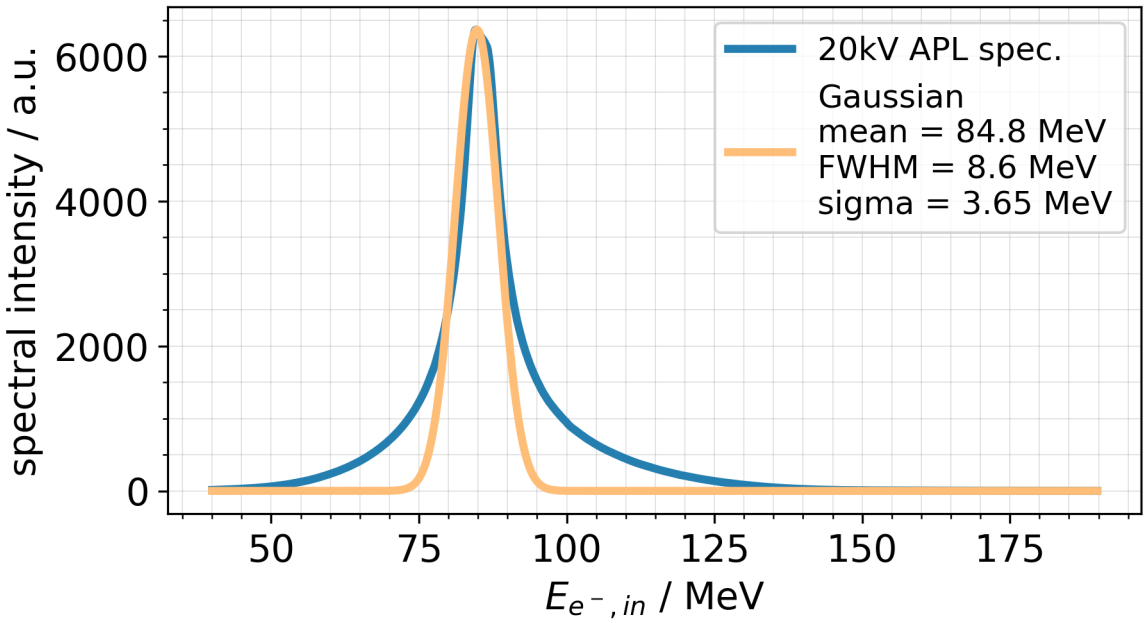

Figure 8.29.: Comparison of average 20 kV APL input spectrum and Gaussian with same central value and FWHM.

$11.724 \pm 0.001\%$. While this has no immediate impact on the current measurement, it highlights the critical importance of precisely knowing the energy spectrum for future measurements. Moreover, the narrower it is, the better, all the more so with lower central values (cf. figure 6.7).

8.8.3. Uncertainties of other measured input parameters

To minimise the influence of the extensively fluctuating input parameters observed in the experiment, the `GEANT4` simulations described in section 8.8.1 were repeated, each time varying one parameter by its previously determined uncertainty. For measured distances, such as between the solenoid and the calorimeter or the position of the calorimeter in the room, an accuracy of 2 mm was assumed based on the laser distance meters precision. A standard deviation of 0.02 mm from the central value was used for the spot size (see section 8.4.3). Since the cross sections for physical interactions during particle passage through iron depend on energy (see section 3.1), energy fluctuations are expected to have the greatest influence. Although the exact spectral shape during run 50379 is unknown, the plasma lens current is known to have fluctuated by ± 3 A

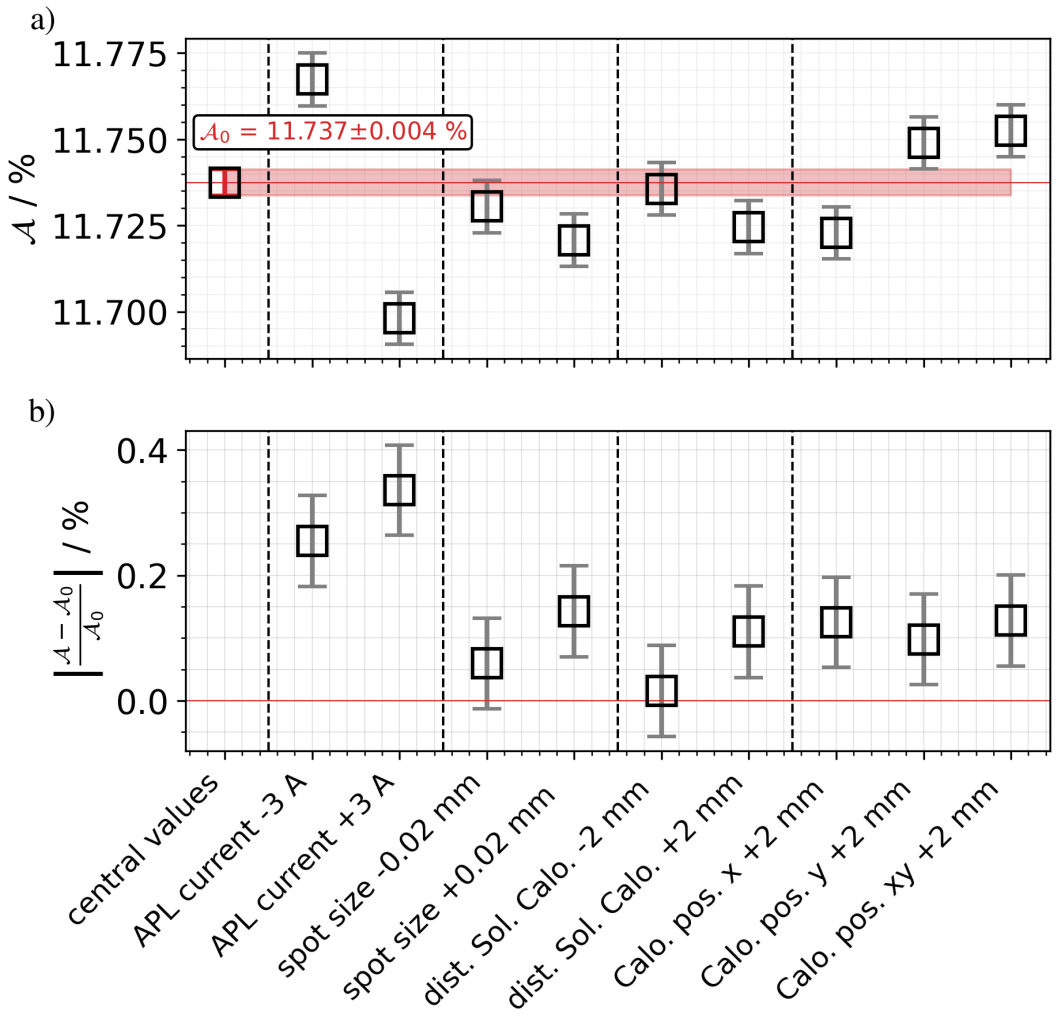

Figure 8.30.: a) Simulated analysing power and b) the associated relative distance to the central value for different simulation input parameters. Central value $\mathcal{A}_0$ and its statistical uncertainty highlighted in red. Central simulation parameters in table 8.3.

around the central value of 423 A. Corresponding spectral deviations were simulated to account for this (see fig. 8.12c). A visual representation of the results is provided in figure 8.30.
As expected, the variation of the plasma lens current, and thus the central value of the incoming electron energy spectrum, has the largest influence. However, the resulting relative error is only about three times as large as that caused by the uncertainty in the spot size.

8.8.4. Calorimeter Corrections

An additional, non-negligible source of uncertainty arises from the non-linear response of the calorimeter to low-energy particles. The exact values simulating this response depend on the `GEANT4` physics list used (see section 5.2.3) and are taken from the analysis presented in [52], which estimates a relative systematic uncertainty of 1.5 %. Although this uncertainty is not directly derived here, it is the largest contributing factor to the overall uncertainty in the analysis.

8.8.5. Final Error Assessment and Consolidation of Results

In the end all uncertainties on the analysing power add up quadratically

$$\begin{aligned}\frac{\Delta\mathcal{A}}{\mathcal{A}} &= 0.035\,\%\ (\text{Statistical Monte Carlo Uncertainty})\\ &\oplus 0.34\,\%\ (\text{Central value of energy spectrum (APL current)})\\ &\oplus 0.14\,\%\ (\text{Beam spot size})\\ &\oplus 0.11\,\%\ (\text{Distance between solenoid and calorimeter})\\ &\oplus 0.13\,\%\ (\text{Calorimeter } x\text{-}y \text{ position})\\ &\oplus 1.5\,\%\ (\text{Calorimeter energy response})\\ &= 1.55\,\% \end{aligned} \tag{8.13}$$

resulting in an analysing power of $\mathcal{A} = 11.74 \pm 0.18$ %.
Systematic errors primarily arise from the input parameters used in the simulation, particularly with respect to how accurately they represent the true experimental conditions and the extent of fluctuations. Compared to uncertainties arising from false

asymmetries or inaccurate charge measurements, the error on the analysing power is relatively small. Further discussion can be found in section 8.9. However, it is important to note that in the current simulation, the solenoid was modelled with either the magnetic field or polarisation, but not both simultaneously, as this could not be achieved with the current code implementation. For more accurate spin tracking and a more complete simulation of the transverse motion components of particles, future work should include the combination of both effects in the simulation.

8.9. Evaluation of Polarimeter Performance

To finalise the polarisation analysis, the measured asymmetry and calculated analysing power are combined here to determine the polarimeters accuracy in polarisation measurement. The initial focus is on evaluating the precision of the zero-polarisation measurement as a baseline test of sensitivity. This is followed by a projection of the polarimeters performance with future beam conditions, offering insight into its accuracy under varied experimental setups.

8.9.1. Precision of Zero Polarisation Measurement

Given that the incident electron beam is unpolarised, one would ideally expect the measured asymmetry –and consequently, the measured polarisation– to be consistent with zero within the measurement uncertainty.
However, energy measurements, combined with simulations, indicated gradual variations in beam energy over time (cf. section 8.6.2). These variations constitute systematic effects that likely occurred during data-taking and were expected to introduce a false asymmetry on the order of $\left|\delta_{\text{false},E}\right| \approx 0.4\%$.[3] Indeed the measured asymmetry was found to be $\delta_m = \delta_{Q_c} = -0.48 \pm 0.07\,\%$, closely aligning with the expected magnitude of the false asymmetry. This suggests that drifts in the electron beam energy over time introduced a systematic error so large that it would mask any true asymmetry arising from beam polarisation, which would be expected at the permille level.
Be that as it may, it is still valuable to combine all the relevant components for the polarisation determination and assess how accurately zero was measured, particularly in the context of the overall uncertainty budget. With the analysing power determined

[3] Variations of charge can of course have a similar effect, but were corrected for (cf. section 8.6.1).

to be $\mathcal{A} = 11.74 \pm 0.18\,\%$ (cf. section 8.8.5), and a polarisation of the electrons within the magnetised solenoid core of $7.23 \pm 0.15\%$, P_{e^-}, can be calculated according to equation 3.30:

$$P_{e^-} = \frac{\delta_m}{\mathcal{A} P_{Fe}} = \frac{-0.48 \pm 0.07\%}{11.74 \pm 0.18\% \cdot 7.23 \pm 0.15\%} = -56.6 \pm 8.4\% \tag{8.14}$$

As expected, the measured polarisation is distinctly non-zero, deviating by more than six standard deviations – well beyond any reasonable statistical fluctuation. The discrepancy is large enough to compromise the reliability of the overall measurement. To ensure reliable polarisation measurements in the future, either the energy spectra must be narrow and stable enough to obviate the need for simultaneous measurement, or shot-to-shot energy information must be available for effective correction.
But apart from the false asymmetry, what are the contributions to the uncertainty of the polarisation? The propagated uncertainty on the polarisation naturally includes contributions from the polarisation of the iron core $\left(\frac{\Delta P_{Fe}}{P_{Fe}} = 2.07\%\right)$, the analysing power $\left(\frac{\Delta \mathcal{A}}{\mathcal{A}} = 1.53\%\right)$, and the measured asymmetry $\left(\frac{\Delta \delta_m}{\delta_m} = 14.58\%\right)$.

$$\frac{\Delta P_{e^-}}{P_{e^-}} = \frac{\Delta P_{Fe}}{P_{Fe}} \oplus \frac{\Delta \mathcal{A}}{\mathcal{A}} \oplus \frac{\Delta \delta_m}{\delta_m} \tag{8.15}$$

where $\oplus$ signifies Pythagorean addition. Among these contributions, the relative uncertainty of the measured asymmetry is by far the largest. The statistical error on δ_m can be calculated using equation 8.8, which depends on the corrected polarimeter signal Q_c. As discussed in section 8.6.1, Q_c has a relative width of $\frac{\sigma_{Q_c}}{\langle Q_c \rangle} = 6.7\%$ and still depends on:

- **Energy fluctuations**: Fluctuations in electron beam energy cause an energy distribution of σ_E.
- **Polarimeter response**: Physical processes inside the solenoid core and the calorimeter introduce additional broadening, characterised by σ_{pol}. Simulations determined the relative width of the polarimeter response function to be $\frac{\sigma_{\text{pol}}}{\langle T_{\text{pol}} \rangle} = 0.74\%$.
- **Accuracy of charge measurement**: While the influence of the actual distribution of charge incident onto the polarimeter is accounted for, the response function of the charge diagnostic, in this case a scintillator screen, still remains and adds an additional width of Δ_{q_m}.

- **The number of shots**: The higher the number of measurements, the more accurate the error on the mean signal can be determined.

Since σ_{pol} has little influence (cf. section 8.6.1), the accuracy of the charge measurement and the number of measurements taken are the primary limiting factors, alongside energy fluctuations.

8.9.2. Projected Performance for Future Beam Parameters

At present, the instability of the incident electron beam parameters makes polarisation measurements infeasible, as false asymmetries dominate and obscure genuine signals. Nevertheless, another important question arises: Can the polarimeter, as a diagnostic device in itself, measure the expected electron polarisation of P_{e^-}=10% with sufficient accuracy in a future experiment?
To address this question, equation (8.15) can be used to calculate the relative statistical uncertainty of the polarisation, $\frac{\Delta P_{e^-}}{P_{e^-}}$. With the contributions from the polarisation of electrons inside the iron core and analysing power known to be 2.07% and 1.53%, respectively, what remains to be determined is the relative uncertainty on the measured asymmetry, $\frac{\Delta\delta_m}{\langle\delta_m\rangle}$.
Assuming an electron beam polarisation of $P_{e^-} = 10\%$ (cf. table 2.1), the anticipated measured asymmetry can be calculated as:

$$\delta_m = P_{e^-} \cdot \mathcal{A} \cdot P_{Fe} = 10\% \cdot 11.74\% \cdot 7.23\% = 0.085\% \tag{8.16}$$

If it is further assumed that the differences between $\langle Q_c^+ \rangle$ and $\langle Q_c^- \rangle$ are marginal – due to the low degree of electron polarisation and analysing power – equation 8.8 simplifies to:

$$\Delta\delta_m \approx \frac{1}{\sqrt{2}} \frac{\Delta\langle Q_c \rangle}{\langle Q_c \rangle} = \frac{1}{\sqrt{2N}} \frac{\sigma_{Q_c}}{\langle Q_c \rangle} \tag{8.17}$$

where $\Delta\langle Q_c \rangle$ represents the uncertainty in the mean corrected polarimeter signal, and σ_{Q_c} denotes the width of the charge-corrected polarimeter signal. As shown in figure 8.21a), the measured relative width of the corrected charge distribution $\frac{\sigma_{Q_c}}{\langle Q_c \rangle}$ is 6.68%. This value is primarily influenced by energy fluctuations and the resolution of the charge measurement, as discussed in section 8.6.1.

The relative uncertainty of the polarisation, $\frac{\Delta P_{e^-}}{P_{e^-}}$, can then be expressed as a function of the total number of shots, $2N$.[4]

$$\frac{\Delta P_{e^-}}{P_{e^-}} = \frac{\Delta P_{Fe}}{P_{Fe}} \oplus \frac{\Delta \mathcal{A}}{\mathcal{A}} \oplus \frac{1}{\delta_m} \frac{1}{\sqrt{2N}} \frac{\sigma_{Q_c}}{\langle Q_c \rangle} \tag{8.18}$$

Solving for $2N$ using equation (8.18), shows that achieving a target relative precision of 20% would require more than 1.5×10^5 shots. At a repetition rate of 2 Hz this translates to approximately 22 hours of uninterrupted beam time for a single measurement, an unrealistic requirement given the current state of the accelerator system. Achieving realistic measurement times necessitates a significant improvement in the accuracy of the charge measurement ($\Delta q_m / q_m$) as well as a reduction in electron beam fluctuations ($\sigma_E / \langle E \rangle$).

While simulation studies suggest that sub-permille energy stability in LPAs could be achieved using additional energy compression schemes [159], these methods have yet to be experimentally realised. However, percent-level shot-to-shot energy stability has already been demonstrated. For instance, Bayesian optimisation of beam control has achieved an energy spread of approximately 1.2% [160, 161]. The accelerator setup described in section 8.1 does not inherently provide this level of stability, but energy filtering – employing a plasma lens, a collimator, and possibly an additional dipole – could allow for an energy spread on the order of 1%. Further research would be required to experimentally verify the feasibility of this approach.

Percent-level accuracy in charge measurement should be achievable by optimising the Turbo-ICT setup. It has been reported to exhibit a noise level of 10 fC for single-shot measurements [153]. With an incident charge in the pC range and careful shielding, a sufficiently precise measurement should be possible. However, achieving this accuracy would require further investigation, as higher charge levels would necessitate adjustments to the PMT setup to maintain linearity (cf. section 8.2.2).

Future requirements for beam energy spread, stability, and charge measurement accuracy can be estimated by replacing the measured $\frac{\sigma_{Q_c}}{\langle Q_c \rangle}$ with the intrinsic polarimeter resolution ($\frac{\sigma_{\text{pol}}}{\langle T_{\text{pol}} \rangle} = 0.74\%$; cf. figure 8.21a)) and incorporating estimates of future energy and charge stability or resolution. Notably, if the charge remains sufficiently stable, it would cancel out from the asymmetry, reducing its impact on the measurement. Assuming that the relative contributions to $\frac{\sigma_{Q_c}}{\langle Q_c \rangle}$ add in quadrature, equation (8.17) can be rewritten as

[4] N shots for every polarisation configuration

Table 8.4.: Expected number of shots required to achieve a precision 20 %, assuming $P_{e^-} = 10\%$ and different accuracies for the energy and charge measurements

Energy and charge measurement uncertainties / %	Number of shots needed	Required measurement time at 2 Hz / hh:mm
current situation	$1.57 \cdot 10^5$	21:52
1	$8.99 \cdot 10^3$	01:15
0.1	$2.00 \cdot 10^3$	00:16

$$\Delta\delta_m \approx \frac{1}{\sqrt{2N}} \left(\frac{\sigma_{\text{pol}}}{\langle T_{\text{pol}} \rangle} \oplus \frac{\sigma_E}{\langle E \rangle} \oplus \frac{\Delta q_m}{\langle q_m \rangle} \right) \tag{8.19}$$

Figure 8.31 and table 8.4 illustrate the relative statistical uncertainty on the polarisation, $\frac{\Delta P_{e^-}}{P_{e^-}}$ as a function of the number of measurements for different values of $\sigma_{Q_c} / \langle Q_c \rangle$. As the uncertainty on the measured asymmetry decreases with the number of measurements taken, so does $\frac{\Delta P_{e^-}}{P_{e^-}}$. It asymptotically approaches a limit determined by the accuracies of $\mathcal{A}$ and P_{Fe}. The blue curve represents the current value of 6.68% discussed above, while the green and orange curves depict scenarios with improved relative widths of energy fluctuations and charge measurement accuracies in front of the solenoid, reduced to 1% and 0.1%, respectively.

In a scenario where near-ideal beam conditions are achieved, with $\Delta q_m / q_m = \sigma E / \langle E \rangle = 0.1\%$ and the simulated σ_{pol} of 0.74%, a relative precision of $\frac{\Delta P_{e^-}}{P_{e^-}} = 20\%$ could be reached with only about 2000 shots. Under a more realistic and achievable scenario, where $\Delta q_m / q_m$ and $\sigma_E / \langle E \rangle$ are improved to 1%, approximately 9000 shots would be needed to reach the same statistical precision. At a bunch repetition rate of 2 Hz, this corresponds to about an hour and 15 minutes of measurement time. If the technical maximum of 10 Hz is reached, the required time would be reduced to just 15 minutes.

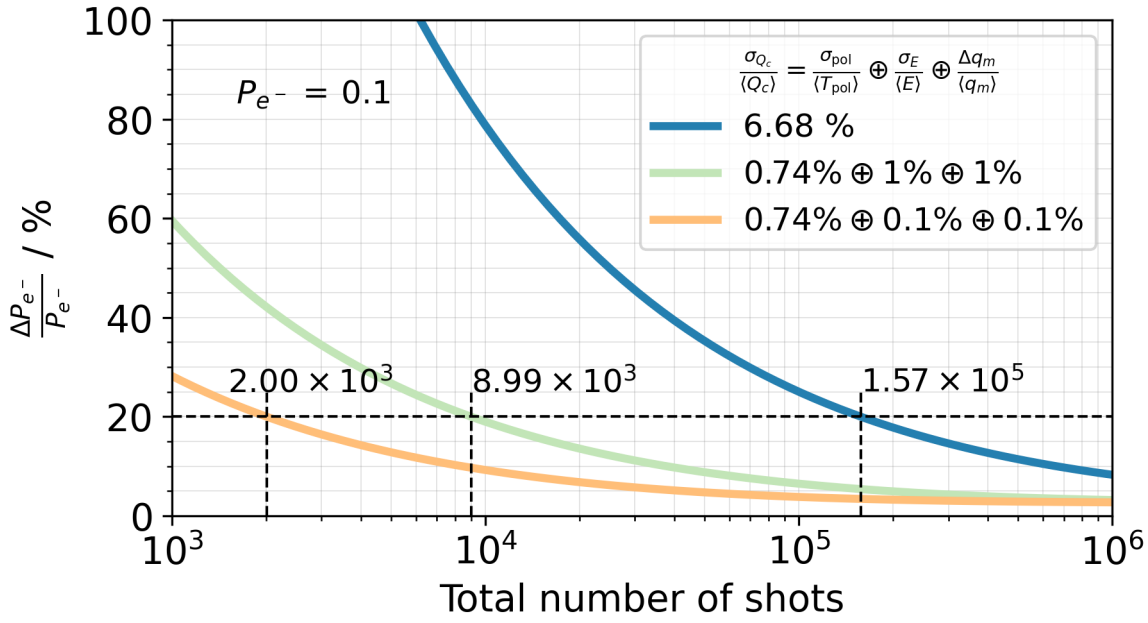

Figure 8.31.: Estimated precision of the polarisation measurement with respect to the total number of shots ($2N$) of an anticipated electron polarisation of $P_{e^-} = 10\,\%$. Results are presented for three cases of $\frac{\sigma_{\mathrm{pol}}}{\langle T_{\mathrm{pol}} \rangle} \oplus \frac{\sigma_E}{\langle E \rangle} \oplus \frac{\Delta q_m}{\langle q_m \rangle}$. The blue curve corresponds to the current measured value of 6.68 %, while the other two curves represent different assumptions for the potential future relative widths of energy fluctuations and charge measurement accuracies in front of the solenoid. This figure was produced with code developed by F. Stehr for an analysis in [52]

Although, as previously stated, the polarimeter itself is not the limiting factor in the accuracy of the polarisation measurement, several improvements could still be made:

- **Electron separation**: The design study showed that the asymmetry of the electrons leaving the absorber is more than 5 times higher than that of the photons (cf. section 6.5). Therefore, it would be highly worthwhile to further investigate this effect by placing a dipole magnet behind the solenoid to separate electrons from Bremsstrahlung photons, enabling an additional energy-resolved measurement of the electrons.

- **Longer absorber**: The analysing power increases with the length of the solenoid's core (cf. sections 3.4 and 6.3). Since the rate of electrons incident onto the solenoid core (or more precisely, the number of Bremsstrahlung photons passing through the absorber) is not the limiting factor when measuring the transmitted energy sums, extending the solenoid core could be a viable option to further enhance the analysing power. At 80 MeV, a core that is twice as long corresponds to an analysing power that is about twice as high.

- **Investigation of low-energy calorimeter response**: The calorimeter's response to low-energy photons introduces a systematic uncertainty ($\Delta\mathcal{A}/\mathcal{A}$ = 1.5 %) that warrants further investigation. A test of the calorimeter using a beam of low-energy X-rays with known energy could help address this issue. Such a test would not only assist in optimising calorimeter calibration but also improve the alignment between simulations and experimental results.

- **Verification of absorber polarisation**: For an accurate determination of the electron polarisation, it is crucial to re-evaluate the polarisation of the electrons within the iron solenoid core. Detailed magnetic field maps and electromagnetic field simulations using dedicated software would be highly beneficial for this purpose.

Even though false asymmetries due to beam energy fluctuations are expected to dominate the systematic errors on the measured asymmetry, other potential sources of systematic error cannot be excluded. To ensure the reliability of the results, it would be beneficial to flip both the polarity of the iron core and the polarisation direction of the incident electron beam. By considering all four possible configurations when calculating the asymmetry, one can use this as a consistency check, ensuring that the results are independent of the chosen configuration. Any systematic effects, such as misalignments causing different solid angles after scattering, would then become

apparent and could be further investigated and corrected.
Finally, it can still be stated that the commissioning of the polarimeter has demonstrated that Compton transmission polarimetry is indeed suitable for the polarimetry of LPA electron beams. More specifically, the polarimeter designed for LEAP is suitable for a polarisation measurement under conditions expected at LEAP (cf. table 2.1), as long as energy fluctuations over time are minimised and the accuracy of charge measurements is improved.

Chapter 9.

Conclusion

Polarised electron beams are widely used in nuclear and particle physics to study spin-dependent processes. Laser-plasma accelerators (LPAs) could provide a compact alternative to conventional sources, and simulations suggest they can produce and sustain polarised electron beams. However, this has yet to be demonstrated experimentally. The LEAP project aims to address this by demonstrating the acceleration of polarised electron beams, using a prepolarised plasma source. This thesis focuses on the design and commissioning of a Compton transmission polarimeter to verify electron beam polarisation in future LEAP experiments.

In Compton transmission polarimetry, an electron beam generates bremsstrahlung radiation that passes through a magnetised absorber, where the attenuation is polarisation-dependent. By flipping the polarity of the magnetised absorber, differences in photon flux can be measured, and the resulting asymmetry allows conclusions to be drawn about the electron beam polarisation.

As part of this work, the LEAP_SIMS software framework was developed to support these efforts. Built around `GEANT4`, it enables Monte Carlo studies that incorporate polarised sources and materials.

Building on the development of LEAP_SIMS, a design study was carried out within the scope of this thesis. It was found that, within the expected energy range of several tens of MeV, the effect of adding a high-Z converter target in front of the iron core on analysing power is minimal, as the core itself acts as a converter. Since Compton scattering decreases with increasing electron beam energy, a low analysing power ($\mathcal{O}10\%$) is expected. With several pC incident on the solenoid core, photon transmission to the calorimeter is not an issue, meaning longer solenoid cores could improve analysing power. At 80 MeV, a core that is twice as long also means an analysing power that is about twice as high. Extrapolated simulation results showed that with several pC charge incident on the polarimeter, TeV-level energy sums are deposited in the calorimeter during each shot. To resolve the small anticipated asymmetries ($\sim 1.5‰$) by averaging over a reasonable number of shots, the calorimeter's energy resolution would need to be better than 2%.

The polarimeter that was eventually built, as part of a collaborative effort, consisted of a solenoid with a 150 mm core and an iron core polarisation of $P_{Fe} = 7.23 \pm 0.15\%$.

To achieve high energy resolution, a homogeneous lead-glass calorimeter was constructed [52]. Test beam measurements at the DESY II test beam facility, in combination with simulations, demonstrated that the design met the required specifications.
During commissioning of the polarimeter, another collaborative effort, an unpolarised electron beam was used to perform system tests and verify the functionality of the polarimeter. A key aspect of this process was a baseline accuracy check to assess how accurately the zero polarisation could be measured and to identify any systematic errors that might influence the results.
Gradual changes in beam parameter values over time were identified as a source of false asymmetries when averaged over different solenoid periods. Drifts in bunch charge over time resulted in a false asymmetry of $\delta_{q_m,\text{false}} = 0.4 \pm 0.3\%$. However, since shot-to-shot charge information was obtained using a scintillator screen camera setup, this charge asymmetry could be corrected. Conversely, drifts in the mean energy of accelerated bunches present a more significant challenge. Dedicated spectrometer runs and simulations indicate that false asymmetries on the order of $\left|\delta_{E,\text{false}}\right| = 0.4\%$ are expected. These cannot be corrected due to the destructive nature of the spectrometer measurement, which precludes simultaneous acquisition with the polarisation measurement. After applying charge fluctuation corrections, an asymmetry of $\delta_m = -0.48 \pm 0.07\%$ was measured using the polarimeter. Since expected asymmetries in future polarisation runs are at the per mille level ($\sim 1.5‰$), it is evident that any true signal would be completely masked by these false asymmetries. A meaningful measurement therefore requires a significant reduction in energy fluctuations.
As a central part of this thesis, LEAP_SIMS simulations were used to determine the analysing power, based on measured beam parameters. The result is $\mathcal{A} = 11.74 \pm 0.18\%$, with the dominant contribution to the uncertainty arising from the nonlinear response of the calorimeter to low energy particles [52], quantified as $\frac{\Delta\mathcal{A}}{\mathcal{A}} = 1.5\%$. This finding warrants further investigation.
An electron polarisation $P_{e^-} = 56.6 \pm 8.4\%$ was obtained. In addition to energy fluctuations, the accuracy of the charge measurement used for polarimeter signal correction (currently at approximately $\frac{q_m}{\Delta q_m} \approx 14\%$) and statistical limitations were identified as key factors constraining measurement accuracy. Given the current precision of the charge-corrected polarimeter signal ($\frac{\Delta Q_c}{Q} = 6.8\%$), measuring a polarisation of 10% with a relative accuracy of 20% would require an impractically long time of 22 hours.
Further research into an energy filtering setup and optimisation of the charge measurement upstream of the solenoid could potentially achieve energy fluctuations and charge measurement accuracies at the 1% level. Under these conditions, the required measurement time at 2 Hz could be reduced to approximately one hour.
In conclusion, the commissioning of the polarimeter has confirmed that it is able to deliver the performance it was designed for. Specifically, the polarimeter developed for LEAP is well-suited for measurements under the expected experimental conditions,

provided that long-term energy fluctuations are minimised and charge measurement accuracy is improved.

Appendix A.

List of LEAP_SIMS Classes

This appendix provides an overview of the custom C++ classes developed for LEAP_SIMS. For more details on its purpose, refer to chapter 5, and for an overview of GEANT4, the underlying simulation toolkit, see chapter 4. The classes are categorised based on their functionality within the simulation framework into four different groups: configuration management, detector geometry, physics and user actions. These are described here one after the other.

Configuration Management

This group of classes handles the setup and management of simulation parameters. It defines the static aspects of the simulation environment, including its configuration, physics models, and initial conditions. These classes ensure that all necessary parameters are properly initialised before the simulation runs.

ConfigReader

- Takes a string as input, specifying the path to a configuration file.
- Parses, retrieves, and interprets parameters from the configuration file.
- Reads the file and organises configuration parameters into sections and key-value pairs.
- Provides type-specific retrieval methods that convert string values to `int`, `double`, or `G4ThreeVector`.

- Includes specialised retrieval methods for certain configuration settings, such as `ReadOutputMode` and `ReadTreesInfo`.
- Designed for modularity, extensibility, and robust error handling.

AnaConfigManager

- Takes an instance of `ConfigReader` as input.
- Serves as the central management hub for configuring and controlling analysis and data output in the Geant4 simulation.
- Provides methods for initial **configuration setup**:
  - Accesses configuration files via `ConfigReader`.
  - Retrieves settings such as output mode, output file name, TTree information for data analysis and storage, and shower development status – essentially interpreting the configuration for analysis purposes.
  - Prepares internal mapping (`fNtupleNameToIdMap`).
- **Data Output Management**: Configures output file format, verbosity, and activation status by integrating with `G4AnalysisManager`.
- **Ntuple Booking**: Dynamically creates ntuples (Geant4's equivalent to ROOT TTrees) and their columns based on specified data types.
- **Data Filling**: Provides methods for populating ntuples in both detailed and summary modes.
- **Finalizing Output**: Saves ntuples to file by invoking `G4AnalysisManager`.
- **Metadata Management**: Generates a dedicated metadata ntuple based on configuration file parameters.

MacroGenerator

- Takes an instance of the configuration manager and a macro file name (string) as input.
- Accesses the configuration file via `ConfigReader`.
- Generates a text file that can be used as a Geant4 macro to configure the simulation at runtime.

Detector Geometry

This group of classes defines the experimental setup, including materials and sensitive volumes.

DetectorConstruction

- Main class for setting up the geometry of the Geant4 simulation.
- Handles the construction and configuration of the simulation's physical environment, including detectors and material specifications.
- Follows a modular approach.
- Takes instances of `ConfigReader` and `AnaConfigManager` as input.
- Subdetector instances, including `Solenoid`, `Calorimeter`, and `BeamLine`, are created and configured within the constructor.
- `Construct()` method: Assembles the world volume and places subcomponents. Material assignments and geometrical parameters are derived from the configuration data.
- `ConstructSDandField()` method: Sets up sensitive detectors and electromagnetic fields. Conditional activation of features is based on the configuration file.

Materials

- No input.
- The `DefineMaterials()` method in the constructor defines the materials used in the detector geometry.
- Includes a getter method for retrieving material properties.

BeamLine

- Takes instances of `ConfigReader` and `AnaConfigManager` as input.
- `ConstructBeamLine()` method: Depending on the status set in the configuration file, either the DESY II setup or the 28m setup is constructed. Returns the logical volume of the BeamLine to be placed in the detector construction.

Solenoid

- Takes instances of `ConfigReader` and `AnaConfigManager` as input.
- `ConstructSolenoid()` method returns logical volume of solenoid
- `ConstructSolenoidSD()` conditionally places sensitive detectore volumes before and behind solenoid core
- `ConstructSolenoidBfield()` adds a longitudinal magnetic field to the solenoid core (B_z)
- `SetBz()` changes the magnitude of B_z

SolenoidMessenger

- Facilitates user interaction with the simulation's solenoid configuration.
- Takes an instance of the `Solenoid` class as input.
- Registers and handles commands in the constructor, enabling the user to use `/solenoid/setBz` in the macro.

Calorimeter

- Takes instances of `ConfigReader` and `AnaConfigManager` as input.
- Constructs the calorimeter based on parameters specified in the configuration file.
- `ConstructCalo()` method returns the logical volume of the calorimeter.
- Utilizes materials defined in the `Materials` class.
- `ConstructCalorimeterSD()` method sets up sensitive detectors for the calorimeter.

BaseSensitiveDetector

- Inherits from `G4VSensitiveDetector`.
- Provides custom hit processing.
- Input: A string `name`, a `layerIdentifier` specifying the detector type, an integer `tupleId` for data recording, and an instance of `AnaConfigManager`.

- `ProcessHits()` method defines custom logic for handling particle interactions within the detector volume on a step level. Differentiates between summary and detailed modes.
- `Reset()` method clears accumulated data in summary mode.
- Base class that can be placed in multiple locations within the geometry.

CaloFrontSensitiveDetector

- Specialized hit processing for the calorimeter front.
- Inherits from `G4VSensitiveDetector`, with the same inputs as the base sensitive detector class.
- Facilitates output for each crystal in both detailed and summary modes.

CaloCrystalSD

- Specialized hit processing for calorimeter crystals.
- Inherits from `G4VSensitiveDetector`, with the same inputs as the base sensitive detector class.
- Accumulates deposited energy per crystal.
- If `fShowerDevStat` is `True`, fills the tuple with detailed information about shower development.
- `Reset()` method to clear accumulated data.

Physics

Specifies the physics processes and interactions included in the simulation.

PhysicsList

- Inherits from `G4VModularPhysicsList`.
- Main class for defining and managing the physics processes in the simulation.
- Inputs: The constructor takes a `G4String version`, which defines the physics configuration.

- The `ConstructParticle()` method constructs different particle types, including bosons, leptons, mesons, baryons, ions, and short-lived particles.
- The `ConstructProcess()` method adds various physics processes, including electromagnetic processes (via `PhysListEmPolarized`) and step limitation processes.
- The `AddPhysicsList()` method allows switching between different electromagnetic physics lists (standard or polarized).
- The `AddStepMax()` method adds the step limitation process to all applicable particles.
- The class uses the `PhysicsListMessenger` to facilitate user interaction and customization of the physics list through macros.

PhysListEmPolarized

- Inherits from `G4VPhysicsConstructor`.
- Defines polarised electromagnetic processes for photons, electrons, and positrons.
- The `ConstructProcess()` method adds relevant processes for polarised photons, electrons, and positrons (e.g., Compton scattering, ionisation, bremsstrahlung, and annihilation).

PhysListOptical

- Inherits from `G4VPhysicsConstructor`.
- Defines optical processes for photons in the simulation.
- The `ConstructProcess()` method adds optical processes such as Cherenkov radiation, scintillation, absorption, Rayleigh scattering, and boundary reflection/refraction.
- Configures the processes with parameters like the maximum number of secondaries generated per step.

StepMax

- Inherits from `G4VDiscreteProcess`, limits step size for charged particles.
- Uses `StepMaxMessenger` for user input.

StepMaxMessenger

- Facilitates user interaction for setting max step size.
- Takes instance of `StepMax` as input.

User Actions

Includes classes that are directly involved in the simulations runtime behaviour.

GPSPrimaryGeneratorAction

- Generates primary particles for each event using using `G4GeneralParticleSource`
- Takes no input.

EventAction

- Handles actions at the beginning and end of each event during simulation.
- The constructor initialises with `RunAction`, `DetectorConstruction`, and options for output type and version.
- The `BeginOfEventAction()` method initialises variables (e.g., energy sums, particle counts) based on event type and used geometry.
- The `EndOfEventAction()` method finalises data collection at the end of an event, depending on the output type and fills ntuple columns with energy and particle information for analysis.

RunAction

- Responsible for managing run-level actions, including the creation of analysis files, event initialization, and finalisation.
- The constructor initialises with `DetectorConstruction`, `PrimaryGeneratorAction`, output file name/type, version, and dipole state.
- **Methods**:
  - `BeginOfRunAction()`: Opens the output file, creates the analysis manager, and initialises histogram booking and process counters.

- `BookHisto()`: Books histograms and ntuples based on output type ("bunch", "single", "shower").
- `CountProcesses()`: Tracks the frequency of different physics processes occurring during the run.
- `EndOfRunAction()`: Finalizes the run, writes data to the output file, and displays process statistics.

Appendix B.

Example Configuration File

```
[Run]
type = asymmetry
flip = core
Nevents = 500000

[PhysicsList]
polarizationStatus = 1
opticalStatus = 0

[World]
material = Air

[Solenoid]
solenoidStatus = 1
type = TP2
convThick = 0
coreRad = 25
coreLength = 150
inFrontCore = 1
behindCore = 1
polDeg = 0.0723
BField = 0
Bz = 2.04
LanexStatus = 1
TableStatus = 1
xRot = 0
yRot = 0

[Calorimeter]
calorimeterStatus = 1
type = full
frontDetector = 1
backDetector = 0
crystDetector = 1
nCrystals = 9
caloMaterial = TF1
dist2Pol = 91
xpos = 0
ypos = 0
xRot = 0
yRot = 0
showerDev = 0
EinLimit = 0

[BeamLine]
beamLineStatus = 0
```

```
[Output]
mode = detailed
binWidthE = 0.5
nbinsProf = 200
fileName = output_filename

[GPS]
particle = e-
energy = histo
polDeg = 0
position = 0 0 -205
posType = Beam
direction = 0 0 1
nBunch = 1
spotSize = 0.0
divergence = 0.0 rad
eneType = User
sigmaE = histo
histname = /path/to/423A_APL_spec.hist

[RandomSeeds]
rndsds1 = 33239
rndsds2 = 44599
```

Appendix C.

Technical Drawings and Specifications

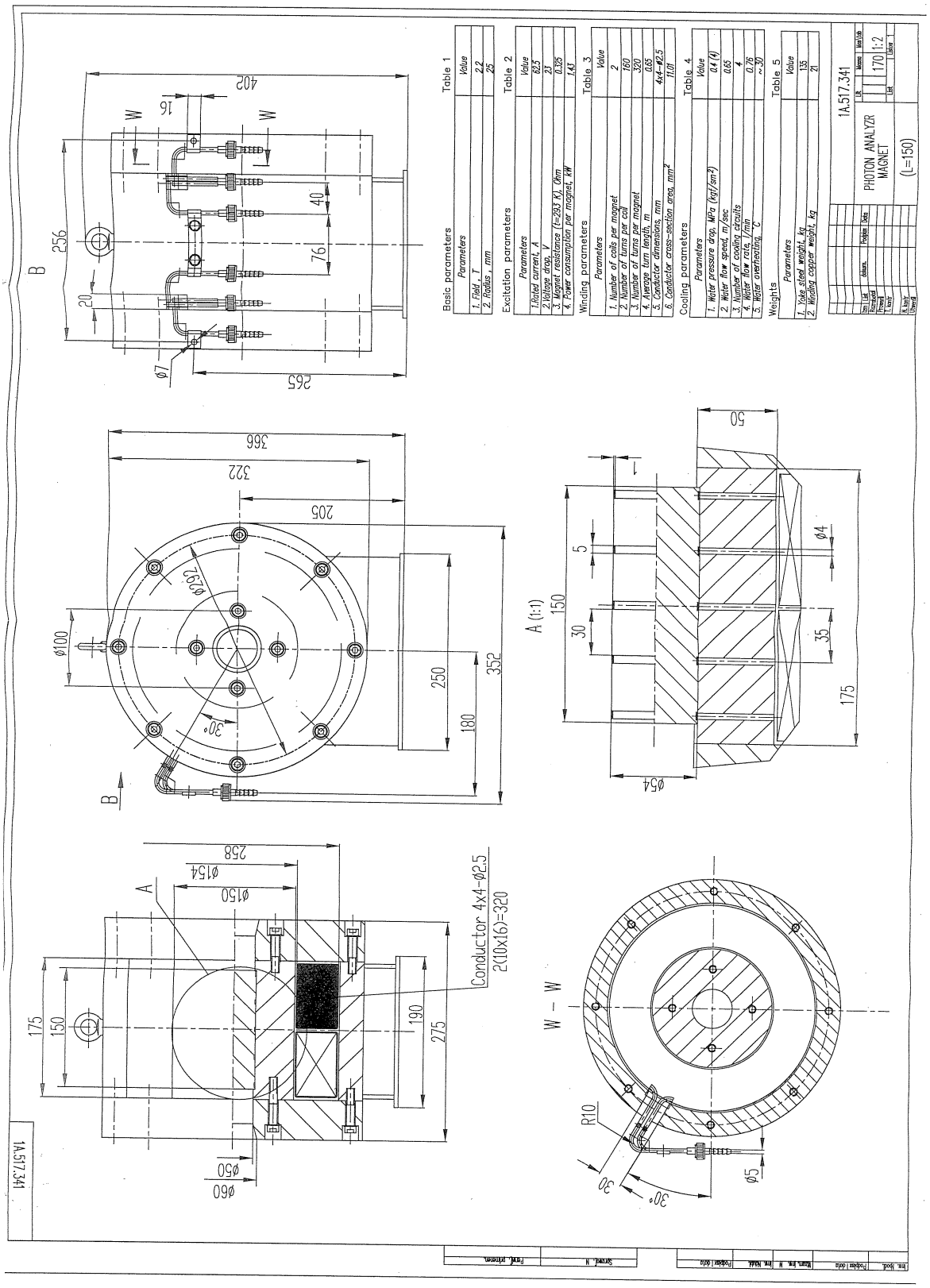

Figure C.1.: Technical drawing of the solenoid used for the LEAP project

Table C.1.: Parameters of the solenoid used in the LEAP-polarimeter

Parameter	value
overall length	275 mm
overall diameter	320 mm
iron core length	150 mm
iron core diameter	50 mm
length of internal Pb absorber	125 mm
overall mass	195 kg
number of coils	2
coil length	86 mm
coil inner diameter	152 mm
coil outer diameter	248 mm
number of turns per coil	175
conductor dimensions	4 x 4 mm
coolant bore diameter	2.5 mm
water cooling circuits	4
water flow rate	˜2 l/min
operating current	$\pm$ 60 A
power	1.37 kW
current reversal time	12.5 s
time between reversals	5 min
Field $B_z^{\max}$ at center	2.165 T
on-axis mean field at center	2.040 T
air field B_0 at center	0.100 T
$\langle P_{Fe} \rangle$ (on axis)	0.0723 $\pm$ 0.0723 T

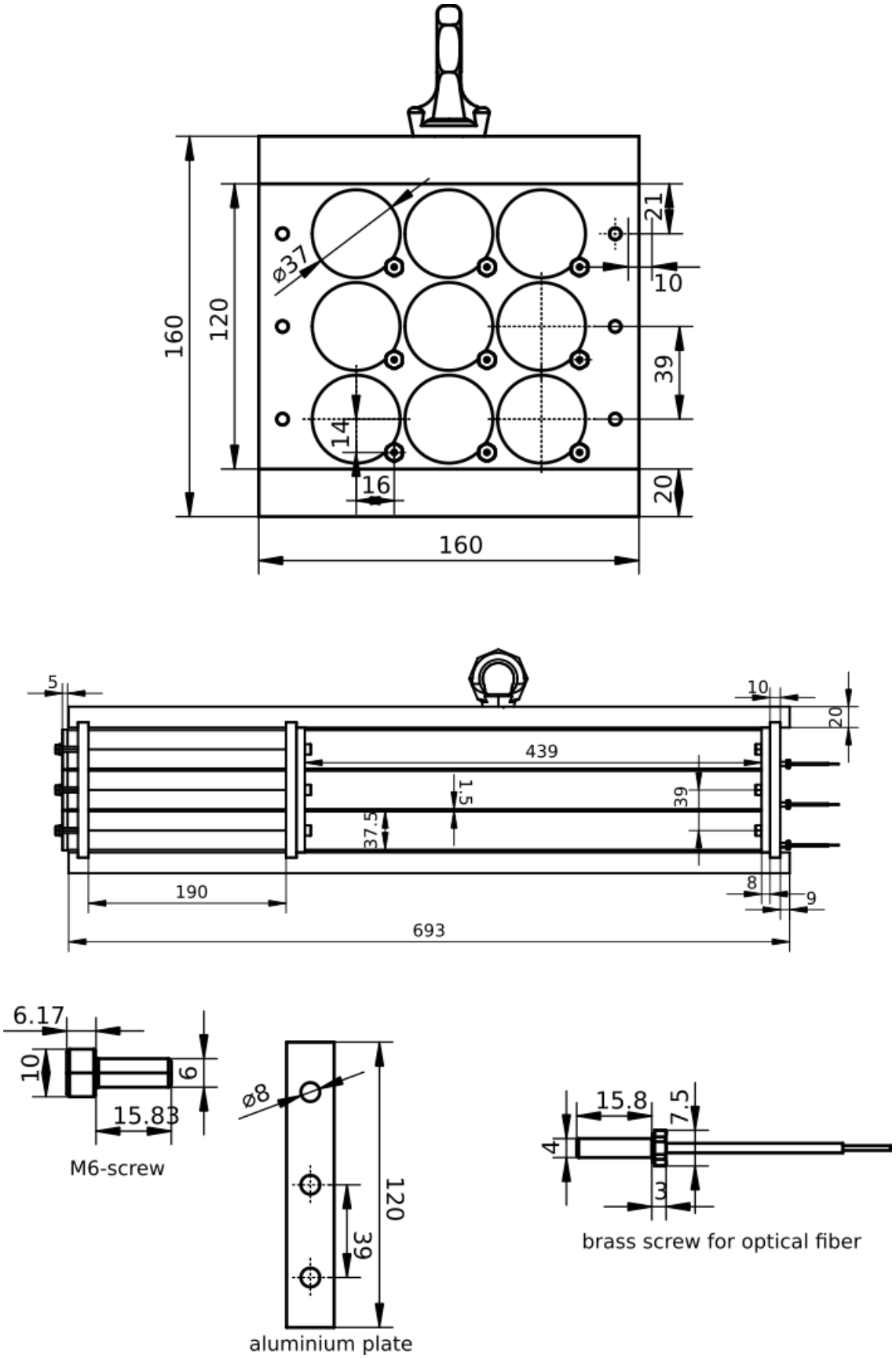

Figure C.2.: Technical Drawing of the LEAP calorimeter

Appendix D.

Experimental Run Overview

Table D.1.: Parameter overview for zero polarisation measurement runs – part 1

Run	V_{APL} / kV	Solenoid	N_{shots}	q_{DaMon} / pC	S_{scint} / a.u.	$\sigma_{S,y}$ / mm	θ / mrad
50280	20	off	492	6.83 ± 1.01	44.8 ± 16.7	0.76 ± 0.03	1.22 ± 0.15
50282	20	off	3728	6.77 ± 1.13	57.5 ± 18.1	0.74 ± 0.02	1.17 ± 0.1
50285	24	off	3563	6.20 ± 1.04	27.3 ± 14.4	0.76 ± 0.07	1.27 ± 0.34
50288	16	off	3417	6.68 ± 1.12	37.4 ± 14.0	0.79 ± 0.03	1.41 ± 0.15
50379	20	on	9239	5.16 ± 1.02	39.7 ± 12.9	0.74 ± 0.02	1.17 ± 0.10
50414	16	on	8207	5.87 ± 0.78	27.8 ± 12.6	0.81 ± 0.03	1.51 ± 0.15
50418	18	on	5741	4.82 ± 0.80	20.7 ± 11.8	0.77 ± 0.05	1.32 ± 0.24
50422	20	on	3600	4.62 ± 0.81	23.9 ± 13.4	0.75 ± 0.03	1.22 ± 0.15
50426	16	on	3434	4.80 ± 0.91	19.0 ± 10.4	0.81 ± 0.05	1.51 ± 0.24

Table D.2.: Parameter overview for zero polarisation measurement runs – part 2

Run	$\delta_{S_{scint}}$ /%	δ_Q /%	δ_{Q_c} /%
50282	-0.57 ± 0.45	-0.30 ± 0.37	0.27 ± 0.45
50285	-0.32 ± 0.64	-0.61 ± 0.47	-0.35 ± 0.24
50288	-1.42 ± 0.51	-1.58 ± 0.46	-0.16 ± 0.15
50379	0.43 ± 0.30	-0.07 ± 0.27	-0.48 ± 0.07
50414	1.18 ± 0.34	0.94 ± 0.31	-0.23 ± 0.09
50418	-0.79 ± 0.46	-0.14 ± 0.40	0.51 ± 0.19
50422	-1.84 ± 0.61	-1.90 ± 0.53	-0.06 ± 0.14
50426	1.13 ± 0.65	0.95 ± 0.60	-0.20 ± 0.19

Glossary

ADC Analog-to-Digital Converter

APL Active Plasma Lens

ASTRA A space charge tracking algorithm, program package developed at DESY [67]

BOND Beam Optimisation and Novel Diagnostics

DaMon Diagnostic tool for non-invasive measurement of electron bunch charge; Name derived from dark current monitor based on its original use.

DAQ Data AQuistion

DESY Deutsches Elektronen-Synchrotron

DOOCS Distributed Object-Oriented Control System Framework, software framework for creating accelerator-based control system applications.

FLARE Facility at DESY that provides infrastructure for research on laser plasma accelerators and their applications.

jddd Java DOOCS Data Display, editor and run-time engine for control system panels

LEAP Laser Electron Acceleration with Polarisation: Name of a project at DESY to accelerate polarised electron beams with a laser plasma accelerator

LEMO cables Refers to single coaxial cables equipped with LEMO 00 series push-pull connectors.

LPA Laser Plasma Acceleration

NIM Nuclear Instrumentation Module, standard defining mechanical and electrical specifications for electronic modules used in experimental particle and nuclear

physics. NIM logic is a fast logic standard. Negative Logic: NIM signals use negative logic, where a logic "1" is represented by a voltage between -0.8V and -1.2V, and a logic "0" is close to 0V. [162]

Opera Simulation Software. Finite Element Analysis software suite that allows engineers to perform simulations of electromagnetic (EM) and electromechanical systems in two and three dimensions. [111]

PCIe Peripheral Component Interconnect Express, high-speed serial computer expansion bus standard for data transfer

PMT Photomultiplier Tube

QAC Charge to Amplitude Conversion

QDC Charge to Digital Conversion

TTL Transistor-Transistor-Logic, uses between 0 and 0.4 V for logical 0 and between 2.4 V and 5 V for logical 1. [163]

VME Versa Module Eurocard, computer bus standard physically based on Eurocard sizes.

Bibliography

[1] E. Leader. *Spin in particle physics*. en. Cambridge, England: Cambridge University Press, 2023. DOI: https://doi.org/10.1017/9781009402040.

[2] G. Moortgat-Pick et al. "The role of polarized positrons and electrons in revealing fundamental interactions at the Linear Collider". *arXiv:hep-ph/0507011* (2005).

[3] The Linear Collider Collaboration Physics WG. "The role of positron polarization for the inital 250 GeV stage of the International Linear Collider". *arXiv:1801.02840 [hep-ph]* (2018).

[4] J. Beebe-Wang et al. *Electron Ion Collider Conceptual Design Report 2021*. Tech. rep. Brookhaven National Laboratory (BNL), 2021. DOI: https://doi.org/10.2172/1765663.

[5] A. A. Sokolov and I. Ternov. "On Polarization and Spin Effects in the Theory of Synchrotron Radiation". *Soviet Physics Doklady* 8 (1964). Provided by the SAO/NASA Astrophysics Data System, p. 1203. URL: https://ui.adsabs.harvard.edu/abs/1964SPhD....8.1203S.

[6] J. Grames and M. Poelker. "Polarized Electron Sources". *Polarized Beam Dynamics and Instrumentation in Particle Accelerators: USPAS Summer 2021 Spin Class Lectures*. Ed. by F. Méot et al. Springer International Publishing, 2023, pp. 261–284. URL: https://doi.org/10.1007/978-3-031-16715-7_11.

[7] D. Schultz et al. "The high peak current polarized electron source of the Stanford Linear Collider". en. *Nucl. Instrum. Methods Phys. Res. A* 340.1 (1994), pp. 127–132. DOI: https://doi.org/10.1016/0168-9002(94)91290-4.

[8] "The International Linear Collider Technical Design Report - Volume 3.II: Accelerator Baseline Design" (2013). Ed. by C. Adolphsen et al. DOI: https://doi.org/10.48550/arXiv.1306.6328.

[9] E. Esarey, C. B. Schroeder, and W. P. Leemans. "Physics of laser-driven plasma-based electron accelerators". *Rev. Mod. Phys.* 81 (3 2009), pp. 1229–1285. DOI: 10.1103/RevModPhys.81.1229.

[10] J. Vieira et al. "Polarized beam conditioning in plasma based acceleration". *Phys. Rev. ST Accel. Beams* 14 (7 2011), p. 071303. DOI: 10.1103/PhysRevSTAB.14.071303.

[11] Y. Wu et al. "Polarized electron-beam acceleration driven by vortex laser pulses". *New J. Phys.* 21.7 (2019), p. 073052. DOI: 10.1088/1367-2630/ab2fd7.

[12] M. Wen, M. Tamburini, and C. H. Keitel. "Polarized laser-WakeField-accelerated kiloampere electron beams". *Phys. Rev. Lett.* 122.21 (2019), p. 214801. DOI: https://doi.org/10.1103/PhysRevLett.122.214801.

[13] H. C. Fan et al. "Control of electron beam polarization in the bubble regime of laser-wakefield acceleration". *New J. Phys.* 24.8 (2022), p. 083047. DOI: 10.1088/1367-2630/ac8951.

[14] S. Bohlen et al. "Colliding pulse injection of polarized electron bunches in a laser-plasma accelerator". *Phys. Rev. Res.* 5 (3 2023), p. 033205. DOI: 10.1103/PhysRevResearch.5.033205.

[15] J. Kessler. *Polarized Electrons*. Springer Series on Atomic, Optical, and Plasma Physics. Berlin, Germany: Springer, 2010. DOI: https://doi.org/10.1007/978-3-662-02434-8.

[16] C. Cohen-Tannoudji, J. Dupont-Roc, and G. Grynberg. *Photons and atoms*. en. Ed. by C. Cohen-Tannoudji, J. Dupont-Roc, and G. Grynberg. Nashville, TN: John Wiley & Sons, 1997.

[17] H. Paetz. *Nuclear Physics with Polarized Particles*. Springer-Verlag Berin Heidelberg, 2012. DOI: https://doi.org/10.1007/978-3-642-24226-7.

[18] H. A. Tolhoek. "Electron polarization, theory and experiment". *Rev. Mod. Phys.* 28.3 (1956), pp. 277–298. DOI: https://doi.org/10.1103/RevModPhys.28.277.

[19] N. Zettili. *Quantum Mechanics*. en. 2nd ed. Hoboken, NJ: Wiley-Blackwell, 2009.

[20] W. Greiner. *Quantum Mechanics*. en. 4th ed. Berlin, Germany: Springer, 2000.

[21] D. Griffiths. *Introduction to elementary particles*. en. 2nd ed. Weinheim, Germany: Wiley-VCH Verlag, 2008.

[22] S. Weinberg. *The Quantum Theory of Fields: Volume I, Foundations*. Cambridge University Press, 1995.

[23] E. Hecht. *Optik, 5. Auflage*. Oldenbourg Wissenschaftsverlag GmbH, 2009. ISBN: 3486588613.

[24] Geant4 Collaboration. *Guide for Physics Lists*. https://geant4-userdoc.web.cern.ch/UsersGuides/PhysicsListGuide/html/index.html [Accessed: 12.03.24].

[25] A. G. Williams. *Introduction to Quantum Field Theory: Classical Mechanics to Gauge Field Theories*. Cambridge University Press, 2022. DOI: https://doi.org/10.1017/9781108585286.

[26] D. Goldberg. *The standard model in a nutshell*. Princeton University Press, 2017.

[27] C. S. Wu et al. "Experimental test of parity conservation in beta decay". *Phys. Rev.* 105.4 (1957), pp. 1413–1415. DOI: https://doi.org/10.1103/PhysRev.105.1413.

[28] J. List and Linear Collider Collaboration. "Polarized Beams at Future e+e- Colliders". *Proceedings of 40th International Conference on High Energy physics — PoS(ICHEP2020)*. Prague, virtual meeting: Sissa Medialab, 2021. DOI: https://doi.org/10.22323/1.390.0691.

[29] T. Tajima and J. M. Dawson. "Laser Electron Accelerator". *Phys. Rev. Lett.* 43 (4 1979), pp. 267–270. DOI: 10.1103/PhysRevLett.43.267.

[30] R. Bingham and R. Trines. "Introduction to plasma accelerators: The basics". *Proceedings of the 2014 CAS-CERN Accelerator School: Plasma Wake Acceleration* (2016). DOI: https://doi.org/10.5170/CERN-2016-001.67.

[31] V. Malka. "Laser Wakefield Acceleration of Electrons". *Applications of laser-driven particle acceleration*. Ed. by P. Bolton, K. Parodi, and J. Schreiber. CRC Press, 2018.

[32] A. Seryi and E. Seraia. *Unifying physics of accelerators, lasers and plasma*. 2nd ed. London, England: CRC Press, 2023. DOI: 10.1201/b18696.

[33] F. F. Chen. *Introduction to plasma physics and controlled fusion*. 3rd ed. Cham, Switzerland: Springer International Publishing, 2015. DOI: https://doi.org/10.1007/978-3-319-22309-4.

[34] J. M. Dawson. "Nonlinear electron oscillations in a cold plasma". *Phys. Rev.* 113.2 (1959), pp. 383–387. DOI: https://doi.org/10.1103/PhysRev.113.383.

[35] P. Sprangle et al. "Laser wakefield acceleration and relativistic optical guiding". *Appl. Phys. Lett.* 53.22 (1988), pp. 2146–2148. DOI: https://doi.org/10.1063/1.100300.

[36] M. Büscher et al. "Generation of polarized particle beams at relativistic laser intensities". *High Power Laser Sci. Eng.* 8.e36 (2020). DOI: https://doi.org/10.1017/hpl.2020.35.

[37] A. Hützen et al. "Polarized proton beams from laser-induced plasmas". *High Power Laser Sci. Eng.* 7.e16 (2019). DOI: doi:10.1017/hpl.2018.73.

[38] T. P. Rakitzis et al. "Spin-polarized hydrogen atoms from molecular photodissociation". *Science* 300.5627 (2003), pp. 1936–1938. DOI: DOI:10.1126/science.1084809.

[39] T. P. Rakitzis. "Pulsed-laser production and detection of spin-polarized hydrogen atoms". *ChemPhysChem* 5.10 (2004), pp. 1489–1494. DOI: https://doi.org/10.1002/cphc.200400108.

[40] D. Sofikitis et al. "Nanosecond control and high-density production of spin-polarized hydrogen atoms". *EPL* 81.6 (2008), p. 68002. DOI: 10.1209/0295-5075/81/68002.

[41] D. Sofikitis et al. "Highly nuclear-spin-polarized deuterium atoms from the UV photodissociation of deuterium iodide". *Phys. Rev. Lett.* 118.23 (2017). DOI: https://doi.org/10.1103/PhysRevLett.118.233401.

[42] D. Sofikitis et al. "Ultrahigh-density spin-polarized H and D observed via magnetization quantum beats". *Phys. Rev. Lett.* 121.8 (2018), p. 083001. DOI: https://doi.org/10.1103/PhysRevLett.121.083001.

[43] A. K. Spiliotis et al. "Ultrahigh-density spin-polarized hydrogen isotopes from the photodissociation of hydrogen halides: new applications for laser-ion acceleration, magnetometry, and polarized nuclear fusion". en. *Light Sci. Appl.* 10.1 (2021), p. 35. DOI: https://doi.org/10.1038/s41377-021-00476-y.

[44] D. Sofikitis et al. "Isolated spin polarized hydrogen atoms as targets for laser-induced polarized electron acceleration". *Front. Phys.* 12 (2024). DOI: https://doi.org/10.3389/fphy.2024.1480868.

[45] B. Friedrich and D. Herschbach. "Polarization of molecules induced by intense nonresonant laser fields". *The Journal of Physical Chemistry* 99.42 (1995), pp. 15686–15693. DOI: https://doi.org/10.1021/j100042a051.

[46] A. K. Spiliotis et al. "Depolarization of spin-polarized hydrogen via collisions with chlorine atoms at ultrahigh density". *Chemical Physics Impact* 2.100022 (2021), p. 100022. DOI: https://doi.org/10.1016/j.chphi.2021.100022.

[47] J. A. Beswick and M. Glass-Maujean. "Interference effects on the H(2p) to H(2s) branching ratio in the photodissociation of hydrogen and deuterium". en. *Phys. Rev. A Gen. Phys.* 35.8 (1987), pp. 3339–3349. DOI: https://doi.org/10.1103/PhysRevA.35.3339.

[48] M. Glass-Maujean, H. Frohlich, and J. A. Beswick. "Experimental evidence of an interference between photodissociation continua". en. *Phys. Rev. Lett.* 61.2 (1988), pp. 157–160. DOI: https://doi.org/10.1103/PhysRevLett.61.157.

[49] L. Drescher et al. "Extreme-ultraviolet spectral compression by four-wave mixing". en. *Nat. Photonics* 15.4 (2021), pp. 263–266. DOI: https://doi.org/10.1038/s41566-020-00758-8.

[50] I. Agapov et al. *The Plasma Injector for PETRA IV: Enabling Plasma Accelerators for Next-generation Light Sources. Conceptual Design Report*. Hamburg: Deutsches Elektronen-Synchrotron DESY, 2025, p. 66. DOI: 10.3204/PUBDB-2024-06078.

[51] S. Bohlen et al. "Stability of ionization-injection-based laser-plasma accelerators". *Phys. Rev. Accel. Beams* 25 (3 2022), p. 031301. DOI: 10.1103/PhysRevAccelBeams.25.031301.

[52] F. P. Stehr. "Towards spin-polarised electrons from a laser-plasma accelerator". PhD thesis. University of Hamburg, 2025.

[53] S. Bohlen. "Measurement of Electron Parameters using Thomson Scattering". PhD thesis. Universität Hamburg, Department of Physics, 2020. URL: https://ediss.sub.uni-hamburg.de/handle/ediss/9042.

[54] D. E.-S. DESY. *DOOCS. The Distributed Object-Oriented COntrol System Framework*. https://doocs.desy.de/ Accessed: 09.09.24 15:07.

[55] E. Sombrowski et al. "JDDD: a Java DOOCS data display for the XFEL". *ICALEPCS07, Knoxville, TN, USA* (2007). URL: https://api.semanticscholar.org/CorpusID:54911335.

[56] S. Schulz et al. "Femtosecond all-optical synchronization of an X-ray free-electron laser". *Nature communications* 6.1 (2015), p. 5938. DOI: https://doi.org/10.1038/ncomms6938.

[57] S. Schreiber and B. Faatz. "The free-electron laser FLASH". *High Power Laser Science and Engineering* 3 (2015), e20. DOI: 10.1017/hpl.2015.16.

[58] D. Lipka et al. "Dark current Monitor for the European XFEL". *Proceedings of DIPAC2011, Hamburg*. 2011.

[59] D. Lipka, J. Lund-Nielsen, and M. Seebach. "Resonator for charge measurement at REGAE". *Proceedings of IBIC2013, Oxford, UK*. 2013. DOI: 10.18429/JACOW-IBIC2023-TUP037.

[60] M. O. LLC. *DRZ screens datasheet*. http://www.mcio.com/Products/drz-screens.aspx [Accessed: 1.08.24 14:57].

[61] R. Morlotti et al. "Intrinsic conversion efficiency of X-rays to light in Gd2O2S : Tb3+ powder phosphors". *Journal of Luminescence* 72-74 (1997). Luminescence and Optical Spectroscopy of Condensed Matter, pp. 772–774. DOI: https://doi.org/10.1016/S0022-2313(96)00330-4.

[62] J.-P. Schwinkendorf et al. "Charge calibration of DRZ scintillation phosphor screens". *Journal of Instrumentation* 14.09 (2019), P09025. DOI: 10.1088/1748-0221/14/09/P09025.

[63] Y. Wu et al. "Note: Absolute calibration of two DRZ phosphor screens using ultrashort electron bunch". *Review of Scientific Instruments* 83.2 (2012). DOI: https://doi.org/10.1063/1.3681442.

[64] Y. Glinec et al. "Absolute calibration for a broad range single shot electron spectrometer". *Review of scientific instruments* 77.10 (2006). DOI: https://doi.org/10.1063/1.2360988.

[65] M. C. Downer et al. "Diagnostics for plasma-based electron accelerators". *Reviews of Modern Physics* 90.3 (2018), p. 035002. DOI: https://doi.org/10.1103/RevModPhys.90.035002.

[66] C. Varma. *Generation and Characterization of Electron Beams from a Laser-driven Plasma Accelerator*. 2023.

[67] K. Flöttman. *ASTRA - A space charge tracking algorithm: User Manual v. 3.2*. https://www.desy.de/~mpyflo/, Accessed: 10.09.24 11:30. 2017.

[68] J. van Tilborg et al. "Active Plasma Lensing for Relativistic Laser-Plasma-Accelerated Electron Beams". *Phys. Rev. Lett.* 115 (18 2015), p. 184802. DOI: 10.1103/PhysRevLett.115.184802.

[69] W. K. H. Panofsky and W. R. Baker. "A Focusing Device for the External 350Mev Proton Beam of the 184Inch Cyclotron at Berkeley". *Review of Scientific Instruments* 21.5 (1950), pp. 445–447. DOI: 10.1063/1.1745611.

[70] M. Meisel. "Tunable narrowband thomson source based on a laser-plasma accelerator". PhD thesis. University of Hamburg, 2023. URL: https://ediss.sub.uni-hamburg.de/handle/ediss/10283.

[71] C. A. Lindstrøm et al. "Emittance Preservation in an Aberration-Free Active Plasma Lens". *Phys. Rev. Lett.* 121 (19 2018), p. 194801. DOI: 10.1103/PhysRevLett.121.194801.

[72] P. D. Group. "Review of Particle Physics". *PTEP* 2022 (2022), p. 083C01. DOI: 10.1093/ptep/ptac097.

[73] G. Knoll. *Radiation Detection and Measurement*. 4th edition. Wiley, 2010. ISBN: 9780470131480.

[74] C. Leroy and P.-G. Rancoita. *Principles of radiation interaction in matter and detection*. 4th edition. World Scientific, 2016. DOI: https://doi.org/10.1142/6872.

[75] H. W. Koch and J. W. Motz. "Bremsstrahlung cross-section formulas and related data". *Rev. Mod. Phys.* 31.4 (1959), pp. 920–955. DOI: https://doi.org/10.1103/RevModPhys.31.920.

[76] L. Landau and I. Pomeranchuk. "Limits of applicability of the theory of bremsstrahlung electrons and pair production for high energies". *Doklady Akademii Nauk SSSR* 92 (1953), pp. 535–36.

[77] A. B. Migdal. "Bremsstrahlung and pair production in condensed media at high energies". *Phys. Rev.* 103.6 (1956), pp. 1811–1820. DOI: https://doi.org/10.1103/PhysRev.103.1811.

[78] M. Berger et al. *ESTAR, PSTAR, and ASTAR: Computer Programs for Calculating Stopping-Power and Range Tables for Electrons, Protons, and Helium Ions (version 2.0.1)*. en. 2017.

[79] A. Rohatgi. *WebPlotDigitizer*. Version 5.2. URL: https://automeris.io.

[80] M. J. Berger and S. M. Seltzer. "Bremsstrahlung and photoneutrons from thick tungsten and tantalum targets". *Phys. Rev. C Nucl. Phys.* 2.2 (1970), pp. 621–631. DOI: https://doi.org/10.1103/PhysRevC.2.621.

[81] S. M. Seltzer and M. J. Berger. "Bremsstrahlung energy spectra from electrons with kinetic energy 1 keV–10 GeV incident on screened nuclei and orbital electrons of neutral atoms with Z = 1–100". *At. Data Nucl. Data Tables* 35.3 (1986), pp. 345–418. DOI: https://doi.org/10.1016/0092-640X(86)90014-8.

[82] H. Olsen and L. C. Maximon. "Photon and electron polarization in high-energy bremsstrahlung and pair production with screening". *Phys. Rev.* 114.3 (1959), pp. 887–904. DOI: https://doi.org/10.1103/PhysRev.114.887.

[83] R. Barday et al. "Compton transmission polarimeter for a very precise polarization measurement within a wide range of electron currents". *Journal of Physics: Conference Series* 298.1 (2011), p. 012022. DOI: 10.1088/1742-6596/298/1/012022.

[84] K. W. McVoy. "Circular polarization of bremsstrahlung from polarized electrons in born approximation". *Phys. Rev.* 110.6 (1958), pp. 1484–1484.

[85] P. A. Cherenkov. "Visible radiation produced by electrons moving in a medium with velocities exceeding that of light". *Phys. Rev.* 52.4 (1937), pp. 378–379. DOI: https://doi.org/10.1103/PhysRev.52.378.

[86] I. Frank and I. Tamm. "Coherent visible radiation of fast electrons passing through matter". *Selected Papers*. Berlin, Heidelberg: Springer Berlin Heidelberg, 1991, pp. 29–35. DOI: https://doi.org/10.1007/978-3-642-74626-0_2.

[87] G. Viehhauser and T. Weidberg. *Detectors in particle physics*. en. London, England: CRC Press, 2024. DOI: 10.1201/9781003287674.

[88] A. H. Compton. "A quantum theory of the scattering of X-rays by light elements". *Phys. Rev.* 21.5 (1923), pp. 483–502. DOI: https://doi.org/10.1103/PhysRev.21.483.

[89] O. Klein and Y. Nishina. "Über die Streuung von Strahlung durch freie Elektronen nach der neuen relativistischen Quantendynamik von Dirac". *Z. Phys.* 52.11-12 (1929), pp. 853–868. DOI: https://doi.org/10.1007/BF01366453.

[90] S. B. Gunst and L. A. Page. "Compton scattering of 2.62-mev gamma rays by polarized electrons". *Phys. Rev.* 92.4 (1953), pp. 970–973. DOI: https://doi.org/10.1103/PhysRev.92.970.

[91] C. K. Sinclair. "Electron beam polarimetry". Stanford, California (USA): AIP, 1998. DOI: https://doi.org/10.1063/1.57045.

[92] K. Aulenbacher et al. "Precision electron beam polarimetry for next generation nuclear physics experiments". *Int. J. Mod. Phys. E* 27.07 (2018), p. 1830004. DOI: https://doi.org/10.1142/S0218301318300047.

[93] V. Tioukine, K. Aulenbacher, and E. Riehn. "A Mott polarimeter operating at MeV electron beam energies". en. *Rev. Sci. Instrum.* 82.3 (2011), p. 033303. DOI: https://doi.org/10.1063/1.3556593.

[94] J. M. Grames et al. "High precision 5 MeV Mott polarimeter". en. *Phys. Rev. C.* 102.1 (2020). DOI: https://doi.org/10.1103/PhysRevC.102.015501.

[95] B. Wagner et al. "A Møller polarimeter for CW and pulsed intermediate energy electron beams". *Nucl. Instrum. Methods Phys. Res. A* 294.3 (1990), pp. 541–548. DOI: 10.1016/0168-9002(90)90296-I.

[96] B. Sobloher et al. "Polarisation at HERA - Reanalysis of the HERA II Polarimeter Data". *arXiv preprint arXiv:1201.2894* (2012).

[97] M. Woods and representing the SLD collaboration. *The scanning Compton polarimeter for the SLD experiment*. 1996.

[98] W. Heil et al. "Improved limits on the weak, neutral, hadronic axial vector coupling constants from quasielastic scattering of polarized electrons". *Nucl. Phys. B.* 327.1 (1989), pp. 1–31. DOI: https://doi.org/10.1016/0550-3213(89)90284-8.

[99] G. Blume et al. "A Compton transmission polarimeter for DC and SRF electron photo-injectors". *Nucl. Instrum. Methods Phys. Res. A* 1062.169224 (2024), p. 169224. DOI: https://doi.org/10.1016/j.nima.2024.169224.

[100] C. Weinrich. *Entwicklung einesvTransmissions-Compton-Polarimeters für das A4-Experiment*. 2000.

[101] C. Weinrich. "The transmission Compton polarimeter of the A4 experiment". *Eur. Phys. J. A* 24.Supplement 2 (2005), s2.129–s2.130. DOI: 10.1140/epjad/s2005-04-030-2.

[102] T. Zwart et al. "Transmission Polarimetry at MIT Bates". *AIP Conference Proceedings*. Upton, New York (USA): AIP, 2003. DOI: 10.1063/1.1607286.

[103] G. Alexander et al. "Undulator-based production of polarized positrons". *Nuclear Instruments and Methods in Physics Research Section A: Accelerators, Spectrometers, Detectors and Associated Equipment* 610.2 (2009), pp. 451–487. DOI: https://doi.org/10.1016/j.nima.2009.07.091.

[104] K. Laihem. "Measurement of the positron polarization at an helical undulator based positron source for the International Linear Collider ILC". PhD thesis. Humboldt-Universität zu Berlin, 2008. DOI: https://doi.org/10.18452/15990.

[105] A. Adeyemi, E. Voutier, et al. "The Calibration of the PEPPo Polarimeter for Electrons and Positrons". *Proceedings of IPAC2013*. 2013.

[106] D. Abbott et al. "Production of highly polarized positrons using polarized electrons at MeV energies". *Phys. Rev. Lett.* 116.21 (2016). DOI: https://doi.org/10.1103/PhysRevLett.116.214801.

[107] M. Goldhaber, L. Grodzins, and A. W. Sunyar. "Evidence for circular polarization of bremsstrahlung produced by beta rays". *Phys. Rev.* 106.4 (1957), pp. 826–828. DOI: DOI:https://doi.org/10.1103/PhysRev.106.826.

[108] M. Berger et al. *XCOM: Photon Cross Section Database (version 1.5)*. en. 2010.

[109] H. Schopper. "Measurement of circular polarization of γ-rays". *Nucl. Instrum.* 3.3 (1958), pp. 158–176. DOI: https://doi.org/10.1016/0369-643X(58)90018-5.

[110] P. C. Macq, K. M. Crowe, and R. P. Haddock. "Helicity of the electron and positron in muon decay". *Phys. Rev.* 112.6 (1958), pp. 2061–2071. DOI: https://doi.org/10.1103/PhysRev.112.2061.

[111] D. Systèmes. *Opera Product Information Page*. https://www.3ds.com/products/simulia/opera, Accessed: 15.09.24 10:24.

[112] R. Wigmans. *Calorimetry*. 2nd ed. International Series of Monographs on Physics. London, England: Oxford University Press, 2017. ISBN: 9780198786351.

[113] C. W. Fabjan and F. Gianotti. "Calorimetry for particle physics". *Reviews of Modern Physics* 75.4 (2003), p. 1243. DOI: https://doi.org/10.1103/RevModPhys.75.1243.

[114] J. Sauvan. Calorimetry in HEP: From concepts to experiments, ESIPAP 2020, https://indico.cern.ch/event/855973/contributions/3602188/attachments/1979913/3296643/calorimetry_sauvan_esipap2020.pdf.

[115] N. T. Thomopoulos. *Essentials of Monte Carlo simulation: Statistical methods for building simulation models*. Springer Science & Business Media, 2012. DOI: https://doi.org/10.1007/978-1-4614-6022-0.

[116] F. James. "Monte Carlo theory and practice". *Reports on Progress in Physics* 43.9 (1980), p. 1145. DOI: 10.1088/0034-4885/43/9/002.

[117] W. L. Dunn and J. K. Shultis. *Exploring Monte Carlo Methods (Second Edition)*. Second Edition. Elsevier, 2023. ISBN: 978-0-12-819739-4.

[118] N. Metropolis and S. Ulam. "The monte carlo method". *Journal of the American statistical association* 44.247 (1949), pp. 335–341. DOI: https://doi.org/10.1080/01621459.1949.10483310.

[119] S. Weinzierl. *Introduction to Monte Carlo methods*. https://arxiv.org/abs/hep-ph/0006269arXiv:hep-ph/0006269. 2000.

[120] M. Bonamente. *Statistics and Analysis of Scientific Data*. 3rd Edition. Springer Nature, 2022.

[121] L. Lista. *Statistical Methods for Data Analysis: With Application in Particle Physics*. Third Edition. Vol. 1010. Lecture Notes in Physics. Springer International Publishing, 2024. DOI: https://doi.org/10.1007/978-3-031-19934-9.

[122] D. Landau and K. Binder. *A guide to Monte Carlo simulations in statistical physics*. 4th edition. Cambridge University Press, 2015. DOI: https://doi.org/10.1017/CBO9781139696463.

[123] F. Martelli et al. "Verification method of Monte Carlo codes for transport processes with arbitrary accuracy". *Scientific reports* 11.1 (2021), p. 19486. DOI: https://doi.org/10.1038/s41598-021-98429-3.

[124] S. Agostinelli et al. "Geant4a simulation toolkit". *Nuclear Instruments and Methods in Physics Research Section A: Accelerators, Spectrometers, Detectors and Associated Equipment* 506.3 (2003), pp. 250–303. DOI: https://doi.org/10.1016/S0168-9002(03)01368-8.

[125] J. Allison et al. "Geant4 developments and applications". *IEEE Transactions on Nuclear Science* 53.1 (2006), pp. 270–278. DOI: 10.1109/TNS.2006.869826.

[126] J. Allison et al. "Recent developments in Geant4". *Nuclear Instruments and Methods in Physics Research Section A: Accelerators, Spectrometers, Detectors and Associated Equipment* 835 (2016), pp. 186–225. DOI: https://doi.org/10.1016/j.nima.2016.06.125.

[127] Geant4 Collaboration. *Overview of Geant4*. https://geant4.web.cern.ch/about/ [Accessed: 6.03.2024].

[128] Geant4 Collaboration. *Introduction to Geant4, Release 11.1*. https://geant4-userdoc.web.cern.ch/UsersGuides/IntroductionToGeant4/html/index.html. Rev 7.1: 31.07.23.

[129] G. Folger. *Physics Lists*. Geant4 Advanced Course, 1. October 2020, CERN.

[130] J. Apostolakis et al. "GEANT4 Physics Lists for HEP". *2008 IEEE Nuclear Science Symposium Conference Record*. 2008, pp. 833–836. DOI: 10.1109/NSSMIC.2008.4774655.

[131] Geant4 Collarboration. *Geant4 Book For Application Developers, Release 11.2*. https://geant4-userdoc.web.cern.ch/UsersGuides/ForApplicationDeveloper/html/index.html[Accessed: 7.03.2024].

[132] M. Asai. *Basic structure of the Geant4 Simulation Toolkit*. Geant4 course at IEEE NSS-MIC, 19. October 2003, Portland.

[133] M. Novak and M. Asai. *User Interface I: UI commands*. Geant4 beginners course at CERN, Geneva, 22-23 January 2019.

[134] Geant4 Collaboration. *Physics Reference Manual, Release 11.1*. https://geant4-userdoc.web.cern.ch/UsersGuides/PhysicsReferenceManual/html/index.html. Rev 7.1: 31.07.23.

[135] W. H. McMaster. "Matrix Representation of Polarization". *Rev. Mod. Phys.* 33 (1 1961), pp. 8–28. DOI: 10.1103/RevModPhys.33.8.

[136] A. Haupt, Y. Kemp, and F. Nowak. "Evolution of Interactive Analysis Facilities: from NAF to NAF 2.0". *Journal of Physics: Conference Series* 513 (3 2014), p. 16. DOI: 10.1088/1742-6596/513/3/032072.

[137] U. o. W.-M. Center for High Throughput Computing Computer Sciences Department. *HTCondor Version 23.4.0 Manual*. https://htcondor.readthedocs.io/en/latest/ [Accessed: 6.03.2024].

[138] J. Popp and F. Stehr. *leap_sims*. https://github.com/JennPopp/leap_sims, Accessed: 03.06.24 13:13.

[139] R. Brun and F. Rademakers. "ROOT An object oriented data analysis framework". *Nuclear Instruments and Methods in Physics Research Section A: Accelerators, Spectrometers, Detectors and Associated Equipment* 389.1 (1997). New Computing Techniques in Physics Research V, pp. 81–86. DOI: https://doi.org/10.1016/S0168-9002(97)00048-X.

[140] M. Verderi. *Random Numbers*. Geant4 PHENIICS & ANF IN2P3 Tutorial, 22-26 May 2023, Orsay.

[141] H. Jansen et al. "Performance of the EUDET-type beam telescopes". *EPJ Tech. Instrum.* 3.1 (2016). DOI: https://doi.org/10.1140/epjti/s40485-016-0033-2.

[142] *Valgrind Documentation*. https://valgrind.org/docs/, Accessed: 13.01.2025 10:42.

[143] D. Jones et al. "Accurate determination of the electron spin polarization in magnetized iron and nickel foils for Møller polarimetry". *Nuclear Instruments and Methods in Physics Research Section A: Accelerators, Spectrometers, Detectors and Associated Equipment* 1043 (2022), p. 167444. DOI: https://doi.org/10.1016/j.nima.2022.167444.

[144] M. Balatz et al. "The lead-glass electromagnetic calorimeter for the SELEX experiment". *Nuclear Instruments and Methods in Physics Research Section A: Accelerators, Spectrometers, Detectors and Associated Equipment* 545.1-2 (2005), pp. 114–138. DOI: https://doi.org/10.1016/j.nima.2005.01.328.

[145] R. A. Khalek et al. "Science requirements and detector concepts for the electron-ion collider: EIC yellow report". *Nuclear Physics A* 1026 (2022), p. 122447. DOI: https://doi.org/10.1016/j.nuclphysa.2022.122447.

[146] P. S.A.S. *Photomuliplier Tubes Catalogue*. https://hallcweb.jlab.org/DocDB/0008/000809/001/PhotonisCatalog.pdf [Accessed: 29.08.24 16:08]. 2007.

[147] C.A.E.N. *Technical Information Manual: SY127 High Voltage System*. https://groups.nscl.msu.edu/nscl_library/manuals/caen/sy127.pdf [Accessed: 30.08.24 10:00]. 1991.

[148] C. Liechti. *pySerial Documentation, Revision 7aeea354*. https://pyserial.readthedocs.io/en/latest/pyserial.html[Accessed: 04.09.2024 15:43].

[149] C.A.E.N. *Technical Information Manual: 16 channel dual range QDC Mod. V965, Manual Rev. 8*. http://orca.physics.unc.edu/orca/VME/V965_files/V965_rev8.pdf [Accessed: 30.08.24 10:20]. 2008.

[150] C.A.E.N. *Technical Information Manual: VME-PCI Optical Link Bridge Mod. V2718, Manual Rev. 11*. 2018. URL: https://wwwusers.ts.infn.it/~rui/univ/Acquisizione_Dati/Manuals/CAEN%20V2718%20rev11.pdf.

[151] C.A.E.N. *Technical Specifications of A3818 PCIe CONET2 Controller*. https://www.caen.it/products/a3818/[Accessed: 05.09.2024 16:01].

[152] R. Diener et al. "The DESY II test beam facility". *Nuclear Instruments and Methods in Physics Research Section A: Accelerators, Spectrometers, Detectors and Associated Equipment* 922 (2019), pp. 265–286. DOI: https://doi.org/10.1016/j.nima.2018.11.133.

[153] B. Instrumentation. *Data Sheet of ICT-VAC-082-Turbo2*. https://www.bergoz.com/wp-content/uploads/Turbo-ICT-manual-3-1-1.pdf [Accessed: 19.08.24 15:56].

[154] L. Fröhlich et al. "Taskomat & Taskolib: A Versatile, Programmable Sequencer for Process Automation". *PCaPAC 2022 hosted by ELI Beamlines* (2022), p. 94. DOI: 10.3204/PUBDB-2022-04664.

[155] B. Hidding et al. "Novel method for characterizing relativistic electron beams in a harsh laser-plasma environment". *Review of Scientific Instruments* 78.8 (2007). DOI: 10.1063/1.2775668.

[156] S. Bohlen et al. *Noninvasive cavity-based charge diagnostic for plasma accelerators*. arXiv:2403.07135v1 [physics.acc-ph]. 2024.

[157] Photonis. *Photomultiplier tubes: Principle & Applications*. https://psec.uchicago.edu/library/photomultipliers/Photonis_PMT_basics.pdf [Accessed: 07.11.24 16:35]. 2002.

[158] Geant4 Collaboration. *Geant4 gitlab repository*. https://gitlab.cern.ch/geant4/geant4 [Accessed: 18.11.24 11:29].

[159] A. Ferran Pousa et al. "Energy compression and stabilization of laser-plasma accelerators". en. *Phys. Rev. Lett.* 129.9 (2022), p. 094801. DOI: https://doi.org/10.1103/PhysRevLett.129.094801.

[160] M. Kirchen et al. "Optimal beam loading in a laser-plasma accelerator". en. *Phys. Rev. Lett.* 126.17 (2021), p. 174801. DOI: https://doi.org/10.1103/PhysRevLett.126.174801.

[161] S. Jalas et al. "Bayesian optimization of a laser-plasma accelerator". *Phys. Rev. Lett.* 126.10 (2021), p. 104801. DOI: https://doi.org/10.1103/PhysRevLett.126.104801.

[162] W. R. Leo. "The NIM Standard". *Techniques for Nuclear and Particle Physics Experiments*. Berlin, Heidelberg: Springer Berlin Heidelberg, 1994, pp. 257–261. DOI: https://doi.org/10.1007/978-3-642-57920-2_12.

[163] R. Prasad. *Analog and digital electronic circuits*. 2021st ed. Undergraduate Lecture Notes in Physics. Cham, Switzerland: Springer Nature, 2021. DOI: 10.1007/978-3-030-65129-9.

[164] A. Buckley. *The hepthesis LaTeX class*.

[165] OpenAI. *ChatGPT*. Large language model, https://openai.com/chatgpt. Accessed: 2025-03-06. 2024.

List of figures

List of tables

Acknowledgements

My name may be on the front of this document, but this project was far from a one-woman show. So many people have contributed, and I want to take this opportunity to acknowledge and thank each of you. If you dont see your name here, please know its not for lack of gratitude but perhaps just my forgetfulness! I truly appreciate each and every one of you.

Above all, I want to thank **Jenny** for her invaluable supervision – always providing guidance, insightful feedback, and encouragement to help us DRs grow as independent researchers. Many thanks also to **Kris** for being a great PI – I very much appreciate your advice and support. And, of course, my sincere thanks to my professor, **Gudi**, and the rest of my committee for taking the time to evaluate my thesis.

Felix, my partner in crime and friend, we faced every obstacle together – whether it was wading through oceans of compiler errors, delving in to the deepest dungeons to source obscure equipment, or enduring countless hours of 'lets just finish this and go home.' While we never managed an experiment with a polarised particle source, we did get the polarimeter up and running, extracted results from Geant4, and found the sweetest blackberries on campus. I truly appreciate and thank you!

I also want to express my deepest appreciation to the members of **SLB** for always being there with both advice and hands-on help whenever needed. A special thanks to **Louis, Tanguy, Antonios**, and the rest of the LUXE crew for their immense contributions to the various experimental campaigns, and to **Bohdan** for helping me navigate many a ROOT conundrum.

Having the opportunity to work with and learn from not just one, but two amazing groups made this journey even more rewarding. That's why I am very grateful to the former **MPA4** and, in particular, to **Simon**, **Martin**, and **Song** for operating the accelerator and for their invaluable support during the BOND-Lab experiments and beyond.

None of the experimental work would have been possible without the incredible efforts of the engineers and technicians who made the LEAP-polarimeter a reality.

You all did an amazing job – constructing the calorimeter, getting the solenoid fully functional and into the second-floor lab, and providing us with the tools and means to control them, take data, and actually save it!
Beyond science and technology, there were many individuals whose encouragement and understanding helped me push trough. In this regard, I want to thank the **FTX-ECRs** for Friday night dinners, game nights, various debates – whether silly or serious – glorious cakes, little duckling, and arts and crafts. Moreover, thanks a lot to my fellow **HeJus** – we've done incredible work, and I truly enjoyed being part of such a dedicated and inspiring group.
I also want to thank **Petra** for reminding me to breathe deeply and for making me run the 7.5K. **Fija, Susi**, and the rest of the DESY choir – our music together is a joy, but it's the time we spend together that I truly cherish. I am also extremely grateful to **my gang of friends from Oldenburg** for providing me with bad jokes and East Frisian tea, pushing me to step out of my comfort zone, and helping me and my books move. Also, to be honest, if we hadn't crammed together so much back in the Ringebene, they probably would never have taken me on at DESY.
Finally, my most heartfelt thanks go to my **family**. You have always believed in me, taken care of me, and worked so hard. That is a very solid foundation to stand on. A special thank you to my mother, **Elke**, for your love and unwavering support!

Colophon

This thesis was made in LaTeX 2_ε using the "hepthesis" class [164].

ChatGPT [165], an AI-based language model, was used for linguistic refinement, specifically for grammar correction and optimization of language flow.